



Thermal Effects and Erosion Rates Resulting from Intense Deposition of Energy in Fusion Reactor First Walls

Ahmed M. Hassanein

March 1982

UWFDM-465

Ph.D. Thesis.

***FUSION TECHNOLOGY INSTITUTE
UNIVERSITY OF WISCONSIN
MADISON WISCONSIN***

**Thermal Effects and Erosion Rates Resulting
from Intense Deposition of Energy in Fusion
Reactor First Walls**

Ahmed M. Hassanein

Fusion Technology Institute
University of Wisconsin
1500 Engineering Drive
Madison, WI 53706

<http://fti.neep.wisc.edu>

March 1982

UWFDM-465

Ph.D. Thesis.

THERMAL EFFECTS AND EROSION RATES RESULTING FROM INTENSE
DEPOSITION OF ENERGY IN FUSION REACTOR FIRST WALLS

BY

AHMED MOUSSA HASSANEIN

A thesis submitted in partial fulfillment of the
requirements for the degree of

DOCTOR OF PHILOSOPHY

(Nuclear Engineering)

at the

UNIVERSITY OF WISCONSIN-MADISON

1982

THERMAL EFFECTS AND EROSION RATES RESULTING FROM INTENSE
DEPOSITION OF ENERGY IN FUSION REACTOR FIRST WALLS

Ahmed Moussa Hassanein

Under the Supervision of Professor Gerald L. Kulcinski

This research is devoted to the development of more precise models to calculate thermal effects and erosion rates due to energy deposition from different radiation species in fusion reactor first walls. These species may include laser light, x-rays, and light or heavy ions in Inertial Confinement Fusion (ICF) reactors. The response of first walls during the deposition of high energy densities resulting from plasma disruptions in magnetic fusion reactors is also included.

Previous models to calculate thermal response and erosion rates ignored many factors that this study showed to be of great importance. Models are developed in this thesis to calculate the temperature rise in fusion first walls with both finite difference techniques and Green's function methods. The heat conduction equation is solved including possible phase changes and two moving boundaries; one for the melt-solid interface, and one for the receding surface due to evaporation. Variations of thermal properties with temperature for both liquid and solid phases are included.

Models to calculate the evaporative erosion of first walls with time dependent kinetics based on transport theory are developed. A model is developed to study the effect of "self-shielding", i.e. the

shielding of the first wall from the incoming plasma ions by the vapor layer produced in front of the surface.

All models developed in this thesis were incorporated into a general computer code (A*THERMAL). Parametric studies with large variations in characteristic spectral parameters for different kinds of radiation in ICF reactors are performed with this code. In addition, the response of the wall to a complete set of spectra incident simultaneously could be examined.

Parametric analyses are also performed with the code to study the response of magnetic fusion first walls during plasma disruptions. The materials considered for the calculations were stainless steel, carbon, and the refractory metal, Mo. The effect of vapor shielding, various disruption times, and different pulse shapes on the amount of melted and evaporated material were also examined.

Results of these analyses showed the importance of developing accurate models to calculate energy depositions, thermal effects and erosion rates. Substantial differences do result between the models developed in this thesis and previous models which ignore many of the factors considered in this work.

Approved:

Jan 18, 1982

Date

Gerald L. Kulcinski
Professor of Nuclear Engineering

THERMAL EFFECTS AND EROSION RATES RESULTING FROM INTENSE
DEPOSITION OF ENERGY IN FUSION REACTOR FIRST WALLS

A thesis submitted to the Graduate School of the
University of Wisconsin-Madison in partial fulfillment of
the requirements for the degree of Doctor of Philosophy

by

AHMED MOUSSA HASSANEIN

Degree to be awarded: December 19____ May 1982____ August 19____

ACKNOWLEDGMENTS

The advice, comments, and sincere help of my advisor, Professor G.L. Kulcinski, are greatly appreciated. Without his guidance, support, and motivation, this work would not have been possible.

I would also like to express my appreciation to Professor W.G. Wolfer whose help and comments were another light for continuing this work.

Sincere thanks go to Dr. M. Sawan for his valuable discussions and helpful suggestions. Helpful discussions with Dr. R. Peterson were also appreciated.

I would like to thank my fellow graduates for their valuable discussions and friendship, especially T. McCarville, R. Watson and all the Radiation Damage Group.

I am also grateful to Ms. Beth Brown for her neatness, diligence, and the many hours spent typing this document. Also I would like to thank Mr. Dennis Bruggink for his helpful assistance.

Both the endurance and encouragement of my wife, Clara, have been essential for the success of this achievement. I am deeply appreciative of her patience and understanding.

Last, but not least, I am absolutely grateful to my parents for their continuous encouragement and support and I would like to dedicate this work to them.

Support for this work was provided by the Division of Laser Fusion Energy (DLFE/DOE), the Wisconsin Electric Utilities Research Foundation (WEURF), and the Kernforschungszentrum Karlsruhe, West Germany.

TABLE OF CONTENTS

	<u>Page</u>
Abstract	ii
Acknowledgment	iv
List of Tables	xii
List of Figures	xiii
I. Introduction	1
II. First Wall Environments in Fusion Reactors	6
References for Chapter II	16
III. Interaction and Deposition of Radiation in Fusion	18
First Wall Materials	
A. Photon Interactions With Materials	18
B. Ion Interactions	20
B.1. Electronic Energy Loss	20
B.2. Nuclear Energy Loss	23
C. Energy Deposition	25
C.1. Laser Light Deposition	25
C.2. Photon Deposition	28
C.3. Ion Deposition	28
C.3.1. Introduction	28
C.3.2. Light Ions ($Z \leq 2$)	30
C.3.3. Heavy Ions ($Z > 2$)	31
C.3.4. Comparison of Results	33
References for Chapter III	39

	<u>Page</u>
IV. Numerical Methods for Calculating the Temperature Increases Using the Green's Function	41
A. Introduction	41
B. Direct Deposition Model	41
C. Simple Deposition Model	47
D. Uniform Deposition Model	49
E. General Deposition Model	52
F. Results and Conclusions	56
G. Approximate Solution for the Nonlinear Heat- Conduction Equation Using the Methods of Green's Function	68
H. Conclusions	78
Appendix A	80
References for Chapter IV	82
V. Thermal Response Models for Fusion First Walls	83
A. Introduction	83
B. Heat Conduction with Moving Boundaries	83
C. Formulation of the Heat Conduction Problem	86
C.1. Before Melting	86
C.2. During and After Melting	88
C.3. Evaporation Moving Boundary	90
D. Numerical Methods	92
D.1 Finite Difference Approximations	92
D.2 Space and Time Increments	93

	<u>Page</u>
D.3. Methods of Solution	93
D.4. Variations of the Thermal Properties with Temperature	94
D.5. Phase Change (Melting and Resolidification)	95
D.6. Initial and Boundary Conditions	96
E. Evaporation Models	96
F. Vapor Shielding	105
G. Summary	107
References for Chapter V	109
VI. The A*THERMAL Computer Code	111
A. Introduction	111
B. Code Description	112
B.1. Laser Response	114
B.2. Photon Response	114
B.3. Ion Response	116
B.4. Deposition Function Generation	121
B.5. Supporting Routines	124
B.5.1. Filing	124
B.5.2. Plotting	126
References for Chapter VI	128
VII. Applications	129
A. Application (A): Response of First Wall Material to ICF Pulsed Spectra	129
A.1. Introduction	129

	<u>Page</u>
A.2. Representative Spectra	130
A.3. Photon Spectra	130
A.4. Ion Spectra	131
A.5. Mechanical Wall Loading	135
A.6. Gas Protection as an Example of First Wall Protection Methods	136
A.6.1. Introduction	136
A.6.2. Wall Loading	137
A.6.3. Energy Deposition	137
A.6.4. Temperature Response	140
A.7. Evaporation and Melting of ICF First Walls	143
A.7.1. Introduction	143
A.7.2. First Wall Evaporation from Gas Reradiation and Unattenuated X-Rays	145
A.7.3. The Dependence of First Wall Evaporation on Cavity Gas Density	150
A.7.4. Conclusions	158
References for Application (A)	160
B. Application (B): Analysis of Plasma Disruption in Magnetic Fusion Reactors	163
B.1. Introduction	163
B.2. Plasma Disruptions	163
B.2.1. Assumptions for INTOR	163

	<u>Page</u>
B.2.2. Chronological Description of Disruption Sequence Used for This Study	174
B.3. Calculational Models	180
B.4. Parametric Analysis	183
B.5. Results and Discussion	184
B.5.1. Surface Temperature	185
B.5.1.a. Stainless Steel	185
B.5.1.b. Molybdenum	191
B.5.1.c. Carbon	195
B.5.2. Comparison of Surface Temperature	197
B.5.3. Surface Velocity	203
B.5.4. Vapor Shielding	222
B.5.4.a. Effect of Vapor Shielding on Surface Temperature	222
B.5.4.b. Effect of Vapor Shielding on Melting Thickness	228
B.5.4.c. Effect of Vapor Shielding on Material Vaporized	232
B.5.5. Effect of Disruption Time	235
B.5.6. Effect of Pulse Shape	238
B.6. Conclusions	240
References for Application (B)	245

	<u>Page</u>
C. Application (C): The Solution of the Moving Boundary Problem Using the Green's Function	246
C.1. Introduction	246
C.2. Method of Solution	246
C.3. Test Case	252
C.4. Results and Discussion	252
C.5. Conclusions	261
References for Application (C)	266
D. Application (D): Simulation of Fusion First Wall Environment in Fission Reactors	267
D.1. Introduction	267
D.2. Calculational Model	269
D.2.1. General Features	269
D.2.2. Heat Flux	273
D.2.3. Sputtering Rate	277
D.2.3.a. Introduction	277
D.2.3.b. Simulation Calculation	279
D.2.4. Displacement Response	280
D.3. Calculational Procedure	284
D.4. Results and Observations	285
D.5. Observations	286
D.5.1. Particle and Heat Flux	286
D.5.2. Erosion Rate	298
D.5.3. Implantation	299

	<u>Page</u>
D.5.4. Damage Rate	300
D.6. Conclusions	300
References for Application (D)	302
VIII. Summary and Conclusions	304
A. Conclusions from Application of Models to ICF Reactor	306
B. Conclusions from Application of Models to Study Plasma Disruptions in Magnetic Fusion Reactors	307
C. Conclusions from the Models Developed Using the Green's Function Solution	309
D. Conclusions from Simulation of Fusion First Wall Environment in Fission Reactors	309
E. Other Applications and Future Work	310

LIST OF TABLES

	<u>Page</u>
I-1. Summary of Author's Publications Related to This Thesis	4
II-1. Time Scale of Events for LCTR Pellet Fusion Pulse	9
VII.A-1. Reference Spectra for 100 MJ Target	138
VII.A-2. The Fluence and Flux of Gas Reradiation and Unattenuated Pellet X-Rays at the First Wall	153
VII.B-1. Summary of Selected Disruption Factors for INTOR and Other Tokamak Devices	166
VII.B-2. Possible Values Used to Determine the Energy Flux to the INTOR First Wall	174

LIST OF FIGURES

		<u>Page</u>
II-1.	Time of arrival of microexplosion energy at a first wall radius of 3.5 m.	8
II-2.	Typical energy release mechanisms from a 100 MJ pellet microexplosion.	12
II-3.	X-ray pulse spectrum of a megajoule DT fusion microexplosion.	13
II-4.	Neutron pulse spectrum of a megajoule DT fusion microexplosion.	13
III-1.	Ratio of electric and nuclear energy loss for helium in carbon.	26
III-2.	Total photon cross sections for different materials.	29
III-3.	General electronic energy loss function.	32
III-4.	Total energy deposition of Ta on aluminum.	34
III-5.	Energy deposition rate of Ta on aluminum.	35
III-6.	Total energy deposition of C on aluminum.	36
III-7.	Energy deposition rate of C on aluminum.	38
IV-1.	Uniform energy deposition profile.	50
IV-2.	General ion energy deposition profile.	54
IV-3.	Energy deposition rate of H on aluminum.	57
IV-4.	Comparison of surface temperature rise using deposition model.	58
IV-5.	Comparison of surface temperature rise using simple deposition model.	60
IV-6.	Comparison of surface temperature rise using three different models.	61
IV-7.	Comparison of temperature rise at $x = 0.5$ microns using simple deposition model.	62

	<u>Page</u>
IV-8. Energy deposition rate of Ta onto aluminum as a function of penetration depth.	64
IV-9. Energy deposition rate of Ta onto aluminum as a function of time.	65
IV-10. Comparison of surface temperature rise using different codes.	66
IV-11. Comparison of surface temperature rise using direct and general deposition models.	67
IV-12. Surface temperature rise with and without the variation of thermal properties.	77
IV-13. Temperature rise at $x = 0.5$ microns with and without the variation of thermal properties.	79
V-1. Schematic representation of solid-liquid-vapor interfaces.	89
V-2. Schematic of heat fluxes to first walls during plasma disruptions.	108
VI-1. General sections of A*THERMAL code.	113
VI-2. Basic functions of A*THERMAL code.	115
VI-3. A*THERMAL code block diagram.	118
VI-4. Block diagram for deposition function creation routine.	123
VI-5. Filing code.	125
VI-6. Plotting code.	127
VII.A-1. Blackbody photon spectrum for $kT = 1$ keV.	132
VII.A-2. Integrated ion energy deposition for the reference spectra.	139
VII.A-3. Component temperature increase for the given spectra.	141
VII.A-4. Comparison of surface temperature rise with and without 0.5 torr of Ne gas.	142

	<u>Page</u>
VII.A-5. Cavity phenomena in gas filled ICF reactors.	144
VII.A-6. The evaporation of carbon and stainless steel as a function of the x-ray spectrum and energy fluence.	147
VII.A-7. The evaporation of carbon and stainless steel as a function of the gas reradiation time and energy fluence.	149
VII.A-8. Stainless steel melting zone thickness as a function of reradiation time for different input energy densities.	151
VII.A-9. The thermal response of stainless steel for different cavity gas densities.	154
VII.A-10. The thermal response of carbon for different cavity gas densities.	156
VII.A-11. First wall evaporation of carbon and steel vs. cavity gas density for conditions outlined in Table VII.A-2.	157
VII.B-1. Schematic of factors to be considered for calculating energy deposition densities from plasma disruptions.	165
VII.B-2. Effect of deposition area on energy flux from INTOR plasma disruption.	171
VII.B-3. Effect of x-rays on energy flux from INTOR plasma disruption.	172
VII.B-4. Effect of spatial peaking factor on energy flux from INTOR plasma disruption.	173
VII.B-5. Schematic representation of disruption-vaporization process.	176
VII.B-6. Procedure for calculating the erosion resulting from a plasma disruption.	181
VII.B-7. Surface temperature rise of stainless steel for energy density of 325 J/cm ² and different disruption times (no vapor shielding).	186

	<u>Page</u>
VII.B-8. Surface temperature rise of stainless steel for energy density of 650 J/cm ² and different disruption times (no vapor shielding).	187
VII.B-9. Surface temperature rise of stainless steel for energy density of 1300 J/cm ² and different disruption times (no vapor shielding).	188
VII.B-10. Stainless steel melting zone thickness with no vapor shield as a function of energy density.	190
VII.B-11. Surface temperature rise of Mo for energy density of 325 J/cm ² and different disruption times (no vapor shielding).	192
VII.B-12. Surface temperature rise of Mo for energy density of 650 J/cm ² and different disruption times (no vapor shielding).	193
VII.B-13. Surface temperature rise of Mo for energy density of 1300 J/cm ² and different disruption times (no vapor shielding).	194
VII.B-14. Molybdenum melting zone thickness with no vapor shield as a function of energy density.	196
VII.B-15. Surface temperature rise of carbon for energy density of 325 J/cm ² and different disruption times (no vapor shielding).	198
VII.B-16. Surface temperature rise of carbon for energy density of 650 J/cm ² and different disruption times (no vapor shielding).	199
VII.B-17. Surface temperature rise of carbon for energy density of 1300 J/cm ² and different disruption times (no vapor shielding).	200
VII.B-18. Comparison of surface temperature rise for SS, Mo, and C for energy density of 325 J/cm ² and 20 ms disruption time (no vapor shield).	201
VII.B-19. Comparison of surface temperature rise for SS, Mo, and C for energy density of 325 J/cm ² and 10 ms disruption time (no vapor shield).	202

	<u>Page</u>
VII.B-20. Comparison of surface temperature rise for SS, Mo, and C for energy density of 325 J/cm ² and 5 ms disruption time (no vapor shield).	204
VII.B-21. Comparison of surface temperature rise for SS, Mo, and C for energy density of 650 J/cm ² and 20 ms disruption time (no vapor shield).	205
VII.B-22. Comparison of surface temperature rise for SS, Mo, and C for energy density of 650 J/cm ² and 10 ms disruption time (no vapor shield).	206
VII.B-23. Comparison of surface temperature rise for SS, Mo, and C for energy density of 650 J/cm ² and 5 ms disruption time (no vapor shield).	207
VII.B-24. Comparison of surface temperature rise for SS, Mo, and C for energy density of 1300 J/cm ² and 20 ms disruption time (no vapor shield).	208
VII.B-25. Comparison of surface temperature rise for SS, Mo, and C for energy density of 1300 J/cm ² and 10 ms disruption time (no vapor shield).	209
VII.B-26. Comparison of surface temperature rise for SS, Mo, and C for energy density of 1300 J/cm ² and 5 ms disruption time (no vapor shield).	210
VII.B-27. Surface velocity of stainless steel for energy density of 325 J/cm ² and different disruption times (no vapor shielding).	211
VII.B-28. Surface velocity of stainless steel for energy density of 650 J/cm ² and different disruption times (no vapor shielding).	212
VII.B-29. Surface velocity of stainless steel for energy density of 1300 J/cm ² and different disruption times (no vapor shielding).	214
VII.B-30. Surface velocity of SS, Mo, and C for energy density of 325 J/cm ² and 20 ms disruption time (no vapor shield).	215
VII.B-31. Surface velocity of SS, Mo, and C for energy density of 325 J/cm ² and 10 ms disruption time (no vapor shield).	216

	<u>Page</u>
VII.B-32. Surface velocity of SS, Mo, and C for energy density of 325 J/cm ² and 5 ms disruption time (no vapor shield).	217
VII.B-33. Surface velocity of SS, Mo, and C for energy density of 650 J/cm ² and 20 ms disruption time (no vapor shield).	218
VII.B-34. Surface velocity of SS, Mo, and C for energy density of 650 J/cm ² and 10 ms disruption time (no vapor shield).	219
VII.B-35. Surface velocity of SS, Mo, and C for energy density of 650 J/cm ² and 5 ms disruption time (no vapor shield).	220
VII.B-36. Surface velocity of SS, Mo, and C for energy density of 1300 J/cm ² and 5 ms disruption time (no vapor shield).	221
VII.B-37. Surface temperature rise of stainless steel for energy density of 325 J/cm ² and different disruption times with vapor shield.	223
VII.B-38. Surface temperature rise of stainless steel for energy density of 1300 J/cm ² and different disruption times with vapor shield.	225
VII.B-39. Surface temperature rise of SS, Mo, and C for energy density of 650 J/cm ² and 20 ms disruption time with vapor shield.	226
VII.B-40. Surface temperature rise of SS, Mo, and C for energy density of 650 J/cm ² and 10 ms disruption time with vapor shield.	227
VII.B-41. Stainless steel melting zone thickness with vapor shield as a function of energy density.	229
VII.B-42. Effect of vapor shielding on melt layer thickness of stainless steel.	230
VII.B-43. Molybdenum melting zone thickness with vapor shield as a function energy density.	231
VII.B-44. Evaporation thickness of stainless steel for 1000 disruptions for different energy deposited.	233

	<u>Page</u>
VII.B-45. Evaporation thickness of molybdenum for 1000 disruptions as a function of energy density.	234
VII.B-46. Evaporation thickness of carbon for 1000 disruptions as a function of energy density.	236
VII.B-47. Effect of disruption on the amount of melted and evaporated material from SS for 325 J/cm^2 with no vapor shield.	237
VII.B-48. Effect of disruption on the amount of melted and evaporated material from SS for 650 J/cm^2 with no vapor shield.	239
VII.B-49. Comparison of SS surface temperature rise for square and triangular pulse shape.	241
VII.B-50. Comparison of SS surface velocity for square and triangular input pulses.	242
VII.C-1. Comparison of surface temperature rise for carbon for 400 J/cm^2 deposited in 20 ms by different methods.	253
VII.C-2. Surface temperature rise for carbon by finite difference and Green's function methods.	255
VII.C-3. Carbon surface velocity for 400 J/cm^2 deposited in 20 ms by different methods.	256
VII.C-4. Surface vleocity of carbon for 400 J/cm^2 deposited in 20 ms with finite difference and Green's function methods.	257
VII.C-5. Evaporated material from carbon by different methods.	259
VII.C-6. Carbon material evaporated as calculated by finite difference and Green's function methods.	260
VII.C-7. Comparison of temperature rise for carbon for 400 J/cm^2 deposited in 20 ms by different methods at $x = 14$ microns.	262
VII.C-8. Temperature rise of carbon at $x = 14$ microns by finite difference and Green's function methods.	263

	<u>Page</u>
VII.C-9. Comparison of temperature rise for carbon for 400 J/cm ² deposited in 20 ms by different methods at x = 70 microns.	264
VII.C-10. Temperature rise of carbon at x = 70 microns by finite difference and Green's function methods.	265
VII.D-1. Simplified schematic drawing of fusion blanket test module proposed by EG&G to be placed in the thermal fission test reactor.	268
VII.D-2. Schematic representation used in modeling the problem.	270
VII.D-3. Dependence of distance r on angle θ .	275
VII.D-4. Particle and heat flux to the inside wall at 1.0 atm of He ³ gas for protons and tritium.	287
VII.D-5. Implantation and damage rate to the inside wall at 1.0 atm of He ³ gas for protons and tritium.	288
VII.D-6. Particle and heat flux to the outside wall at 1.0 atm of He ³ gas for protons and tritium.	289
VII.D-7. Implantation and damage rate to the outside wall at 1.0 atm of He ³ gas for protons and tritium.	290
VII.D-8. Particle and heat flux to the inside wall at 32.7 atm of He ³ gas for protons and tritium.	291
VII.D-9. Implantation and damage rate to the inside wall at 32.7 atm of He ³ gas for protons and tritium.	292
VII.D-10. Particle and heat flux to the outside wall at 32.7 atm of He ³ gas for protons and tritium.	293
VII.D-11. Implantation and damage rate to the outside wall at 32.7 atm of He ³ gas for protons and tritium.	294
VII.D-12. Total particle flux as a function of He ³ gas pressure at the inside and outside wall for protons and tritium.	295
VII.D-13. Heat flux and erosion rate as a function of He ³ gas pressure for protons.	296

	<u>Page</u>
VII.D-14. Heat flux and erosion rate as a function of He ³ gas pressure for tritium.	297

CHAPTER I

INTRODUCTION

The prospects for obtaining energy from thermonuclear fusion reactions has become quite optimistic. The early approach (1950's) was to develop a magnetically confined system capable of holding the deuterium-tritium (D-T) plasma long enough and at high enough temperatures and particle densities, to release substantially greater amounts of energy than that required to promote the reaction. This approach is still being actively pursued, mainly in tokamak and mirror machine devices. Another approach to the fusion reactor design, based on the inertial confinement concept was proposed in the 1960's. The basic concept of Inertial Confinement Fusion (ICF) is to compress and heat a small target of D-T fuel to thermonuclear conditions. These conditions must then be maintained for a time long enough to allow the energy from thermonuclear reactions to exceed the energy expended in initiating the reaction.

One of the main obstacles to the successful operation of a fusion power reactor is the ability of its structural components to withstand the severe radiation damage environment and to maintain structural integrity over an extended period of time. Such a severe radiation environment can cause considerable degradation in mechanical properties and erosion of the first wall. This normally means that the first wall will probably have to be replaced before the design lifetime of the plant has been achieved. Such a replacement

not only will complicate the design but also be very expensive and the principle of cheap fusion energy sources will no longer be true.

The research in this thesis is concerned with the thermal and damage response of materials exposed to radiation from thermonuclear burn in ICF reactors or deposition of plasma ions during instabilities in magnetic confinement fusion reactors. The main objectives of this thesis are to:

- (1) Develop more precise models to calculate the temperature increase (including possible phase changes) produced by ICF target debris or by plasma disruptions in magnetic fusion reactors.
- (2) Develop more precise evaporation models, with time dependent kinetics, based on transport theory results.
- (3) Analyze and study the effect of "self-shielding" or the stopping of incoming ions by the vapor on the net evaporation and melting zone thickness.
- (4) Simulate and parametrically study the plasma disruptions in magnetic fusion reactors. Investigate and test different first wall materials during the disruption process.
- (5) Develop and compare methods of solution of the above problems using the Green's function methods developed in this research, as well as the finite difference techniques.
- (6) Investigate methods to simulate the fusion first wall environment in a fission reactor. Models for heat flux, sputtering rate, implantation and damage rate are developed.

- (7) Develop a computer code (A*THERMAL) in which these models are incorporated.

A more detailed description of the nature of the problems associated with fusion reactors is given in Chapter II. Chapter III is a review of previous work in the area of deposition and interaction of target debris with reactor first walls (including some modifications made in this study). The use of the Green's function to solve the transient heat conduction problem (with perturbation techniques developed in this work to account for the thermal variation of thermal properties) is illustrated in Chapter IV. Chapter V is devoted to the development of first wall response models to the incoming radiation. Phase change, evaporation, and vapor shielding models are also discussed. A description of the computer code A*THERMAL developed for this kind of work is given in Chapter VI. Finally, Chapter VII is devoted to examples of the application of the code to typical problems associated with inertial and magnetic fusion reactors. A simulation of fusion first wall environment in fission reactors and other applications is also given in that chapter.

Some of the work presented here has been published during its development either as a journal publication or in University of Wisconsin Fusion Engineering Design Reports (UWFDM's). However, a considerable amount of work has not been published elsewhere and will be presented for the first time in this thesis. A summary of the related publications by the author is presented in Table I-1.

Table I-1. Summary of Publications Related to This Thesis

Reference	Date	Authors	Title
VII.A-13	November 1978 ^a	T.J. McCarville A.M. Hassanein G.L. Kulcinski	"The Response of Stainless Steel to the Pellet Debris in a Laser Fusion Reactor" (University of Wisconsin Fusion Engineering Program Report - UWFD-282)
VII.A-14	August 1979	A.M. Hassanein G.L. Kulcinski	"Effect of Gas Pressure on the Amount of X-Ray Energy Absorbed in the First Wall of an ICF Reactor" (University of Wisconsin Fusion Engineering Program Report - UWFD-306)
II-9	March 1980	G.L. Kulcinski A.M. Hassanein	"Thermal Response of Unprotected Al, C, and Ta First Walls to Thermonuclear Target Spectra" (University of Wisconsin/Westinghouse Electric Corporation)
VII.D-15	October 1980 ^b	A.M. Hassanein G.L. Kulcinski G.R. Longhurst	"Heat Flux, Erosion Rate, Implantation, and Damage Rate to the Walls of the EG&G Fusion Blanket Test Module" (University of Wisconsin Fusion Engineering Program Report - UWFD-389)
VII.C-1	November 1980	A.M. Hassanein G.L. Kulcinski	"Numerical Methods for Calculating the Temperature Increase in ICF First Walls" (University of Wisconsin Fusion Engineering Program Report - UWFD-397)
VII.B-8	August 1981 ^c	A.M. Hassanein G.L. Kulcinski W.G. Wolfer	"Vaporization and Melting of Materials in Fusion Devices" (University of Wisconsin Fusion Engineering Program Report - UWFD-427)

Table I-1. (continued)

Reference	Date	Author	Title
VII.A-19	August 1981 ^c	A.M. Hassanein T.J. McCarville G.L. Kulcinski	"First Wall Evaporation in Inertial Confinement Reactors Utilizing Gas Protection" (University of Wisconsin Fusion Engineering Program Report - UWFD-423)
II-7	October 1981 ^d	R.R. Peterson D.K. Sze A.M. Hassanein L. Pong	"Gas Dynamics and Heat Transfer Phenomena in Liquid Metal ICF Reactor First Surfaces" (University of Wisconsin Fusion Engineering Program Report - UWFD-443)
VII.B-9	December 1981 ^e	A.M. Hassanein G.L. Kulcinski W.G. Wolfer	"Surface Melting and Evaporation Caused by Plasma Disruptions"
VI-1	January 1982	A.M. Hassanein G.L. Kulcinski	"A* THERMAL Computer Code Description," University of Wisconsin Fusion Engineering Program Report UWFD-461, to be published

^a Presented at the 5th International Conference on Structural Mechanics in Reactor Technology, Berlin, Germany, Vol. N, August 1979.

^b Accepted for publication in Nuclear Technology/Fusion, September 1981.

^c Presented at Second Topical Meeting on Fusion Reactor Materials, 9-12, August 1981, Seattle, WA. To be published in Journal of Nuclear Materials.

^d Presented at 9th Symposium on Engineering Problems of Fusion Reactors, 26-29 October 1981, Chicago, IL.

^e To be submitted to Nuclear Fusion.

CHAPTER II

FIRST WALL ENVIRONMENTS IN FUSION REACTORS

Currently proposed inertial confinement fusion reactor concepts have several design and operational features in common. First, each concept employs a blast chamber in which the thermonuclear micro-explosion occurs and is contained. Laser light, or ion beams, which provide the heating and compression of the fuel pellet to ignition temperatures, is beamed into the blast chamber from final mirrors or focusing elements through ports located on the periphery of the cavity. The number and location of these ports varies among the designs. The fuel pellet is injected into the blast chamber to a predetermined location where the laser light or the ion beam is focused and the thermonuclear reaction occurs. As a result of the reaction, various fusion products are emitted and they could impinge upon the blast chamber wall if the chamber is pumped to a hard vacuum. The thermonuclear burn of the fuel and the subsequent emission of fusion products which strike the first wall occurs over a very short time scale (less than 10 nsec). As a result, large amounts of energy are deposited in the wall in very short times and hydrodynamic stress waves are produced. One effect of the rapidly repeated micro-explosions is to quickly deteriorate any unprotected solid blast chamber surfaces. Therefore, some type of first wall protection is needed to maintain the structural integrity of the blast chamber. However, the main objective is to convert the heat, which is generated in the blast chamber and surrounding blanket, efficiently into

usable energy. Therefore, in addition to shielding the blast chamber first wall, the protection system must permit rapid recovery of the energy in a form which is suitable for utilization in the energy conversion cycle. Thus, the first wall protection method establishes many of the reactor design characteristics. Most CTR designs also provide possible means of breeding tritium which is used in the fuel for the fusion process. The tritium may be bred in a lithium blanket surrounding the blast chamber, or as in some designs, directly in the lithium used as the first wall protection device (see for example the HYLIFE or HIBALL concept).⁽¹⁻³⁾

Most current ICFR designs assume that the fuel pellet will contain a deuterium (D) and tritium (T) mixture, and as well as some low Z ablator (e.g., C, O) and high Z (e.g., Fe, Ta, Pb) elements. The DT fuel is compressed to the required conditions of temperature and density by the beam. The surface of the target (usually low Z material) with an inner layer of frozen DT is violently heated and boiled off (ablated) by intense beams. Very high pressures are generated, accelerating the ablatively cooled DT inward. The high Z material (pusher) serves as a carrier of kinetic energy away from the microexplosion as well as a moderator for the alpha particles emitted as a product of the reaction. Ignition occurs when the rapidly moving inner region of the DT is suddenly braked by the pressure generated in the compressed matter and ignition temperatures are reached. The time scale of events for laser CTR pellet fusion pulse are concisely illustrated in Fig. II-1⁽⁴⁾ and Table II-1.⁽⁵⁾ Time

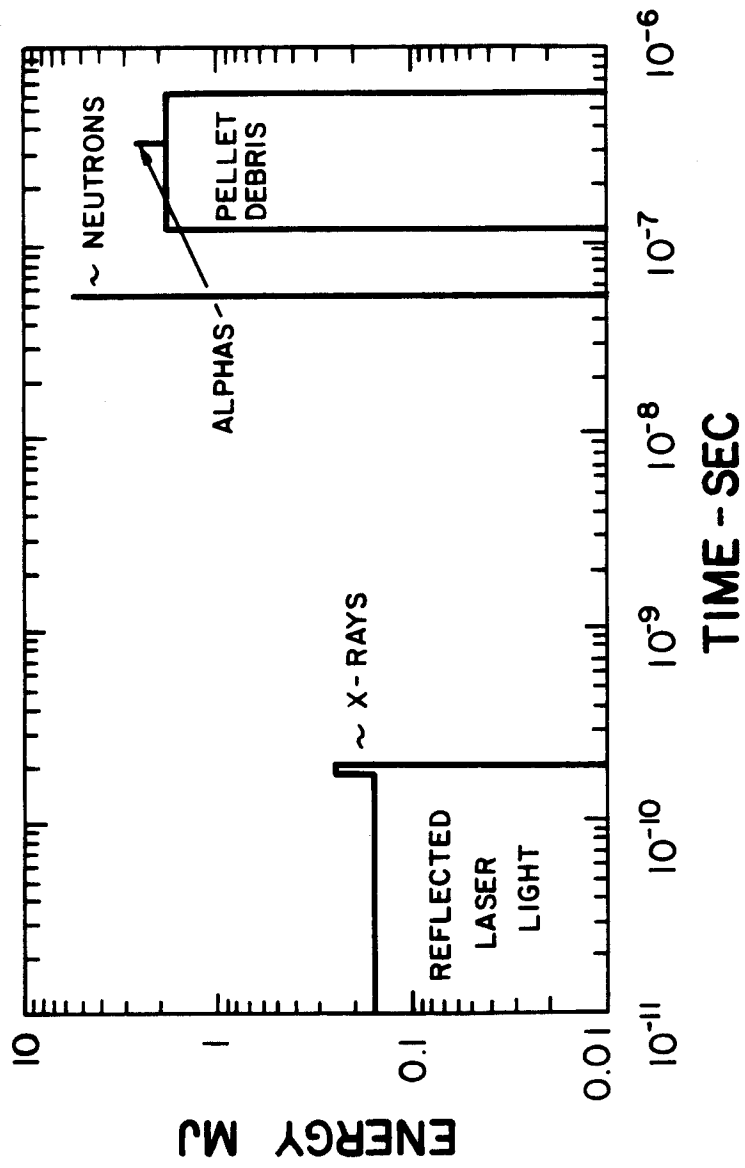


Fig. II-1. Time of arrival of microexplosion energy at a first wall radius of 3.5 m.

Table II-1. Time Scale of Events for LCTR Pellet Fusion Pulse

Time	Primary Events	Secondary Events
-20 to -5 ms	Pellet enters cavity	
-150 ns	Laser pulsed fired	
-10 ns	Laser pulse arrives at pellet surface	
0	Thermonuclear burn begins	
+10 ps	Thermonuclear burn complete	
+6 ns	X-rays strike first wall	
		Ablative material begins expansion from first wall
+30 ns	X-rays strike last optical surface	
+20 to +100 ns	Neutrons deposited in reactor vessel	Shock wave induced in lithium
+60 ns	Neutrons strike last optical surface	
		Ablative material and pellet debris interact
+0.3 to +1.2 μ s	Pellet debris strikes first wall	
		Cavity atmosphere equilibrated
+1 ms	Cavity blowdown begins	
+0.01 to +10 s	Restoration of original cavity conditions complete	Wetted-wall blowdown complete, lithium vortex restored, turbulence in rarefied dry-wall cavity dissipated

scale of events for other ICF reactor designs using ion beams as drivers will be similar to that given in Table II-1.

First, the DT fuel pellet enters the blast chamber and a high intensity laser light pulse (or ion beam) is fired and focused on the pellet. The surface of the DT pellet is instantly vaporized into a low density plasma. This ablated outer mass accelerates out into the blast chamber and generates an equal and opposite force which forces the remainder of the DT pellet inward toward its center. This effect greatly increases the density of the fuel in the pellet and as a result of the compressive work, the pellet temperature also increases greatly. Provided that suitable conditions exists, ignition of the fuel at the center of the highly compressed, high temperatures occurs. The thermonuclear burn wave then propagates outward due to the energy deposition of the alpha particles in the "cold" pellet. The thermonuclear reaction will continue until the temperature and/or the density of the remaining fuel decreases to a point, where there will no longer be any net generation of energy. The total elapsed time to this point is approximately 10 picoseconds. Typically, approximately 25% of the DT in the original fuel pellet will be consumed, while the remainder becomes part of the blast debris.^(4,5)

For a simple, bare DT pellet microexplosion, the energy released is partitioned among four species: x-rays, alpha particles which have escaped the plasma, plasma debris, and neutrons. The primary fusion reaction which has occurred and gives rise to the neutrons and alpha particles is:



The plasma debris consists of alpha particles which were unable to escape the plasma, deuterons, and tritons. Also, in case of a laser driven system, the laser light will contribute to the total energy release through reflection mechanism. A theoretical energy release and energy partition for a 100 MJ microexplosion is shown in Fig. II-2.⁽⁵⁾ The energy spectrum for the x-rays which are emitted from the 100 MJ microexplosion can vary over a wide range. One study shows that for a bare DT pellet, the average x-ray energy is around 4 keV (see Fig. II-3⁽⁶⁾). Softer x-ray energy spectra than that given in Fig. II-3 could result from structured targets.^(3,7) The bulk of these x-rays are produced during the 10 picosecond thermonuclear burn, part of these x-rays are emitted promptly.

The 14.1 MeV neutrons which contain about 77.1% of the thermonuclear energy yield (Fig. II-2) are also released during the short burn time. Figure II-4 shows a typical spectrum of the fusion neutrons which remains virtually unchanged until the neutrons reach the first shield and blanket region.^(6,8) The pellet debris, including the thermalized alpha particles and unburned D and T, could possess about 15% of the total thermonuclear energy yield. In addition, the alpha particles that escape may contain about 7% of the total energy yield and have an average energy of about 2 MeV.^(4,5) These previous results were estimated for a solid DT sphere. If, however, the compressed pellet density-radius product is approxi-

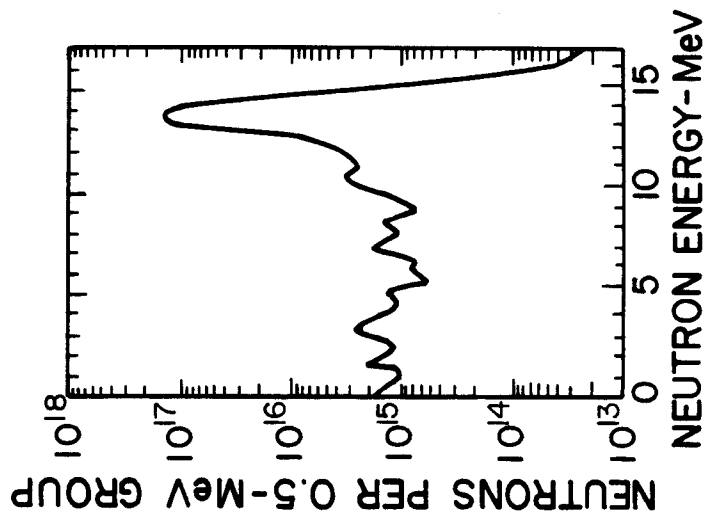
Mechanism	Fraction of Total Energy Release	Particles Per Pulse	Average Energy Per Particle
X-rays	0.01		4 keV peak
α particles that escape plasma	0.07	2.2×10^{19}	2 MeV
Plasma kinetic energy	0.15		
α particles		1.3×10^{19}	0.6 MeV
Deuterons		1.2×10^{20}	0.3 MeV
Tritons		1.2×10^{20}	0.4 MeV
Neutrons	0.77	3.3×10^{19}	14.1 MeV

Total

Average

0.37 MeV

Fig. II-2. Typical energy release mechanisms from a 100 MJ DT pellet microexplosion.



13

Fig. II-4. Neutron pulse spectrum of a megajoule DT fusion microexplosion.

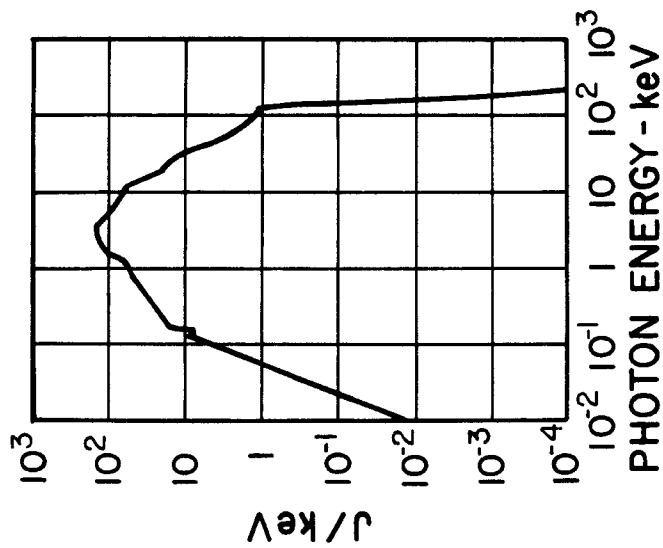


Fig. II-3. X-ray pulse spectrum of a megajoule DT fusion microexplosion.

mately 3, the 3.5 MeV alpha particles will deposit nearly all their energy in the plasma to assist the thermonuclear fusion. In this case, approximately 22% of the thermonuclear energy yield will be in the form of plasma debris. The energy of this debris is nearly a Maxwellian distribution with an average energy equal to the energy deposited in the pellet from the laser or ion beam plus the fraction of the thermonuclear reaction energy divided by the number of pellet particles. Thus, the energy partition and energy spectrum are quite dependent upon the pellet design.

Energy deposition by x-rays, alpha particles, and particles from the target debris occurs, or very near, free surfaces of incidence in structural and coolant materials; whereas the kinetic energy of 14 MeV neutrons is deposited throughout relatively large material volumes. A bare cavity wall (e.g., a bare refractory metal) would be the simplest reactor cavity enclosure. However, the interior surface of such a cavity wall would have to withstand repeated energy deposition amounting to about 23% of the thermonuclear yield within a few microns of its surface, and unless extremely large cavities were used, very high surface temperature increases would result.⁽⁹⁾ Tolerable surface-temperature increases of such structural components have not been established either theoretically or experimentally.

There are several reactor cavity concepts that employ evaporative or ablative materials to protect interior cavity wall surfaces. For such concepts, it is necessary that the protective material be renewable between target microexplosions, otherwise

cavity-wall lifetimes would be uneconomically short. Protection of exposed surfaces by a liquid metal such as lithium has many attractive features and is utilized in the wetted-wall concept proposed by the Los Alamos National Laboratory^(10,11) and the suppressed ablation concept proposed by the Lawrence Livermore Laboratory.⁽¹²⁾ Another protection method using an array of porous SiC tubes through which a liquid lithium lead ($\text{Pb}_{83}\text{Li}_{17}$) is flowing was recently proposed.⁽³⁾

Externally applied magnetic fields in a cylindrical cavity could be used to divert the alpha particles and ionized plasma debris out the ends of the cylinder leaving only the x-ray energy to be accommodated by the cavity wall surface. This approach was also proposed by the Los Alamos National Laboratory.^(13,14)

A gas-filled chamber concept to protect the wall was investigated by the Wisconsin group.⁽¹⁵⁾ In this design a low pressure (a few torr) inert gas was maintained in the chamber during micro-explosions to absorb and modify target debris and x-rays energy spectra.⁽¹⁶⁾ The gas pressure was kept low so that it would not interfere with the propagation of the driver beam to the target and also so that the target trajectory would not be significantly altered.

References for Chapter II

1. M. Monsler et al., "Electric Power from Laser Fusion: The HY LIFE Concept," in Proc. of IECEC Conf., San Diego, CA, Aug 1978.
2. W.R. Meier and J.A. Maniscalco, "Reactor Concepts for Laser Fusion," in Proc. of Am. Inst. of Chem. Engineers, 13-17 Nov. 1977.
3. B. Badger et al., "HIBALL - A Heavy Ion Beam Driven Fusion Conceptual Reactor Study," University of Wisconsin Fusion Engineering Program Report UWFD-450/KfK-3202, (August 1981).
4. J. Hovingh, "First Wall Studies of a Laser-Fusion Hybrid Reactor Design," Proc. of 2nd Topical Mtg. on the Technology of Controlled Nuclear Fusion, Richland, WA, 1976.
5. J. Williams, "Laser-Controlled Thermonuclear Reactor Design Problems," Fusion Reactor Design Problems - Proc. of an IAEA Workshop, Culham, United Kingdom, Jan. 1974, p. 219.
6. J. Hovingh et al., "The Preliminary Design of a Suppressed Ablation Laser-Induced Fusion Reactor," Proc. of 1st Topical Mtg. on Technology of Controlled Nuclear Fusion, San Diego, CA, May 1974, p. 96.
7. R.R. Peterson, D.K. Sze, A.M. Hassanein, and L. Pong, "Gas Dynamics and Heat Transfer Phenomena in Liquid Metal ICF Reactor First Surfaces," presented at 9th Symposium on Engineering Problems of Fusion Research, Chicago, IL, 26-29 October 1981.
8. R. Hyde et al., "Physics and Engineering Considerations in Laser CTR Reactor Design," Proc. of the First Topical Mtg. on the Technology of Nuclear Fusion, San Diego, CA, May 1974, p. 154.
9. G.L. Kulcinski and A.M. Hassanein, "Thermal Response of Unprotected Al, C, and Ta First Walls to Thermonuclear Target Spectra," University of Wisconsin/Westinghouse Electric Corporation, March 1980.
10. L.A. Booth (compiler), Los Alamos National Laboratory Report LA-4858-MS, Vol. I (February 1972).
11. J. Williams, T. Merson, et al., Proc. 1st Topical Meeting on the Technology of Controlled Nuclear Fusion, Am. Nuc. Soc., San Diego, CA, (April 1974), p. 70.

12. J. Hovingh et al., "Proc. 1st Topical Meeting on the Technology of Controlled Nuclear Fusion, Am. Nuc. Soc., San Diego, CA, (April 1974), p. 96.
13. T.G. Frank et al., Proc. 1st Topical Meeting on Technology of Controlled Nuclear Fusion, Am. Nuc. Soc., San Diego, CA, (April 1974), p. 83.
14. D.A. Freiwald et al., presented at the 1975 Winter Meeting of the Am. Nuc. Soc., San Francisco, CA, (Nov. 16-21, 1975).
15. R.W. Conn et al., University of Wisconsin Fusion Engineering Program Report UWFD-220, (1977).
16. T.O. Hunter and G.L. Kulcinski, University of Wisconsin Fusion Engineering Program Report UWFD-232, (1977).

CHAPTER III
INTERACTION AND DEPOSITION OF RADIATION
IN FUSION FIRST WALL MATERIALS

This chapter is divided into two main parts. The first part is to briefly review the basic theory available for the primary interaction of ICF microexplosion outputs, i.e. photons, ion debris, and neutrons, with materials. The 10 to 14 MeV neutrons produced as a result of the thermonuclear burn have a large mean free path compared to the first wall thickness, will pass through without depositing a significant amount of energy, and will not be considered in this thesis. The second part of this chapter is devoted to a brief review of the previous work in the area of energy deposition and a comparison with the modifications made in this thesis. Examples for comparison of the modified deposition methods and previous calculations are also given. Discussion of energy deposition will be restricted to those energy ranges of interest in fusion reactors. Emphasis is made on those models which can be used to reproduce deposition function cross sections in a numerically efficient form. Strain energies resulting from thermal expansion and ablation of the wall are very small and will be neglected in this thesis.

A. Photon Interactions With Materials

As a result of the thermonuclear burn in ICF reactors, the first wall could be exposed to photon radiation with energies ranging from a few electron volts to hundreds of kilo-electron volts. The primary interactions of photons with materials in these energy ranges are:

- a. photoelectric effect;
- b. coherent scattering;
- c. incoherent or Compton scattering;
- d. pair production.

At low photon energies the total photon cross section is dominated by the photoelectric cross section in which a photon transfers all its energy to an electron in the vicinity of a nucleus. The energy of the electron emitted is equal to the photon energy minus the electron's binding energy. The cross section for this interaction shows a very strong material and spectral dependence. Simple approximations for these dependencies are given by Evans.⁽¹⁾ A convenient form for fitting the photoelectric cross section has been proposed by Biggs and Lighthill⁽²⁾ in which a set of parameters are used to fit the data within discrete energy intervals. These discrete intervals are necessary to properly account for absorption edges.

The pair production process is a photon-matter interaction in which the incident photon is annihilated and a positron-negatron pair is created. This reaction occurs at high energy, where the incident photon energy is equal or greater than 1.02 MeV. The interaction rate is dependent on the nuclear cross section and is therefore proportional to the atomic number square of the absorbing material. Both the differential and the total cross section have analytic expressions and accurate approximations.^(2,3)

Incoherent or Compton scattering occurs at intermediate photon energies. In this process, energy is given by an incident photon to

an electron and results in a scattered photon. The portion of the incident photon energy which is deposited as kinetic energy of the electrons can be expressed in terms of an energy absorption cross section. Exact analytical expression of the differential scattering cross section is given by Evans⁽¹⁾ but it is not convenient for numerical approximation. Convenient formulae for efficient numerical calculations is again given by Biggs.⁽⁴⁾

Coherent scattering occurs when the energy of the incident photon is reduced to low enough frequencies where the momentum can be ignored. Because coherent scattering is elastic, it does not result in any net loss of photon energy and consequently there is no significant local deposition of photon energy.

B. Ion Interactions

The interaction of charged particles with materials is primarily due to two processes. The first interaction is between the electric fields of the ion and the electrons in the material which is an inelastic collision. The second interaction is between the collision of the ions with material nuclei which is an elastic interaction. The dominant mechanism of ions slowing down in materials is dependent upon the instantaneous energy of the ion. The energy loss associated with each mechanism can be determined upon specifying appropriate interaction potentials.

B.1. Electronic Energy Loss

The slowing down of a charged particle due to interaction with the electrons in a material is usually divided into three energy

regimes, i.e. high, intermediate, and low energy regimes. The high energy regime is one in which the velocity of the particle much exceeds the velocities of the orbital electrons. An intermediate energy regime is one in which these velocities are of the same order. In the low energy regime the velocity of the particle is much smaller than the orbital velocities of the material electrons.

The Bethe-Block⁽⁵⁾ formula, which is a quantum mechanical derivation of the original classical result by Bohr,⁽⁶⁾ is widely used to describe the interaction in the high energy region. This formula is given by:

$$\left(\frac{dE}{dx}\right)_e = \frac{4\pi Z_1^2 e^4 N Z_o}{m_o v^2} \ln \frac{2m_o v^2}{I} \quad (1)$$

where Z_1 = particle charge number

e = electron charge

N = atom density

Z_o = material atomic number

m_o = electron mass

v = particle velocity

I = mean ionization potential.

The formula given in Eq. (1) is only valid for nonrelativistic velocities which is the energy range of interest in fusion reactors. A general treatment of fast particles with relativistic velocities is given by Fermi.⁽⁷⁾ Relativistic treatments might be important in

case of a heavy ion beam fusion reactor in which the driver beam misses the target and deposits its energy directly in the first wall.

At low particle energies, where the particle velocities are below the orbital velocity of the target electrons, the interaction with these electrons can be modeled by treatments developed by Lindhard and coworkers (LSS).⁽⁸⁾ In this model the particle energy loss is proportional to its velocity and is usually presented in non-dimensional form as:

$$\frac{d\varepsilon}{d\rho} = k\varepsilon^{1/2} \quad (2)$$

where: ε = reduced energy = E/E_L

ρ = reduced length = R/R_L

$$k = \frac{0.0793 \, z_1^{2/3} z_2^{1/2} (1 + A)^{3/2}}{(z_1^{2/3} + z_2^{2/3})^{3/4} M_2^{1/2}}$$

where: Z_1e = particle charge

Z_2e = target charge

A = ratio of target mass to particle mass

M_2 = target mass (amu)

and
$$E_L = \left(\frac{1 + A}{A}\right) \frac{Z_1 Z_2 e^2}{a} \quad (\text{ergs})$$

$$R_L = \frac{(1 + A)^2}{4\pi A N a^2} \quad (\text{cm})$$

$$a = 0.4683 \times 10^{-8} (Z_1^{2/3} + Z_2^{2/3})^{-1/2} \quad (\text{cm})$$

N = target atom density .

The intermediate energy regime between the upper limit of LSS theory and the lower limit of the Bethe-Block has no basic theoretical treatment at the present time. In this region the particle is partially ionized. Modifications made to account for an effective charge for the incident particle in the Bethe-Block model usually predicts greater stopping power than observed experimentally.

A semi-empirical model based on adjustable parameters determined from experiments has been proposed by Brice.⁽⁹⁾ This model can predict the electronic stopping for all three energy regimes. Three adjustable parameters are needed. One parameter is necessary for the low energy region and the other two are used for extrapolating to higher energies. A tabulation for these parameters of a large number of calculations for various ion-target combinations is given in Ref. (10).

Another tabulation of stopping powers and range data have been published by Ziegler and Anderson.⁽¹¹⁾ Experimental and theoretical data for hydrogen, helium, and heavier ions are also given. Other tabulation of stopping powers for different materials are given by Northcliffe and Schilling.⁽¹²⁾

B.2. Nuclear Energy Loss

The second mechanism of slowing down a charged particle is the elastic collision of these particles with material nuclei. The rate of interaction will be determined through the nuclear cross sections.

Accurate theoretical values for nuclear cross sections are determined by the interatomic potential chosen between the nuclei and the particle.

A relatively simple analytic expression for the nuclear cross section derived by Lindhard⁽⁸⁾ using a shielded Coulomb interaction with a Thomas-Fermi atomic model. The differential cross section is given by:⁽¹⁰⁾

$$d\sigma(E,T) = \frac{\pi a^2 f(t) dt}{t^2} \quad (3)$$

where: E = particle energy

T = kinetic energy of the struck atom after the collision

a = screening parameter given by

$$0.8853 a_o (Z_1^{2/3} + Z_2^{2/3})^{-1/2}$$

a_o = Bohr radius.

$f(t)$ = a tabulated scattering function (Ref. 10)

$$t = E/E_o \sqrt{T/T_m}$$

$$E_o = Z_1 Z_2 e^2 (m_1 + m_2) / a m_2$$

$$\text{and } T_m = \text{maximum energy transfer} = \frac{4m_1 m_2 E}{(m_1 + m_2)^2}$$

The total elastic cross section is obtained by integrating Eq. (3) over all possible energy transfers. An approximation for a non-dimensional nuclear cross section is given by Oen and Robinson as:⁽¹³⁾

$$\left(\frac{d\epsilon}{d\rho}\right)_n = \frac{9}{8\epsilon} \{ \ln[u + (1 + u^2)^{1/2}] - u(1 + u^2)^{-1/2} \} \quad (4)$$

where: $\epsilon = E/E_L$

$\rho = R/R_L$

$u = (2\lambda)^{1/3} \epsilon^{4/9}$

$\lambda = 1.309.$

For high energy particles the nuclear energy deposition is negligible compared to the electronic energy loss. This can be seen from Fig. III-1 which shows the relative loss for both mechanism electronic versus nuclear as a function of helium energy into a carbon target.⁽¹⁰⁾ The domination of the electronic energy loss continues down to a few keV.

C. Energy Deposition

C.1. Laser Light Deposition

Laser light absorption, especially for high intensity beams, has limited coverage in the open literature. A simple model for laser deposition into materials based on experimental results is presented. The discussion for laser light interaction with materials is not only applicable for ICF reactor first walls but also for laser annealing of materials by laser pulses several nanoseconds long.⁽¹⁴⁾ This model will be coupled with the models developed in Chapter V to solve the heat conduction equation with moving boundaries and to calculate the dynamics of melting and evaporation. Most of the recent existing models for materials annealing with lasers do not account for the two moving boundaries, the variations of thermal properties with temperature or take into account the thermal radiation losses.⁽¹⁴⁻¹⁷⁾

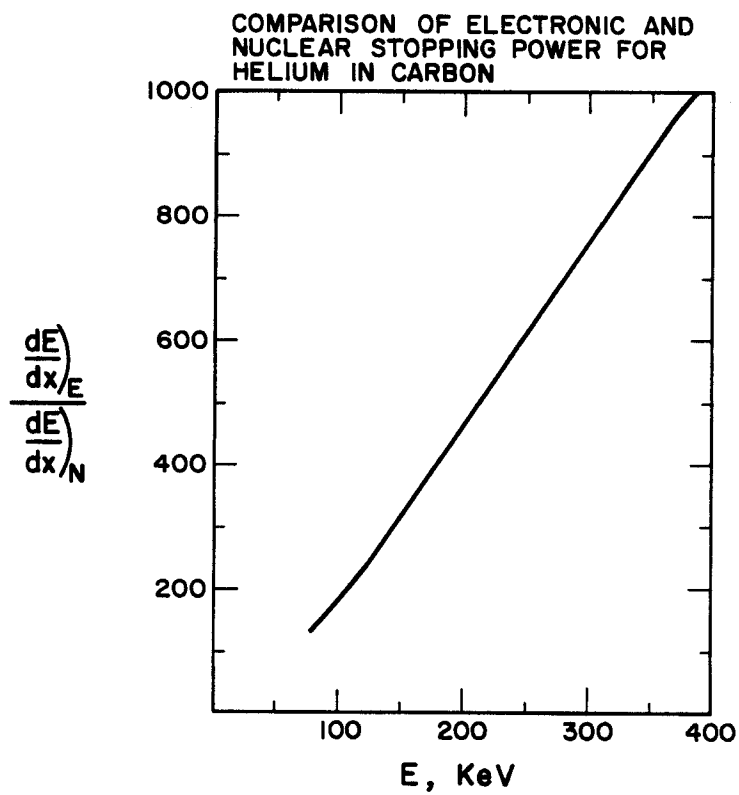


Fig. III-1. Ratio of electric and nuclear energy loss for helium in carbon.

The deposition function for the laser radiation absorption in materials can be written as:

$$\dot{q}(x,t) = \alpha P(x,t) \quad (5)$$

where: α = the absorption coefficient of the material

$P(x,t)$ = the power absorbed at time t in the material per unit volume due to the laser pulse passing through it.

The power absorbed can be written as

$$P(x,t) = (1 - R(t))F(t)e^{-\alpha(t)x} \quad (6)$$

where: $F(t)$ = the incident power density

$R(t)$ = the reflection coefficient.

Then the laser deposition function is given by

$$\dot{q}(x,t) = \alpha(t)(1 - R(t))F(t)e^{-\alpha(t)x} \quad (7)$$

The absorption coefficient in some materials, like the reflectivity, is found to be strongly dependent on the melting of the near-surface layer.⁽¹⁷⁾ As a result, in this thesis work, the absorption coefficient as well as the reflection coefficient are allowed to be a function of time (i.e. whether the material is in solid or liquid phase) for a certain depth from the front surface. This depth depends on the absorption length of the material.

C.2. Photon Deposition

The photoelectric cross sections library developed by Hunter⁽¹⁸⁾ which is based on the work of Biggs⁽²⁾ has been incorporated into this study. Incoherent cross sections are also developed by Biggs based on the representation of the Klein-Nishina formula.⁽¹⁾ For high energy photons the photoelectric cross sections are negligible compared to the cross sections from the incoherent scattering. The total incoherent cross sections are used in this case. Examples of the sum of the photoelectric and incoherent total cross section for C, Cu, Mo, and Ta are shown in Fig. III-2.⁽¹⁸⁾

C.3. Ion Deposition

C.3.1. Introduction

The energy deposited from incident ions into a material can be calculated upon the knowledge of the energy loss mechanism. Recently a model was developed by Hunter⁽¹⁸⁾ to use the Brice⁽⁹⁾ formulation to generate electronic energy loss data for light ions and a fitted deposition function for heavy ions. The Brice formulation consists of semi-empirical relations which can reproduce the experimental data with reasonable accuracy. In this research different fitting functions are used for the Brice formulation which satisfy the conservation of energy between the incident ion spectrum and the total deposited energy into the material. In this way, a more accurate representation of the deposited energy inside the material is obtained. Hence, a more accurate temperature and displacement response is obtained. The fitting functions developed in this research are

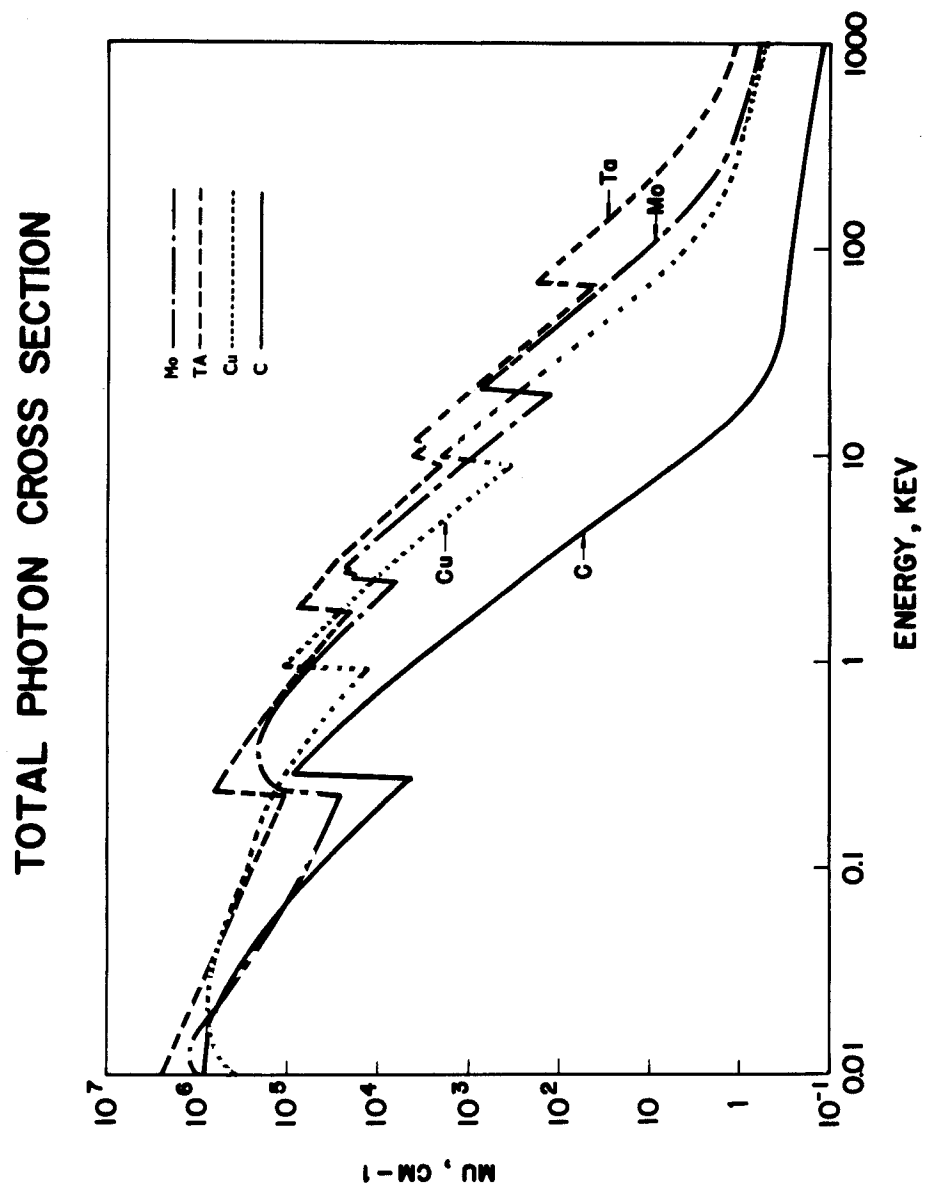


Fig. III-2. Total photon cross sections for different materials.

compared with Hunter's model through two examples of ion spectra incident on an aluminum first wall.

C.3.2. Light Ions ($Z \leq 2$)

Incident light ions, with energies higher than a few keV, lose their kinetic energy in materials mainly by electronic interaction (see Fig. III-1). This is true for light ions that are present in ICF reactors, mainly helium, deuterium, and tritium. The ions resulting from the thermonuclear burn have energies ranging from a low energy region, through intermediate, and high energy regions as discussed in Section B.1.

Hunter⁽¹⁸⁾ developed a set of analytic forms for the spatial distribution which could be evaluated by knowing the electronic energy loss data which could be obtained from Brice. The stopping power data were divided into three regions similar to those energy regions as shown in Fig. III-3. In each region, a function was found which could reproduce the data.

The following functions were found:⁽¹⁸⁾

$$\frac{dE}{dx}(E) = -S_0 \left(\frac{E}{E_0}\right)^{1/2} \quad (\text{Region 1}) \quad (8)$$

$$\frac{dE}{dx}(E) = -A_1(1 - e^{-B_1 E}) \quad \} \quad (\text{Region 2}) \quad (9)$$

$$\frac{dE}{dx}(E) = [D^2 - P^2(E - B_2)^2]$$

$$\frac{dE}{dx}(E) = -Ae^{-E/B_3} \quad (\text{Region 3}) \quad (10)$$

where S_0 , E_0 , A_1 , B_1 , D , P , B_2 , A_3 , B_3 , are all constants. These constants for each region can be determined by selecting reference points, as shown in Fig. III-3, from the stopping power curve which in turn could be determined from the Brice formulation. As a result of determining the energy loss functions the deposition and local mean ion energy were determined in terms of a standard set of functions of space.

C.3.3. Heavy Ions ($Z > 2$)

For heavy ions, the energy deposition must account for the nuclear energy loss and the transport equation must be solved taking into account the energy dependent nuclear interaction cross sections. Among the various approximate solution methods for such calculations are those of Brice,⁽¹⁹⁾ Winterbon,⁽²⁰⁾ and Manning and Mueller.⁽²¹⁾ Hunter's idea was to use the computer codes or published data developed by Brice⁽¹⁹⁾ and then develop a method which could produce the deposition distribution for a wide range of incident ion energies. This method is based on a set of deposition functions which consisted of polynomials to reproduce the spatial profile of the deposition distributions. In this research different deposition functions are used for the Brice deposition calculation in which the conservation of energy between the incident ion spectrum and the total deposited energy into the material is satisfied. Such conservation of energy assures a more accurate representation of the energy deposited and consequently more accurate temperature and displacement responses inside the material. The coefficients for each ion-target

GENERAL ELECTRONIC ENERGY LOSS FUNCTION

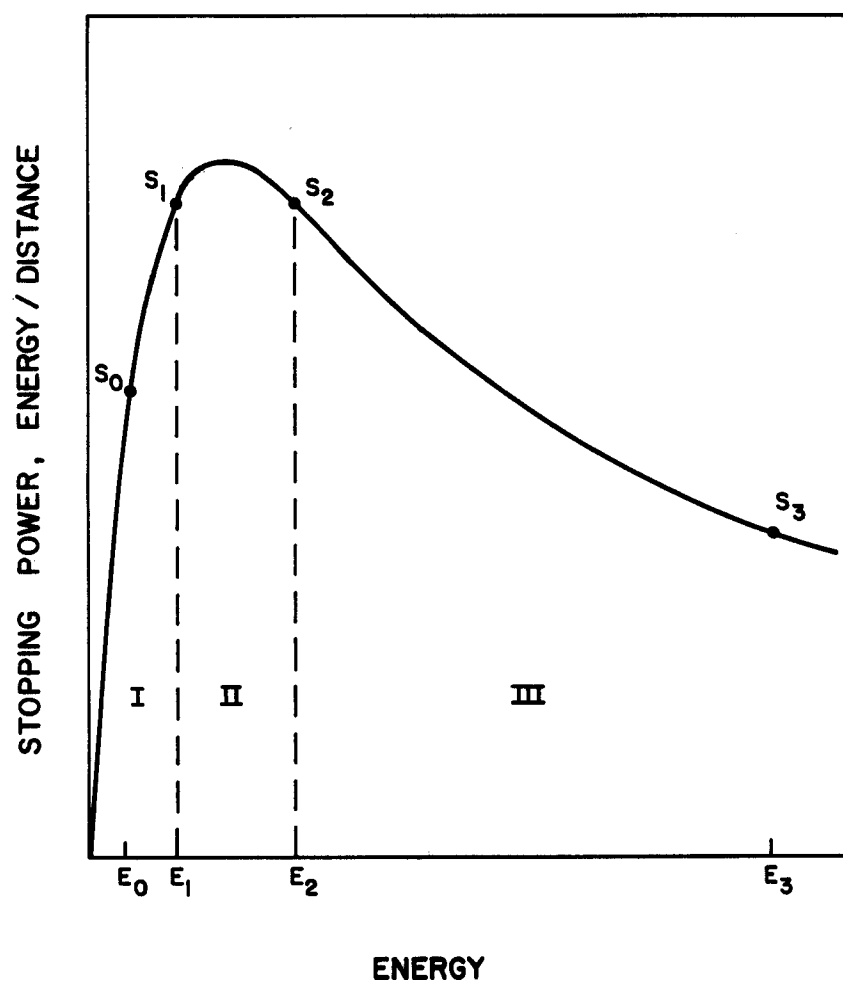


Fig. III-3. General electronic energy loss function.

combination deposition function are stored in a separate file which could be accessed easily for the deposition calculations.

C.3.4. Comparison of Results

Two examples are considered here to compare the energy deposition rate and the total integrated energy deposition using the deposition functions developed in this thesis and the one developed by Hunter. The solution for the deposition functions developed in this work is contained in the computer code A*THERMAL.⁽²²⁾ This code will be briefly described in Chapter VI. Hunter's model is contained in the computer code T*DAMEN.⁽²³⁾ In the first example tantalum ions are incident having a Maxwellian spectrum with 905 keV characteristic energy on an aluminum first wall.⁽²⁴⁾ Figure III-4 shows the total energy deposited as a function of distance into aluminum. In the A*THERMAL calculation the energy deposited is found to be conserved within less than 2% of the incident ion energy content. Apparently T*DAMEN overestimates the total energy contained in Ta ions by about 15%. The energy deposition rate at the end time of the spectrum is shown in Fig. III-5. This deposition rate as given by T*DAMEN extends further into the material. In the second example where carbon ions are incident on aluminum with a 60 keV Maxwellian spectrum,⁽²⁴⁾ these differences are more noticable. Figure III-6 shows about 50% higher total energy deposited given by T*DAMEN than that given by A*THERMAL. In this case the energy deposited was conserved in A*THERMAL within less than 1%. Again T*DAMEN overestimates the energy deposition of carbon ions by over 50% compared to that contained

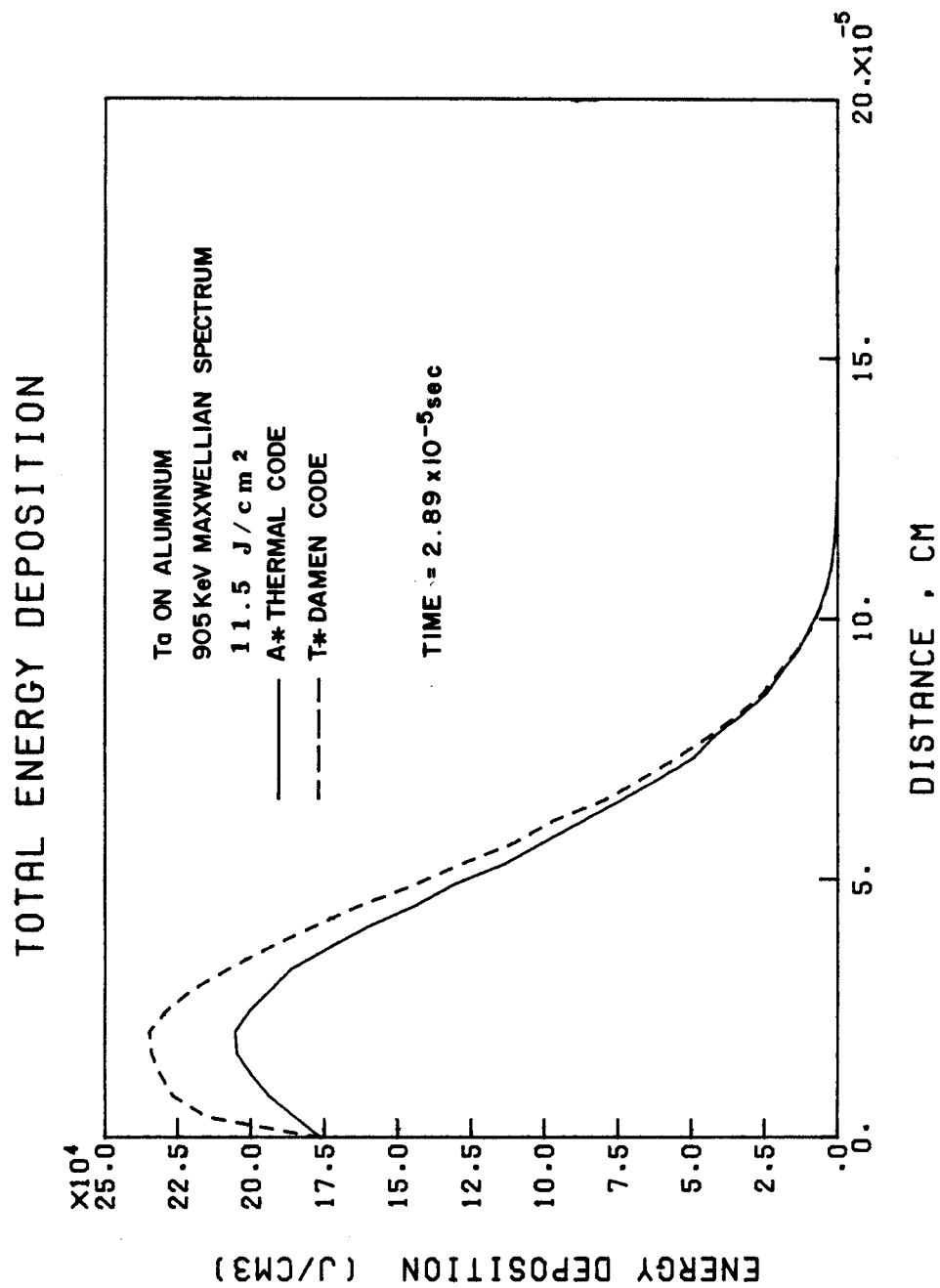


Fig. III-4. Total energy deposition of Ta on aluminum.

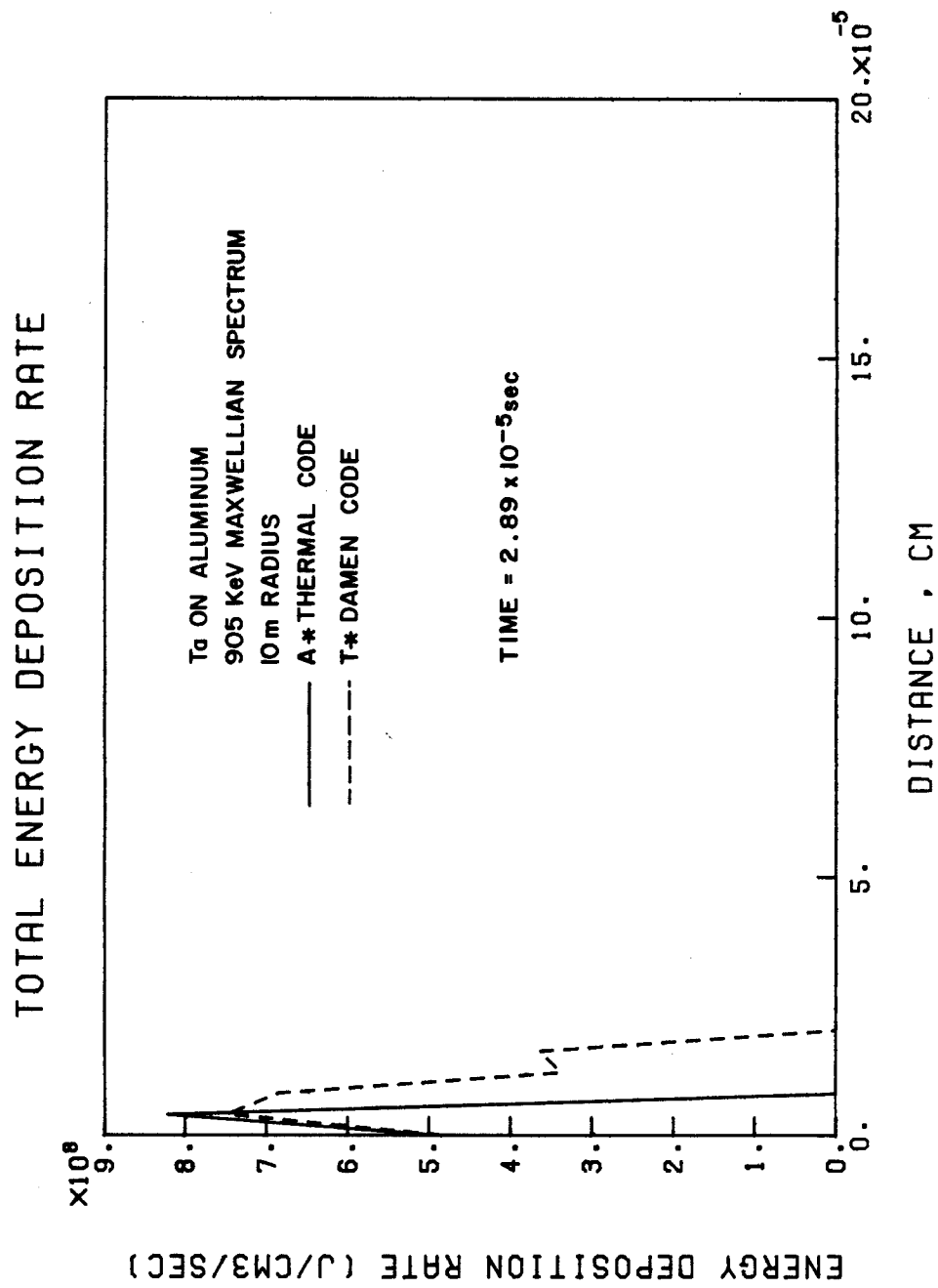


Fig. III-5. Energy deposition rate of Ta on aluminum.

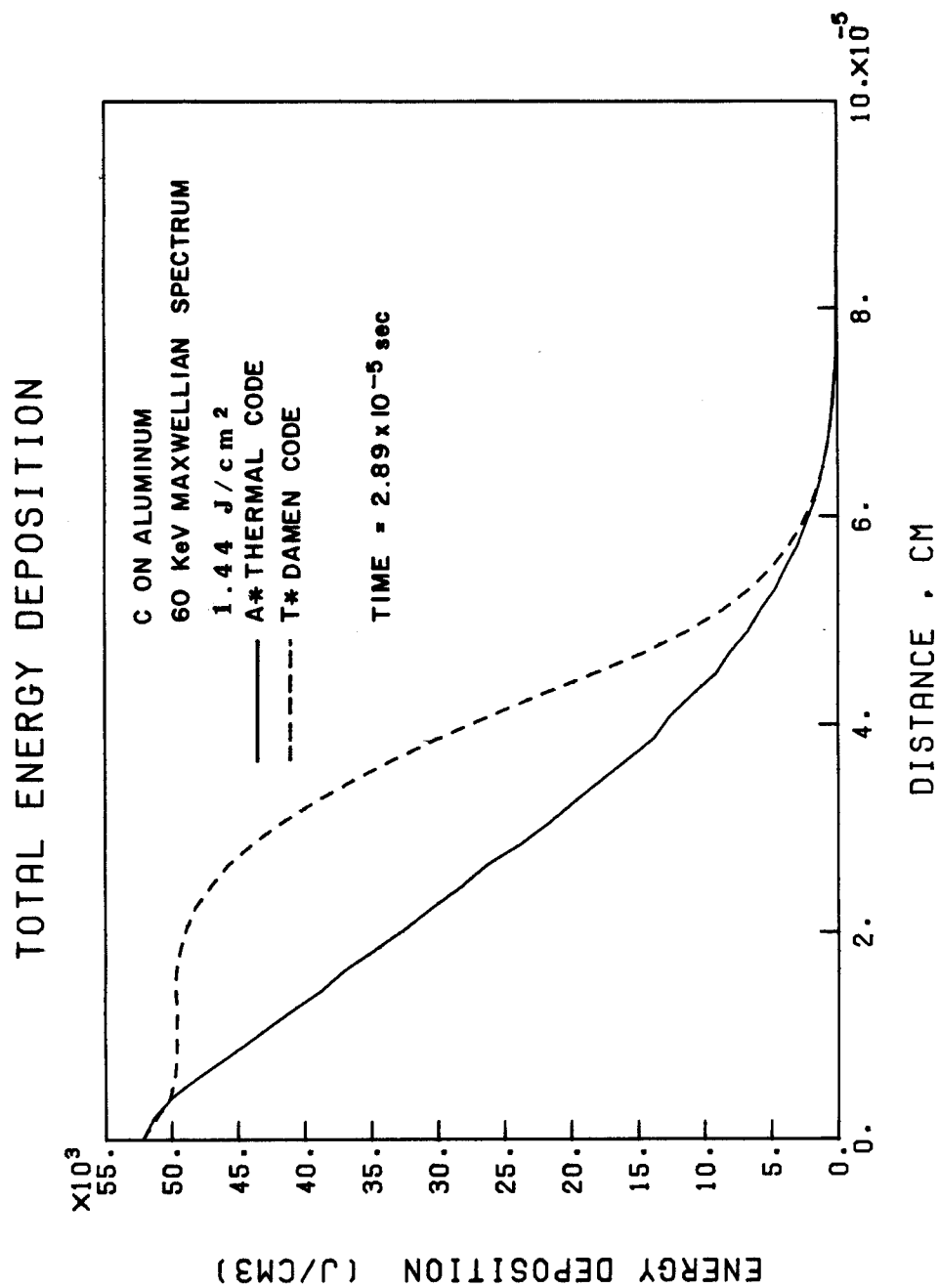


Fig. III-6. Total energy deposition of C on aluminum.

in the ions. The deposition rate as a function of space is much different and has much larger depth into aluminum than the one developed in this thesis as shown in Fig. III-7. These differences could have large effects on the accuracy of the thermal and displacement response calculations which require knowledge of the deposition function.

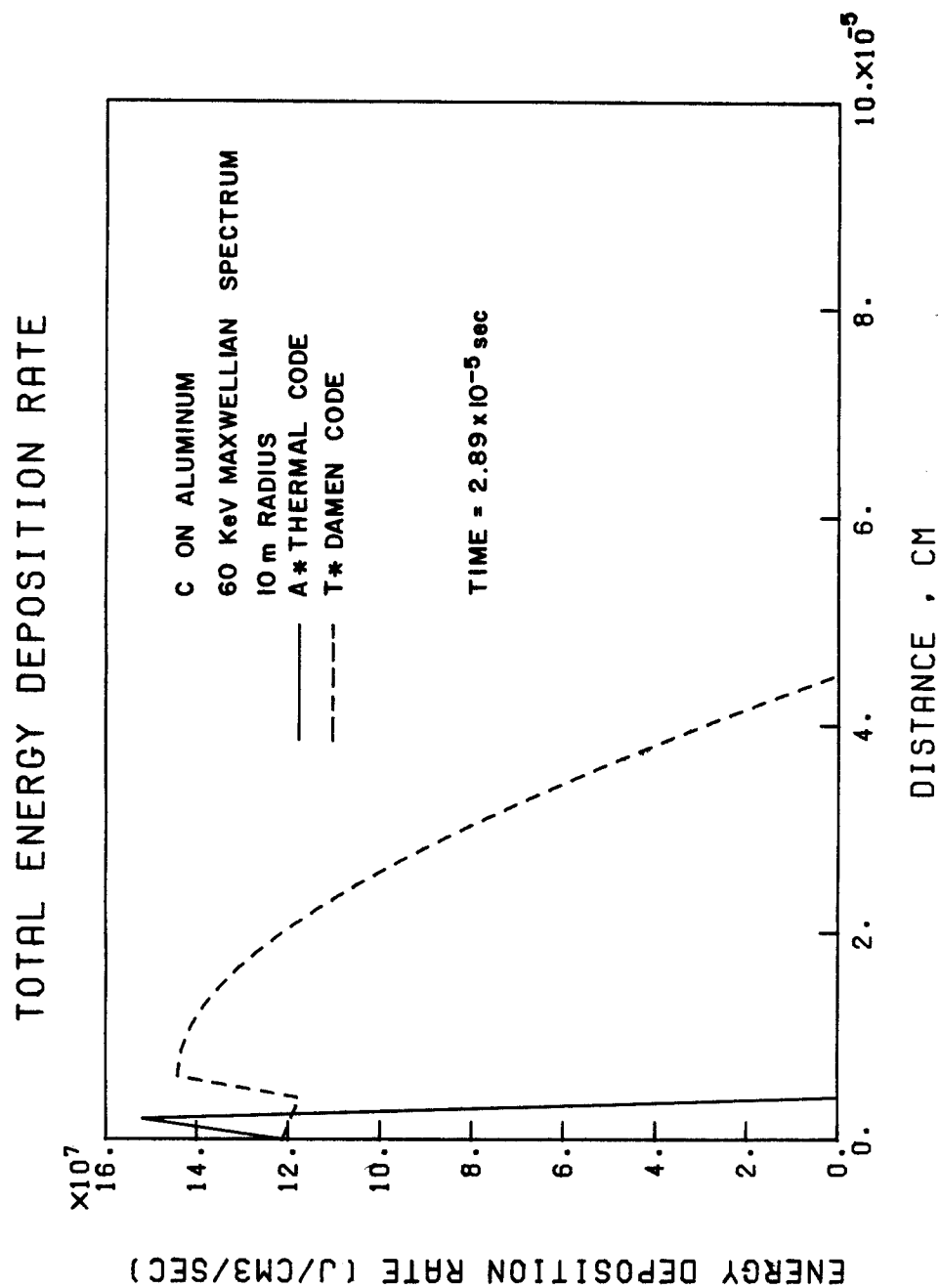


Fig. III-7. Energy deposition rate of C on aluminum.

References for Chapter III

1. R.E. Evans, The Atomic Nucleus, McGraw-Hill, 1955, pp. 672-745.
2. F. Biggs and R. Lighthill, "Analytical Approximations for X-Ray Cross Sections II," SC-PR-71-0507, Sandia Labs., Albuquerque, NM, December 1971.
3. K.G. Adams and F. Biggs, "Efficient Computer Access to the Sandia Photon Cross Sections," SC-PR-72-0683, Sandia Labs., Albuquerque, NM, December 1973.
4. F. Biggs and R. Lighthill, "Analytical Approximations for Total and Energy Absorption Cross Sections for Photon-Atom Scattering," SC-PR-72-0685, Sandia Labs., Albuquerque, NM, December 1972.
5. L.T. Chadderton, Radiation Damage in Crystals, John Wiley and Sons, Inc., New York.
6. N. Bohr, Mat. Fys. Medd. Dan. Vid. Selsk. 18(8), (1948).
7. J.D. Jackson, Classical Electrodynamics, 2nd Ed., John Wiley and Sons, 1975, pp. 284-292.
8. J. Lindhard et al., Range Concepts and Heavy Ion Ranges, "Mat. Fys. Medd. Dan. Vid. Selsk. 33(14), (1963) 3.
9. D.K. Brice, "Three-Parameter Formula for the Electronic Stopping Cross Section at Non-Relativistic Velocities," Physical Review A 6(5), (Nov. 1972) 1791.
10. D.K. Brice, "Ion Implantation Range and Energy Deposition Distribution," Vol. 1, IFI/Plenum, New York (1975).
11. J.F. Ziegler and H.H. Anderson, The Stopping and Ranges of Ions in Matter, Vol. 1-5, Pergamon Press, New York (1977).
12. L.C. Northcliffe and R.F. Schilling, "Range and Stopping-Power Tables for Heavy Ions," Nuclear Data Sec. 7(3-4), (1970).
13. O.S. Oen and M.T. Robinson, "Slowing-Down Time of Energetic Ions in Solids," Journal of Applied Physics 46(12), (December 1975) 5069.
14. L. Doná dalle Rose and A. Miofello, Rad. Eff. 53, (1980) 7.
15. G. Della Mea, L. Doná dalle Rose, P. Mazzoldi, and A. Miofello, Rad. Eff. 46, (1980) 133.

16. G.K. Celler, J.M. Poate, and L.C. Kimerling, Appl. Phys. Lett. 32, (1978) 464.
17. R.F. Wood and G.E. Giles, Physical Review B 23(6), (1981) 2923.
18. T.O. Hunter, Ph.D. Thesis, Department of Nuclear Engineering, University of Wisconsin-Madison, (July 1978).
19. D.K. Brice, "Ion Implantation Range and Energy Deposition Codes COREL, RASE 4, and DAMG2," SAND75-0622, Sandia Labs., Albuquerque, NM, July 1977.
20. K.B. Winterbon, "Heavy-Ion Range Profiles and Associated Damage Distributions," Rad. Eff. 13, (1972) 215.
21. I. Manning and G.P. Mueller, "Depth Distribution of Energy Deposition by Ion Bombardment," Computer Physics Communication 6, (1973).
22. A.M. Hassanein and G.L. Kulcinski, "A*THERMAL Code Description," University of Wisconsin Fusion Engineering Program Report, to be published.
23. T.O. Hunter and G.L. Kulcinski, "T*DAMEN, A Computer Code for Analysis of Transient Radiation Damage," University of Wisconsin Fusion Engineering Program Report UWFD-247, (May 1978).
24. G.L. Kulcinski and A.M. Hassanein, "Thermal Response of Unprotected Al, C, and Ta First Walls to Thermonuclear Target Spectra," University of Wisconsin/Westinghouse Electric Corporation, March 1980.

CHAPTER IV
 NUMERICAL METHODS FOR CALCULATING THE
 TEMPERATURE INCREASE USING THE GREEN'S FUNCTION

A. Introduction

The temperature response of a material exposed to thermonuclear radiation may be determined when the time and space dependent energy deposition functions are known. Typically, the Green's function is used to determine the thermal response of the first wall material.⁽¹⁾ The object of this chapter is to discuss a new method of using the Green's function to solve the heat conduction equation which avoids the singularities unique to this problem. A comparison is made between this calculation and a previous one,⁽²⁾ which did not treat the singularities, and corrections to the previous calculation will be presented. Finally, an approximate analytical solution for the non-linear heat-conduction equation using the perturbation theory, in which thermal properties vary with temperature, will be discussed.

B. Direct Deposition Model

The general heat-transfer equation is given by⁽³⁾

$$\rho c \frac{\partial T}{\partial t} - \nabla \cdot k \nabla T = \dot{q}(x, t) \quad (1)$$

where: ρ is the density of the material;

c is the specific heat;

k is the thermal conductivity.

All of the above properties vary with temperature. For the case of

constant thermal properties, this equation reduces to:

$$\rho_o c_o \frac{\partial T}{\partial t} - k_o \nabla^2 T = \dot{q}(x, t) \quad (2)$$

where ρ_o , c_o , k_o are independent of temperature.

The general solution for the temperature rise due to any deposition function can be obtained from the theory of Green's functions providing that the thermal properties do not vary with temperature and assuming that the Green's function is known:

$$T(x, t) = \int_{t'} \int_{x'} \frac{1}{\rho c} \dot{q}(x', t') G(x, t, x', t') dx' dt' \quad (3)$$

where: $\dot{q}(x, t)$ is the volumetric energy deposition rate

$G(x, t, x', t')$ is the Green's function.

For a semi-infinite medium, with insulated boundary, the Green's function is given by⁽³⁾

$$G(x, t, x', t') = \frac{1}{2\sqrt{\pi\alpha(t-t')}} \left\{ e^{-\frac{(x-x')^2}{4\alpha(t-t')}} + e^{-\frac{(x+x')^2}{4\alpha(t-t')}} \right\} \quad (4)$$

where α is the thermal diffusivity.

Unfortunately, problems arise when we try to perform the last integral in Eq. (3) either analytically or numerically. The Green's function possesses a singularity at $t' \rightarrow t$ and $x' \rightarrow x$. A method will be discussed to avoid these singularities when the integration is done analytically or numerically.

First, if we want to integrate analytically, then

$$T(x,t) = \int_{t'=0}^t \int_{x'=0}^{\infty} \frac{1}{\rho c} \dot{q}(x',t') G(x,t,x',t') dx' dt' .$$

At $t' \rightarrow t$ the Green's function has a singularity. To avoid that we integrate from $\int_{t'=0}^{t-\epsilon} + \int_{t-\epsilon}^t$ and take the limit when $\epsilon \rightarrow 0$, i.e.

$$\begin{aligned} T(x,t) = & \lim_{\epsilon \rightarrow 0} \int_0^{t-\epsilon} \int_{x'} \frac{1}{\rho c} \dot{q}(x',t') G(x,t,x',t') dx' dt' \\ & + \int_{t-\epsilon}^t \int_{x'} \frac{1}{\rho c} \dot{q}(x',t') G(x,t,x',t') dx' dt' . \end{aligned} \quad (5)$$

It can be shown that

$$\lim_{\epsilon \rightarrow 0} \frac{1}{2\sqrt{\pi\alpha\epsilon}} e^{-\frac{(x-x')^2}{4\alpha\epsilon}} \rightarrow \delta(x - x') \quad (\text{see Appendix A}) .$$

Equation (5) can then be written as

$$\begin{aligned} T(x,t) = & \int_0^{t-\epsilon} \int_{x'} \frac{1}{\rho c} \dot{q}(x',t') G(x,t,x',t') dx' dt' \\ & + \int_{t-\epsilon}^t \int_{x'} \frac{1}{\rho c} \dot{q}(x',t') \lim_{\epsilon \rightarrow 0} G(x,t,x',t') dx' dt' . \end{aligned} \quad (6)$$

The second part of the last form can be written as:

$$\int_{t-\epsilon}^t dt' \int_0^{\infty} \frac{1}{\rho c} \dot{q}(x',t') [\delta(x - x') + \delta(x + x')] dx' \quad (7)$$

or

$$\int_{t-\varepsilon}^t dt' [\dot{q}(x, t') + \dot{q}(-x, t')] \quad (8)$$

where: $\dot{q}(-x, t') = 0$.

Equation (8) then becomes

$$\int_{t-\varepsilon}^t dt' \dot{q}(x, t') \approx \dot{q}(x, t) \int_{t-\varepsilon}^t dt \approx \varepsilon \dot{q}(x, t) = 0$$

as $\varepsilon \rightarrow 0$. Substituting this result into Eq. (6) we find

$$T(x, t) = \int_0^{t-\varepsilon} dt' \int_0^\infty \frac{1}{\rho c} \dot{q}(x', t') G(x, x', t, t') dx' \quad (9)$$

The last integral can be performed analytically for reasonable deposition functions $\dot{q}(x, t)$, and we can then take the limit when $\varepsilon \rightarrow 0$.

In most practical cases, it is difficult to find an easy analytic deposition function so that it is very difficult to perform this integration analytically. This usually means that in order to accommodate different energy spectra and consequently different deposition functions, it is necessary to do the integration numerically. Assuming that we divide space and time into many divisions, the solution for the temperature increase is given by:

$$T(x_n, t_n) = \sum_{t'_i=0}^{t_n} w_i \Delta t_i \int_0^\infty \frac{1}{\rho c} \dot{q}(x', t'_i) G(x_n, t_n, x', t'_i) dx' \quad (10)$$

where: $T(x_n, t_n)$ is the temperature at any point x_n and time t_n
 w_i is a weighting factor depending on the method of
 integration
 Δt_i incremental time.

In this last integral the Green's function possesses a singularity at $t'_i \rightarrow t_n$. To avoid this singularity, first we integrate from $t_i = 0$ up to $t_i = t_{n-1}$ and the last term in this integration will be treated separately, i.e.,

$$\begin{aligned}
 T(x_n, t_n) = & \sum_{t'_i=0}^{t_{n-1}} w_i \Delta t_i \int_0^{\infty} dx' \frac{1}{\rho c} \dot{q}(x', t'_i) G(x_n, t_n, x', t'_i) \\
 & + w_n \Delta t_n \lim_{t'_i \rightarrow t_n} \int_0^{\infty} \frac{1}{\rho c} \dot{q}(x', t'_i) \frac{1}{2\sqrt{\pi\alpha(t_n - t'_i)}} \\
 & \cdot \left\{ e^{-\frac{(x_n - x')^2}{4\alpha(t_n - t'_i)}} + e^{-\frac{(x_n + x')^2}{4\alpha(t_n - t'_i)}} \right\} dx' .
 \end{aligned} \tag{11}$$

As before,

$$\begin{aligned}
 T(x_n, t_n) = & \sum_{t'_i=0}^{t_{n-1}} w_i \Delta t_i \int_0^{\infty} dx' \frac{1}{\rho c} \dot{q}(x', t'_i) G(x_n, t_n, x', t'_i) \\
 & + w_n \Delta t_n \int_0^{\infty} dx' \frac{1}{\rho c} \dot{q}(x', t_n) \{ \delta(x_n - x') + \delta(x_n + x') \}
 \end{aligned} \tag{12}$$

which can also be expressed as,

$$\begin{aligned}
T(x_n, t_n) = & \sum_{t'_i=0}^{t_{n-1}} w_i \Delta t_i \int_0^{\infty} \frac{1}{\rho c} \dot{q}(x', t'_i) G(x_n, t_n, x', t'_i) dx' \\
& + \frac{1}{\rho c} w_n \Delta t_n \dot{q}(x_n, t_n) \quad .
\end{aligned}
\tag{13}$$

Care should be taken in choosing the time increments. For more accurate results the last time increment should be very small and should give a stable solution for small changes around it, i.e.

$$\Delta t_n \ll \Delta t_i, \quad i \neq n$$

and

$$t_{n-1} = t_n - \Delta t_n$$

so that the approximation of the Green's function by a δ -function is reasonable.

Thus, by this method we avoided the Green's function singularities and for any given deposition function we can calculate the temperature increase at any point and at any time.

The solution of the last equation (13) is contained in the computer code A*THERMAL⁽⁴⁾. When the deposition function, $\dot{q}(x, t)$, is directly used in the solution it is called the direct deposition method. Since the solutions for different models of the energy deposition discussed by Hunter⁽⁵⁾ in the computer code T*DAMEN⁽⁶⁾ did not contain corrections for these singularities, we have included the complete and correct solution for any deposition function in the

code, A*THERMAL.⁽⁴⁾ The modified methods will be discussed here and the difference in the results obtained directly from the deposition function will also be illustrated.

C. Simple Deposition Model

For low energy ions, where the energy loss can be expressed with a modified Lindhard model, the volumetric energy deposition rate can be written as,⁽²⁾

$$\dot{q}(x,t) = f(t) g(x) \quad (14)$$

and

$$g(x) = \left. \begin{aligned} & \left(\frac{A_1}{t} - A_2 x \right) & x < x_{\max} \\ & = 0 & x > x_{\max} \end{aligned} \right\} \quad (15)$$

where $f(t)$ is the incident particle flux

x_{\max} is the maximum range of the ions

A_1, A_2 are constants.

The temperature rise due to this deposition function can be obtained by performing the integral,

$$T(x,t) = \int_{t'} f(t') \int_{x'} \left(\frac{A_1}{t'} - A_2 x' \right) G(x,t,x',t') dx' dt' \quad (16)$$

To solve this integral by methods developed in this paper, the temperature at any point x_n and time t_n is given by

$$\begin{aligned}
T(x_n, t_n) &= \sum_{t'=t_1}^{t_{n-1}} w_1 f(t_1) \Delta t_1 \int_{x'=0}^{x_{\max}} \frac{1}{\rho c} \left(\frac{A_1}{t'} - A_2 x' \right) G(x_n, t_n, x', t') dx' \\
&\quad + w_n \Delta t_n f(t_n) \lim_{t' \rightarrow t_n} \int_0^{x_{\max}} \frac{1}{\rho c} \left(\frac{A_1}{t'} - A_2 x' \right) G(x_n, t_n, x', t') dx' .
\end{aligned} \tag{17}$$

The second integral can be reduced to

$$= \frac{1}{\rho c} w_n \Delta t_n f(t_n) \int_0^{x_{\max}} \left(\frac{A_1}{t_n} - A_2 x' \right) \{ \delta(x_n - x') + \delta(x_n + x') \} dx'$$

where $\delta(x + x') = 0$ since $x' > 0$

$$\begin{aligned}
&= \frac{1}{\rho c} w_n \Delta t_n f(t_n) \left(\frac{A_1}{t_n} - A_2 x_n \right) \quad \begin{matrix} x_n < x_{\max} \\ \\ \\ \end{matrix} \\
&= 0 \quad \begin{matrix} x_n > x_{\max} \end{matrix} \quad \} \tag{18}
\end{aligned}$$

Then the complete solution is given by

$$\begin{aligned}
T(x_n, t_n) &= \sum_{t'=t_1}^{t_{n-1}} w_1 f(t_1) \Delta t_1 \int_{x'=0}^{x_{\max}} \frac{1}{\rho c} \left(\frac{A_1}{t'} - A_2 x' \right) G(x_n, t_n, x', t') dx' \\
&\quad + \left\{ \begin{aligned} &\frac{1}{\rho c} w_n \Delta t_n f(t_n) \left(\frac{A_1}{t_n} - A_2 x_n \right) \quad x_n < x_{\max} \\ &0 \quad x_n > x_{\max} \end{aligned} \right. \tag{19}
\end{aligned}$$

D. Uniform Deposition Model

The work of Frank et al.,⁽⁶⁾ considered the response of an infinite half space subject to a uniform spatial and temporal energy deposition as shown in Fig. IV-1. The solution was only given for the resulting surface temperature as a function of time. Hovingh^(7,8) used the same deposition assumption, but evaluated the temperature numerically with the Chart-D Code.⁽⁹⁾ The response at any time and position was derived by Hunter,⁽¹⁰⁾ but the numerical solution for the time integral used in the T*DAMEN code did not treat the singularities correctly. In this study, the complete solution using numerical integration for the time integral to allow different spectra is derived below. The deposition function is given by

$$\dot{q}(x,t) = \frac{F(t)}{\delta x(t)} \frac{1}{K}$$

where: $F(t)$ = incident energy/unit area

$\delta x(t)$ = deposition region

K = deposition duration.

The temperature rise is then give by

$$T(x,t) = \frac{1}{\rho c} \int_{t'} \frac{f(t')}{K \delta x(t')} dt' \int_0^{\delta x} G(x,t,x',t') dx' \quad (20)$$

The spatial integral can be reduced to⁽³⁾

$$\int_0^{\delta x} G(x,t,x',t') dx' = \frac{1}{2} \left[\operatorname{erf}\left(\frac{\delta x - x}{2\sqrt{\alpha(t-t')}}\right) + \operatorname{erf}\left(\frac{\delta x + x}{2\sqrt{\alpha(t-t')}}\right) \right] \quad (21)$$

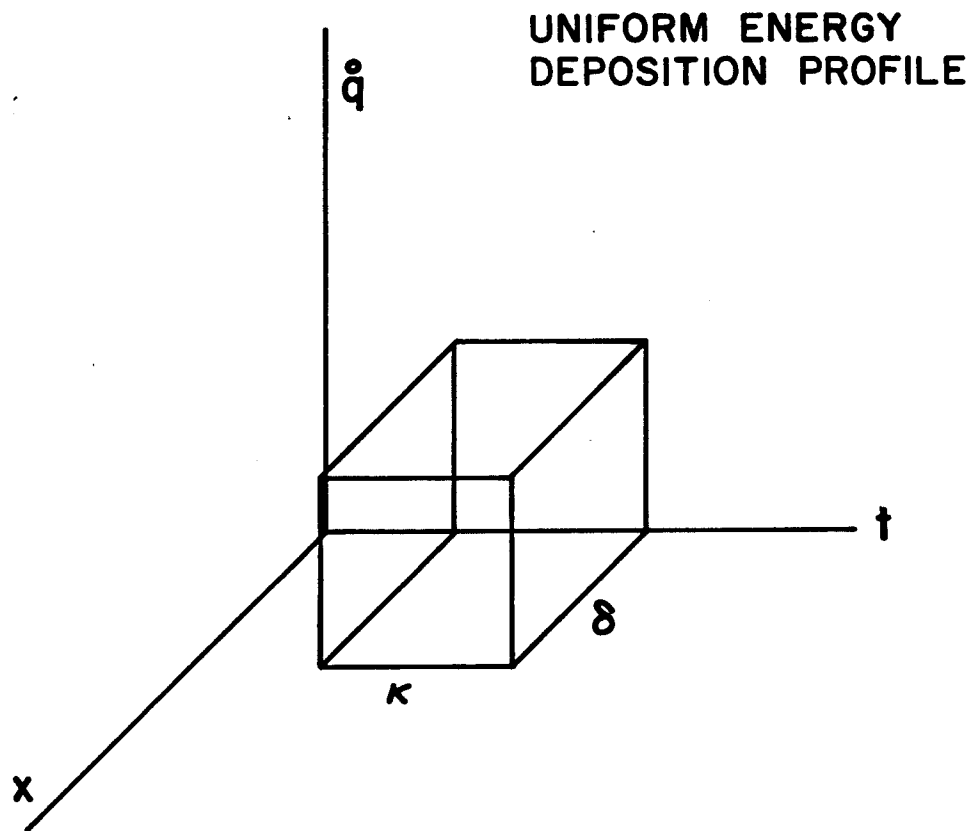


Fig. IV-1. Uniform energy deposition profile.

where: erf = error function.

Then,

$$T(x, t) = \frac{1}{2} \frac{1}{\rho c} \int_{t'} \frac{f(t')}{K \delta x(t')} \left[\operatorname{erf}\left(\frac{\delta x - x}{2\sqrt{\alpha(t - t')}}\right) + \operatorname{erf}\left(\frac{\delta x + x}{2\sqrt{\alpha(t - t')}}\right) \right] dt' \quad (22)$$

where $0 \leq t' \leq K$. Now to integrate numerically with respect to time

$$\begin{aligned} T(x_n, t_n) &= \frac{1}{2} \sum_{t_i=0}^{t_{n-1}} \frac{1}{\rho c} w_i \Delta t_i \frac{f(t_i)}{K \delta x(t_i)} \left[\operatorname{erf}\left(\frac{\delta x - x_n}{2\sqrt{\alpha(t_n - t_i)}}\right) \right. \\ &\quad \left. + \operatorname{erf}\left(\frac{\delta x + x_n}{2\sqrt{\alpha(t_n - t_i)}}\right) \right] + \frac{1}{2} \frac{1}{\rho c} \frac{f(t_n)}{K \delta x(t_n)} w_n \Delta t_n \\ &\quad \cdot \lim_{t_i \rightarrow t_n} \left\{ \operatorname{erf}\left(\frac{\delta x - x_n}{2\sqrt{\alpha(t_n - t_i)}}\right) + \operatorname{erf}\left(\frac{\delta x + x_n}{2\sqrt{\alpha(t_n - t_i)}}\right) \right\} \end{aligned} \quad (23)$$

since

$$\lim_{t_i \rightarrow t_n} \operatorname{erf}\left(\frac{\delta x - x_n}{2\sqrt{\alpha(t_n - t_i)}}\right) = \begin{cases} \operatorname{erf}(\infty) = 1 & \text{if } x_n < \delta \\ \operatorname{erf}(-\infty) = -1 & \text{if } x_n > \delta \end{cases}$$

and

$$\lim_{t_i \rightarrow t_n} \operatorname{erf}\left(\frac{\delta x + x_n}{2\sqrt{\alpha(t_n - t_i)}}\right) = \operatorname{erf}(\infty) = 1$$

and the last term reduces to

$$\begin{aligned}
&= \frac{1}{\rho c} w_n \Delta t_n \frac{f(t_n)}{K \delta x(t_n)} & x_n < \delta \\
&= 0 & x_n > \delta .
\end{aligned}$$

This result could also be obtained directly from the Green's function since

$$\lim_{t_i \rightarrow t_n} \int_0^{\delta} G(x_n, t_n, x', t_i) dx' = \int_0^{\delta} \{ \delta(x_n - x') + \delta(x_n + x') \} dx' = 1 .$$

Then, the temperature rise is given by

$$\begin{aligned}
T(x_n, t_n) &= \frac{1}{2} \frac{1}{\rho c} \sum_{t_i=0}^{t_{n-1}} w_i \Delta t_i \frac{f(t_i)}{K \delta x(t_i)} \left[\operatorname{erf} \left(\frac{\delta x - x_n}{2\sqrt{\alpha(t_n - t_i)}} \right) \right. \\
&\quad \left. + \operatorname{erf} \left(\frac{\delta x - x_n}{2\sqrt{\alpha(t_n - t_i)}} \right) \right] + \left\{ \begin{array}{ll} \frac{1}{\rho c} w_n \Delta t_n \frac{f(t_n)}{K \delta x(t_n)} & x_n < \delta \\ 0 & x_n > \delta . \end{array} \right. \quad (24)
\end{aligned}$$

E. General Deposition Model

In this model, first developed by Hunter,⁽²⁾ the deposition function is transformed into the general form of a polynomial with coefficients determined by the energy of the ion, i.e.,

$$\dot{q}(x, t) = f(t) g(x) \quad (25)$$

where

$$g(x) = \sum_{i=0}^4 C_i x^i \quad (26)$$

and C_i are in general functions of time. The solution for the temperature will be given by

$$T(x,t) = \int_{t'} f(t') \int_{x'} \frac{1}{\rho c} \left(\sum_{i=0}^4 C_i x'^i \right) G(x,t,x',t') dx' dt' . \quad (27)$$

The spatial integral becomes the evaluation of the following sequence

$$S_i = \frac{C_i}{\sqrt{\pi}} \int \left(\frac{x'^i}{A} e^{-\frac{(x'-x)^2}{A^2}} + \frac{x'^i}{A} e^{-\frac{(x'+x)^2}{A^2}} \right) dx' \quad (28)$$

where: $A = 2\sqrt{\alpha(t-t')}$.

The solutions for these S_i integrals are given in reference (9). The complete solution for the temperature rise is then

$$T(x,t) = \int dt' \frac{f(t')}{\rho c} \frac{1}{\sqrt{\pi}} \sum C_i S_i \mid \text{evaluated at limits of } x' . \quad (29)$$

The spatial contribution is contained in the evaluation of the function $\sum C_N S_N$ at the limits of the deposition region while the temporal contribution can be done numerically to allow for arbitrary spectra.

In the general deposition profile, the deposition function is divided into three regions as shown in Fig. IV-2. Each region has

GENERAL ENERGY DEPOSITION PROFILE

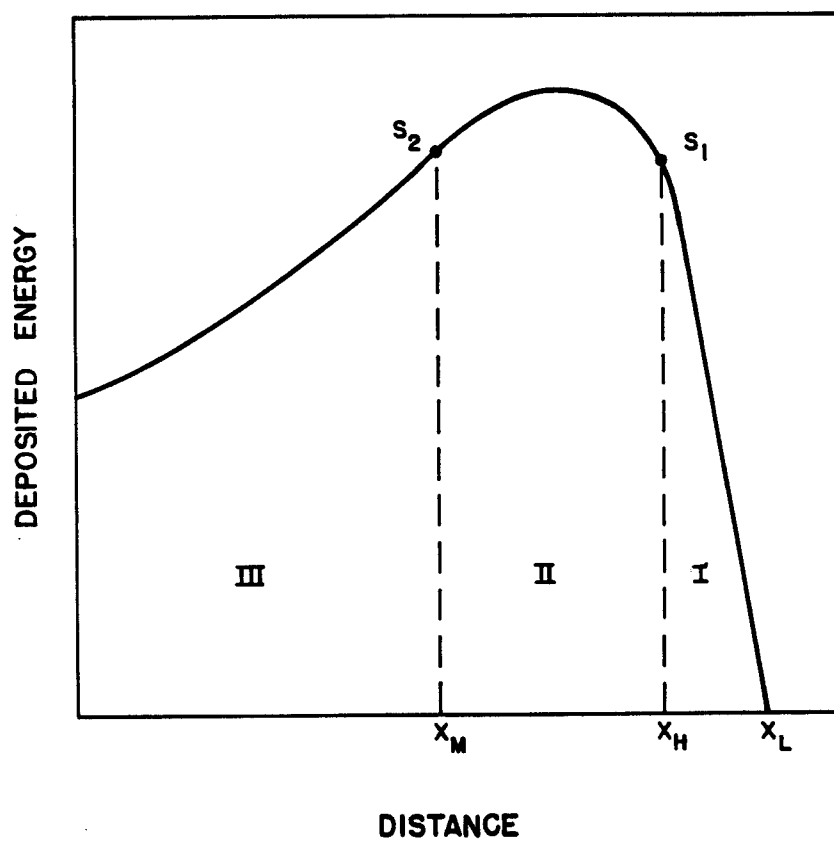


Fig. IV-2. General ion energy deposition profile.

different coefficients C_i 's. The temperature rise can be written as

$$T(x,t) = \int dt' \frac{f(t')}{\rho c} \frac{1}{\sqrt{\pi}} \left\{ \sum_{i=0}^4 C_{1i} S_i|_{III} + \sum_{i=0}^4 C_{2i} S_i|_{II} + \sum_{i=0}^4 C_{3i} S_i|_I \right\} \quad (30)$$

where: C_{1i} = the coefficient of the deposition function in region I

$S_i|_I$ = the value of the function S_i at the limits of region I.

It is now possible to integrate numerically over time by the methods developed in this paper. The temperature rise at any point x_n and time t_n is given by

$$T(x_n, t_n) = \frac{1}{\rho c \sqrt{\pi}} \sum_{i=0}^{t_n-1} w_i \Delta t_i f(t_i) \left\{ \sum_{i=0}^4 C_{3i} S_i|_{x'=x_M} + \sum_{i=0}^4 C_{2i} S_i|_{x'=x_H} + \sum_{i=0}^4 C_{1i} S_i|_{x'=x_L} \right\} + \frac{1}{\rho c \sqrt{\pi}} w_n \Delta t_n f(t_n) \cdot \lim_{t_i \rightarrow t_n} \int g(x') G(x_n, t_n, x', t') dx' \quad (31)$$

where: x_M, x_H, x_L are the three limits of the deposition region.

The second integral can be written as:

$$= \frac{1}{\rho c \sqrt{\pi}} w_n \Delta t_n f(t_n) \left\{ \left(\int_0^{x_M} \sum_i C_{3i} x'^i + \int_{x_M}^{x_H} \sum_i C_{2i} x'^i + \int_{x_H}^{x_L} \sum_i C_{1i} x'^i \right) \delta(x' - x_n) dx' \right\}$$

$$\begin{aligned}
& \sum_{i=0}^4 C_{3i} x_n^i & 0 \leq x_n \leq x_M \\
= \frac{1}{\rho c \sqrt{\pi}} w_n \Delta t_n f(t_n) & \left[\left\{ \begin{array}{ll} 0 & \text{otherwise} \end{array} \right\} \right. & (32) \\
& \sum_i C_{2i} x_n^i & x_M < x_n \leq x_H \\
& + \left\{ \begin{array}{ll} 0 & \text{otherwise} \end{array} \right\} \\
& \sum_i C_{1i} x_n^i & x_H < x_n \leq x_L \\
& + \left\{ \begin{array}{ll} 0 & \text{otherwise} \end{array} \right\} \left. \right] .
\end{aligned}$$

F. Results and Conclusions

In this section, we compare the differences between the methods developed in this paper with previous calculations.^(1,2) Two examples are considered in this study. In these examples we calculate the thermal response of a material, for example a first wall in an inertial confinement fusion reactor, due to a given spectrum of incident ions.

In the first example we considered hydrogen ions with a 5 keV Maxwellian spectrum incident on an aluminum wall. Figure IV-3 shows the energy deposition rate of hydrogen ions into aluminum. It can be seen that the range of hydrogen is about 0.3 micron. Figure IV-4 shows a comparison of the time dependent temperature response of the Al surface as predicted by the A*THERMAL and T*DAMEN codes. The same deposition function given in Fig. IV-1 was used by the two codes.

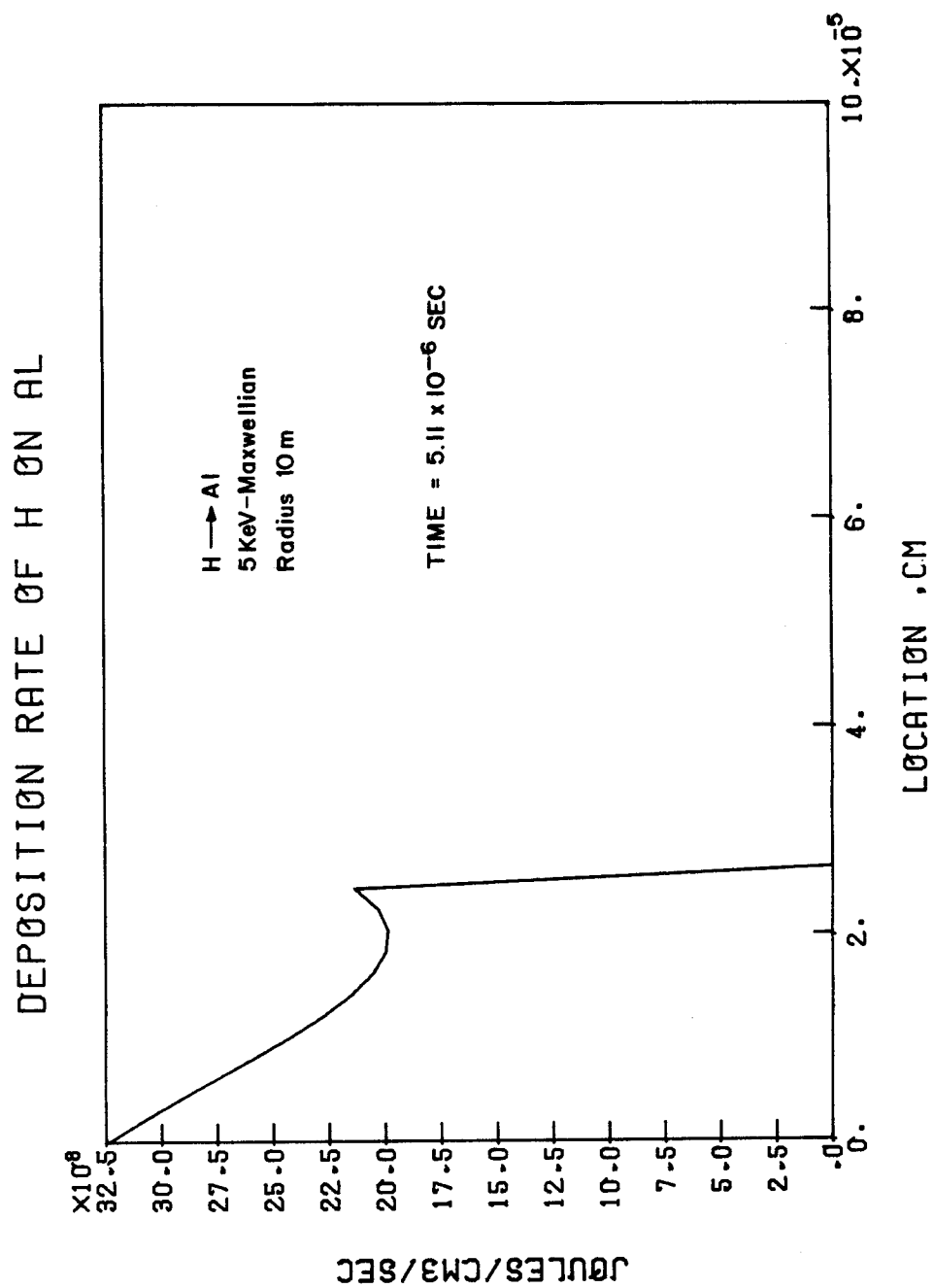


Fig. IV-3. Energy deposition rate of H on aluminum.

A-THERMAL.CODE (DEP MOD.) VS T-DAMEN.

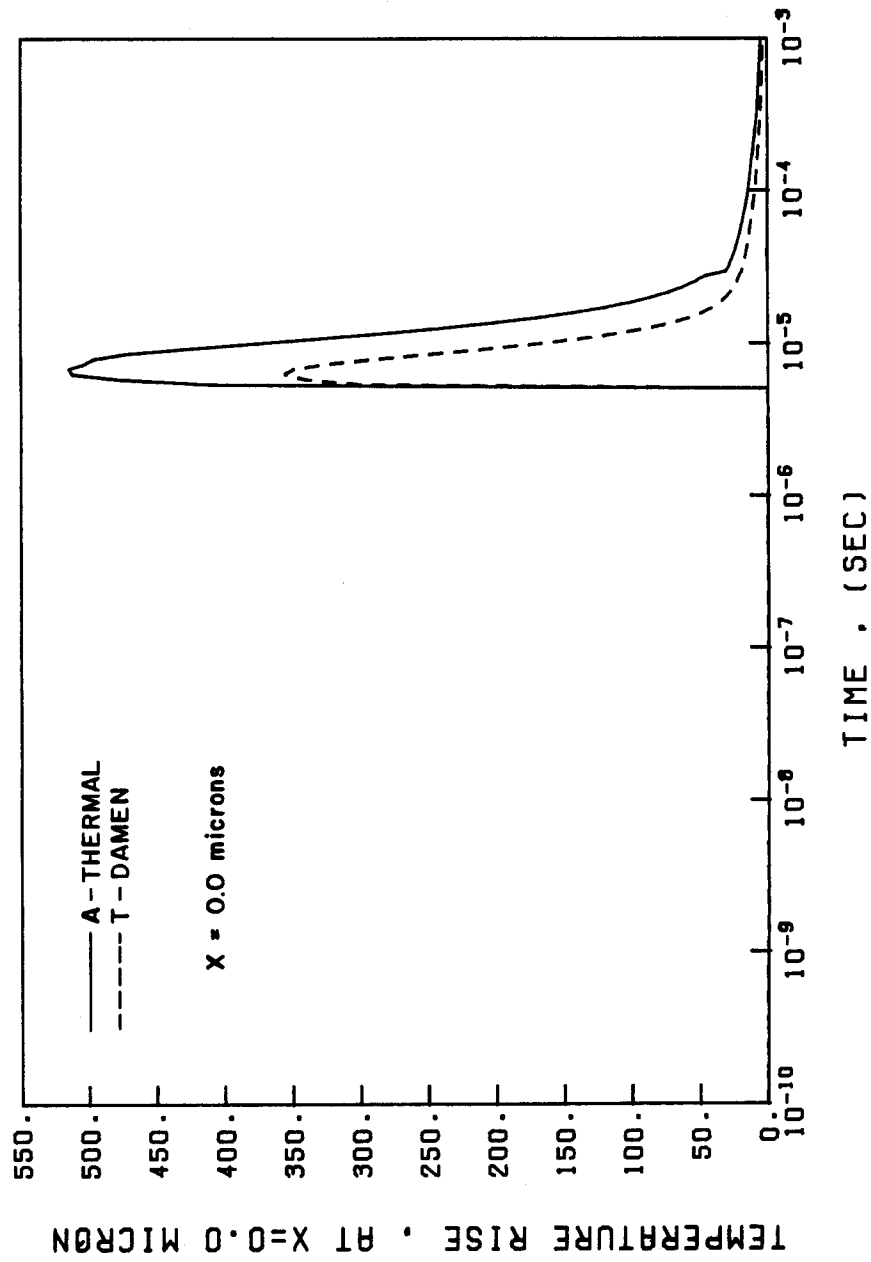


Fig. IV-4. Comparison of surface temperature rise using deposition model.

The difference between the two codes with respect to the peak temperature rise at the surface is about 30%, being lower for the T*DAMEN code. The direct deposition model, developed earlier in this paper, was used to compare with the general deposition model of T*DAMEN.

Figure IV-5 shows a comparison between the codes A*THERMAL and T*DAMEN both using the simple deposition model discussed before. A*THERMAL, using the correct solution of the simple deposition model, yields almost the same result as the direct deposition model shown in Fig. IV-4. Again the T*DAMEN estimation is about 30% lower than that predicted by the A*THERMAL code. As mentioned before, these differences arise from the improper treatment of the Green's function singularities when integrating numerically over time.

Figure IV-6 shows a comparison between the direct deposition model and the correct solution of the simple and the general deposition models, developed in this paper. The agreement among these different models is fairly good except that the simple deposition model underestimates the temperature rise at later times because of the simple representation of the deposition function.

A comparison between the codes A*THERMAL and T*DAMEN in calculating the temperature rise at 0.5 micron (beyond the end of range of the hydrogen) from the Al surface is shown in Fig. IV-7. The comparison is made using the same model, i.e. the simple deposition model. It is noted that at $x = 0.5$ micron, both codes agree fairly well. This can be explained by noting from Fig. IV-3 that there is no deposition at $x = 0.5$ micron and all hydrogen ions are stopped

A* THERMAL . VS T* DAMEN . CODE (MOD. 1)

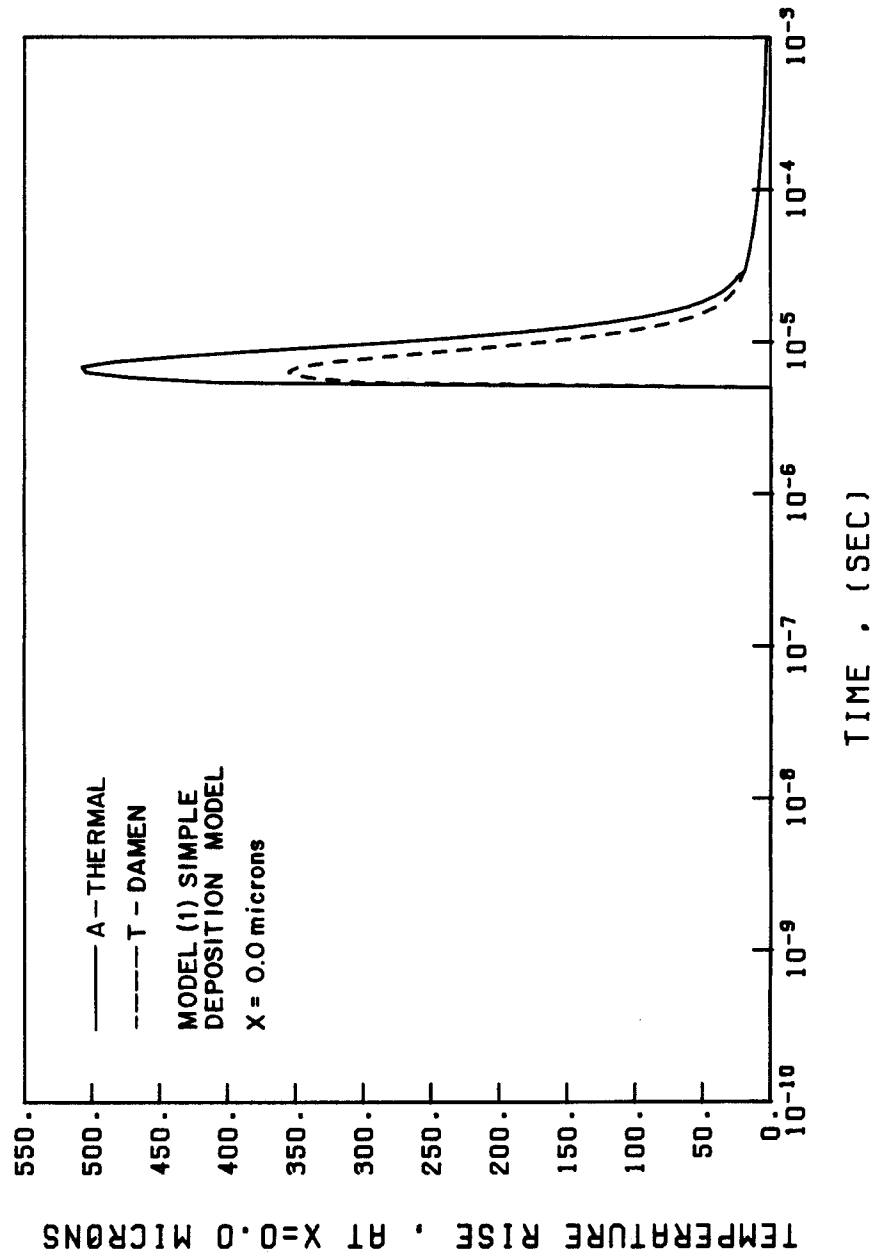


Fig. IV-5. Comparison of surface temperature rise using simple deposition model.

A-THERMAL CODE (DIFFERENT MODELS)

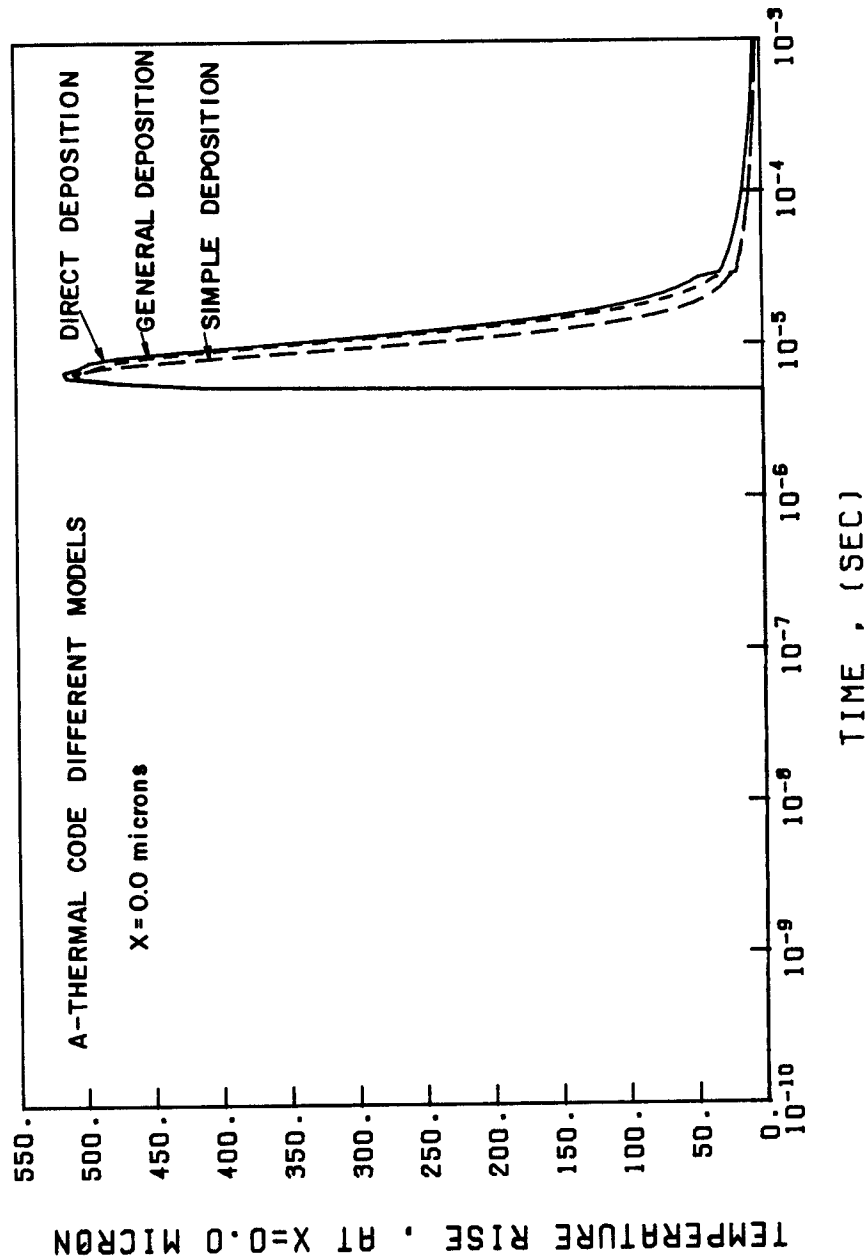


Fig. IV-6. Comparison of surface temperature rise using three different models.

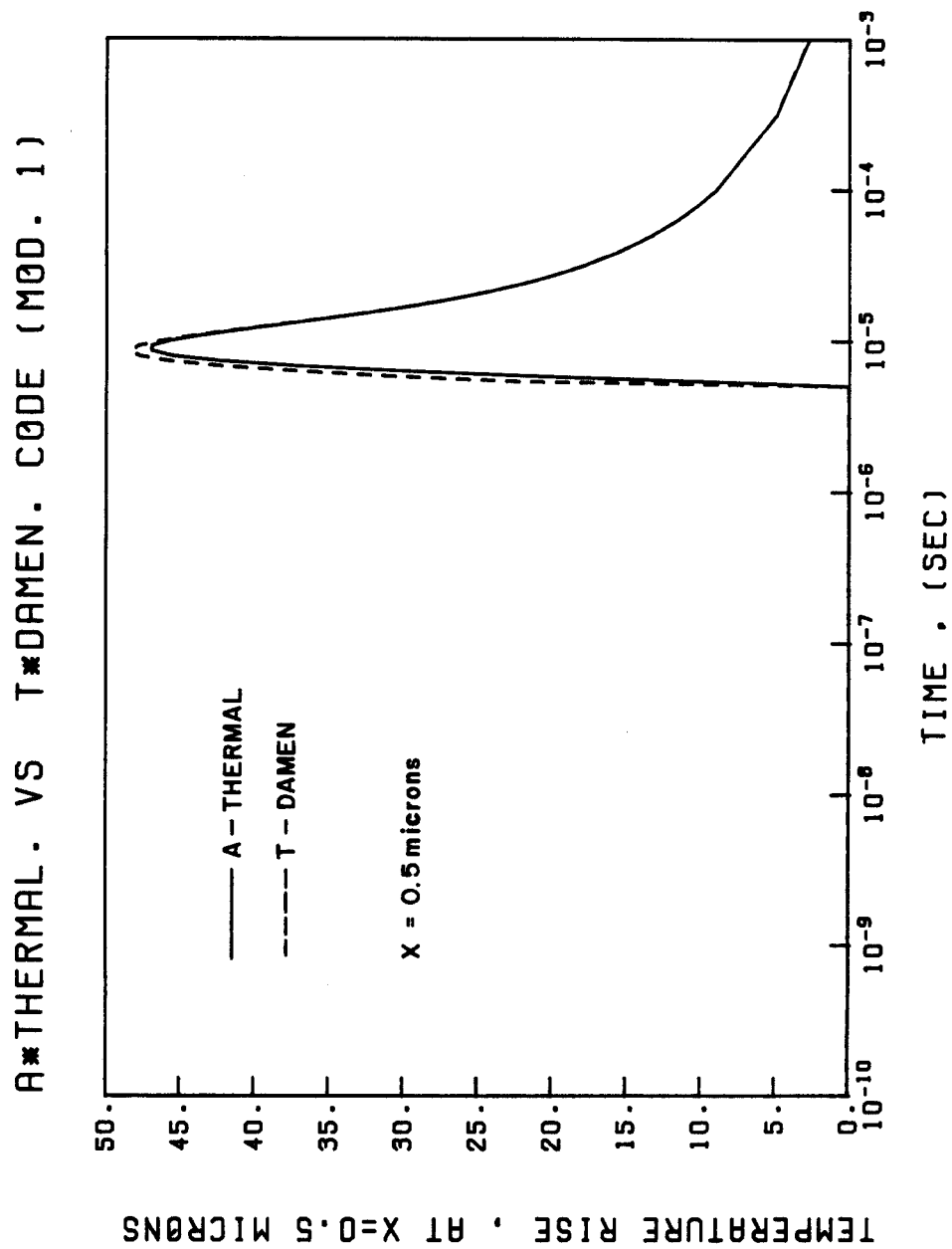


Fig. IV-7. Comparison of temperature rise at $x = 0.5$ microns using simple deposition model.

within a distance of 0.3 micron. This means that

$$\dot{q}(x = 0.5 \text{ micron}, t) = 0$$

and the correction due to the Green's function singularity goes to zero.

Another example to illustrate these differences uses Ta ions incident on an Al wall. The tantalum spectrum is assumed to be 905 keV Maxwellian. Figure IV-8 shows the energy deposition rate as a function of distance into Al wall at 5.11 microseconds and Fig. IV-9 shows the deposition rate as a function of time. In this calculation of the temperature rise of Al, it is assumed that no phase change takes place, i.e., as if Al were to stay as a solid; phase change and vaporization are considered in the next chapters. Figure IV-10 represents the temperature rise of an Al first wall surface as calculated from the codes A*THERMAL and T*DAMEN. In these cases T*DAMEN overestimates the temperature rise by about 20%, compared to an underestimation of about 30% due to incident hydrogen ions. This is again because of the improper treatment of the Green's function singularities. Figure IV-11 shows a comparison between the direct deposition model and the modified general deposition model in the A*THERMAL code. The agreement is very good.

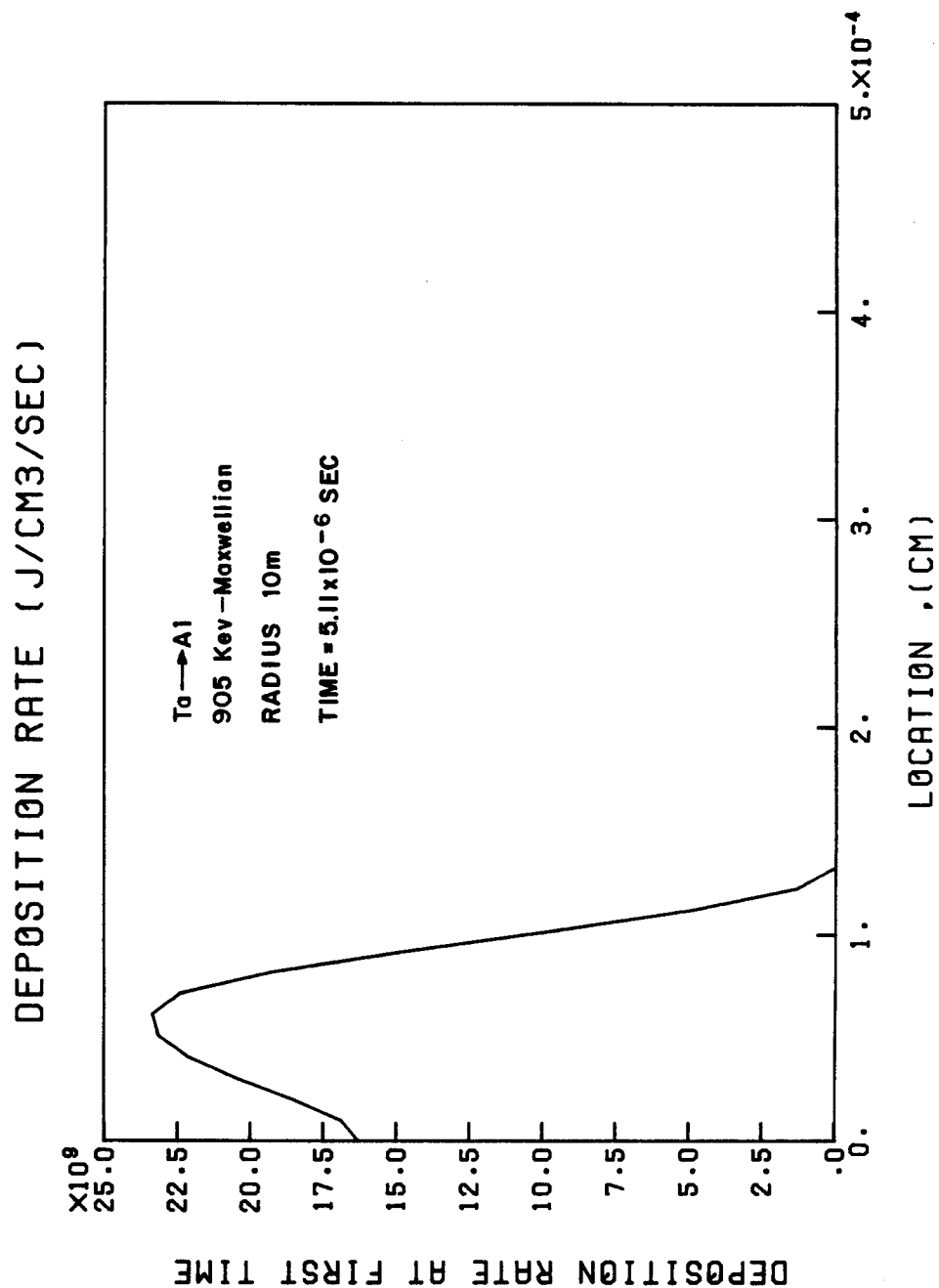


Fig. IV-8. Energy deposition rate of Ta onto aluminum as a function of penetration depth.

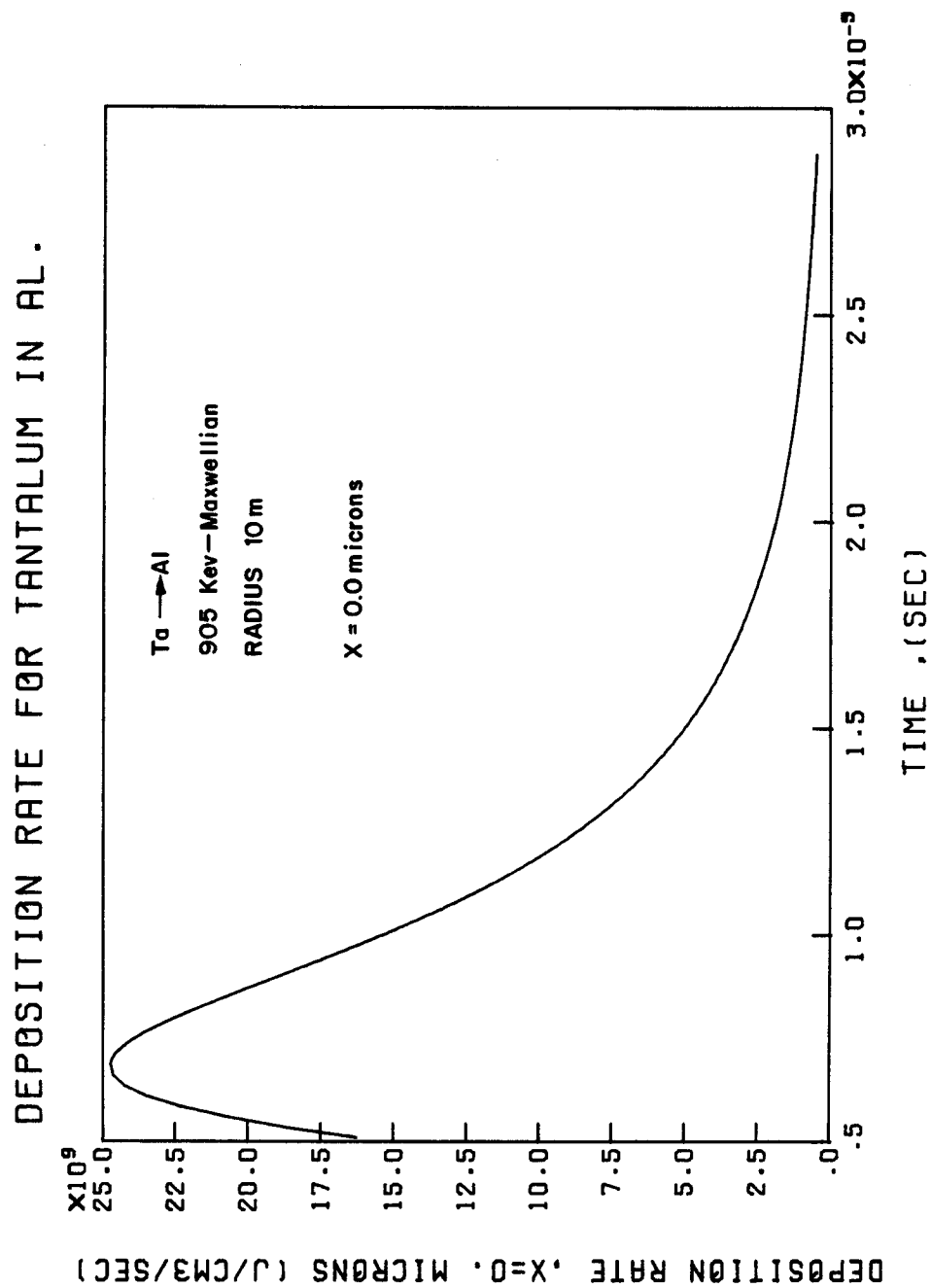


Fig. IV-9. Energy deposition rate of Ta onto aluminum as a function of time.

A* THERMAL VS T* DAMEN CODE

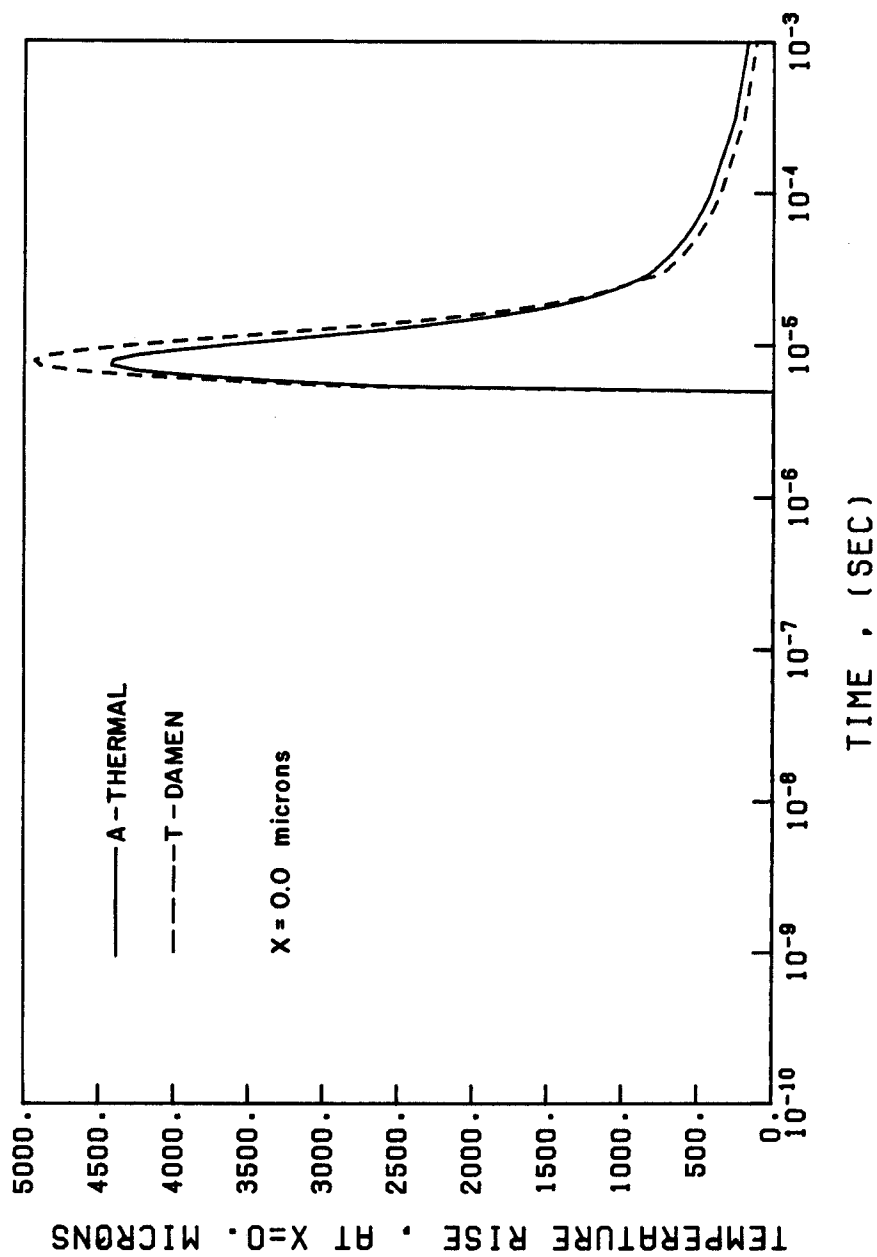


Fig. IV-10. Comparison of surface temperature rise using different codes.

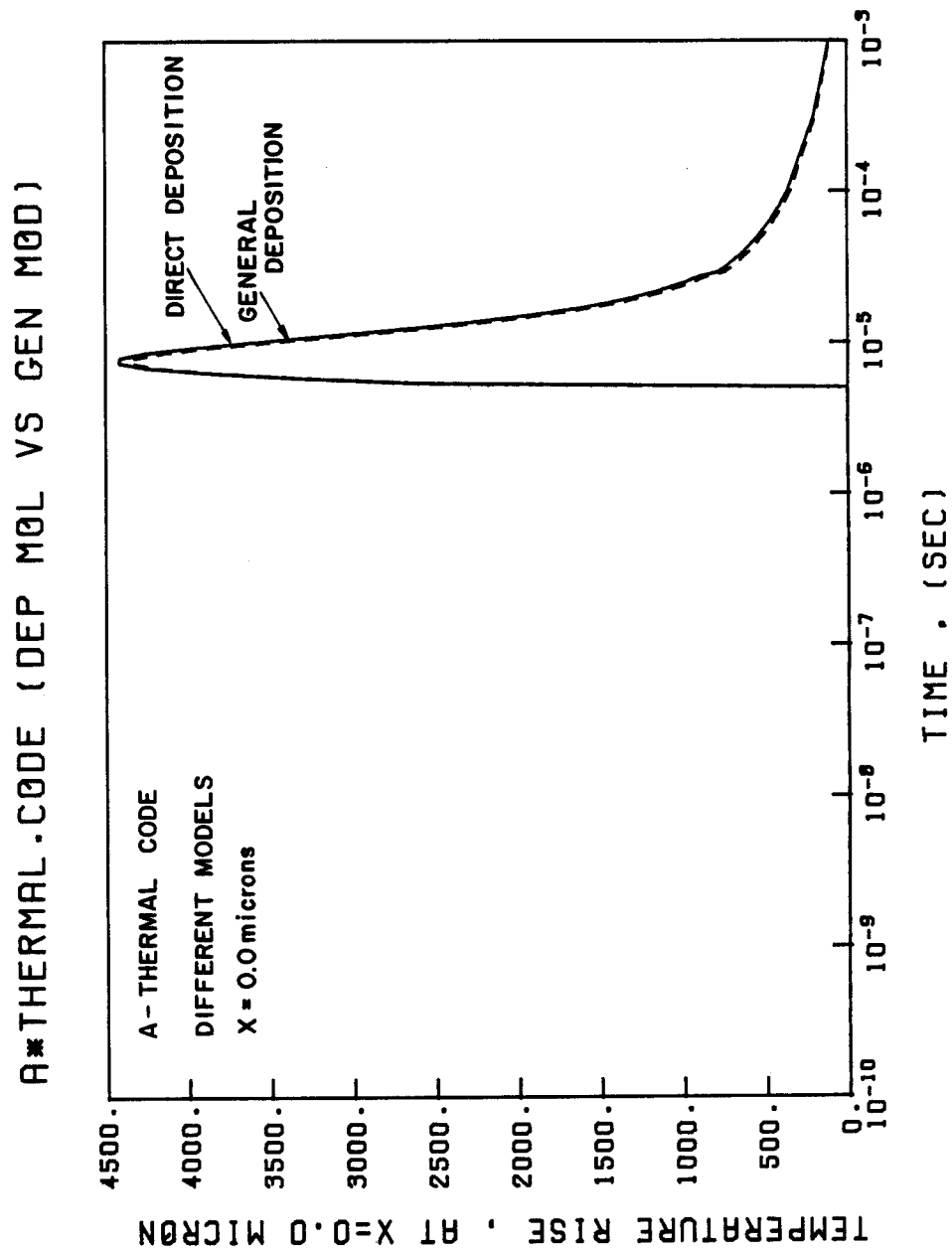


Fig. IV-11. Comparison of surface temperature rise using direct and general deposition models.

G. Approximate Solution for the Nonlinear Heat Conduction Equation
Using the Methods of Green's Function

In this section, we consider the case where the thermal properties vary with temperature. In most cases, it is a good approximation to assume that the thermal properties, i.e. thermal conductivity and specific heat vary linearly with temperature,

$$k = k_o (1 + bT) \quad (33)$$

$$C = C_o (1 + aT) \quad (34)$$

where a , b are constants. If the density ρ also varies with temperature, we can use

$$\rho C = \rho_o C_o (1 + a_1 T) \quad .$$

Substituting Eqs. (33) and (34) into Eq. (1) yields

$$\rho C_o (1 + aT) \frac{\partial T}{\partial t} - k_o \nabla \cdot (1 + bT) \nabla T = \dot{q}(x, t)$$

$$\rho C_o \frac{\partial T}{\partial t} - k_o \nabla^2 T = \dot{q}(x, t) + [bk_o \nabla \cdot (T \nabla T) - a\rho C_o T \frac{\partial T}{\partial t}]$$

or

$$\rho C_o \frac{\partial T}{\partial t} - k_o \nabla^2 T = \dot{q}(x, t) + bf_1(x, t) - af_2(x, t) \quad (35)$$

where

$$f_1(x, t) = k_o \nabla \cdot (T \nabla T) = k_o [T \nabla^2 T + (\nabla T)^2] \quad (36)$$

$$f_2(x,t) = \rho C_o T \frac{\partial T}{\partial t} = \rho C_o T \dot{T} \quad (37)$$

Using first order perturbation methods^(11,12) the solution of Eq. (35) can be obtained by analogy to the solution of Eq. (2). That is

$$T_1(x,t) = T(x,t) + bF_1(x,t) - aF_2(x,t) \quad (38)$$

where $T(x,t)$ is the solution for the heat conduction equation with constant thermal properties, i.e.

$$T(x,t) = \int_{t'} \int_{x'} \frac{\dot{q}(x',t')}{\rho C_o} G(x,t,x',t') dx' dt' \quad (39)$$

$$F_1(x,t) = \alpha_o \int_{t'} \int_{x'} \nabla \cdot (T_1 \nabla T_1) G(x,t,x',t') dx' dt' \quad (40)$$

$$F_2(x,t) = \int_{t'} \int_{x'} T_1(x',t') \dot{T}_1(x',t') G(x,t,x',t') dx' dt' \quad (41)$$

where $\alpha_o = \frac{k_o}{\rho C_o}$.

Since $F_1(x,t)$ and $F_2(x,t)$ are functions of $T_1(x,t)$ which is not known, these integrals cannot be performed. However, it is a good approximation to set $T_1(x,t) = T(x,t)$ in these integrals, i.e. the solution for the same equation but for constant properties. This solution $T(x,t)$ is usually known exactly for many cases in heat conduction.

So, substituting $T_1(x,t) = T(x,t)$ in Eqs. (40), (41) yields

$$F_1(x,t) \approx \alpha_0 \int_{t'} \int_{x'} \nabla \cdot (TVT) G(x,t,x',t') dx' dt' \quad (42)$$

$$F_2(x,t) \approx \int_{t'} \int_{x'} T(x',t') \dot{T}(x',t') G(x,t,x',t') dx' dt' \quad (43)$$

To simplify the term $\nabla \cdot (TVT)$ in Eq. (42), we make use of the vector relations⁽¹³⁾

$$\nabla \cdot \psi a = a \cdot \nabla \psi + \psi \nabla \cdot a$$

i.e.

$$GV \cdot (TVT) = \nabla \cdot (GTVT) - TVT \cdot \nabla G \quad .$$

Also

$$\int_{\text{vol.}} GV \cdot (TVT) dx' = \int_{\text{vol.}} \nabla \cdot (GTVT) dx' - \int_{\text{vol.}} TVT \nabla G dx' \quad ,$$

but

$$\int_{\text{vol.}} \nabla \cdot (GTVT) dv = \oint_{\text{surface}} GTVT ds \quad .$$

Assuming that we have an insulated face, i.e. $\nabla T(0,t) = 0$, then,

$$\int_{\text{vol.}} \nabla \cdot (GTVT) dv = \oint GTVT ds = 0 \quad .$$

So, the function $F_1(x,t)$ reduces to

$$F_1(x,t) = - \alpha_0 \int_{t'} \int_{x'} T(x',t') \nabla T(x',t') \cdot \nabla G(x,t,x',t') dx' dt' \quad (44)$$

which is now easier to calculate. Substituting in Eq. (38), the first order solution to account for variation of thermal properties with temperature is given by

$$\begin{aligned}
 T_1(x,t) = T(x,t) - b\alpha_0 \int_{t'} \int_{x'} T(x',t') \nabla T(x',t') \nabla G(x,t,x',t') dx' dt' \\
 - a \int_{t'} \int_{x'} T(x',t') \dot{T}(x',t') G(x,t,x',t') dx' dt' .
 \end{aligned}
 \tag{45}$$

Now to solve the last equation numerically using the techniques discussed earlier, we will integrate both integrals numerically over time from $t_i = 0$ to $t_i = t_{n-1}$, and the last term will be treated separately, i.e.

$$\begin{aligned}
 F_1(x_n, t_n) = \alpha_0 \sum_{t_i=0}^{t_{n-1}} w_i \Delta t_i \int_{x'} T(x',t') \nabla T(x',t') \nabla G(x,t,x',t') dx' \\
 + \alpha_0 \lim_{t_i \rightarrow t_n} w_n \Delta t_n \int_{x'} T(x',t') \nabla T \nabla G dx' \\
 = \dots + \alpha_0 w_n \Delta t_n \int_{x'} T(x',t') \nabla T \lim_{t_i \rightarrow t_n} \nabla G dx'
 \end{aligned}
 \tag{46}$$

from the theory of δ -functions:

$$\lim_{t_i \rightarrow t_n} \nabla G \rightarrow \nabla \delta(x_n - x')$$

$$F_1(x_n, t_n) = \dots + \alpha_o w_n \Delta t_n \int T(x', t') \nabla T(x', t') \cdot \nabla \delta(x_n - x') dx'$$

since

$$\int f(x') \nabla \delta(x - x') dx' = \nabla f(x)$$

Then the last integral could be written as:

$$F_1(x_n, t_n) = \dots + \alpha_o w_n \Delta t_n \nabla (T(x_n, t_n) \nabla T(x_n, t_n)) \quad (47)$$

from vector relationships⁽¹³⁾

$$\nabla(a \cdot b) = (a \cdot \nabla)b + (b \cdot \nabla)a + ax(\nabla_x b) + bx(\nabla_x a)$$

last two terms equal 0 for one dimensional geometry, i.e.

$$\nabla(T \cdot \nabla T) = T \cdot \nabla \nabla T + \nabla T \cdot \nabla T$$

$$= T \nabla^2 T + (\nabla T)^2$$

and

$$\nabla^2 T = \frac{1}{\alpha_o} \dot{T}(x, t) - \dot{q}(x, t)/k_o \quad .$$

Substituting in $F_1(x, t)$, yields

$$\begin{aligned}
F_1(x_n, t_n) &= \sum_{t_i=0}^{t_{n-1}} w_i \Delta t_i \int_{x'} T(x', t') \nabla T(x', t') \nabla G(x, t, x', t') dx' \\
&+ w_n \Delta t_n \left\{ \left[\frac{1}{\alpha_0} T(x_n, t_n) \dot{T}(x_n, t_n) - \frac{\dot{q}(x_n, t_n) T(x_n, t_n)}{k_0} \right] \right. \\
&\left. + (\nabla T(x_n, t_n))^2 \right\} .
\end{aligned} \tag{48}$$

And for the second integral, i.e.

$$F_2(x, t) = \int_{t'} \int_{x'} T(x', t') \dot{T}(x', t') G(x, t, x', t') dx' dt'$$

$$\begin{aligned}
F_2(x_n, t_n) &= \sum_{t_i=0}^{t_{n-1}} w_i \Delta t_i \int_{x'} T(x', t') \dot{T}(x', t') G(x, t, x', t') dx' \\
&+ \lim_{t_i \rightarrow t_n} w_n \Delta t_n \int_{x'} T(x', t') \dot{T}(x, t) G(x, t, x', t') dx'
\end{aligned} \tag{49}$$

$$\begin{aligned}
F_2(x_n, t_n) &= \sum_{t_i=0}^{t_{n-1}} w_i \Delta t_i \sum_{x_i} T(x_i, t_i) \dot{T}(x_i, t_i) G(x_n, t_n, x_i, t_i) \Delta x_i' \\
&+ \lim_{t_i \rightarrow t_n} w_n \Delta t_n \int_{x'} T(x', t') \dot{T}(x', t') G(x_n, t_n, x', t') dx' \\
&= \dots + w_n \Delta t_n \int_{x'} T(x', t') \dot{T}(x', t') \delta(x_n - x') dx'
\end{aligned}$$

$$F_2(x_n, t_n) = \dots + w_n \Delta t_n T(x_n, t_n) \dot{T}(x_n, t_n) . \tag{50}$$

And finally the temperature at any point x_n , and time t_n for linear variations of thermal properties can be given by

$$T_1(x_n, t_n) = T(x_n, t_n) - bF_1(x_n, t_n) - aF_2(x_n, t_n) \quad . \quad (51)$$

However, in the solution for $T_1(x, t)$ we do not have to evaluate both functions $F_1(x, t)$ and $F_2(x, t)$. It can be shown that the sum of these two functions, i.e. $F_1(x, t) + F_2(x, t)$ is a solution for a medium in which the thermal properties, specific heat and thermal conductivity, vary in the same way. That is, this is the solution for constant thermal diffusivity α .

The solution for constant thermal diffusivity, but with C and k , varying with temperature in the same way, can be shown⁽³⁾ to be of the same form as that for constant thermal diffusivity where both C and k are constants. The initial and boundary conditions will be changed.

Suppose Eq. (2),

$$\rho C_o \frac{\partial T}{\partial t} - k_o \nabla^2 T = \dot{q}(x, t) \quad (2)$$

has the solution, $T(x, t)$, with the boundary conditions,

$$T(L, t) = H$$

$$T(x, 0) = h \quad .$$

To get the solution for the equation

$$\rho C \frac{\partial T}{\partial t} - \nabla \cdot k \nabla T = \dot{q}(x, t) \quad (1)$$

where

$$C/C_0 = k/k_0 = 1 + \mu T \quad (\text{where } \mu \text{ is either } a \text{ or } b)$$

C_0 and k_0 are calculated at any arbitrary temperature T_0 . If we write

$$T' = \int_{T_0}^T (1 + \mu T) dT \quad (52)$$

where T_0 is any arbitrary temperature, one can easily show that the equation satisfied by T' is obtained from (2) on replacing T by T' , providing that the initial and boundary values of T' , say h' and H' , are obtained by setting h and H as the upper limits of the integral.

So, the solution $T'(x, t)$ also is equal to:

$$T'(x, t) = F_1(x, t) + F_2(x, t) \quad (53)$$

Since the values of $T'(x, t)$ are easily obtained, it is only necessary to perform one integral $F_1(x, t)$ or $F_2(x, t)$ to get the solution $T_1(x, t)$ that we are looking for, i.e.

$$T_1(x,t) = T(x,t) - bF_1(x,t) - aF_2(x,t)$$

$$= T(x,t) - b[T'(x,t) - F_2(x,t)] - aF_2(x,t)$$

$$T_1(x,t) = T(x,t) - bT'(x,t) - (a - b) F_2(x,t) \quad (54)$$

or

$$T_1(x,t) = T(x,t) - aT'(x,t) + (a-b) F_1(x,t) \quad (55)$$

Now, only $F_1(x,t)$ or $F_2(x,t)$ need to be evaluated. This is useful especially when one of these functions gets complicated as in the case of a non-insulating face of the first wall.

In some cases, the variations of thermal properties with temperature may be very large over the range from room temperature up to the melting point and these variations must be taken into account. Problems involving phase transformations might account for large variations since, most of the time, the thermal properties undergo a wide variation at the transformation temperature.

As an example to illustrate the methods discussed in this paper, consider the case of hydrogen ions incident on Al as a first wall. The thermal properties of Al, i.e. specific heat and thermal conductivity, are fitted linearly with temperature. Figure IV-12 shows the temperature rise in the Al surface with and without the variation of thermal properties with temperature; there is about a 10% decrease in the maximum temperature when considering the variation of thermal properties with temperature. At lower temperatures, the differences

A* THERMAL.CODE

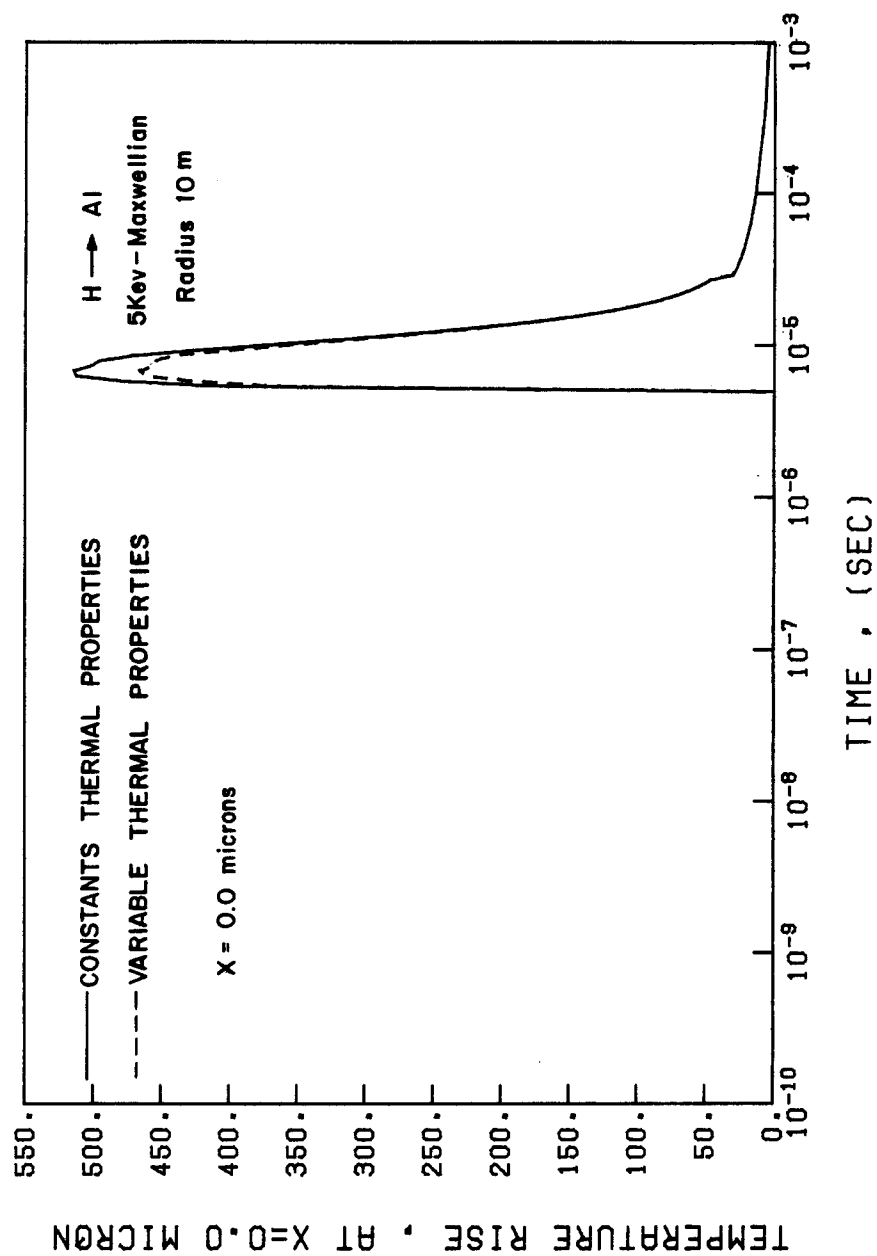


Fig. IV-12. Surface temperature rise with and without the variation of thermal properties.

are very small, and the variations of thermal properties with temperature can be neglected (Fig. IV-13). At higher temperatures the differences become larger and the variations of thermal properties must be included.

H. Conclusion

The temperature rise due to ion energy deposition into a first wall material has been calculated using the method of Green's function. A new method has been developed to avoid the singularities associated with the Green's function. Several models for calculating the temperature increase are discussed using this new method. A large difference in the temperature rise in the regions where there is an energy deposition is noticed between the present model calculation and a previous similar calculation which did not treat the singularities of the Green's function. An approximate solution for the non-linear heat-conduction equation using perturbation theory in which the specific heat and the thermal conductivity vary linearly with temperature is discussed. The effect of the variation of the thermal properties over wide temperature fluctuations could be substantial and should be included for accurate solution.

A comparison between finite difference techniques in calculating the thermal response of fusion first walls and these developed Green's function methods is given in the next chapters.

A* THERMAL .CODE

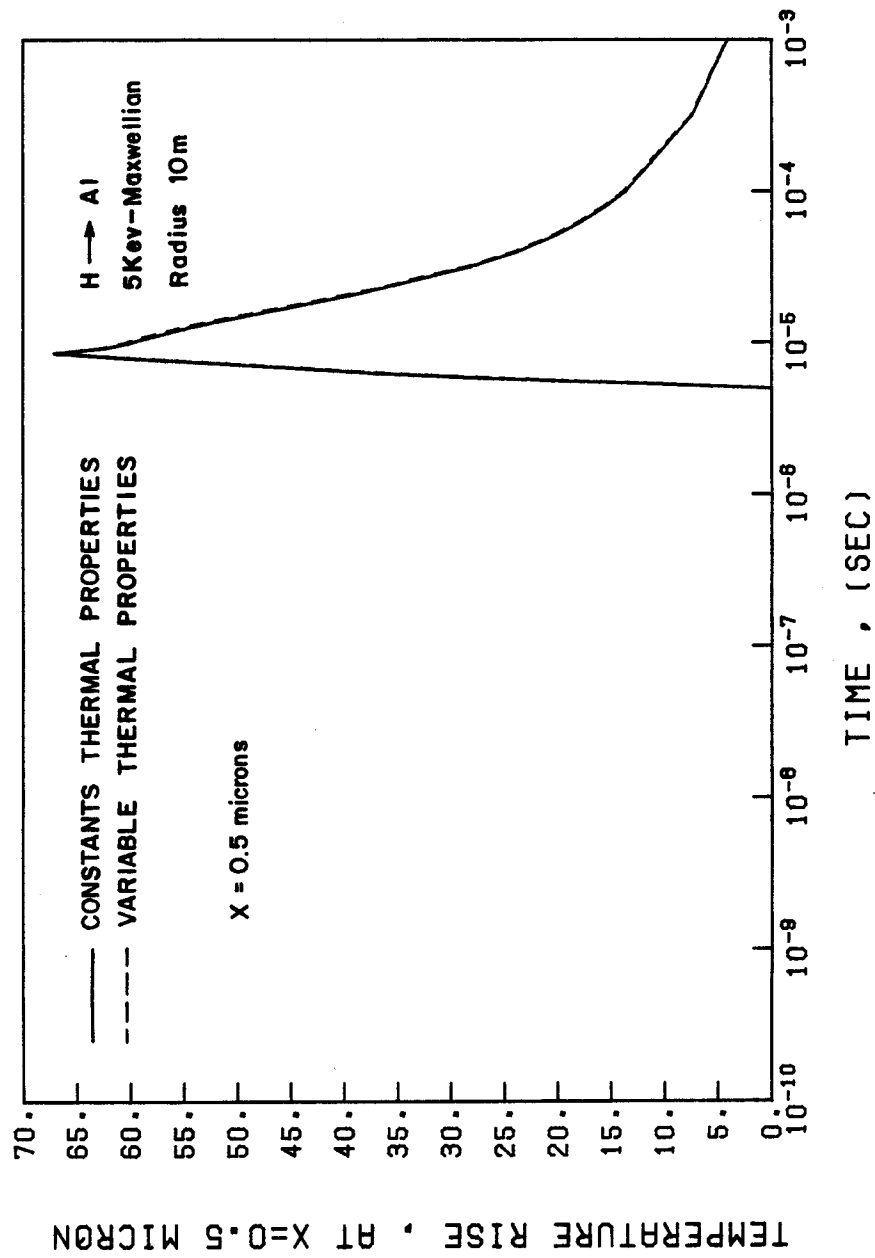


Fig. IV-13. Temperature rise at $x = 0.5$ microns with and without the variation of thermal properties.

Appendix A

To show that the Green's function for the thermal response of a semi-infinite medium behaves like a δ -function, consider the function

$$\Delta(x) = \frac{1}{\sqrt{\pi b}} e^{-x^2/b} \quad , \quad b = 4\alpha(t - t') \quad .$$

We want to show that

$$\lim_{b \rightarrow 0} \Delta(x) = \delta(x)$$

i.e.

$$\lim_{b \rightarrow 0} \frac{1}{\sqrt{\pi b}} e^{-x^2/b} = \delta(x) \quad .$$

To evaluate the total area under the curve of this function, i.e.

$$\int_{-\infty}^{\infty} \Delta(x) \, dx = \int_{-\infty}^{\infty} \frac{1}{\sqrt{\pi b}} e^{-x^2/b} \, dx \quad ,$$

substitute $y = x^2/b$ $dy = 2x/b \, dx$, i.e.

$$dx = \frac{b}{2\sqrt{by}} \, dy \quad .$$

Substitute

$$\begin{aligned}\int_{-\infty}^{\infty} \Delta(x) dx &= 2 \int_0^{\infty} \frac{1}{\sqrt{\pi b}} e^{-y} \frac{\sqrt{b}}{2} y^{-1/2} dy = \frac{1}{\sqrt{\pi}} \int_0^{\infty} e^{-y} y^{-1/2} dy \\ &= \frac{1}{\sqrt{\pi}} \Gamma\left(\frac{1}{2}\right)\end{aligned}$$

where Γ = gamma function⁽¹⁴⁾

$$\Gamma\left(\frac{1}{2}\right) = \sqrt{\pi}$$

i.e.

$$\int_{-\infty}^{\infty} \Delta(x) dx = 1$$

or

$$\int_{-\infty}^{\infty} \frac{1}{\sqrt{\pi b}} e^{-x^2/b} dx = 1$$

which is equivalent to $\int_{-\infty}^{\infty} \delta(x) dx = 1$. We conclude that

$$\lim_{t \rightarrow t'} \frac{1}{\sqrt{4\pi\alpha(t-t')}} e^{-\frac{(x-x')^2}{4\alpha(t-t')}} = \delta(x - x') \quad .$$

References for Chapter IV

1. T. O. Hunter, G. L. Kulcinski, "Description of the Response of Materials to Pulsed Thermonuclear Radiation (Part I)," UWFD-196, Dept. of Nucl. Engr., Univ. of Wisconsin-Madison (March 1977).
2. T. O. Hunter and G. L. Kulcinski, "Description of the Response of Materials to Pulsed Thermonuclear Radiation (Part II)," UWFD-217, Dept. of Nucl. Engr., Univ. of Wisconsin-Madison (October 1977).
3. H. S. Carslaw and J. C. Jaeger, Conduction of Heat in Solids, 2nd Ed., Oxford, 1959.
4. A. M. Hassanein, G. L. Kulcinski, to be published.
5. T. O. Hunter and G. L. Kulcinski, "T-DAMEN, A Computer Code for Analysis of Transient Radiation Damage," UWFD-247, Nucl. Engr. Dept., Univ. of Wisconsin, Madison (May 1978).
6. T. G. Frank, Heat Transfer Problems Associated with Laser Fusion, 16th National Heat Transfer Conference, St. Louis, MO, August 1976.
7. J. Hovingh, First Wall Studies of a Laser-Fusion Hybrid Reactor Design, Proc. of 2nd Topical Mtg. on the Technology of Controlled Nuclear Fusion, Richland, Washington, 1976.
8. J. Hovingh, First Wall Response to Energy Deposition in Conceptual Laser Fusion Reactors, California Univ., Livermore (USA). Lawrence Livermore Lab., February 1976, p. 13.
9. S.L. Thompson, "Improvements in the CHART-D Energy Hydrodynamic Code V," Sandia Laboratories, SLA-73-0477, October 1973.
10. T. O. Hunter, "A General Model for the Analysis of the Transient Radiation Damage Environment from Pulsed Thermonuclear Radiation," Ph.D. Thesis, Dept. of Nucl. Engr., Univ. of Wisconsin-Madison, July 1978.
11. M. R. Hopkins, Proc. Physical Society 50, (1938).
12. J. H. Awbery, Proc. Physical Society 48, 118 (1936).
13. G. A. Korn and T. M. Korn, Mathematical Handbook for Scientists and Engineers, McGraw-Hill, 1961.
14. Handbook of Mathematical Functions, U.S. Dept. of Commerce AMS 55, M. Abramowitz and I. A. Stegun, editors, June 1964.

CHAPTER V

THERMAL RESPONSE MODELS FOR FUSION FIRST WALLS

A. Introduction

The rapid heating of fusion first wall components either due to x-ray and ion debris deposition in ICF reactors or during a plasma dump in magnetic fusion reactors may lead to melting and subsequently to intense evaporation.⁽¹⁻²⁾ As a result, an accurate analysis of this heat conduction problem requires the solution of two moving boundaries problem. A moving face where vaporization occurs becomes one boundary in addition to the moving internal boundary between the liquid and solid. Because of the moving boundaries and the difference between the properties of the liquid and solid states of the same material, the distribution is nonlinear.

This chapter will discuss models developed in this thesis using finite difference techniques to solve the boundary-value problems of heat conduction. The two moving boundaries problem is solved including phase changes (melting and resolidification). Evaporation models for first walls, with time dependent kinetics, based on transport theory are also developed. Finally, a model is developed for "self-shielding" or the stopping of plasma ions by the vapor species of the vaporized first wall and the effect of this shielding on the net amount of evaporation is analyzed.

B. Heat Conduction with Moving Boundaries

Moving boundary problems are difficult to solve, and they present challenging mathematical and numerical questions. Although an

extensive literature exists on moving boundary problems, the present one, to be formulated explicitly below, has apparently not been solved before. Analytical and approximate solutions to simple classical Stefan problems of melting and solidification are treated at an introductory level in the recent book by Oziski.⁽³⁾ An extensive literature review up to 1964 has been given by Muehlbauer and Sunderland.⁽⁴⁾ In the meantime, many more articles have appeared in the literature as a result of the increasing interest in laser and electron beam processing of semiconductor microcircuits and materials.^(5,6) The advances made in the mathematical and numerical treatment of moving boundary problems have also been the subject of recent conferences.^(7,8)

Whereas most moving boundary problems (also called Stefan problems) deal with melting, solidification, and slow evaporation where the interface is mathematically characterized by a fixed value of the temperature whose value is known in advance (such as the melting and the boiling point), problems involving intense evaporation or ablation must satisfy a moving boundary condition that is derived from energy and mass balances. As a result, these moving boundary conditions yield highly nonlinear equations whose determination is now an integral part of the solution for the entire problem.

In order to avoid this added complication, previous treatments of intense evaporation were based on various simplifying assumptions for the condition at the moving boundary. Ready⁽⁹⁾, in evaluating laser-induced evaporation, assumed that evaporation begins and

proceeds at a constant boiling temperature when the laser pulse duration is large compared to the pre-heat time required to reach the boiling point. On the other hand, for irradiations with Q-switched lasers, Ready⁽¹⁰⁾ assumes that the vapor will be superheated to the critical point, and that the evaporation rate is determined by the thickness of the material heated beyond the critical point.

Andrews and Atthey⁽¹¹⁾ developed a convenient analytical solution to the evaporation problem when it can be assumed that vaporization occurs at a constant boiling temperature. Their analytical solution is based on a perturbation approach in which the ratio of heat loss by conduction to that by evaporation is considered as a small parameter. This ratio, the so-called Stefan number, is indeed of the order of 0.2 or less for most materials.

The solution by Andrews and Atthey has been used by Loebel and Wolfer⁽¹²⁾ to estimate the erosion by vaporization of various first wall materials. However, melting has been neglected in this approach, and the thermophysical properties of both solid and liquid were assumed to be the same and independent of temperature. Furthermore, the boiling temperature was determined by setting the ambient pressure equal to the saturation vapor pressure. Although the latter assumption may be justified when the ambient pressure is large, it becomes untenable for ambient pressures existing either in an ICF reactor chamber or in the plasma chamber of a magnetic fusion device.

The above principles can be easily demonstrated by considering evaporation into a vacuum. Here, the rate of evaporation and the

associated surface temperature are entirely determined by the kinetic processes involved in the vaporization and by the energy partitioning between heat conduction, melting, evaporation, recondensation, and radiation. As a result, the surface temperature will change as a function of the heat input.

Few attempts have been made to solve the problem of evaporation into a vacuum. Osadin and Shapovalov⁽¹³⁾ derived an integral equation for the surface temperature as a function of the heat input. However, they neglected the motion of the surface as a result of the evaporation and the presence of a melt layer. Furthermore, constant thermophysical properties were assumed, and no allowance was made for recondensation.

Golodenki and Kuz'michev⁽¹⁴⁾ also treated pulse evaporation into a vacuum under the same assumptions as in Ref. (13), except that the motion of the surface boundary was included approximately in the analysis of heat conduction.

C. Formulation of the Heat Conduction Problem

C.1. Before Melting

Consider the first wall as a semi-infinite medium. This is reasonable in view of the short heat penetration depth during a plasma disruption or target debris deposition in ICF reactors.⁽¹⁵⁾ Under a heat flux $F(t)$, the temperature distribution $T_s(x,t)$ in the solid phase must then satisfy the heat conduction equation:

$$\rho_s C_s \frac{\partial T_s}{\partial t} - \nabla \cdot k_s \nabla T_s = \dot{q}(x,t) \quad (1)$$

where ρ_s = density

C_s = specific heat

k_s = thermal conductivity

$\dot{q}(x,t)$ = volumetric energy deposition rate.

All these thermophysical properties are functions of the local temperature. The boundary conditions are that $T_s(x,t) \rightarrow T_b =$ constant for large depth distances x , and that on the surface $x = 0$,

$$F(t) = -k_s(T_v) \frac{\partial T_s}{\partial x} + \rho_s(T_v)L_v v(T_v) + \sigma(T_v^4 - T_o^4) \quad (2)$$

where $T_v(t) = T_s(0,t)$, L_v is the heat of vaporization, and $v(T_v)$ is the velocity of the receding surface. This velocity is a function of the instantaneous surface temperature and other materials parameters. Furthermore, the radiative heat transfer term contains the Stefan-Boltzmann constant, σ , and the surface temperature, T_o , of the cold portion of the first wall. For the radiative heat loss, it is assumed that parts of the first wall (mainly in magnetic fusion reactors) not struck by the plasma dump remain at the steady state temperature T_o . In ICF reactors this term goes to zero since micro-explosion reaction is assumed to be symmetrical. The second term in Eq. (2), which will be discussed shortly in connection with the evaporation energy loss, is negligible for temperatures below the melting point.

C.2. During and After Melting

Once melting occurs, the condensed phase consists of two regions:

- a. $s(t) \leq x \leq m(t)$ for the melt layer
- b. $m(t) \leq x$ for the solid phase

where: $s(t)$ is the instantaneous location of the melted surface

$m(t)$ is the distance of the melted layer from the surface

(as shown in Fig. V-1).

Equation (1) applies again to the solid phase, but the boundary conditions at the solid liquid interface $x = m(t)$ is given by

$$T_s(x,t) = T_\ell(x,t) = T_m \quad \text{at } x = m(t) \quad (3)$$

where $T_s(x,t)$ and $T_\ell(x,t)$ are the temperatures of the solid and the liquid phases, respectively, and T_m is the melting (or solidification) temperature which is constant for a given substance.

The energy equation at the solid-liquid interface is given by

$$-k_\ell \frac{\partial T_\ell}{\partial x} \Big|_{m(t)} = -k_s \frac{\partial T_s}{\partial x} \Big|_{m(t)} + \rho_s L_f \frac{dm(t)}{dt} \quad (4)$$

where L_f is the latent heat of fusion.

We note that in Eq. (4) the quantity $dm(t)/dt$ is the velocity of the melt-solid interface. If we denote this velocity by $w(t)$, we can write

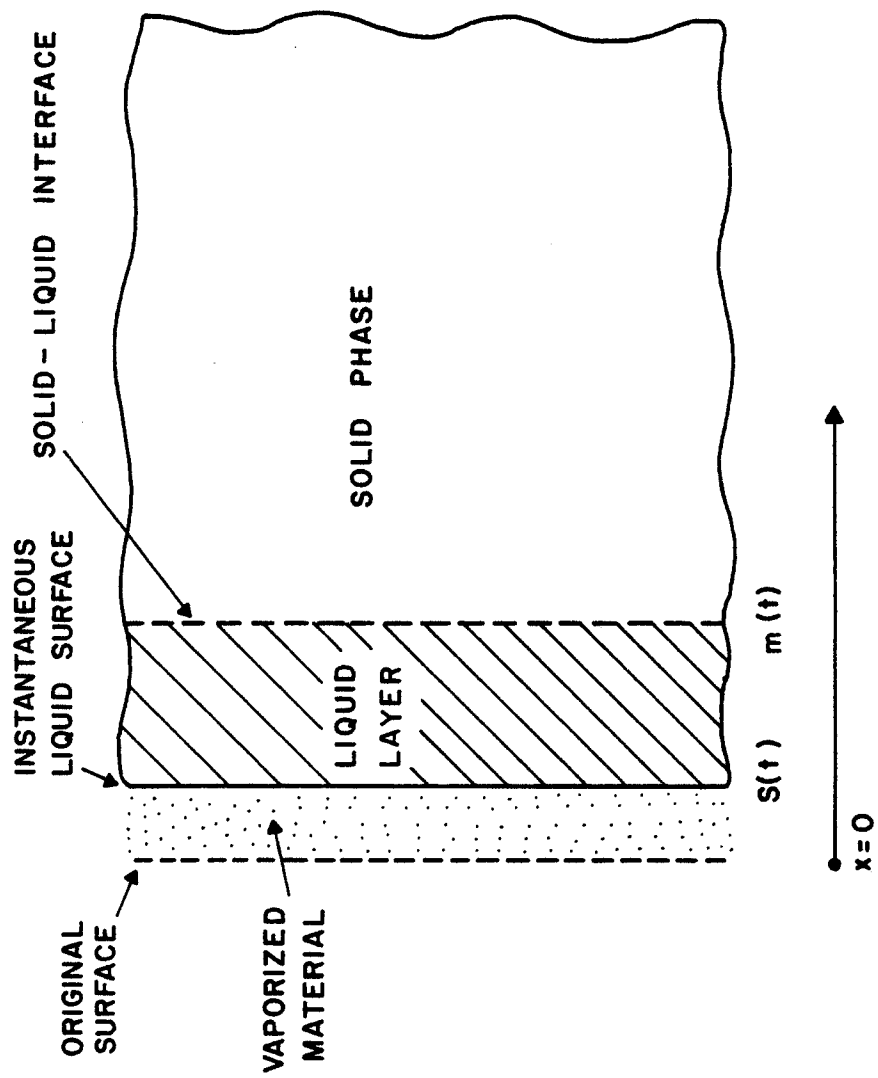


Fig. V-1. Schematic representation of solid-liquid-vapor inter-
faces.

$$\frac{dm(t)}{dt} = w(t) \quad . \quad (5)$$

Then Eq. (4) is written as

$$k_s \frac{\partial T_s}{\partial x} - k_l \frac{\partial T_l}{\partial x} = \rho_s L_f w(t) \quad \text{at } x = m(t) \quad . \quad (6)$$

In the melt layer, the heat conduction equation is given by

$$\rho_l C_l \frac{\partial T_l}{\partial t} - \nabla \cdot k_l \nabla T_l = \dot{q}(x, t) \quad . \quad (7)$$

The solution in this melt layer must satisfy the boundary conditions (3) and (4) on $x = m(t)$ and the condition

$$F(t) = -k_l \left. \frac{\partial T_l}{\partial x} \right|_{s(t)} + \rho_l (T_v) L_v v(t) + \sigma(T_v^4 - T_o^4) \quad (8)$$

on the surface $x = s(t)$.

C.3. Evaporation Moving Boundary

If the heating is continued long enough and at a sufficiently high rate, significant vaporization may occur from the surface assuming that the melting material stays in place. It is necessary to account for the receding surface at the interface between vapor and solid or liquid. This can be done by introducing a moving coordinate system:

$$z(t) = x - s(t) \quad (9)$$

for which the surface always remains at $z = 0$. Transforming the heat conduction Eqs. (1) and (7) to this moving coordinate frame gives

$$\rho C \left(\frac{\partial T}{\partial t} + \frac{\partial T}{\partial z} \cdot \frac{dz}{dt} \right) - \nabla \cdot k \nabla T = \dot{q}(z, t) \quad (10)$$

where

$$\frac{dz}{dt} = - \frac{ds(t)}{dt} = -v(t) \quad (11)$$

$v(t)$ = velocity of the receding surface. Substituting Eq. (11) into Eq. (10) gives

$$\rho C \frac{\partial T}{\partial t} - \rho C v(t) \frac{\partial T}{\partial z} - \nabla \cdot k \nabla T = \dot{q}(z, t) \quad (12)$$

The main difference in this equation is that it includes the convective term $v(t) \frac{\partial T}{\partial z}$. This term is important in the cases of intensive evaporation if we are to obtain accurate calculations of the temperature. The velocity of the receding surface, i.e. $v(t)$ is highly non-linear function of temperature as will be shown later. This heat conduction equation along with boundary conditions given by Eqs. (2) or (8) has not been solved before. A complete solution of this problem has been developed and it exists in the computer code A*THERMAL in both finite difference and Green's function methods.

D. Numerical Methods

The solution of the transient heat transfer problems involving melting or solidification is inherently difficult because the interface between the solid and liquid phases is moving as the latent heat is absorbed or released at the interface. Furthermore, the solution is more complicated in case of additional moving boundary at the surface between vapor and solid or liquid. Exact analytic methods for solving these kind of boundary-value problems of heat conduction are very limited.⁽¹⁶⁾ Numerical methods are useful and may be the only accurate solution for handling problems involving nonlinearities, complex geometries, complicated boundary conditions or a system of coupled partial differential equations.

D.1. Finite Difference Approximations

In numerical solution of heat conduction problems with the method of finite difference, the partial differential equation is approximated with finite difference expressions at each nodal point. Each node is associated with a small volume. In order to define the nodes, a system of orthogonal planes is superimposed on the problem. The planes may be unequally spaced, but they must extend to the outer boundaries. Variable zone thickness is very important in both achieving good accuracy and saving computer time. Good accuracy near the surface (in order to calculate the evaporation and melting thickness) requires a smaller zone thickness than that far away from the surface. By choosing the increments between nodal lattice points and time steps to be small enough, the solution to the system of

equations yields an accurate approximation to the appropriate differential equation.

D.2. Space and Time Increments

Increments on the space and time grids can be chosen to give satisfactory results for a variety of different problems. These problems may involve x-ray and laser radiation, light and heavy ions with volumetric energy deposition, and surface heat flux. Each of these problems may have large differences in the time domain ranging from nanoseconds to milliseconds. The choice of space and time grids almost always involve a compromise between accuracy and computer time.

D.3. Methods of Solution

There are several schemes available to express the time dependent heat conduction equation in finite difference form. These schemes, ranging from the so-called explicit form to the fully implicit form, for finite differencing of the one-dimensional time dependent heat conduction equation is listed in Ref. (17). Each of these differencing schemes has its advantages and limitations. The modified implicit method of Crank and Nicolson⁽¹⁸⁾ is used in this analysis. The advantage of this method is that for given values of the space and time steps, the resulting solution is stable and involves less truncation error due to the time step than the other explicit and the implicit forms. On the other hand the Crank-Nicolson form involves additional computation. If there are N

internal mesh points over the region, this method involves the solution of N simultaneous algebraic equations for each time step.

Of the many possible methods for solving a system of simultaneous equations, an implicit alternating direction method suggested by Peaceman and Rachford⁽¹⁹⁾ is selected. Although this method is only valid for linear equations, it may be used here by transforming the nonlinear system (material properties may be temperature dependent and moving boundary conditions) into quasi-linear system in which the nonlinear factors are frequently re-evaluated.

Other forms of the alternating-direction implicit method include the Douglas-Rachford implicit scheme,⁽²⁰⁾ its modification by Brian,⁽¹²⁾ and the alternative form given by D'Yakonov.⁽²²⁾ Barakat and Clark⁽²³⁾ describe an explicit scheme that is unconditionally stable for the solution of the time dependent, multi-dimensional heat conduction equation.

D.4. Variations of the Thermal Properties With Temperature

In the solution of Eq. (2), all the thermophysical properties are allowed to vary with the temperature. This variation can take the form

$$f(t) = a + b \cdot T + c \cdot T^2 + d \cdot T^3$$

where $f(t)$ = density or specific heat or thermal diffusivity

a, b, c, d = coefficients of variation of these properties

T = temperature.

These coefficients may be different for both solid and liquid phases. Other functions for the variation of thermal properties with temperature could be incorporated easily in the computer code A*THERMAL.

D.5. Phase Change (Melting and Resolidification)

Materials are allowed to undergo a phase change during the transient heat conduction calculations. This is done by checking the node's temperature at every time step and compared to the melting temperature of the material used. If the material is ready to undergo a change of phase, the node's temperature is maintained at the transition temperature until the net heat content exceeds the total heat needed to complete the phase change for this node. After the phase change, the node's temperature is again determined by the conductive heat transfer equation. During resolidification the temperature of the node is also held at the transition temperature due to the production of heat until the conductive cooling of the node exceeds the latent heat, then the temperature is again determined by the conductive heat transfer equation.

Only pure substances are allowed to change phase in this research where the melting (or solidification) takes place at a unique temperature, and the solid and liquid phases are separated by a sharp moving interface. On the other hand, in the solidification of mixtures, alloys, and impure materials the solidification takes place over an extended temperature range,⁽²⁴⁾ and as a result the solid and liquid phases are separated by a two-phase moving region.

D.6. Initial and Boundary Conditions

Because of the complexity of the problem, a change in the boundary conditions may require a completely different solution. In this analysis we tried to generalize the problem to include those conditions that are closely related to the design of fusion reactors.

The boundary conditions which can be applied over the surface of a region are:

- The initial temperature of the wall is assumed to be constant.
- The heat flux across the surface of a region can be specified directly as a constant or a function of time.
- The heat flux across the surface of a region can be specified indirectly by defining a radiation cooling mechanism.
- The back side of the wall may be infinite or finite slab with either an insulated boundary or cooled by a forced convection mechanism.
- A surface moving boundary condition as in the case of intensive evaporation could be included.

E. Evaporation Models

According to the Hertz-Knudsen-Langmuir theory of evaporation and condensation the net flux of atoms leaving the surface of the condensed phase is given by

$$J = (2\pi mkT)^{-1/2} (\sigma_e P_s - \sigma_c P_c) \quad (13)$$

where: J = net vaporization flux,
 m = mass per atom,
 k = Boltzmann constant,
 σ_e, σ_c = evaporation and condensation coefficients,
 P_c = ambient partial pressure in the chamber,
 P_s = saturation vapor pressure.

The coefficients σ_e and σ_c are used to compensate for nonideal evaporation or condensation. They are usually taken to be the same. The saturation vapor pressure, P_s , is given by

$$P_s = P_o \exp(-\Delta H/kT) \quad (14)$$

where: P_o = derived constant,
 ΔH = activation energy for evaporation.

Equation (13) consists of two opposite fluxes, $J = J_e - J_c$, an evaporation and a condensation flux.

Although Eq. (13) is valid only for thermal equilibrium, it can be modified for non-equilibrium evaporation or condensation. If the surface temperature T_v of the condensed phase is different from the temperature T_c of the ambient vapor, the evaporation and condensation flux may be written as

$$J_e^{eq} = (2\pi mkT_v)^{-1/2} \sigma_e P_s(T_v) \quad (15)$$

and

$$J_c = (2\pi mkT_c)^{-1/2} \sigma_c P_c \quad (16)$$

The evaporation flux J_e^{eq} represents a maximum for evaporation into a vacuum provided the vapor expands at a sufficient rate so the vapor density in front of the surface always remains low.

The net evaporation flux may be computed according to

$$J = J_e^{\text{eq}}(T_v) - J_c(T_c) \quad (17)$$

if the two fluxes do not interact. This will only be the case for slow evaporation, i.e., when both J_e^{eq} and J_c are small or when they are almost of equal magnitude.

Unfortunately, for conditions encountered for example in a plasma disruption, Eq. (17) cannot be considered valid. Since the evaporation flux is expected to be high, the vapor density in front of the surface is finite even if the vapor gas expands into a vacuum. As a result, J_v^{eq} is not the maximum evaporation flux into a vacuum for intense evaporation.

One may be tempted to assume that the maximum evaporation flux is determined by the velocity of an adiabatically expanding gas. Therefore, we consider for the moment a gas of initial density n and initial temperature T_v . It expands into one direction with a maximum velocity of⁽²⁵⁾

$$U_{\text{max}} = 4 c_o \quad (18)$$

where

$$c_o = \sqrt{\gamma k T_v / m} \quad (19)$$

is the speed of sound in a gas of temperature T_v and density n , and γ is the ratio of the specific heats for constant pressure and constant volume. For a monatomic gas, $\gamma = 5/3$.

The maximum flux of evaporation according to this model would be given by

$$\begin{aligned} J_e^{\max} &= 4 c_o n_s = 4 \left(\frac{3kT_v}{2m} \right)^{1/2} \frac{P_s}{kT_v} \\ &= 4\sqrt{3\pi} J_e^{\text{eq}} \end{aligned} \quad (20)$$

Since this is larger than J_e^{eq} , we conclude that hydrodynamic considerations alone cannot be invoked to limit the rate for intense evaporation below the maximum equilibrium rate.

It is therefore necessary to derive the rate of recondensation of the expanding vapor from gas-kinetic considerations. In an early analysis by Schrage,⁽²⁶⁾ the vapor is treated as a gas with a Maxwellian velocity distribution superimposed on an average velocity \bar{u} . This average velocity must be equal to the average forward velocity of a stationary Maxwellian gas. Hence

$$\bar{u} = (kT_v / 2\pi m)^{1/2} \quad (21)$$

The fraction of recondensing atoms is now given by⁽²⁶⁾

$$\Gamma = \exp(-a^2) - a\sqrt{\pi} \operatorname{erfc}(a) \quad (22)$$

where

$$a = \bar{u}/u_o$$

and

$$u_o = \sqrt{2kT_v/m}$$

is the most probable velocity of the Maxwellian gas. Then "a" can be written as

$$a = \frac{1}{2\sqrt{\pi}} = 0.282 \quad .$$

The net evaporation flux is then equal to

$$J = J_e^{\text{eq}} \left(1 - \frac{\sigma_c}{\sigma_e} \Gamma\right) \quad (23)$$

Assuming that coefficients of condensation and evaporation are equal, i.e. $\sigma_c = \sigma_e$, one obtains for $a = 0.282$ a maximum net evaporation flux of

$$J = 0.422 J_e^{\text{eq}} \quad (24)$$

More accurate transport calculations for intense evaporation have been performed more recently by Anisimov and Rakhmatulina.⁽²⁷⁾ In their work the following problem was considered: The surface of a material which occupies the half-space is suddenly raised and held at a constant surface temperature T_v for times $t \geq 0$. The material begins to vaporize and the vapor expands freely into the vacuum. Initially, the evaporation flux leaving the surface is equal to J_e^{eq} , but it decreases thereafter due to recondensation. This process of recondensation arises from two facts. First, the density of vapor expanding into a vacuum retains a finite value for $t > 0$ in front of the surface. Second, atoms evaporated subsequently from the surface may collide with the already present vapor phase and be backscattered towards the surface where they may be reabsorbed. The fraction of recondensing atoms will increase as the vapor density and the spatial extension of the vapor phase increases with time. However, an asymptotic value of 0.2 is reached for this fraction after about 20 collision times. The collision time τ_c for the vapor atoms is given by

$$\frac{1}{\tau_c} = 16 \sqrt{\pi} n a_0^2 (kT_v/m)^{1/2} \quad (25)$$

where πa_0^2 is the elastic scattering cross section for the vapor atoms and n the vapor density in front of the surface. The latter can be related to the maximum vacuum evaporation rate according to

$$J_e^{\text{eq}} = \frac{1}{4} \bar{v} n = n (kT_v/2\pi m)^{1/2} \quad (26)$$

where we used the relation

$$\bar{v} = (8kT_v/\pi m)^{1/2}$$

for the average velocity of the vapor atoms.

For the elastic scattering cross section we may use the approximation that

$$\frac{4\pi}{3} a_o^3 = \Omega$$

where Ω is the atomic volume. Then, the collision time τ_c is given by

$$\frac{1}{\tau_c} = 16 \sqrt{2} \pi^{1/3} \left(\frac{3}{4} \Omega\right)^{2/3} J_e^{\text{eq}} \quad (27)$$

The numerical results of Anisimov and Rakhmatulina for the time-dependent net evaporation rate may be approximated by

$$J(t) = J_e^{\text{eq}} [0.8 + 0.2 \exp(-t/\tau_R)] \quad (28)$$

where τ_R is defined as a relaxation time for full condensation. The relaxation time τ_R to reach, say 98% of the full amount of recondensation after 20 collision times τ_c , is then given by

$$\tau_R = 20 \tau_c / \ln 10 \approx 10 \tau_c$$

or

$$\frac{1}{\tau_R} = 1.6 \sqrt{2} \pi^{1/3} \left(\frac{3}{4} \Omega\right)^{2/3} J_e^{\text{eq}}. \quad (29)$$

In the above equations, $J_e^{\text{eq}}(T_v)$ is a constant for $t \geq 0$, since it was assumed that T_v remains constant.

For our present application, however, the surface temperature $T_v(t)$ varies with time. Nevertheless, as the numerical results in the following section show, the surface temperature rapidly approaches a saturation value once intense evaporation begins. Accordingly, the time variable in Eq. (28) should be replaced by $(t-t_v)$ where the preheat time t_v may be estimated as follows.

In order for recondensation to become significant, the thickness of the vapor zone in front of the surface should be of the order of the mean free collision path

$$\ell = [\sqrt{2} n \pi a_o^2]^{-1}.$$

The thickness Δx of material evaporated to produce a vapor zone of thickness ℓ is then

$$\Delta x(t_v)/\Omega = n\ell$$

or

$$\Delta x(t_v) = \frac{1}{\sqrt{2\pi}} \left(\frac{4}{3}\right)^{2/3} \left(\frac{\Omega}{\pi}\right)^{1/3} = 0.585 \Omega^{1/3} \quad (30)$$

and in terms of a_0 , $\Delta x(t_v)$ can be written as

$$\Delta x(t_v) = \frac{4}{3\sqrt{2}} a_0 \quad (31)$$

This corresponds roughly to a monolayer of atoms evaporated from the surface. The relationship (Eq. 31) determines the preheat time t_v .

The evaporation flux of atoms is then equal to J_e^{eq} , for $t < t_v$ and

$$J(t) = J_e^{\text{eq}}(T_v(t)) [0.8 + 0.2 \exp(-(t-t_v)/10\tau_c)] \quad (32)$$

for $t > t_v$. It should be noted, that the collision time τ_c is a very strong function of the surface temperature through its dependence on J_e^{eq} . Therefore, if we consider τ_c as a function of time, it will be a very large number before intense evaporation commences, i.e., for $t < t_v$. As a result, the second term in Eq. (28) will then be equal to 0.2, so that automatically $J(t) \cong J_e^{\text{eq}}$, for $t < t_v$. Therefore, by considering the collision time τ_c as a continuous function of the changing surface temperature $T_v(t)$, the Eqs. (28) and (32) are practically identical. In other words, it is not necessary to

compute the preheat time t_v in order to obtain the time-dependent evaporation flux $J(t)$ correctly according to Eq. (28).

Finally, we note that the velocity of the receding surface is given by

$$v(t) = \Omega J(t) \quad (33)$$

A recent model has been developed by Merrill⁽²⁸⁾ to calculate the evaporation in magnetic fusion first wall reactors. In this model, the fluid conservation equations of mass, momentum and energy were solved to calculate the dynamics of the vapor phase adjacent to the first wall surface. The transient vapor properties of pressure, density, and energy are then used in the modified kinetic theory phase change relationship proposed by Schrage⁽²⁶⁾ to calculate the vaporization of the surface. A comparison made between the model developed in this thesis and Merrill's model, to calculate the first wall evaporation in a magnetic fusion reactor, showed a very good agreement.⁽²⁹⁾

F. Vapor Shielding

The heat flux $F(t)$ on the first wall, for example during a disruption in a magnetic fusion reactor, is due largely to the plasma ions. It is generally believed that a sheath potential of the order of 10 keV exists at the onset of the plasma disruption. The plasma ions will therefore strike the first wall with a kinetic energy of about 10 keV. The average range of the plasma ions in a

stainless steel wall is about 7.5×10^{-8} m. Because of this short range, it is indeed appropriate to treat the energy deposition as a surface heat flux rather than a volumetric heat deposition.

On the other hand, if a vapor layer of sufficient thickness has been produced, the plasma ions will be stopped in this vapor layer rather than in the condensed material of the first wall. The vapor layer, in the process of stopping the plasma ions, will be partially ionized, excited, and heated. Subsequently, the energy stored in this vapor layer will be emitted in the form of x-rays, optical radiation, and thermal diffusion of the hot vapor atoms. As a result, the energy flux of the plasma particles is converted from a unidirectional one into a more isotropic one. If we assume in fact that the converted energy flux has become isotropic, only one half of the original, unidirectional energy flux will now strike the part of the first wall exposed to the plasma disruption.

Accordingly, we have modeled the effect of vapor shielding in the following manner. If F_0 is the magnitude of the initial energy flux, and R the range of plasma ions in the condensed phase of the first wall, a vapor layer produced by the evaporation of a thickness $\Delta x(t) \leq R$ will reduce the surface heat flux to the first wall to the value of

$$\begin{aligned}
 F(t) &= F_0 [1 - \Delta x(t)/R] + \frac{1}{2} F_0 \Delta x(t)/R \\
 &= F_0 [1 - \Delta x(t)/2R] .
 \end{aligned}
 \tag{34}$$

When the evaporation thickness $\Delta x(t) > R$, then

$$F(t) = \frac{1}{2} F_o . \quad (35)$$

Figure V-2 shows schematically the effect of vapor shielding on the surface heat flux according to the present model and for a constant plasma particle flux during the disruption time.

G. Summary

A model has been developed to solve the heat conduction problem, using finite difference techniques, with phase changes (melting and resolidification) and two moving boundaries. One moving boundary being the melt-solid interface, and the other the receding surface as a result of evaporation. Evaporation models for fusion first walls, with time dependent kinetics, based on transport theory are also developed. The surface temperature of first walls is determined by both the boundary condition as well as by the kinetics of the evaporation process. The correct boundary condition entails partitioning of the incident energy flux into conduction, melting, evaporation, and radiation. Finally, a model is developed for vapor shielding or the stopping of plasma ions by the vapor species of the vaporized first wall material. The effect of this self-shielding on the net amount of evaporation is studied. Examples of application of the models developed in this chapter to calculate the thermal response of fusion first walls will be given in Chapter VII.

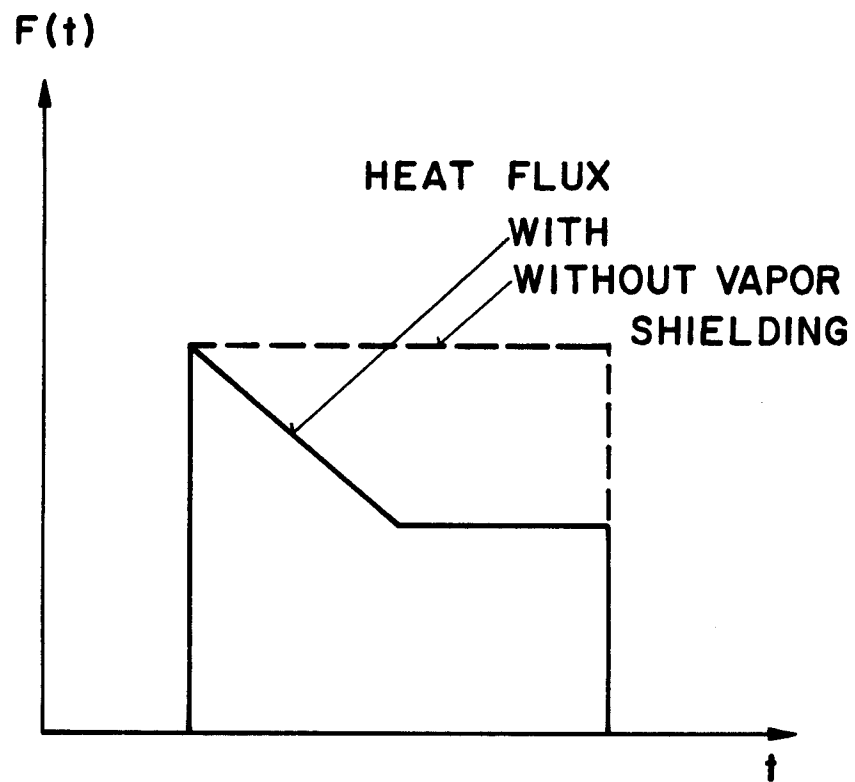


Fig. V-2. Schematic of heat fluxes to first walls during plasma disruptions.

References for Chapter V

1. G.L. Kulcinski and A.M. Hassanein, "Thermal Response of Unprotected Al, C, and Ta First Walls to Thermonuclear Target Spectra," University of Wisconsin/Westinghouse Electric Corporation, March 1980.
2. E. Glock and PULSATOR Team, "Types, Causes, and Effects of Limiter Damage in Pulsator Tokamak," *Journal of Nuclear Materials* 93&94, (1980) 305-309.
3. M.N. Ozisik, "Heat Conduction" Chapter 10, J. Wiley & Sons, New York (1980).
4. J.C. Muehlbauer and J.E. Sunderland, "Heat Conduction With Freezing and Melting," *Applied Mechanics Reviews* 18(12), (1965).
5. S.D. Ferris, H.J. Leamy, and J.M. Poate, "Laser-Solid Interactions and Laser Processing," Amer. Inst. Physics, New York, 1978.
6. C.W. White and P.S. Pearch, eds., "Laser and Electron Beam Processing of Materials," Acad. Press, New York, 1980.
7. J.R. Ockendon and W.R. Hodgkins, eds., "Moving Boundary Problems in Heat Flow and Diffusion," Clarendon Press, Oxford, 1975.
8. A.B. Crowley, "On the Weak Solution of Moving Boundary Problems," *J. Ins. Maths. Applics.* 24, (1979) 43-57.
9. J.F. Ready, *Appl. Phys. Letters* 3, (1963) 11.
10. J.F. Ready, *Journal of Applied Physics* 36, (1965) 2.
11. J.G. Andrews and D.R. Atthey, *J. Inst. Maths. Applics.* 15, (1975) 59.
12. L.L. Loebel and W.G. Wolfer, "Evaporation Under Intense Energy Deposition," University of Wisconsin Fusion Engineering Program Report UWFD-370 (August 1980).
13. B.A. Osadin and G.I. Shapovalov, *Teplofizika Vysokikh Temp.* 10, (1972) 361.
14. N.N. Golodenko and V.M. Kuz'michev, *Teplosizika Vysokikh Temp.* 10, (1972) 1126.

15. A.M. Hassanein, G.L. Kulcinski, and W.G. Wolfer, "Vaporization and Melting of Materials in Fusion Reactors," presented at Second Topical Meeting on Fusion Reactor Materials, 9-12 August 1981, Seattle, WA, (to be published in Journal of Nuclear Materials).
16. H.S. Carslaw and J.C. Jaeger, Conduction of Heat in Solids, 2nd Ed., Clarendon Press, London, 1959.
17. R.D. Richtmeyer and K.W. Morton, Difference Methods for Initial Value Problems, 2nd Ed., Interscience Publishers, Inc., New York, 1965.
18. J. Crank and P. Nicolson, Proc. Camb. Phil. Soc. 43, (1947) 50-67.
19. D.W. Peaceman and H.H. Rachford, J. Soc. Indust. appl. Math. 3, (1955) 28-41.
20. J. Douglas and H.H. Rutherford, Trans. Am. Math. Soc. 82, (1956) 421-439.
21. P.L.T. Brian, AIChE Journal 7, (1961) 367-370.
22. Y.G. D'Yakonov, Z. Vycise. Mati. Mat. Fiz. 3, (1963) 385-388.
23. H.A. Barakat and J.A. Clark, J. Heat Transfer 88C, (1966) 421-427.
24. A.B. Crowley and J.R. Ockendon, "On the Numerical Solution of an Alloy Solidification Problem," Int. J. Heat Mass. Transfer. 22, (1979) 941-947.
25. Ya. B. Zel'dovich and Yu. P. Raizer, "Physics of Shock Waves and High Temperature Hydrodynamic Phenomena," Acad. Press, 1966.
26. R.W. Schrage, "A Theoretical Study of Interphase Mass Transfer," Columbia University Press, New York, 1953.
27. S.I. Anisimov and A. Kh. Rakhmatulina, Sov. Phys. - JETP 37, (1973) 441.
28. B. Merrill, Contribution to U.S. INTOR/NUC/81-7, June 1981.
29. M.A. Abdou, paper presented at INTOR Mtg. in Vienna, Dec. 1981.

CHAPTER VI

THE A*THERMAL COMPUTER CODE

A. Introduction

The A*THERMAL⁽¹⁾ computer code is a program for analysis of the transient dynamic thermal and surface damage response of fusion reactor first walls. The various models contained in this code are discussed in Chapters III, IV, and V. Some typical examples of how this code could be used to examine the behavior of fusion first walls are discussed in the next chapter. The code was developed to provide analysis of the energy deposition, temperature response, melting and vaporized thickness of first walls and other subsequent effects produced in materials such as displacement production and sputtering erosion. The solution to the problems of ion and photon transport, radiation energy deposition and heat conduction with two moving boundaries is sufficiently efficient to allow parametric and simultaneous analysis of a wide range of applications. Such applications as the response of first wall materials both in inertial and magnetic confinement fusion reactors are given in Chapter VII.

Finite difference methods as well as the numerical methods developed in this thesis using the Green's function are both used in the A*THERMAL solution of the thermal response of fusion materials. A comparison between using the finite difference and the Green's function methods in solving the heat conduction equation with moving boundary conditions is given in Chapter VII.

The A*THERMAL code is written in Fortran V for the UNIVAC-1110 at the University of Wisconsin, Madison.⁽²⁾ The finite difference calculation was written using double the precision mode to ensure higher accuracy in the thermal response of the materials. Instructions and example problems to use the code are too extensive to be listed here but can be obtained in Ref. (1).

B. Code Description

The A*THERMAL code calculates the response of fusion first walls for different incident radiation. This radiation may include laser light, x-rays, heat flux (e.g., from gas cavity reradiation in ICF reactors), and light or heavy ions. Deposition and thermal response including melting and evaporation of materials could be obtained for any kind of incident radiation.

Thermal response to a complete set of spectra incident instantaneously on an ICF reactor first wall could also be obtained from the code. This set may consist of x-rays, surface heat flux, and several light or heavy ions. This is done by first calculating a total deposition function for all the incident ions. Then the total ion deposition combines with the x-rays deposition function and then is used in the temperature routine to solve the heat conduction equation with moving boundary conditions and variable thermal properties.

The major sections of the code are shown in Fig. VI-1. The block diagrams show the functional relationship between each routine within a given section. The filing and plotting routines are modified

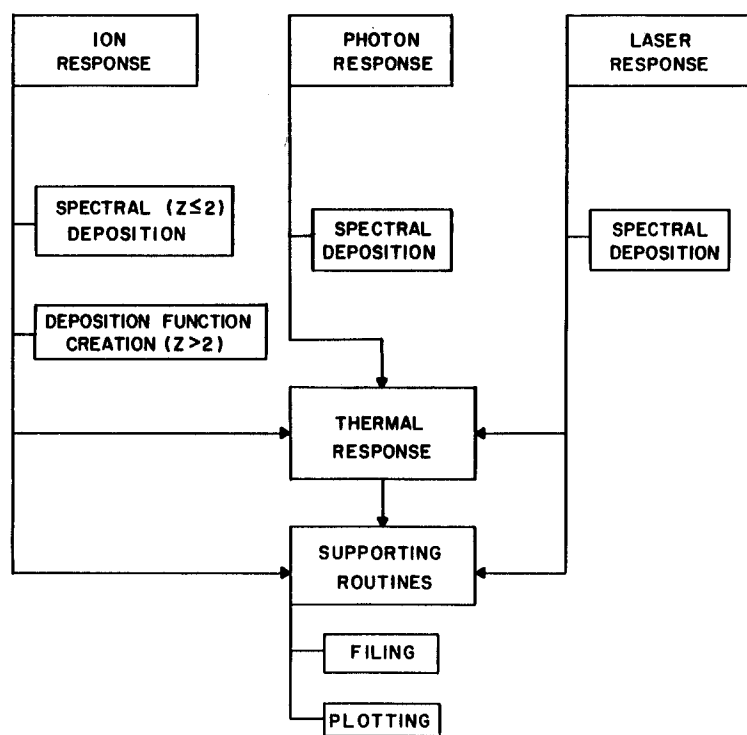


Fig. VI-1. General sections of A*THERMAL code.

versions of those contained in the T*DAMEN⁽³⁾ code. The modifications are made to improve the efficiency and increase the number of data points to be filed, and to include the finite difference routines. In the plotting routine, more flexibility is introduced by including different line characteristics for plotting. A more detailed description for using these routines are given in Ref. (1). A description of the general functions of the code for the deposition and the thermal response routines are shown in Fig. VI-2.

B.1. Laser Response

This section of A*THERMAL calculates the thermal response of inertial fusion first walls to laser light deposition. The response of materials to laser pulses which are several nanoseconds long (which could be used for surface annealing) can also be calculated. The deposition model presented in Chapter III, in which the absorption and reflection coefficients are functions of time near a surface region (depending on whether the material is in solid or liquid phase), is used with the models developed in Chapter V to calculate the thermal response and hence the melting and evaporated zone thickness. The dynamics of the melted layer as a function of time can also be obtained from the code.

B.2. Photon Response

In this section the volumetric energy deposition for x-ray spectra is calculated. Spectra may be specified as black body or histogram form. Deposition is based on a general library of photoelectric and incoherent cross sections.⁽³⁾ This library includes all

A * THERMAL CODE

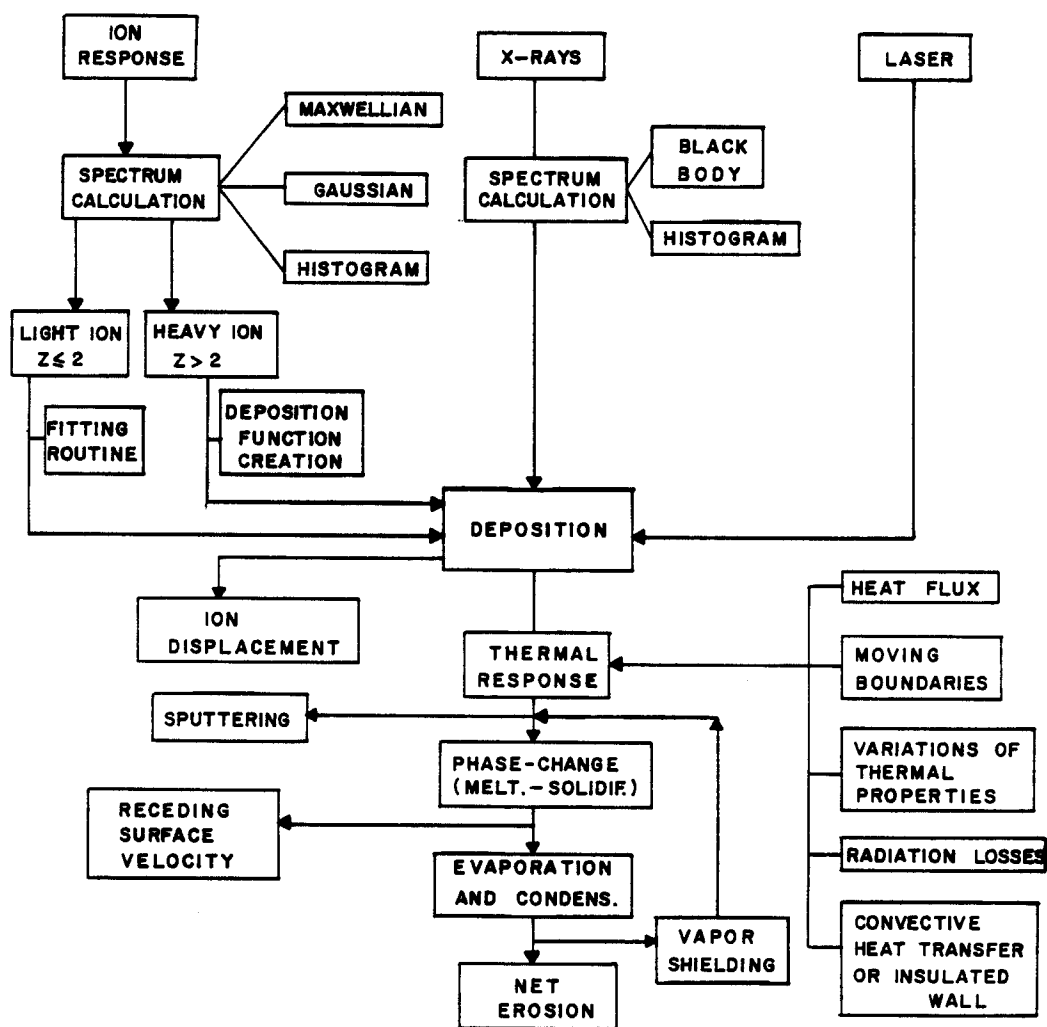


Fig. VI-2. Basic functions of A* THERMAL code.

elements and is accessed by specifying the element atomic number and the photon energy. The deposition of photon energy is assumed to be over a finite duration in time. This duration usually extends up to several nanoseconds long. Temperature calculation, melting zone thickness, and evaporated material due to photon deposition can also be obtained as in the case for laser deposition.

B.3. Ion Response

The fusion first wall response to ion radiation is calculated by first generating ion spectra which may be in the form of a Maxwellian, a Gaussian, or a histogram. The flux which strikes the material is transformed into the time and energy dependent deposition profiles which are in the form of polynomials as discussed in Chapter III. These polynomials are then used to determine the volumetric energy deposition as a function of space and time. The coefficients of the deposition polynomials can then be used in the temperature routine to determine the temperature histories at various locations. Surface velocity, melting, and evaporation thicknesses can be determined following the temperature routine by the finite difference methods discussed in Chapter V or by the Green's function methods developed in Chapter IV. Temperature from Green's function may be calculated on a time base which is determined by the ion arrival times or on a predetermined standard time base which allows comparison of response from various components. In finite difference calculations, since the time step needs to be small for accurate values of the temperature, only specified number of points are allowed to be printed.

The output from all previous routines can be sent to a data file for future use such as plotting and comparison between different methods or input to other routines. The related thermal response solution for any of the incident radiation discussed above on a finite slab with the back side of the wall either an insulated boundary or cooled by a forced convection is also contained as an independent routine.

The block diagram for the different subroutines used in calculating the deposition and the thermal response for each kind of radiation is shown in Fig. VI-3. The following is a brief description of some of these subroutines and their function.

- MASTER. Master routine for calling different subroutine sections.
- DLASER. Calculates laser light deposition into materials.
- SPECP. Calculates a blackbody spectrum for a given temperature and total flux.
- DEPOP. Calculates x-rays volumetric energy deposition.
- INITIA. Calls CROS to get cross section data from ELT/ATOM.
- CROS. Calculates the photoelectric and incoherent photon cross section for a given material.
- ELT/ATOM. All photon cross sections for elements with atomic number 1 to 100.
- GEN/XMU. Calculates photon cross section for a given energy from coefficients in CROS.
- SPECFLU. Generates the particle fluxes from the spectra.
- SPECTR. Generates Maxwellian or Gaussian spectrum.

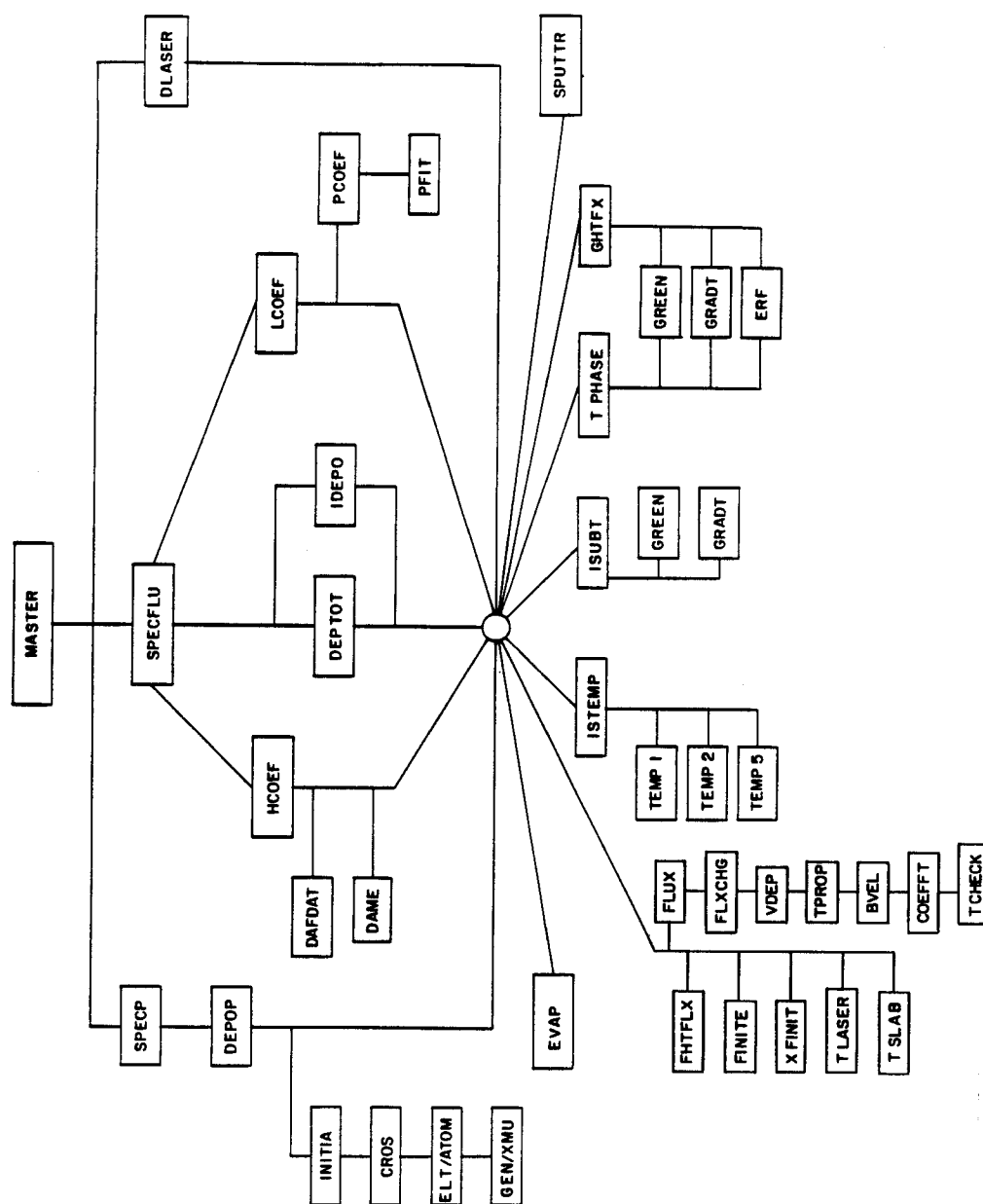


Fig. VI-3. A*THERMAL code block diagram.

HCOEF. Generates coefficients matrix for heavy ion deposition.

LCOEF. Generates coefficients matrix for light ion deposition.

PCOEF. Generates polynomial coefficients for set of incident energies.

DAME. Calculates coefficients of damage functions at a given value of energy.

DAFDAT. Reads damage functions from file 11.

PFIT. A general polynomial interpolation routine.

IDEPO. Calculates energy deposition for the ions.

DEPTOT. Calculates total energy deposition for several number of incident ions.

GHTFX. Calculates the temperature as a function of space and time for input heat flux and moving boundaries by the methods of Green's function.

TPHASE. Calculates the temperature with phase change using the Green's function.

ISUBT. Calculates the temperature using perturbation theory to account for the variation of thermal properties with temperature by the methods of Green's function.

ISTEMP. Evaluates the temperature for standard times and locations for ion deposition by the Green's function.

GREEN. Generates the Green's function at each position and time step.

GRADT. Calculates the gradient of Green's function at each position and time step.

<u>ERF.</u>	Calculates the error function.
<u>TEMP1.</u>	Evaluates the temperature at one time for linearly decreasing deposition.
<u>TEMP2.</u>	Evaluates the temperature at one time for uniform energy deposition.
<u>TEMP5.</u>	Calculates the general temperature response model for deposition in form of polynomial coefficients.
<u>FHTFLX.</u>	Calculates the temperature due to input heat flux by the finite difference methods. Moving boundaries, phase changes, variation of thermal properties with temperature, and vapor shielding calculations could be included for all of the routines using the finite difference methods.
<u>FINITE.</u>	Calculates the temperature by finite difference methods due to ion deposition and surface heat flux.
<u>XFINIT.</u>	Calculates the temperature by finite difference methods for x-ray volumetric energy deposition, ion deposition, and surface heat flux.
<u>TLASER.</u>	Calculates the temperature by finite difference for laser light deposition.
<u>TSLAB.</u>	Calculates the temperature by finite difference methods for finite thickness wall with convective heat transfer boundary condition on the back side of the wall or insulated boundary if possible burn-out occurs.
<u>FLUX.</u>	Calculates the heat flux to the wall at one time step.

- FLXCHG. Calculates the net heat flux to the wall at one time step in case of vapor shielding calculation.
- TPROP. Evaluates the thermal properties as a function of temperature at one time step.
- BVEL. Calculates the velocity of the receding surface at one time step.
- COEFFT. Evaluates the coefficients for the temperature calculation at one time step.
- TCHECK. Checks at each time step if the material is ready to undergo change of phase and do the phase change calculation.

More descriptions of this section and other routines to set the space-time arrays for different kinds of problems are given in Ref. (1).

B.4. Deposition Function Generation

This section of the code generates the deposition functions of heavy ions which are used to calculate the volumetric energy deposition from both nuclear and electronic processes. This routine is a modified version of the one used in the T*DAMEN code. In this code different deposition functions are developed to ensure conservation of energy between the incident ion energy content and the total deposited energy into the material. Large differences between the deposition functions developed in T*DAMEN, which do not satisfy the conservation of energy, and the one developed in A*THERMAL are shown through examples given in Chapter III.

The generation of the deposition functions could be used in conjunction with either the Brice implantation codes or with tabulated deposition profiles given in the literature. The Brice codes are used to obtain deposition profiles of a few energies for a specific ion target combination. These data are transformed to proper format and placed in a data file. Then the spatial profiles are fit with polynomials by a least squares technique. The polynomials and their associated energies are stored in another data file to be assigned to the run during calculations. For tabulated data the procedure is similar except the data are first placed in a data element.

The polynomial coefficients are stored in a data file named 11 which must be assigned to the run during the deposition or displacement calculations. Currently this file contains the combinations of carbon, oxygen, aluminum, and tantalum each as both incident ion and as a target for the other ions. The block diagram for the deposition function creation routine is shown in Fig. VI-4.⁽³⁾ The instructions for using Brice codes are given in Ref. (4). The following is a brief description of some of the subroutines used in the deposition functions calculation.

<u>DEPFUN.</u>	Master routine for calling different subroutine sections.
<u>BRYOUT.</u>	Reads file 26 for deposition profile from Brice code.
<u>GENOR.</u>	Reads tabulated data from files of deposition data.

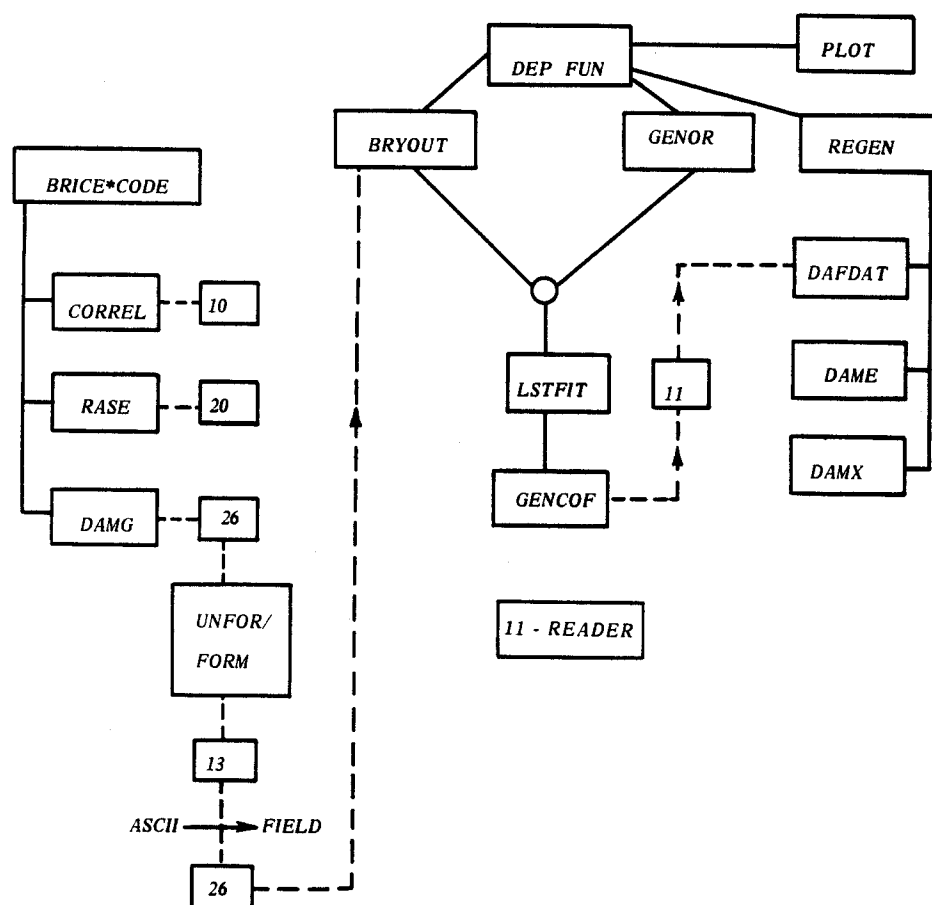
DEPOSITION FUNCTION CREATION

Fig. VI-4. Block diagram for deposition function creation routine.

LSTFIT. Fits the data (nuclear deposition) from GENOR or BRYOUT up to a 4th degree polynomial for each energy.

LSTFEL. Fits the data (electronic deposition) from GENOR or BRYOUT up to a 4th degree polynomial for each energy.

GENCOF. Generates the energy coefficient matrix from LSTFIT data and stores it in file 11.

REGEN. Produces a deposition profile from data in file 11 for specified values of energy.

DAMX. Calculates the damage function at a position for a previous call to DAME.

11-READER. Reads coefficients stored in file 11.

UNIFORM/FORM. Changes Brice data from unformatted to formatted.

B.5. Supporting Routines

B.5.1. Filing

This routine is a general data handling system based on the IODR random access file system on the UNIVAC-1110. Data which are generated by the interaction of different radiation with materials may be placed in a data file. A directory of file contents is always maintained so that different calculations may be identified. Printing and plotting of this data from the file can be done easily. Block diagram for this section of the code is shown in Fig. VI-5. The following is a brief description of the subroutines used in this section and their functions.

IFILE/IODR. Routine for filing common blocks in the code.

ENTRYS/IODR. Basic IODR handling subroutines.

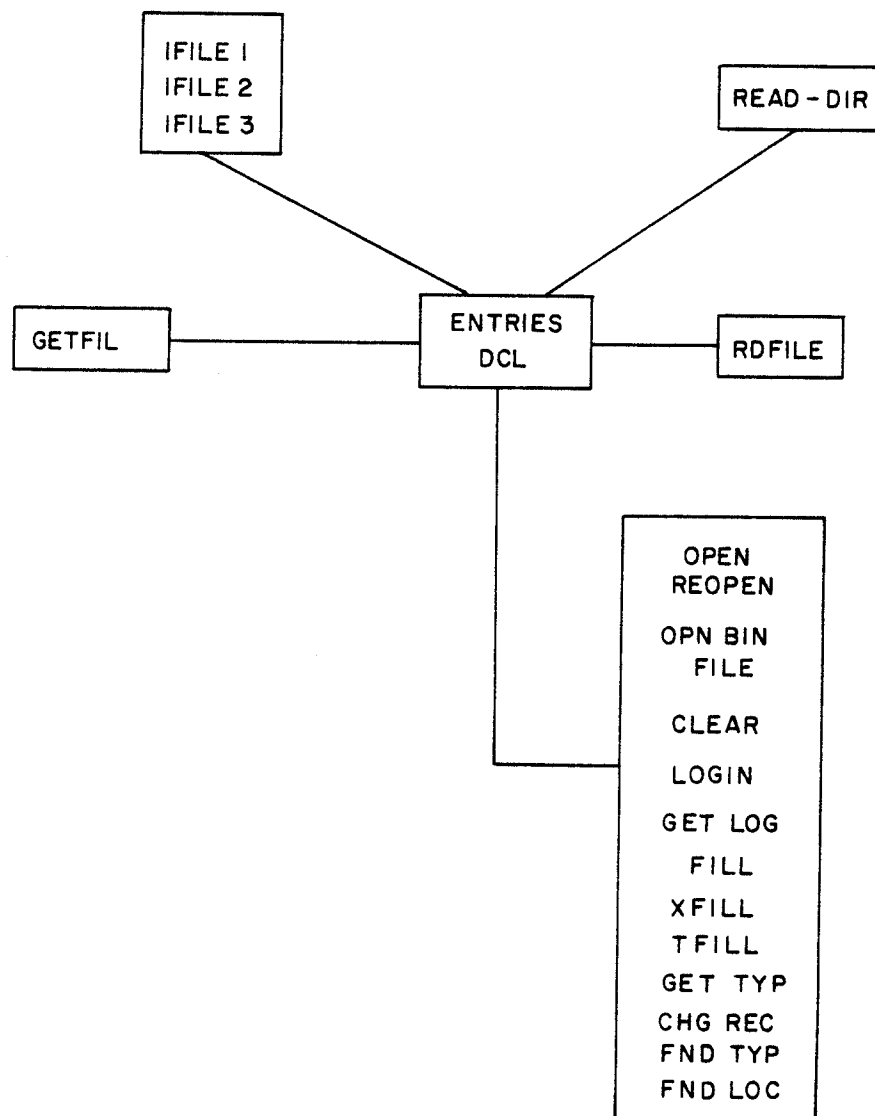


Fig. VI-5. Filing code.

READ-DIR/IODR. Reads complete directory of any IODR file.

DCL/IODR. Structure of data blocks in IODR files.

RDFILE/IODR. Reads filed data and prints out desired data.

GETFIL/IODR. Reads data into common blocks.

More descriptions of this section and other routines of the code are given in Ref. (1).

B.5.2 Plotting

Two-dimensional plots of several selected variables from laser, x-rays, heat flux, and ion calculations are available from this routine. The format is set up for interactive graphics terminals and allows for many selections of plotting line characteristics. Linear or logarithmic scales could be used. Block diagram for this routine is shown in Fig. VI-6. The following is a brief description of some of the elements used in this plotting section.

PLOT/IODR. Basic plot routine for plotting from any IODR file.

PLOTNUM/IODR. This is to plot a specified number points.

PLOT CROSS/IODR. This is to plot from different data files in one plot.

Again, more information and instructions to use this section are also given in Ref. (1).

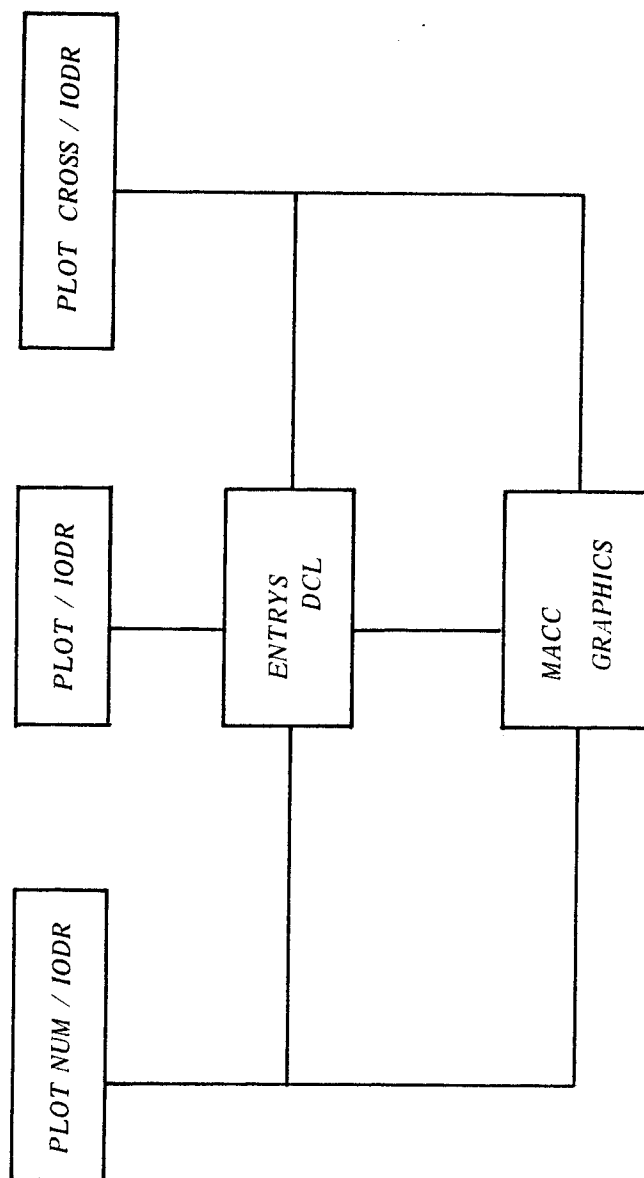


Fig. VI-6. Plotting code.

References for Chapter VI

1. A.M. Hassanein and G.L. Kulcinski, "A*THERMAL Computer Code Description," University of Wisconsin Fusion Engineering Program Report UWFD-461, to be published.
2. MACC Computing Handbook, Academic Computing Center, University of Wisconsin-Madison (November 1973).
3. T.O. Hunter and G.L. Kulcinski, "T*DAMEN, A Computer Code for Analysis of Transient Radiation Damage," University of Wisconsin Fusion Engineering Program Report UWFD-247, May 1978.
4. D.K. Brice, "Ion Implantation Range and Energy Deposition Codes COREL, RASE4, and DAMG2," SAND75-0622, Sandia Laboratories, Albuquerque, New Mexico, July 1977.

CHAPTER VII

APPLICATIONS

A. Application (A): Response of First Wall Material to ICF Pulsed Spectra

A.1. Introduction

One of the difficulties of designing ICF reactors for commercial use is to construct a cavity first wall capable of withstanding the pulsed thermal loads that result from the fusion process. About 25% of the energy released as a result of the thermonuclear burn is in the form of charged particles and x-rays. These products have a very short range in the metallic first walls under consideration. The deposition of this energy in a very short time will result in very high surface temperatures which may cause melting and evaporation.

In this chapter, the models developed in this thesis are used to determine the response of ICF first wall materials to radiation spectra. Representative spectra are used to simulate the various radiation components from the fusion reaction. Examples of the time history of first wall heat fluxes for typical photon and ion spectra are given. Finally an application of a specific reactor design using a gas filled cavity for protection is investigated. In this specific study, two candidate first wall materials are analyzed, i.e. stainless steel and carbon. The thickness of the melted zone for steel and the evaporated material thickness for both carbon and steel are given as a function of cavity gas pressure.

A.2. Representative Spectra and Wall Loading

The response of a first wall can be determined if the photon and ion spectra are specified. However, these spectra are dependent on the details of the target design and can only be described in detail by sophisticated computer codes such as LASNEX,⁽¹⁾ which is very expensive to run and not always available. In this research, the response of the walls can be determined if the photons and ions are characterized by common spectral forms. The wall loading can then be found by determining the spectral dependence of the energy deposition.

A.3. Photon Spectra

A commonly used spectrum for low energy photons is the blackbody or Planckian spectrum⁽²⁾ which is used when radiation emission is specified by the temperature of the emitter. The mathematical representation of the blackbody spectrum is given by

$$S(E) = \frac{15 F}{kT\pi^4} \left(\frac{U^3}{e^U - 1} \right) \quad (\text{J/keV-cm}^2) \quad (1)$$

where: $U = E/kT$

kT = characteristic energy, (keV)

F = total fluence or energy density (J/cm^2).

The wall loading from source photons will occur at a time equal to the cavity radius divided by the speed of light. This is only true for a medium where the dielectric constant is independent of the frequency, so that the propagation of all energies will be at the

same velocity. The spectrum of 1 keV blackbody with a total fluence of 1 Joule/cm² is shown in Fig. VII.A-1. The temporal shape of the source will be the temporal shape of the loading pulse. The deposition time for x-ray energy spectrum is assumed to be between 1 and 10 nsec. The deposition of x-rays into first wall materials will strongly depend on the energy spectrum of these x-rays. Soft x-rays deposit their energy within a micrometer of the wall's surface, very rapidly heating a thin layer of the first wall to a higher temperature. Harder x-ray energy spectra penetrate relatively larger distances into material, therefore heating a larger mass to a lower temperature.

A.4. Ion Spectra

Target debris calculations using sophisticated codes⁽²⁾ to predict the actual ions spectra indicate that reasonable characterization can be made with either a Maxwellian or Gaussian distribution. A Maxwellian distribution is characterized by a mean energy E_m and can be represented in the form:

$$S(E) = \frac{2N}{E_m \sqrt{\pi}} \sqrt{\frac{E}{E_m}} e^{-E/E_m} \quad (1/\text{keV}) \quad (2)$$

where: E_m = characteristic energy (keV)

E = ion energy (keV)

N = total number of ions/cm².

When a spectrum of a specific width is required the Gaussian distribution is used. The mean energy E_m and the standard deviation

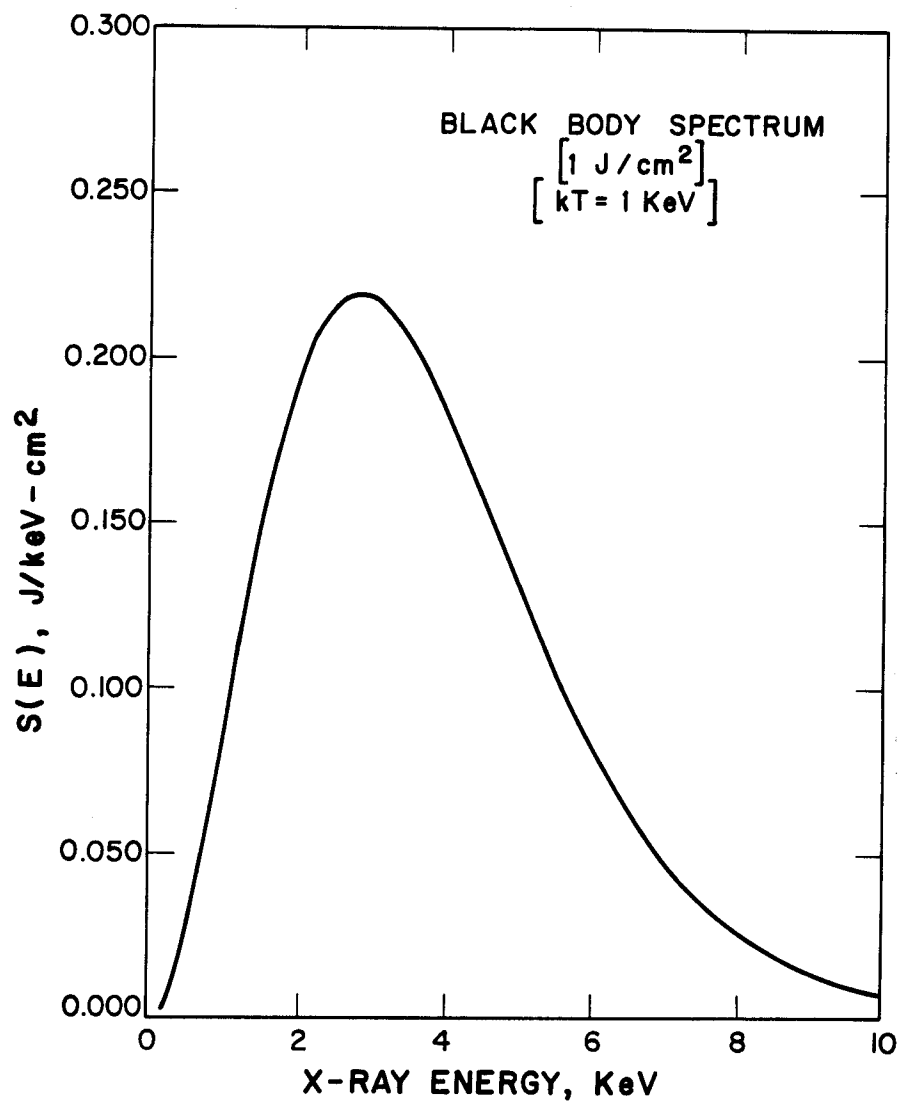


Fig. VII.A-1. Blackbody photon spectrum for $kT = 1$ keV.

σ are necessary to describe the distribution as:

$$S(E) = \frac{N}{\sqrt{2\pi}\sigma} e^{-\frac{1}{2} \left(\frac{E-E_m}{\sigma}\right)^2} \quad (1/\text{keV}) \quad (3)$$

where both E_m and σ are in keV units. The time duration of the first wall loading due to ion irradiation will be determined by the time for each species to arrive. Because of the differences in energy, hence velocity, the various components of the target debris strike the wall at different times and for different pulse durations. The pulse duration spread will depend on the ion spectrum as well as on the reactor dimensions. This assumption is valid only for a collisionless plasma which does not have significant self-encounters or existence of gas species in the reactor chamber. Significant collision with gas atoms in the cavity will generate a spherical blast wave and hence a pressure pulse to the first wall material.^(3,4)

The relation between the energy spectra and the time flux, and hence the loading function for the first wall, in the case of no collisions occurring with any chamber gas atoms, can be derived by using the relations:⁽⁵⁾

$$S(E) dE = -F(t) dt \quad (4)$$

and

$$E = \frac{1}{2} m v^2 = \frac{1}{2} m \left(\frac{R}{t}\right)^2 \quad (5)$$

From Eq. (5), the time of arrival of target ions is given by

$$t = \frac{B}{\sqrt{E}} \quad \text{sec} \quad (6)$$

where: $B = 2.284 \times 10^{-6} R\sqrt{A}$

R = wall radius (meters)

A = ion mass (amu).

Hence, Eq. (4) can be written as

$$F(t) = S(E) \frac{2E^{3/2}}{B} \quad (\text{cm}^{-2} \text{sec}^{-1}) \quad (7)$$

The pressure due to the momentum impact of target debris can be given by

$$P(t) = 7.29 \times 10^{-17} A^{1/2} E^{1/2} F(t) \quad (\text{dynes/cm}^2) \quad (8)$$

where E is in keV units.

The impact of the target debris on an unprotected first wall has three major consequences. First, it can generate extremely high temperatures for a short period of time. Second, the sudden heating can produce shock waves in the first wall. Third, the implantation of the various gaseous particles can cause blistering and erosion.

A.5. Mechanical Wall Loading

Inertial confinement fusion reactors will require a strong reaction chamber to contain pellet microexplosions inside and to withstand the pressure waves due to the sudden deposition of the microexplosion energy. These pressure pulses are due to three main effects. First, pressure from the momentum of pellet debris. Second, when the ambient density of the cavity exceeds approximately 10^{14} atoms/cm³ (e.g., 0.3 torr of X_e) the fuel microexplosion will generate a spherical blast wave. The wall pressure generated by this phenomenon is independent of background density at reasonable cavity radii (> 2 m).⁽⁶⁾ Finally, shock waves are generated by material ablated off the first wall which causes a pressure wave to be induced in the wall. The magnitude of these pressures is given in Ref. (6). The variation of these pressures with cavity radius, assuming constant yield and pulse duration is given in Ref. (7). Very high pressures can be generated in the chamber walls with radii less than 7 m. The pressure due to ablation was found the most severe of the three for the conditions given in Ref. (7), and for radii less than 5 m it can reach over 100 atm. The ability of various cavity designs to withstand such pressures will depend on the detailed design. To assure survivability of the first wall on an economic basis, the design should allow the repetition of such loads 10's of millions of times per year.

A.6. Gas Protection as an Example of First Wall Protection Methods

A.6.1. Introduction

The ion debris and x-rays, resulting from thermonuclear fusion reactions, pose serious problems for inertial confinement fusion reactors. As a result of these problems, the study of inertial confinement fusion reactor design has concentrated to a large extent on methods to protect the first wall from these serious problems. Among the various methods of protection that have been proposed are magnetic fields,^(8,9) liquid walls,⁽¹⁰⁾ and gas layers (see for example Refs. (11,12)). In this section we summarize a previous work^(13,14) on the analysis of a gas filled cavity concept for ICF reactor first wall protection. This concept has potential application in at least two forms of ICF, laser fusion and light ion beam fusion.

The purpose of the gas in laser fusion reactors is to attenuate the target x-rays and thermalize the ion debris before it reaches the first wall. Noble gases, such as He, Ne or Xe have been proposed. The choice of a noble gas is to avoid many of the possible corrosion problems that might appear in the interaction of the cavity gas with target and wall materials at high temperatures. Another reason for choosing a noble gas is because of fears of laser induced gas breakdown as the beams pass through the gas to the target.

Gas protection of the first wall in a light ion beam fusion reactor is a consequence of the method of transporting the beams to the target. That is, currently ionized channels are formed in a

background gas and these channels contain the high current ion beams.^(15,16)

A.6.2. Wall Response

To simulate the first wall response of an ICF reactor, a typical spectra for a 100 MJ yield could be represented by the components listed in Table VII.A-1.⁽¹⁷⁾ Other target designs indicate that there may be more energy in softer x-rays⁽¹⁶⁾ and some of the kinetic energy of the neutrons⁽¹⁸⁾ is transferred to the ions. Within the present uncertainties of target design, these simulations are meant to identify the major problems in first wall response. Previous calculations⁽¹³⁾ with this spectra did not include the modified energy deposition methods discussed in Chapter III. Also, these calculations did not include the variation of thermal properties with temperature, possible phase change, or any moving boundaries in the heat conduction solution. Similar calculations which include accurate energy deposition models, phase change and thermal property variations, and evaporation models developed earlier in this thesis will be shown later in this chapter.

A.6.3. Energy Deposition

The total energy deposition of x-rays and ions with no gas for protection is shown as a function of distance into stainless steel in Fig. VII.A-2. The target spectrum, used in this calculation, is given in Table VII.A-1. All the laser light (reflected from the target) is assumed to be absorbed in an isotropic, homogeneous, conducting media. The exponential x-ray attenuation is attributed to

Table VII.A-1. Reference Spectra (100 MJ)

	<u>Energy (MJ)</u>	<u>Spectrum</u>
Laser	.2	10.6 μ
X-ray	2.0	1.0 keV-BB
D	4.6	160 keV-M
T	6.9	240 keV-M
He (Slow)	1.2	320 keV-M
He (Fast)	5.4	2 \pm .5 MeV-G
Silicon	2.7	800 keV-M
Neutrons	77.	14 \pm 1 MeV-G

BB = blackbody

M - Maxwellian

G = Gaussian

INTEGRATED DEPOSITION WITHOUT GAS VS. X AT 5×10^{-6} SECONDS

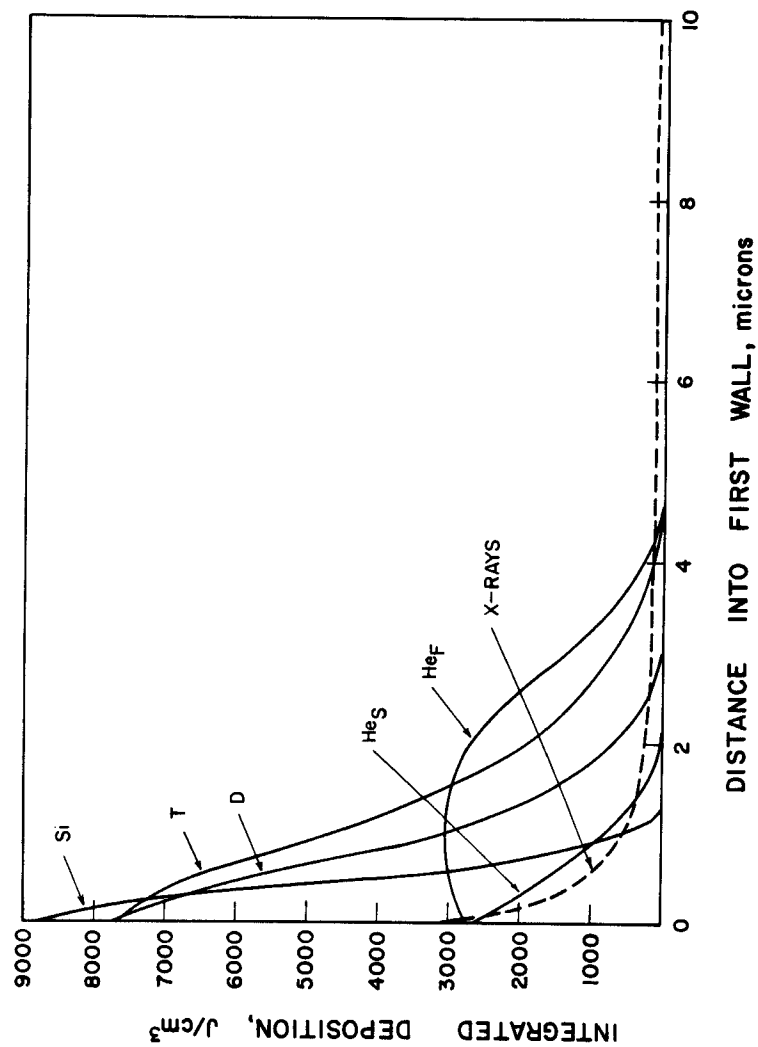


Fig. VII.A-2. Integrated ion energy deposition for the reference spectra.

photoelectric absorption and incoherent scattering, assuming that no spectrum of second photons is created. As seen from this figure, over 90% of the x-ray's energy is deposited within 5 microns of the surface of the first wall. Almost all the energy from the charged particles is deposited within the first 4 microns.

A.6.4. Temperature Response

The temperature increase at the front surface ($x = 0$) for each component of the spectrum in the first wall with no gaseous protection is given in Fig. VII.A-3. In this calculation, the thermal properties of the first wall material are assumed to be constant, that is, independent of temperature. The initially large temperature rise, is due to the x-rays and the reflected laser light. Before the heat from the photons is completely dissipated away from the surface, the ions arrive and deposit all their energy within 4 microns. The temperature rise from each component is not predictable by the magnitude of the total energy deposition alone. Shorter deposition times tend to increase the temperature rise. As can be seen from the same figure, the total temperature increase generated at 7 m from a 100 MJ explosion exceeds the melting point of stainless steel and temporary melting might occur. Obviously, the temperature above the melting point represented by the dotted line has no real meaning because the heat of melting was not included in these calculations.

The effect of 0.5 torr Ne gas on the temperature rise at the front surface is shown in Fig. VII.A-4. The decrease in magnitude of the temperature rise as compared to case of no gas is mainly due to

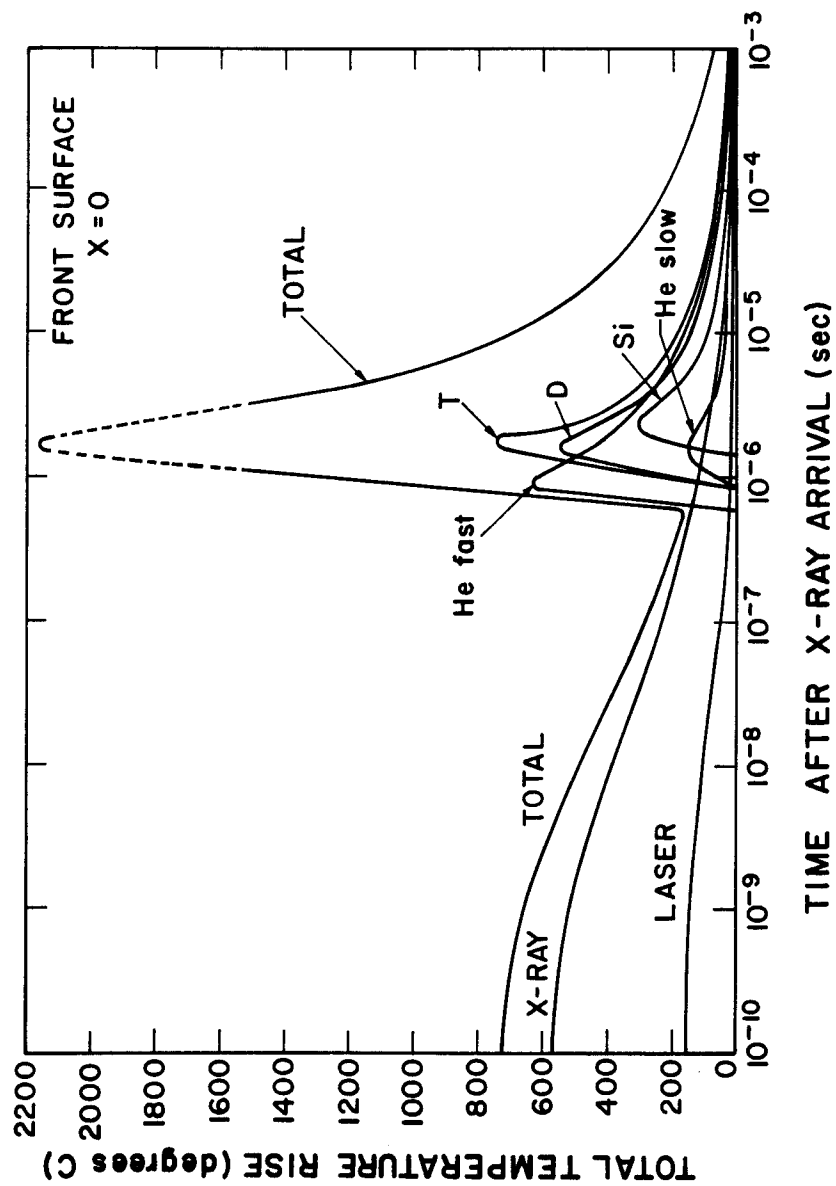


Fig. VII.A-3. Component temperature increase for the given spectra.

EFFECT OF CHAMBER GAS ON TEMPERATURE

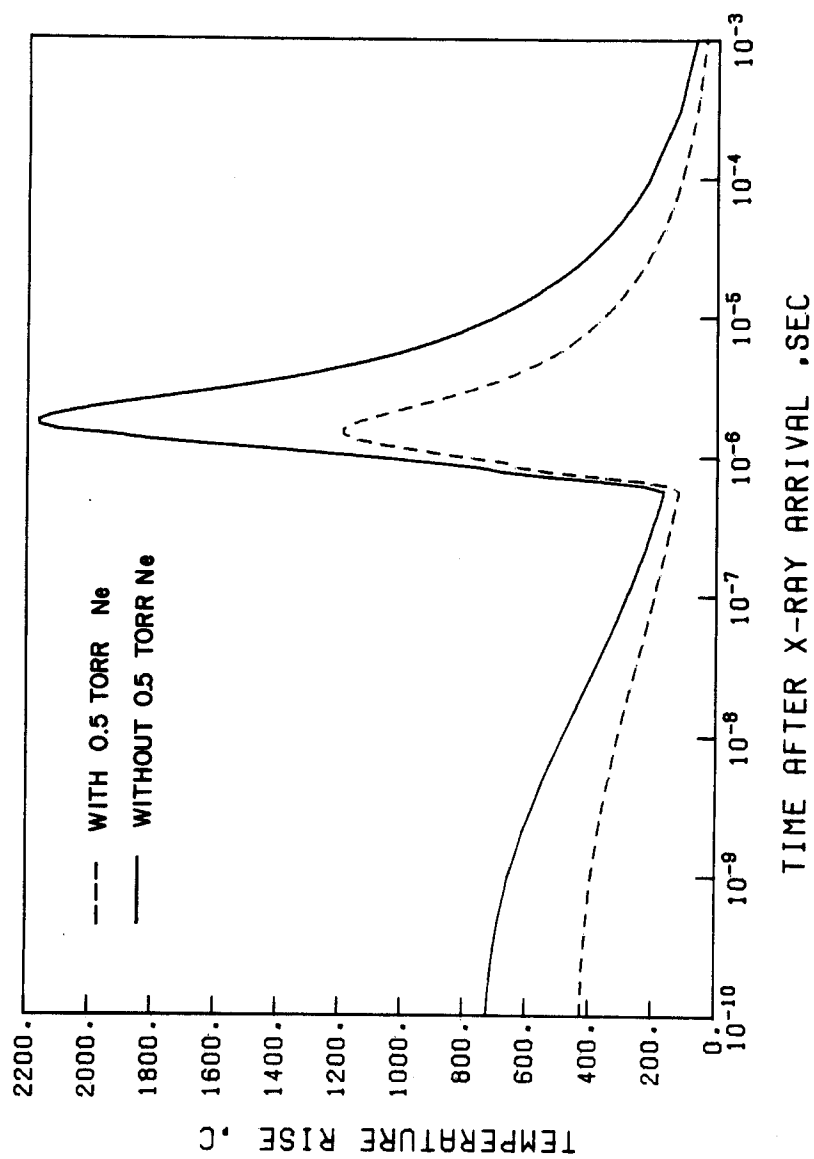


Fig. VII.A-4. Comparison of surface temperature rise with and without 0.5 torr of Ne gas.

the energy deposited in the gas. Another reason that the temperatures are slightly lowered is due to the broadening of the deposition times. It can be seen that the gas reduces the maximum x-ray temperature rise by over 50% of the case where no gas is used.

A.7. Evaporation and Melting of ICF First Walls

A.7.1. Introduction

In this section, the models developed earlier in this thesis are used to determine the evaporation and melting of the first wall of fusion reactors utilizing gas protection.⁽¹⁹⁾ If the lifetime of a commercial ICF reactor first wall is to be on the order of 20 full power years, the erosion rate must not exceed a few angstroms per shot. However, previous studies⁽²⁰⁾ have shown that the evaporation of an unprotected first wall will be a few microns per shot due to the target x-rays and debris.

The target explosion, gas response, and first wall response are depicted schematically in Fig. VII.A-5. The x-ray and debris energy of the target is attenuated by the gas, which reradiates the absorbed energy to the first wall. Even if the debris is completely attenuated by the gas, unattenuated target x-rays and gas reradiation may still cause significant evaporation. One objective of this work is to identify characteristics of the unattenuated x-ray and gas reradiation that lead to excessive evaporation. To meet this objective, the evaporation of both carbon and stainless steel has been computed for various x-ray spectra and gas reradiation characteristics.

RESPONSE OF A GAS FILLED ICF REACTOR

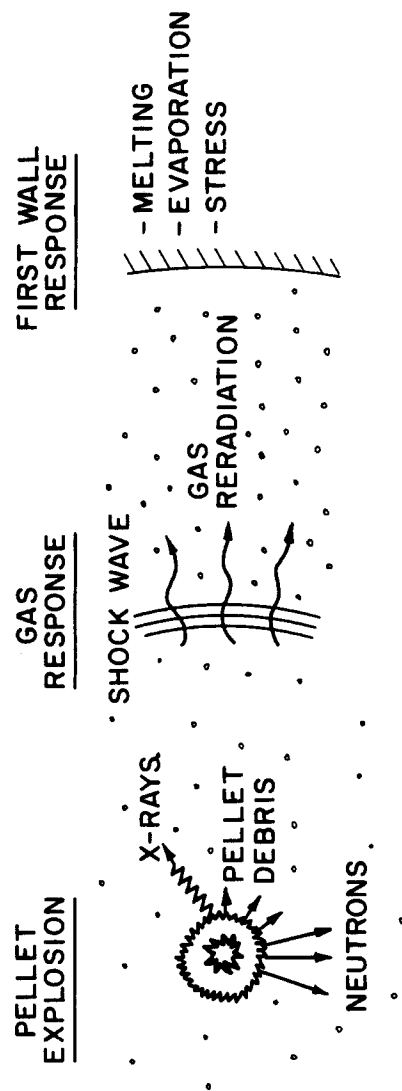


Fig. VII.A-5. Cavity phenomena in gas filled ICF reactors.

The different types of drivers being considered for ICF reactors have widely varying restrictions on the allowable cavity gas density. Hence, the second objective of this research is to investigate the first wall evaporation from unattenuated x-rays and gas reradiation as a function of the buffer gas density. To meet the second objective, a particular reactor geometry, target x-ray and debris spectra, and buffer gas have been selected. The evaporation of a carbon and a stainless steel first wall is compared for gas densities corresponding to 0.05, 0.5, and 5.0 torr (0°C) and the ambient temperature is assumed to be 573°K.

A.7.2. First Wall Evaporation from Gas Reradiation and Unattenuated

X-Rays

The first wall thermal response and evaporation calculations that are presented here were computed with the A*THERMAL computer code.⁽²¹⁾ The code solves the heat conduction equation with temperature varying thermal properties, and uses the surface temperature to compute the evaporation rate. Moving boundary conditions are used to account for surface recession from evaporation and also for the solid-liquid interface. The models used here to calculate the surface temperature, melting, and evaporation thickness are those developed in Chapter V. The thermal properties of Type 316 stainless steel and Type 3474 D graphite used in this study are given in Refs. (22,23).

The general characteristics of first wall evaporation from unattenuated target x-rays can be identified without specifying a

particular target design or buffer gas. Figure VII.A-6 shows the evaporated thickness of carbon and stainless steel as a function of the x-ray energy spectrum and energy fluence. In Figure VII.A-6, it is assumed that the x-ray pulse is 10 nanoseconds long, and that the energy spectrum absorbed by the wall has a blackbody distribution. An exponential energy deposition profile for x-rays is assumed. It is based on the analytical approximations for the absorption cross sections given by Biggs.⁽²⁵⁾ Figure VII.A-6 shows how strongly the evaporated thickness depends on the energy spectrum of the x-rays. To relate cavity dimensions to energy fluence, note that for a spherical cavity 4 meters in radius, 1 J/cm^2 corresponds to about 2 MJ of energy. The x-ray absorption cross sections are such that x-ray penetration into the first wall decreases as the blackbody temperature of the spectrum decreases. As implied in Fig. VII.A-6 a reduction in penetration depth leads to a larger specific energy density, and consequently to greater evaporation. Hence, even 1 J/cm^2 of x-ray energy with a 0.1 keV blackbody distribution will limit the life of a stainless steel first wall to less than the life of a commercial plant. If there is a gas in the cavity, the softer part of the x-ray spectrum tends to be absorbed by the gas, thereby reducing the evaporation significantly.

There are a number of reasons why a given spectrum of x-rays evaporates less carbon than stainless steel. The primary reason is that the lower atomic number of carbon leads to a lower x-ray absorption cross section, and consequently to a lower specific energy

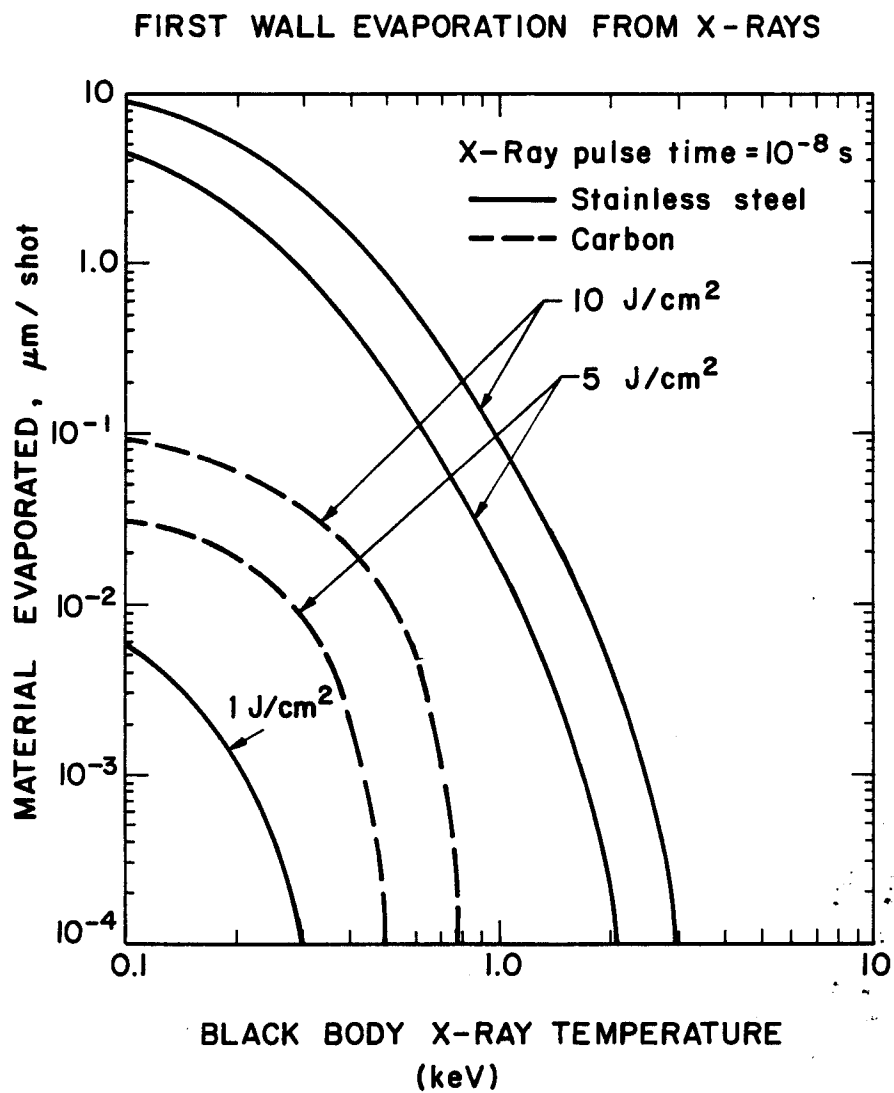


Fig. VII.A-6. The evaporation of carbon and stainless steel as a function of the x-ray spectrum and energy fluence.

density. Also, at a given temperature carbon has a lower vapor pressure than stainless steel. For absorbing ICF x-ray pulses, the advantage of carbon is only slightly compromised by its low thermal conductivity.

First wall evaporation from gas reradiation can also be studied without specifying the details of the target spectra, reactor geometry, or reradiation properties of the gas. Figure VII.A-7 shows the evaporation of carbon and stainless steel for various reradiation pulse times and energy fluences. In Fig. VII.A-7, the reradiation heat flux was assumed to be constant over the reradiation time. It was also assumed that the photons reradiated by the gas have a small enough penetration depth into the wall that a surface heat flux model can be used in solving the temperature equation.

As shown in Fig. VII.A-7, the evaporation of stainless steel decreases monotonically as the reradiation time increases since more time is available for conduction into the material. Heat conduction is more sluggish in carbon, and an increase in the pulse width may increase the time available for evaporation without a significant decrease in the surface temperature. The result is that for the shorter radiation times shown in Fig. VII.A-7, the evaporation of carbon increases as the pulse width increases. As the pulse width continues to increase, conduction again becomes the dominant surface cooling mechanism and the evaporation decreases monotonically. In this paper, the vapor species is assumed to be monatomic carbon, which may slightly underestimate the evaporated thickness. This is

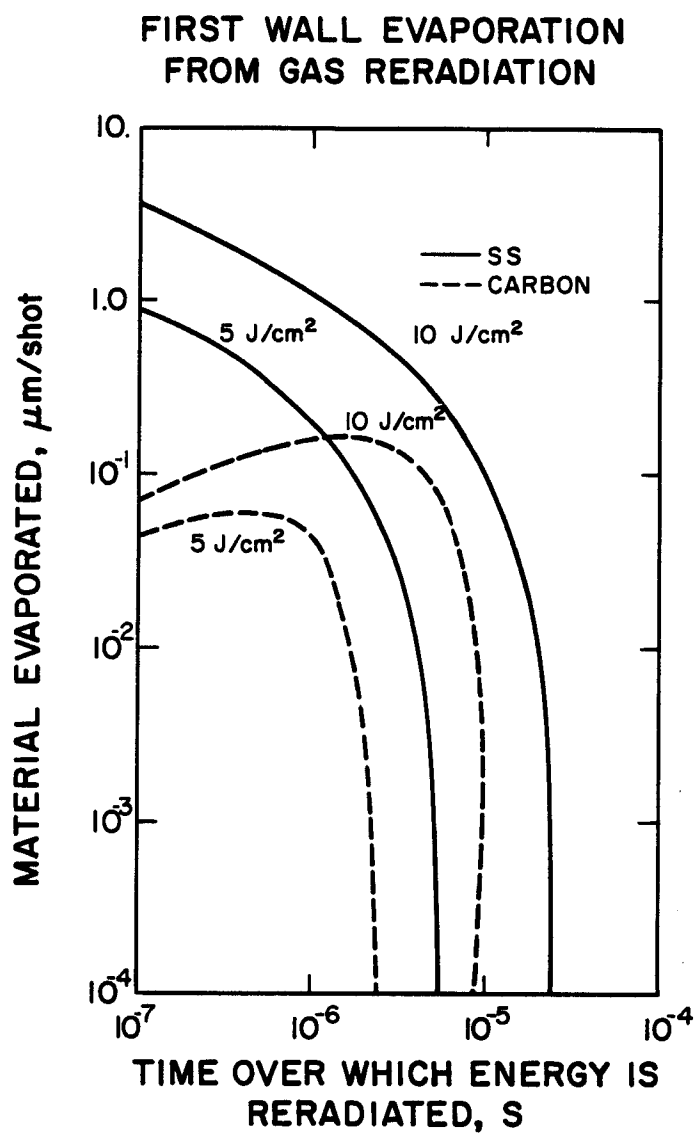


Fig. VII.A-7. The evaporation of carbon and stainless steel as a function of the gas reradiation time and energy fluence.

because at high temperature the dominant vapor species is C_3 rather than monatomic carbon.⁽²⁴⁾ For a reradiated energy fluence of 1 J/cm^2 or less, the evaporated thickness was found to be insignificant for both carbon and stainless steel.

Figure VII.A-8 shows the melt zone thickness of stainless steel as a function of the reradiation time of the gas. For the smaller reradiation times shown, a larger melt thickness is obtained for 5 J/cm^2 than 10 J/cm^2 because evaporative erosion of the melt thickness is larger for an energy fluence of 10 J/cm^2 . As the reradiation time increases, the thickness of the melt layer passes through a maximum and is larger for larger input energies. It then decreases as conduction becomes effective at larger times. The melt depth from x-ray energy deposition depends on the energy density as well as the energy spectrum. For very soft x-rays, which can be modeled as a surface heat flux, Fig. VII.A-8 would predict a melt depth of less than 2 microns at 10 nsec pulse duration.

A.7.3. The Dependence of First Wall Evaporation on Cavity Gas

Density

A specific reactor geometry, target x-ray and debris spectrum, and buffer gas have been chosen to illustrate how the cavity gas density affects first wall evaporation. A spherical reactor cavity with a 4 meter radius was assumed. The cavity was assumed to be filled with an argon buffer gas that contains 0.2 atom percent sodium. This buffer gas was chosen because it has been used in other ICF reactor studies.⁽²⁶⁾ The target was assumed to emit 15 MJ of x-ray

STAINLESS STEEL MELTING ZONE THICKNESS

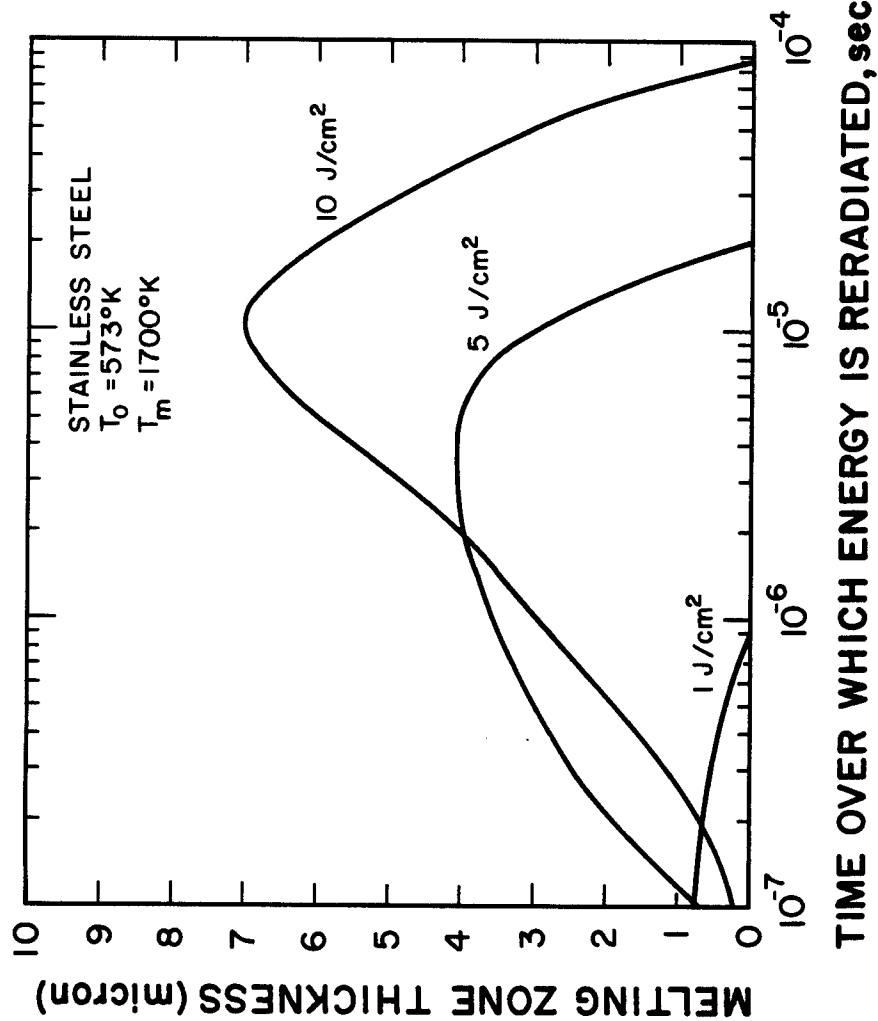


Fig. VII.A-8. Stainless steel melting zone thickness as a function of reradiation time for different input energy densities.

energy in 10 nanoseconds. The energy spectrum of the target x-rays corresponds to that of a 0.3 keV blackbody. The target debris was assumed to consist of one gram of iron expanding into the buffer gas with 15 MJ of kinetic energy (15 keV/iron ion).

In the examples that follow, the FIRE code⁽²⁷⁾ was used to compute the deposition of target x-rays and debris in the gas, as well as the subsequent radiation hydrodynamic response. The equation of state and reradiation properties of the gas that were used by FIRE were computed with the MIXER code.⁽²⁸⁾ The reradiation heat flux from the gas and the spectrum of the unattenuated target x-rays were input into the A*THERMAL code to study the first wall thermal response. The flux and fluence of energy from unattenuated x-rays and gas reradiation are shown in Table VII.A-2. The argon gas densities examined correspond to 0.05, 0.5, and 5.0 torr (0°C). Although the average gas reradiation heat flux is listed in Table VII.A-2, the detailed reradiation flux history from the FIRE code was used in computing the results that follow.

Figure VII.A-9 shows the thermal response of a stainless steel first wall for the three gas densities considered in this study. The delay before the temperature rises above the ambient temperature ($T_0 = 573^\circ\text{K}$) is the time for the x-rays to reach the wall after the target burn. For the two lower cavity gas densities, the first wall temperature increase from x-rays is limited mainly by evaporative cooling. More unattenuated target x-rays reach the wall for the lower cavity gas densities, and consequently the lower cavity gas

Table VII.A-2. The Fluence and Flux of Gas Reradiation
and Unattenuated Pellet X-Rays at the First Wall

Ar (0.2% Na)	Unattenuated X-Rays		Gas Reradiation	
	Energy Fluence, J/cm^2	Average Flux, W/cm^2	Energy Fluence, J/cm^2	Average Flux, W/cm^2
0.05	5.66	6.55×10^8	8.5	8.5×10^5
0.5	2.33	2.33×10^8	12	2.4×10^5
5.0	0.15	0.15×10^8	14	1.4×10^5

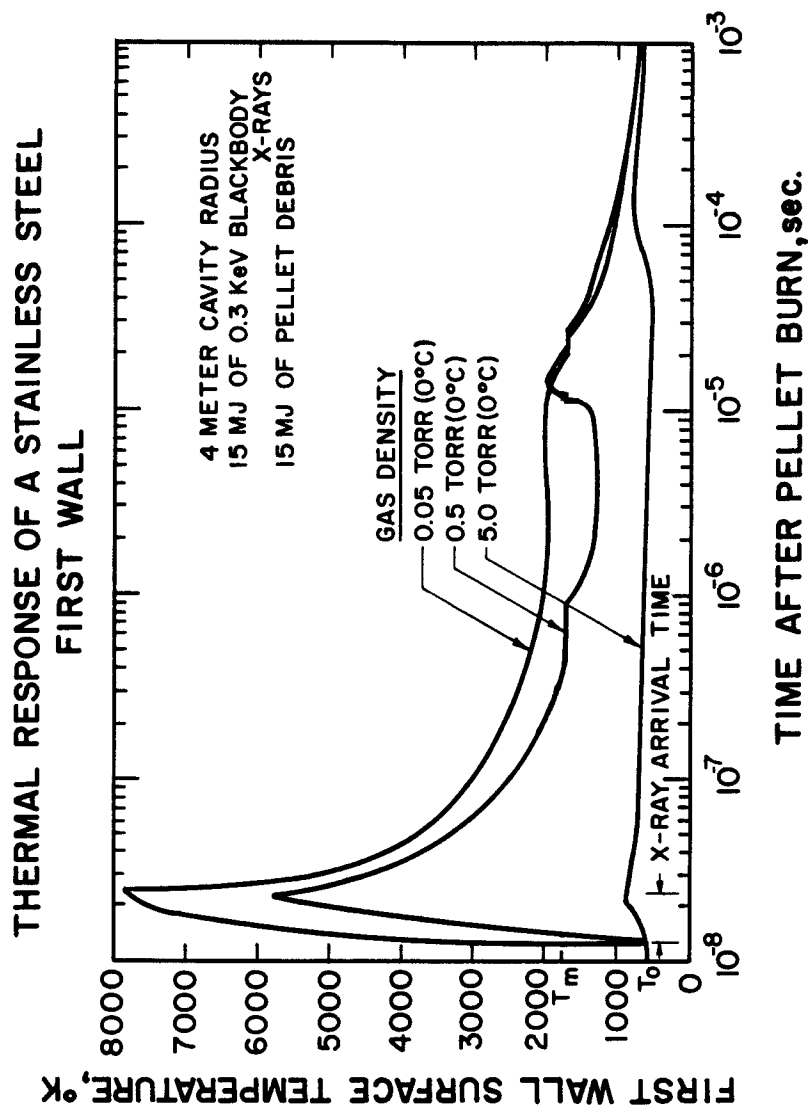


Fig. VII.A-9. The thermal response of stainless steel for different cavity gas densities.

densities result in a higher temperature pulse from x-rays. The very high surface temperatures from x-rays at low gas pressure will actually change the surface into an ionized plasma. A lower gas density also implies a shorter reradiation pulse width, and that too will produce higher first wall temperatures. With a gas density corresponding to 0.5 torr (0°C), the temperature cools to below the melting temperature ($T_m = 1700^\circ\text{K}$) before the gas reradiation induces another temperature rise. In the case of 0.05 torr, the gas reradiation keeps the surface from solidifying until about 20 μsec . A gas density corresponding to 5.0 torr keeps the surface temperature far below the melting temperature for both the x-ray pulse and the reradiation heat flux.

Figure VII.A-10 shows the thermal response of a carbon first wall subject to the same target x-rays and gas reradiation. The lower x-ray absorption cross section of carbon keeps the temperature rise from x-rays below that computed for stainless steel. In addition, the lower thermal conductivity of carbon prevents the temperature from dropping rapidly after the x-ray pulse. In carbon, heat conduction is sluggish enough that with a gas density corresponding to 0.05 torr, the gas reradiation continues to drive the surface temperature up slightly after the x-ray deposition. With a gas density corresponding to 5.0 torr (0°C), the temperature rise from x-rays and gas reradiation never exceeds 20°C .

Figure VII.A-11 compares the evaporation of a carbon and stainless steel first wall as a function of the cavity gas density. For

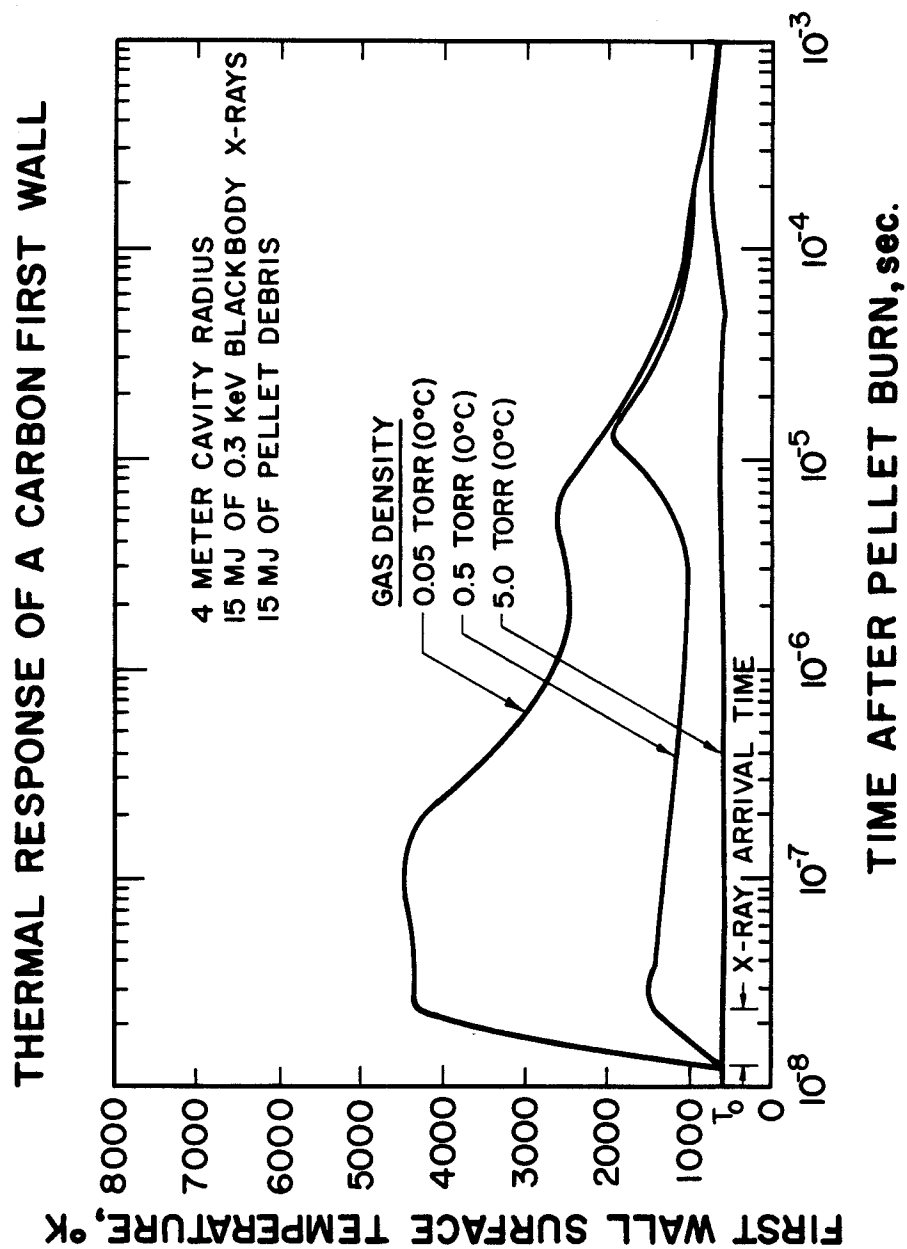


Fig. VII.A-10. The thermal response of carbon for different cavity gas densities.

FIRST WALL EVAPORATION FROM REFERENCE PELLET AND BUFFER GAS

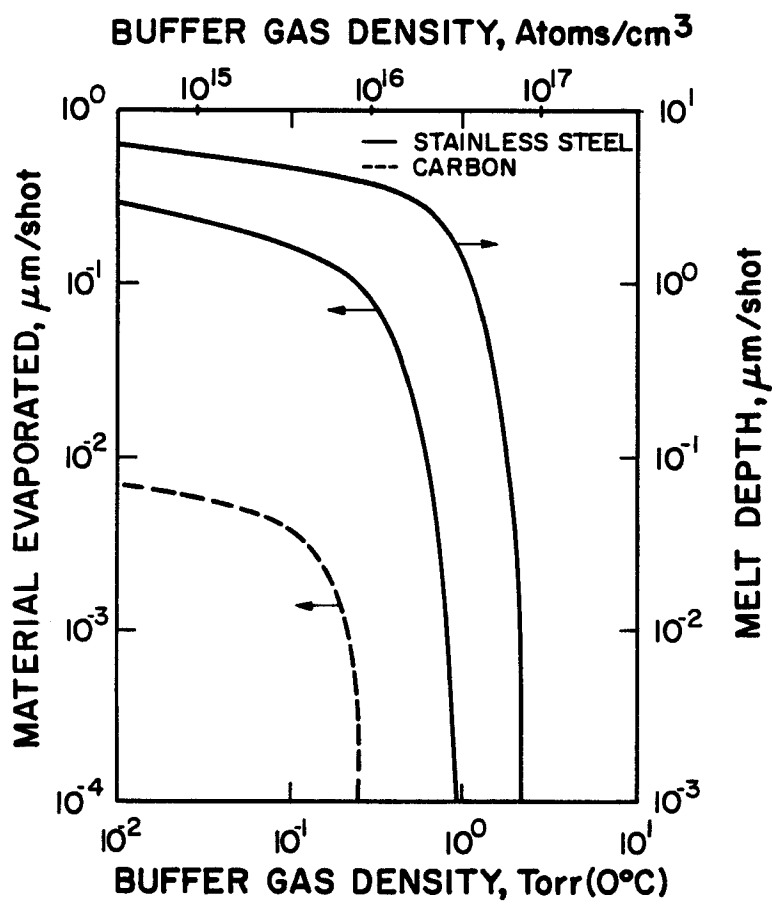


Fig. VII.A-11. First wall evaporation of carbon and steel vs. cavity gas density for conditions outlined in Table VII.A-2.

the target, buffer gas, and reactor geometry chosen in this study, the evaporative erosion will not limit the lifetime of a carbon first wall unless the gas density is less than 0.3 torr (0°C). For a permanent stainless steel first wall in a commercial ICF reactor, the gas pressure should be above 0.9 torr (0°C) to avoid excessive erosion. The maximum melt depth of stainless steel is also shown in the figure (a melt depth curve for carbon is not shown because of carbon sublimation). If the cavity gas density is much below 10^{-2} torr (0°C), sputtering by debris ions begins to enhance the erosion rate.

A.7.4 Conclusions

The parametric study of first wall evaporation from x-rays shows that the lower x-ray attenuation coefficient of carbon gives it an advantage over stainless steel as a permanent first wall material. It is also shown that softer x-rays have a greater tendency to induce evaporation than hard x-rays.

The parametric study of first wall evaporation from gas reradiation shows that the low vapor pressure of carbon causes it to have a lower evaporative erosion rate than stainless steel. Also, it was observed that the evaporative erosion of carbon could increase as the time over which energy is reradiated by the gas increases if heat conduction is too sluggish. This phenomenon was not observed for stainless steel because of its relatively higher thermal conductivity.

The evaporation from unattenuated x-rays and gas reradiation has been computed for various buffer gas densities. This is done for a specific reactor geometry, target x-ray and debris spectra, and type of buffer gas. The results show that for the parameters specified in this study, the evaporative erosion of stainless steel falls to a negligible value as the ambient argon buffer gas density is increased to about 1 torr (0°C). The evaporative erosion of carbon is negligible if the ambient Ar gas density is greater than about 0.3 torr (0°C). Below these densities, the evaporation will keep a carbon or stainless steel first wall from lasting the life of a commercial ICF plant.

References for Section VII.A

1. G.J. Zimmerman, "Numerical Simulation of Laser-Initiated Fusion," Comments on Plasma Physics and Controlled Fusion, Vol. II (1976).
2. E.U. Condon and H. Odishaw, eds., Handbook of Physics, 2nd Ed., McGraw-Hill, 1967, pp. 7-126, 7-138.
3. M.J. Tobin and A.P. Fraas, "Fusion by Laser," Scientific American, No. 6, (June 1971), 224.
4. R.R. Peterson and G.A. Moses, "Blast Wave Calculations in Argon Cavity Gas for Light Ion Beam Fusion Reactors," University of Wisconsin Fusion Engineering Program Report UWFD-315 (October 1979).
5. T.O. Hunter, "A General Model for the Analysis of the Transient Radiation Damage Environment from Pulsed Thermonuclear Radiation," Ph.D. Thesis, Department of Nuclear Engineering, University of Wisconsin-Madison (1978).
6. I.O. Bohachevsky, "Scaling of Reactor Cavity Wall Loads and Stresses," Los Alamos Scientific Lab., LA-7014-MS, November 1977.
7. A.M. Hassanein, "Deposition of Thermonuclear Target Debris and X-Rays in a Solid or Liquid First Wall Including the Resulting Vapor," Preliminary Proposal, Department of Nuclear Engineering, University of Wisconsin-Madison (May 1980).
8. T. Frank et al., "A Laser Reactor Concept Utilizing Magnetic Fields for Cavity Wall Protection," Proc. of the First Topical Mtg. on the Technology of Controlled Nuclear Fusion, San Diego, CA, April 1974, p. 96.
9. D.A. Friewald et al., "Laser Fusion Generating Stations Based on the Magnetic Protected Reactor Cavity," LA-UR-75-2035, Los Alamos National Laboratory; also Trans. ANS 22, (1975) 68.
10. J. Maniscalco and Meier, "Liquid-Lithium 'Waterfall' Inertial Confinement Fusion Reactor Concept," Lawrence Livermore Laboratory, Trans. ANS 26, (1977) 62.
11. R. Conn et al., "SOLASE - A Conceptual Laser Fusion Reactor Design," University of Wisconsin Fusion Engineering Program Report UWFD-220 (Dec. 1977).
12. G.L. Kulcinski, "First Wall Protection Schemes for ICF Reactors," J. Nucl. Mat. 85 & 86, (1979) 87.

13. T.J. McCarville, A.M. Hassanein, and G.L. Kulcinski, University of Wisconsin Fusion Engineering Program Report UWFD-282 (Nov. 1978).
14. A.M. Hassanein and G.L. Kulcinski, "Effect of Gas Pressure on the Amount of X-Ray Energy Absorbed in the First Wall of an ICFR," University of Wisconsin Fusion Engineering Program Report UWFD-306 (Aug. 1979).
15. S.G. Varando and G.A. Carlson, "Considerations in the Design of Electron-Beam Induced Fusion Reactor Systems," Nucl. Technology 29, (June 1976) 415.
16. D. Cook and M.A. Sweeney, "Design of Compact Particle-Beam Driven ICF Reactors," Proc. of 3rd ANS Mtg. on the Tech. of Controlled Nuclear Fusion, Santa Fe, NM, May 1978.
17. T.O. Hunter and G.L. Kulcinski, J. Nucl. Mat. 76, (1978) 383.
18. J. Hovingh, J. Maniscalco, M. Peterson, and R.W. Werner, Proc. First Topical Meeting on the Tech. of Controlled Thermonuclear Fusion, G.R. Hopkins, ed., CONF-740402-P1 (1974), p. 96.
19. A.M. Hassanein, T.J. McCarville, and G.L. Kulcinski, "First Wall Evaporation in ICF Reactors Utilizing Gas Protection," presented at the Second Topical Mtg. on Fusion Reactor Materials, Seattle, WA, August 1981, (to be published in J. of Nucl. Mat.); also UWFD-423.
20. T.J. McCarville, A.M. Hassanein, and G.L. Kulcinski, "The Response of Stainless Steel to the Pellet Debris in a Laser Fusion Reactor," presented at the 5th International Conference on Structural Mechanics in Reactor Technology, Berlin, Germany, Vol. N, August 1979.
21. A.M. Hassanein and G.L. Kulcinski, "A*THERMAL Code Description," University of Wisconsin fusion Engineering report, to be published.
22. S. Kim Choong, "Thermophysical Properties of Stainless Steel," ANL-75-55, Argonne National Laboratory, Sept. 1975.
23. N.S. Rasor and J.D. McClelland, "Thermal Properties of Graphite, Molybdenum and Tantalum to Their Destruction Temperatures," J. Phys. Chem. Solids 15, (1959) 17-26.
24. A.M. Hassanein, G.L. Kulcinski, W.G. Wolfer, "Vaporization and Melting of Materials in Fusion Devices," presented at the Second Topical Meeting on Fusion Reactor Materials, Seattle, WA, August 1981, (to be published in J. of Nucl. Mat.); also UWFD-422.

25. F. Biggs and R. Lighthill, "Analytical Approximations for Total and Energy Absorption Cross Sections for Photon-Atom Scattering," SC-PR-720685, Sandia Laboratories, Albuquerque, NM, December 1972.
26. R.R. Peterson, G.W. Cooper, G.A. Moses, "Cavity Gas Analysis for Light Ion Beam Fusion Reactors," Nucl. Tech./Fusion (July 1981).
27. G.A. Moses, T.J. McCarville, R.R. Peterson, "Improvements in the FIRE Code for Simulating the Response of a Cavity Gas to Inertial Confinement Fusion Target Explosions," University of Wisconsin Fusion Engineering Program Report UWFD-407, 1981.
28. R.R. Peterson, G.A. Moses, "MIXER - A Multi-Species Optical Data and Equation of State Computer Code," University of Wisconsin Fusion Engineering Program Report UWFD-372, September 1980.

B. Application (B): Analysis of Plasma Disruption in Magnetic Fusion Reactors

B.1. Introduction

The existence of plasma disruptions in tokamaks has been known ever since that confinement concept was first introduced by Soviet scientists in 1968. These disruptions deposit large amounts of energy on the metallic vacuum chamber walls or limiters in a very short period of time which can result in rather large temperature excursions. In fact, it is anticipated that if the plasma energy in near term tokamaks (PLT, JT-60, TFTR, INTOR) is deposited on such surfaces, melting and even vaporization could take place. The object of this study is to use the models developed in this thesis to calculate the response of metallic first walls to such heat pulses and to identify those parameters which are of major importance in this potentially damaging event.

B.2. Plasma Disruptions

B.2.1. Assumptions for INTOR (International Tokamak Reactor)

One of the first problems encountered in this area of research is the lack of well documented experimental data about disruptions. The cause of disruptions and methods to prevent their occurrence are relatively unknown at this time, so it is generally felt throughout the field that we will have to design chamber walls and limiters which can take hundreds to thousands of such disruptions over the lifetime of a device. The major areas of uncertainty in this field are:

1. Partitioning of plasma and magnetic energy into the first wall.
2. Fraction of the disruption energy which appears as x-rays.
3. Location of the place where the disruptions will hit the wall.
4. Area over which the plasma deposits its energy.
5. Time of plasma disruption.

A schematic of the factors that contribute to the plasma energy flux and how that is partitioned to the wall is given in Fig. VII.B-1 and Table VII.B-1 lists some values for PLT, TFTR, INTOR and STARFIRE.

The total energy content of the INTOR plasma is the sum of the thermal energy of the ions and electrons plus the stored magnetic energy. The value of the plasma thermal energy for INTOR is:

$$\frac{3}{2} \times (\text{average beta}) \times \frac{B^2}{2\mu} \times (\text{plasma volume}) \quad (1)$$

Inserting an average beta of 5.6%, 241 m^3 of plasma, and a magnetic field of 5.5 Tesla we find that the plasma thermal energy for INTOR is 244 MJ.

The stored energy in the INTOR poloidal magnetic field is obtained from

$$\beta_p = \frac{\int dV \frac{3}{2} nKT}{\int dV \frac{B_p^2}{2\mu_0}} = 2.6 \quad . \quad (2)$$

This means that the stored energy is then 94 MJ. Adding the thermal

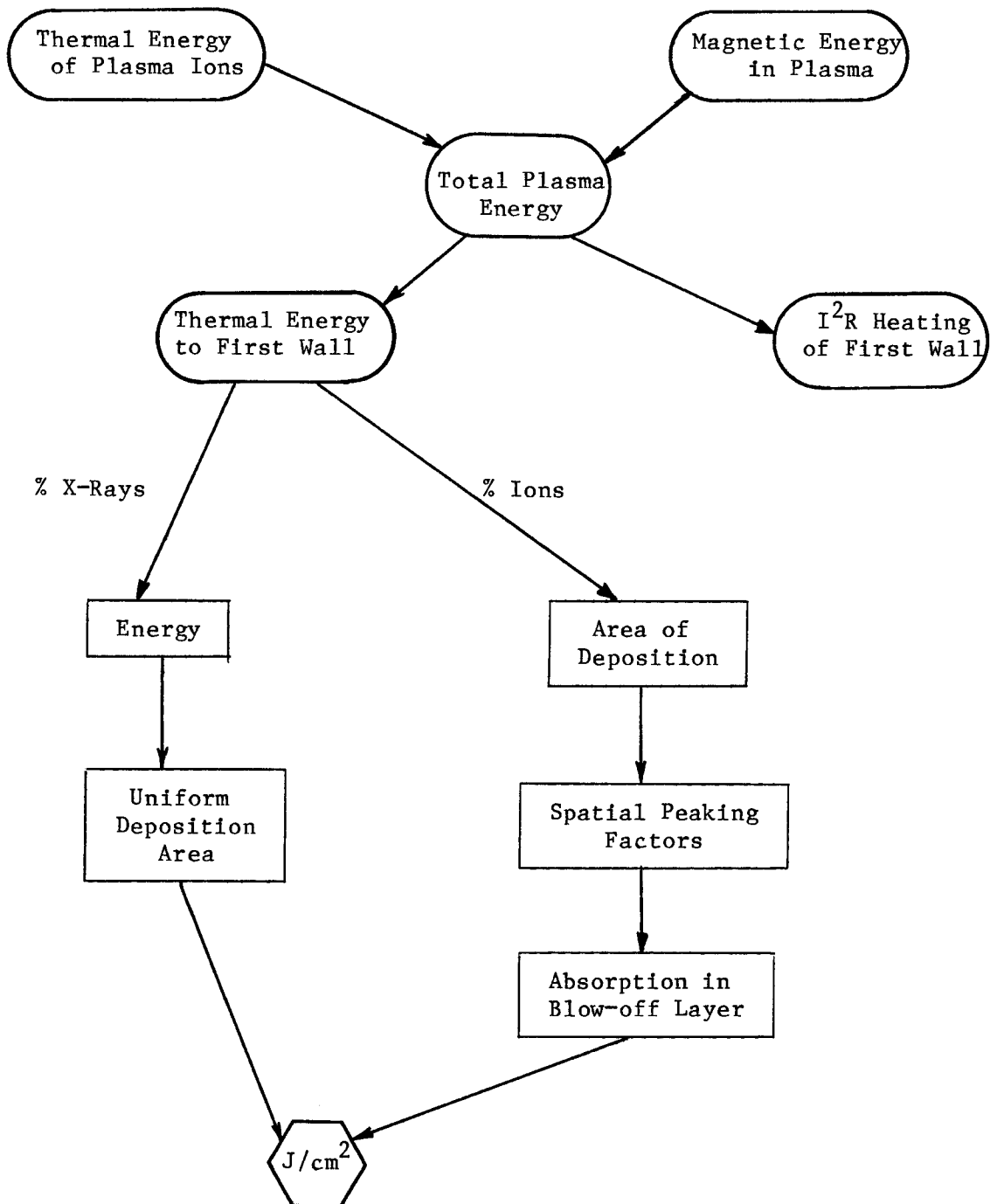


Fig. VII.B-1. Schematic of factors to be considered for calculating energy deposition densities from plasma disruptions.

Table VII.B-1. Summary of Selected Disruption Factors for INTOR
and Other Tokamaks Devices

<u>Parameter</u>	<u>PLT</u>	<u>TFTR</u>	<u>INTOR</u> <u>(Assumed)</u>	<u>INTOR</u> <u>(Corrected)</u>	<u>Starfire</u> <u>Projected</u>
Plasma Ion Plus					
Elec. Energy - MJ				244	1050
Magnetic Energy - MJ				94	~350*
Total Plasma Energy					
- MJ	0.3	10	220*	338	1400*
I ² R Loss in FW - MJ			0	47*	~175*
Avail. for FW Depo- sition - MJ			220*	291*	~1225*
% of Plasma Energy in x-ray			30*	30*	30*
X-ray Energy to FW					
- MJ			66*	87*	368*
Total FW Area - M ²	24	82	380	380	780
X-ray Energy Flux					
- J/cm ²			17*	23*	47*
Total Energy Plasma Ions - MJ	0.3	10	154*	204*	857*
% of Area Plasma Deposited	10	10*	30*	25*(a)	30*(a)
Total Area of Depo- sition - m ²	2.4	8.*	114*	96*	234*
Ave. Ion Energy Deposition - J/cm ²	12	120*	135*	213*	366
Peaking Factor			2.0*	1.7(b)	2*
Maximum Ion Energy Flux - J/cm ²			270*	361*	732*
Max. Ion + Elec. Energy Flux - J/cm ²			287*	384*	779*
Plasma Radius - m	0.45	0.85	1.3	1.3	1.9
Electron Temperature - keV	4		10	10	17.4
Disruption Time - ms	0.2	0.38*	20*	20*	100*
Disruption Frequency	0.01	?	0.005 Phase I (0.001 Phase II & III)*		?
Total Disruptions	?	?	1064*	1064*	?

(a) If plasma is moved straight inward to inboard wall, correcting for asymmetries in INTOR.

(b) Calculated from collapsed plasma with $(1 - (r/r_m)^2)$ density profile.

* Assumptions.

and magnetic energy we find that the total INTOR plasma energy is 338 MJ.

The amount of stored magnetic energy that appears as heat in the plasma and eventually to the first wall is also unknown, but it is commonly assumed to be 1/2 of the total.⁽¹⁾ For INTOR, this value was assumed to be zero. The mechanism by which the magnetic energy is converted to thermal energy is by frictional losses as the flux lines move through the plasma.

The next step to calculating the first wall energy flux is to determine how much of the plasma energy goes to the wall as x-rays and how much is transported by ions. When the plasma contains a large amount of impurities, essentially all of the plasma energy could be radiated uniformly to the wall as x-rays. If the plasma is relatively "clean", essentially all of the energy will be transferred to the walls in the form of kinetic energy of the plasma particles. During disruptions in present machines, it is commonly observed that the radiation load increases by factor of 5 to 10 over the steady-state values. Since only a few percent of the plasma energy is radiated during equilibrium, then values of 15-30% are probably reasonable for the fraction of disruption energy to the wall in x-rays. The value assumed for INTOR is that 30% of the plasma energy will be radiated away as x-rays. Since this energy is uniformly deposited around the chamber, the energy flux from the x-rays in INTOR is 87 MJ divided by 380 m^2 or 23 J/cm^2 .

The plasma energy left in the ions is then 204 MJ and the area of deposition has been arbitrarily assumed to be 30% of the total first wall (toroidal symmetry is also assumed). Furthermore this area is assumed to be located on the inboard side and 100% of the disruptions are assumed to be deposited in that area. Currently, 90% of the disruptions in Alcator A and Alcator C occur on the inboard side. Mechanisms to insure that all disruptions occur on the inboard side are still to be developed.

The 30% area fraction presumably comes about by forcing the plasma to move exactly inward. However, the plasma is not symmetric and the ion density in the upper region is greater than that in the lower region of the torus. Recent calculations,⁽²⁾ taking into account the above fact, estimated the area of deposition to be 25% of the total first wall. This value is entered in the INTOR (corrected) column of Table VII.B-1. The energy flux by the ions to the first wall of INTOR (assumed) is now 135 J/cm^2 (or 213 J/cm^2 for the corrected case).

Perhaps the most controversial quantity in the disruption calculation is the uniformity of the energy deposition. It is unreasonable to assume that all the plasma particles will evenly distribute themselves over the surface area of the disruption. One method of estimating this peaking factor is to numerically integrate the ion density in strips horizontally across the most dense part of the plasma, i.e., the upper region. This would probably represent the minimum spatial peaking factor.

Using the assumed peaking factor of 2.0 from INTOR and the value calculated from the collapse of the INTOR plasma we find the maximum ion and electron energy flux to be 270 J/cm^2 for the IAEA INTOR reference case and 361 J/cm^2 for the corrected INTOR case. Adding the x-ray flux, we find a total energy flux of 287 J/cm^2 (384 J/cm^2 for the corrected version).

Finally, we come to the duration of the plasma disruption. Current experimental evidence for disruption times are listed below.

<u>Device</u>	<u>Disruption Time - ms</u>
Alcator	0.1
PLT	0.2
Doublet-III	0.5

A group⁽¹⁾ in the U.S. recently assessed the disruption possibilities and recommended a value of 5 ms for INTOR. Another way of estimating the disruption time is to assume it scales as $T_e^2 a$ or $T_e^3 a^2$ where T_e is the electron temperature and a is the minor radius of the torus.⁽²⁾

Using values for PLT as a reference we predict disruption times of 4 ms to 26 ms in INTOR. The IAEA workshop in Vienna assumed a value of 20 ms. While we will use the IAEA value for our "base" case, one should consider variations to as low as 5 ms in a parametric study.

The number of disruptions to be experienced in INTOR is also subject to a great deal of uncertainty. Currently disruption frequencies of 1 in a 100 are typical. Presumably, we will do better once the machine is running and the INTOR workshop assumed a frequency of 0.001 in stages II and III. For INTOR operation this

amounts to 1075 disruptions over the entire lifetime (using the 200 second burn in stages II and III versus 100 seconds in stage I).⁽¹⁾

A summary of the possible values that could be used to determine the energy flux to the INTOR first wall is given in Table VII.B-2 with the INTOR values underlined.

In order to reduce the number of permutations of this data we will use the following assumptions made by the INTOR group in Vienna even though a more careful analysis might yield results that are 35% higher.

1. None of the stored magnetic energy in the plasma appears as thermal energy for the disruption.
2. The plasma energy available for the disruptions in INTOR is 220 MJ.

With these assumptions, the possible values in energy flux to the first wall varies as shown in Figs. VII.B-2, VII.B-3, and VII.B-4. The specific data is listed in Table VII.B-2. The assumptions on ion deposition area alone cause the energy flux to vary from 287 J/cm² to 828 J/cm² for the INTOR conditions. Similarly, the assumptions on the fraction of disruption energy in x-rays causes the energy flux to vary from 287 to 353 J/cm². Finally, the effect of peaking factor on the INTOR condition causes a variation from 220 to 355 J/cm². In addition to the possible spread in energy flux value close to the INTOR reference conditions, we find that other combinations could push the energy flux up to 1308 J/cm². If the corrected INTOR values were used the maximum heat flux could be as high as 1730 J/cm².

•

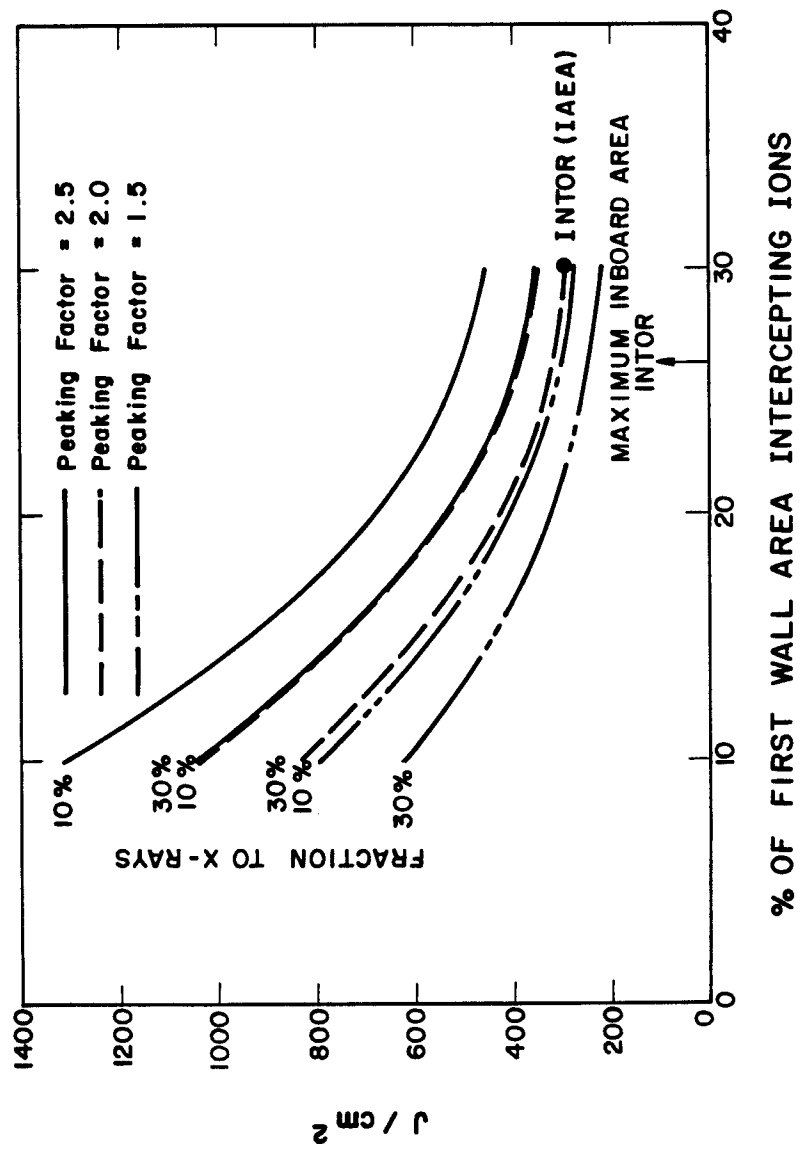


Fig. VII.B-2. Effect of deposition area on energy flux from INTOR plasma disruption.

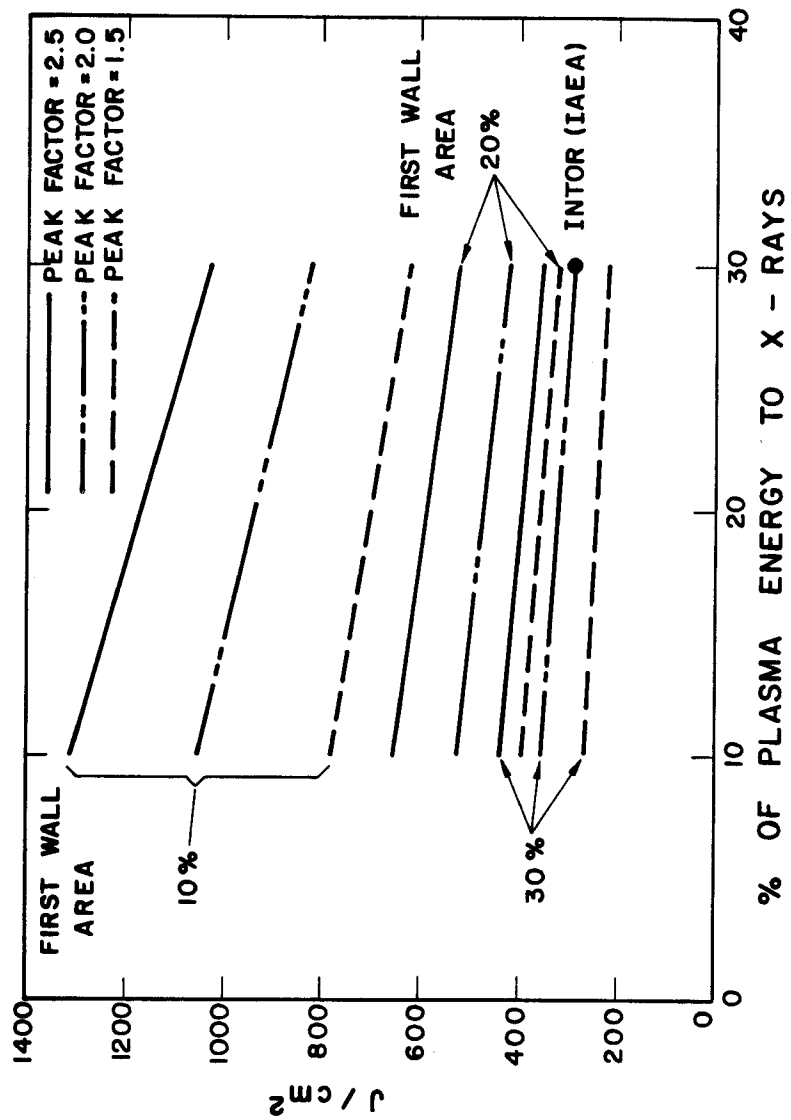


Fig. VII.B-3. Effect of x-rays on energy flux from INTOR plasma disruption.

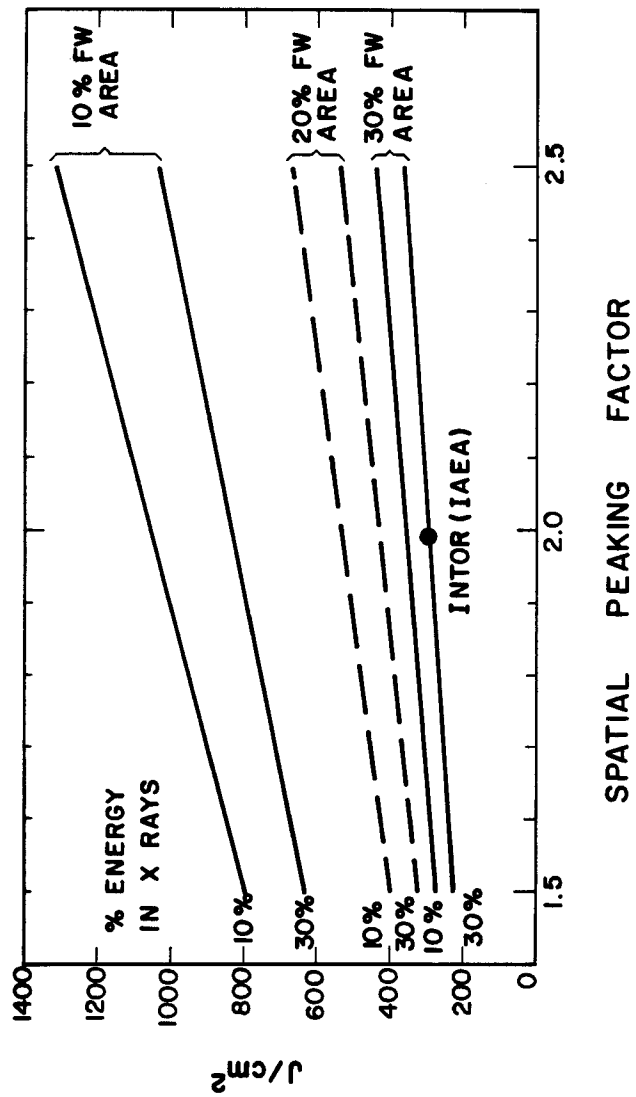


Fig. VII.B-4. Effect of spatial peaking factor on energy flux from INTOR plasma disruption.

Table VII.B-2. Possible Values Used to Determine the
Energy Flux to the INTOR First Wall*

Fraction of plasma magnetic energy that ends up in the plasma	<u>0.0</u> , 0.5
Fraction of plasma energy that appears as x-rays	0.1, <u>0.3</u>
Fraction of first wall area for ion deposition	0.1, 0.2, <u>0.3</u>
Spatial peaking factor	1.5, <u>2.0</u> , 2.5
Energy disruption time - ms	5, 10, <u>20</u>

*Underlined values are those used in the INTOR calculation.

In conclusion, we see that the range of energy fluxes to study for INTOR is from of 220 to 1308 J/cm² and studies at 200, 287, 350, 500, 800, and 1300 J/cm² might be appropriate. These numbers should be increased by 10 to 50% if magnetic field energy is included and other mistakes in the INTOR calculations are included.

B.2.2. Chronological Description of Disruption Sequence Used for This Study

The disruption/vaporization process will be broken up into 8 distinct time periods in order to facilitate the examination of

disruption models. Once this scenario has been established we will examine (in the next chapter) how previous models have addressed some of these time periods. Before starting, a few terms need to be defined.

t = time from the start of the disruption,

t_m = time required to raise the temperature of the first wall to its melting point,

t_v = time at which significant vaporization begins,

t_{Ed} = time duration of plasma energy loss,

t_{cd} = time duration of current decay, usually $t_{cd} > t_{Ed}$.

Obviously if $t_{Ed} < t_v$, then we only need to worry about the melt layer and no material will be lost from the front surface.

There are three distances that we need to define.

ΔX_m is the thickness of the melt layer on the front surface,

ΔX_v is the thickness of the first wall vaporized,

X_v is the maximum distance that the vaporized atoms have traveled into the plasma chamber.

Finally, there is the energy flux to the first wall surface, F_o . This flux is composed of x-rays, F_x , and the energy flux from the plasma ions, F_i . The value of F_i depends on the interaction of the "incoming" plasma and the "outgoing" vaporized atoms. Figure VII.B-5 summarizes the disruption/vaporization process considered here.

Step 1.

The initial conditions of the problem are that the first wall is completely solid at a temperature T_{ss} (modifications for a liquid

SCHEMATIC OF DISRUPTION / VAPORIZATION PROCESS






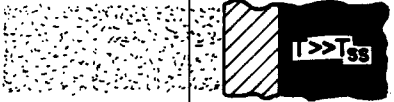


STEP		TIME	SURFACE Heat Flux
①		$t < 0$	F_{ss}
②		$t = 0$	$F_0 = F_x + F_i$
③		$t_m > t > 0$	F_0
④		$t > t_m$	F_0
⑤		$t > t_v$	$F_0 - F_d(t)$
⑥		$t = t_{Ed}$	~ 0
⑦		$t > t_{Ed}$	0
⑧		$t >> t_{Ed}$	0

Fig. VII.B-5. Schematic representation of disruption-vaporization process.

first wall can easily be made) and the energy content of the plasma is E megajoules. The temperature of the wall just before the disruption is determined by the steady state surface heat flux, F_{ss} , the neutron heating, and the method of cooling the first wall. For example, these factors cause the first wall of the INTOR reactor to be at 300°C before the disruption.

Step 2.

At time $t = 0$, it is assumed that the plasma disruption occurs and the plasma is contacting the first wall. In reality, there will be a short time from the time that the instability starts, x-rays are emitted, and the plasma contacts the wall. However, in this scheme we will assume that time is short (< 1 microsecond) and that the x-rays and ions strike the first wall with appropriate energy densities (F_x and F_i , respectively) evenly spread over the disruption time, t_{Ed} . The total energy flux is then $F_o = F_i + F_x$.

Step 3.

The continual bombardment of the first wall with the energetic ions and x-rays from the plasma will cause the surface of the first wall to increase in temperature. Some of this energy will be reradiated from the front surface (less than a few percent during the disruption) and some of this heat will also be conducted into the solid material heating up the first wall over a much larger region than the initial ion or x-ray energy deposition zone. This heating will continue until we reach the next step, melting at time t_m .

Step 4.

As the temperature of the first wall exceeds the melting point, a liquid layer of thickness $\Delta X_m(t)$ will develop. The heat flux to the solid part of the first wall (behind the melt region) will have to reflect the "loss" of the heat of fusion. The boundary between the melted layer and the solid first wall will move into the solid and we are faced with a so-called "moving boundary" problem. The temperature of the melted layer at the front surface continues to rise as the heat flux, F_0 , continues.

Step 5.

After part of the first wall has melted, the liquid will be heated until its vapor pressure is sufficient to cause significant vaporization of the first wall. At that point metallic atoms will absorb the heat of vaporization and be released from the melted layer into the plasma chamber. The velocity of these atoms will depend on the vaporization temperature and the angle at which they are emitted into the chamber will be isotropic (2π steradians). At first the metallic atoms will stream into the vacuum with a large mean free path between collisions. Eventually, the density of evaporated atoms will build up to the point that the mean free path between collisions is so short that the velocity distribution becomes isotropic. At this point some of the vaporized atoms will be redeposited on the original surface.

The atoms leaving the surface will be moving against the flux of plasma particles from the disruption and will also gain energy by

electronic and nuclear collisions. The actual energy flux that reaches the first wall will be less than F_0 because of the plasma ion energy which is deposited in the metal vapor. Therefore, the energy flux that actually reaches the front surface of the liquid will be represented as $F_0 - F_d(t)$ where $F_d(t)$ is the average loss of plasma ion energy in the expanding vapor.

Finally, the actual amount of material removed from the melt layer will be the net sum of the evaporation and condensation. We will assume that the recondensing atoms land on the same area from which they left neglecting transport in the magnetic field or irregularities in the wall design.

Step 6.

At the end of the plasma disruption, that is, when the last plasma ions have hit the first wall, the metallic ions will continue to evaporate until the vapor pressure of the steel melt layer is less than that in the chamber. When this happens, the maximum amount of first wall will have been evaporated (ΔX_v^{\max}) and the final erosion will depend on how much of the evaporated atoms are recondensed on the original surface.

Step 7.

The liquid layer now cools off by conducting the deposited heat into the solid or reradiating the energy to surrounding colder surfaces. During this time period the latent heat of fusion is recovered and the melted zone shrinks. Also during this time period, I^2R heating from the decaying current will be encountered but for the

present problem we will assume that to be small and spread out over a much longer time than the plasma disruption, i.e., $t_{cd} \gg t_{Ed}$.

Step 8.

Once the melted layer has disappeared, the temperature in the solid first wall will continue to fall as the heat is conducted and radiated away. Eventually the temperature falls to a level determined by the input of decay and I^2R heating, and that heat removed by the coolant.

B.3. Calculational Models

The general description of this problem can be conveniently broken up into four parts as illustrated in Fig. VII.B-6. A brief discussion of each step is given below.

1. The temporal, volumetric and surface heat flux to the first wall including x-rays and ions must be given. This heat flux should be appropriately corrected for radiation losses from the front surface and loss of energy by the plasma ions in the blow-off vapor from the first wall, although the former is usually negligible for steel.
2. The temperature distribution that exists in the solid and liquid layer (should any develop) must be calculated. This calculation should include the thermal variation of materials properties and the heat of fusion and vaporization. The temperature profile should be appropriately adjusted for two moving boundaries; that between the vapor and the metal layer as well as that between the melt layer and the solid.

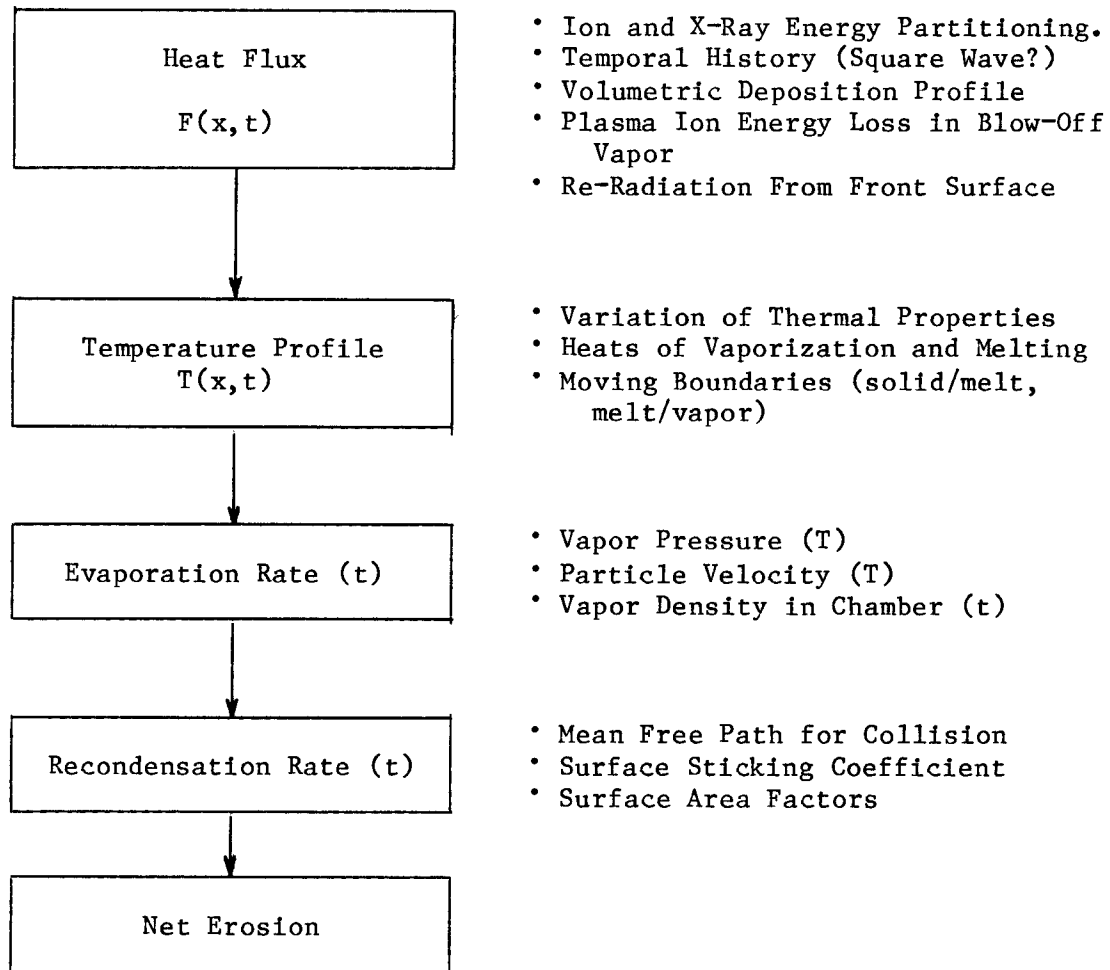
Important Parameters

Fig. VII.B-6. Procedure for Calculating the Erosion Resulting from a Plasma Disruption.

3. The rate at which metallic first wall atoms leave the surface of the melt zone and stream into the vacuum chamber must be determined. This requires a knowledge of the vapor pressure as a function of temperature and the results of such a calculation will reveal the spatial distribution of the evaporated atoms in the chamber.
4. The rate at which metallic atoms are redeposited on the original surface needs to be determined. This is a very difficult calculation because it requires a knowledge of the mean free path for collisions between the evaporated atoms, and any transport processes going on while the atoms are in the chamber.

Once all four steps have been integrated together we can get an accurate picture of the net erosion produced by the intense heat pulse. We have already developed in Chapter V the models needed to do these calculations.

It is also shown in Chapter V that the surface temperature is determined by both the boundary conditions as well as the kinetics of the evaporation process. The correct boundary condition entails partitioning of the incident energy flux into conduction, melting, evaporation, and radiation. The kinetics of evaporation establish the connection between the surface temperature and the net atom flux leaving the surface taking into account the possibility of recondensation.

It is important to evaluate the amount of material evaporated from the exposed material surfaces for two main reasons. First, the

evaporated atoms may contaminate the plasma with high-Z material. Second, both evaporation and melting will contribute to the first wall erosion in addition to sputtering if plasma disruptions occur repeatedly.

B.4. Parametric Analysis

The estimated deposition times for plasma disruption vary widely as discussed before, but it is generally agreed that they are on the order of or less than 100 ms. Longer deposition times result in lower surface temperatures than shorter times. Accordingly, the present calculations were carried out for deposition times equal to 5, 10, and 20 ms, and for energy densities as large as 1300 J/cm^2 . Furthermore, it was assumed that the energy is deposited at a constant rate over the assumed disruption time. The effect of different pulse shapes will be illustrated for some cases by examining the response to a triangular pulse and compare the result to that of a square pulse shape.

Three materials are considered in this analysis, i.e. stainless steel, carbon, and molybdenum. Steel and carbon are two of the main candidate materials for structural or liner components in fusion reactors. Because the high temperature refractory metals offer a range of properties that makes them unique among the candidate materials for limiters in fusion reactors, molybdenum is considered in this analysis.

B.5. Results and Discussion

Due to the large number of parameters involved in this study, i.e. different materials used in this analysis, different amounts of energies deposited into materials, different pulse shape, the results will be presented in the following order. First the surface temperature as a function of time is shown for each material for each of the three disruption times considered in this analysis, i.e. 5, 10, and 20 ms. Each plot will be for one value of the energy deposited. Three values of energy densities will be used in the calculations, i.e. 325, 650, and 1300 J/cm². A melting zone thickness as a function of the input energy density will be shown for each of the two materials, i.e. stainless steel and molybdenum that can undergo phase change. The velocity of the receding surface, as a result of the solution to the two moving boundary problems, will be shown as a function of time and for each of the three materials. The effect of the vapor shielding on the surface temperature, melting zone thickness, and the amount of material evaporated will also be illustrated. The effect of disruption times as low as 100 μ s and as large as 100 ms on the melted and evaporated 316 SS will be shown.

The effect of the pulse shape on the surface temperature, surface velocity, and the amount of melted and evaporated material will be discussed. Square as well as triangular pulse shapes are considered in this analysis.

Any combination of different values other than the ones considered here could be easily obtained from the computer code A*THERMAL.

B.5.1. Surface Temperature

B.5.1.a. Stainless Steel

The surface temperature of stainless steel (SS) as a function of time for the three energy densities, i.e. 325, 650, and 1300 J/cm² is shown in Figs. VII.B-7, VII.B-8, VII.B-9, respectively. All the plots shown in this study will be for the case of no vapor shielding unless explicitly stated. The thermophysical properties used in this work are those given in Ref. (3), and the initial temperature is assumed to be T_0 573°K. Each curve is shown for the three considered disruption times, i.e. 5, 10, and 20 ms. It is shown in Fig. VII.B-7 that the surface temperature exceeds the melting temperature of SS (T_m = 1700°K) for any of the disruption times considered. The shorter the disruption time the higher the surface temperature and the shorter the surface melt duration. Melting duration times might be important when considering issues like stability of the melt layer under different forces existing in the reactor chamber. The resolidification time, which is defined as the time taken from the liquid at the melting temperature to completely solidify, is proportional to the disruption time being longer for longer disruption times. At the end of the disruption time, the surface temperature drops sharply and the material cools down. In Fig. VII.B-8, where the deposited energy is twice the value used in Fig. VII.B-7, the

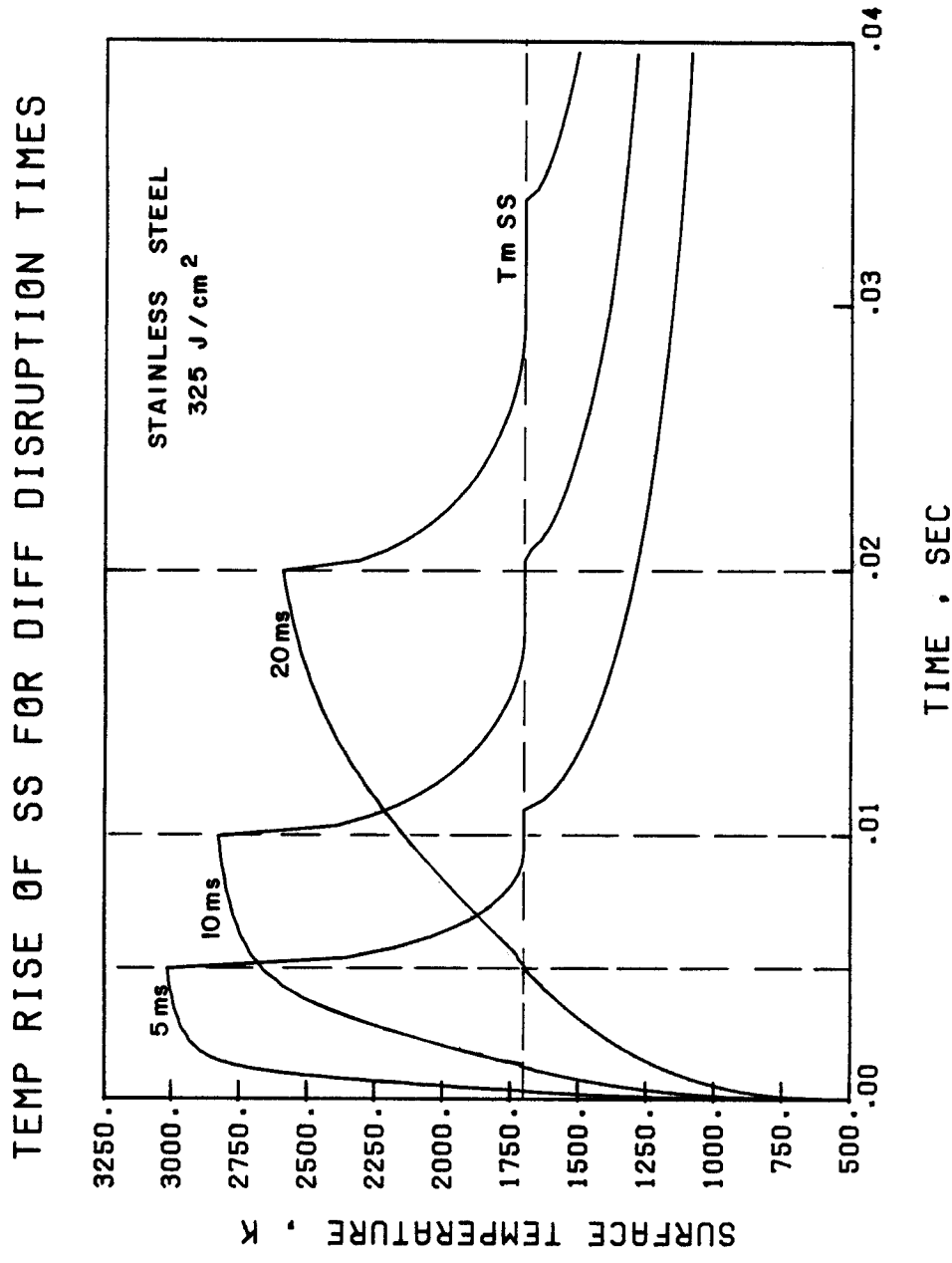


Fig. VII.B-7. Surface temperature rise of stainless steel for energy density of 325 J/cm² and different disruption times (no vapor shielding).

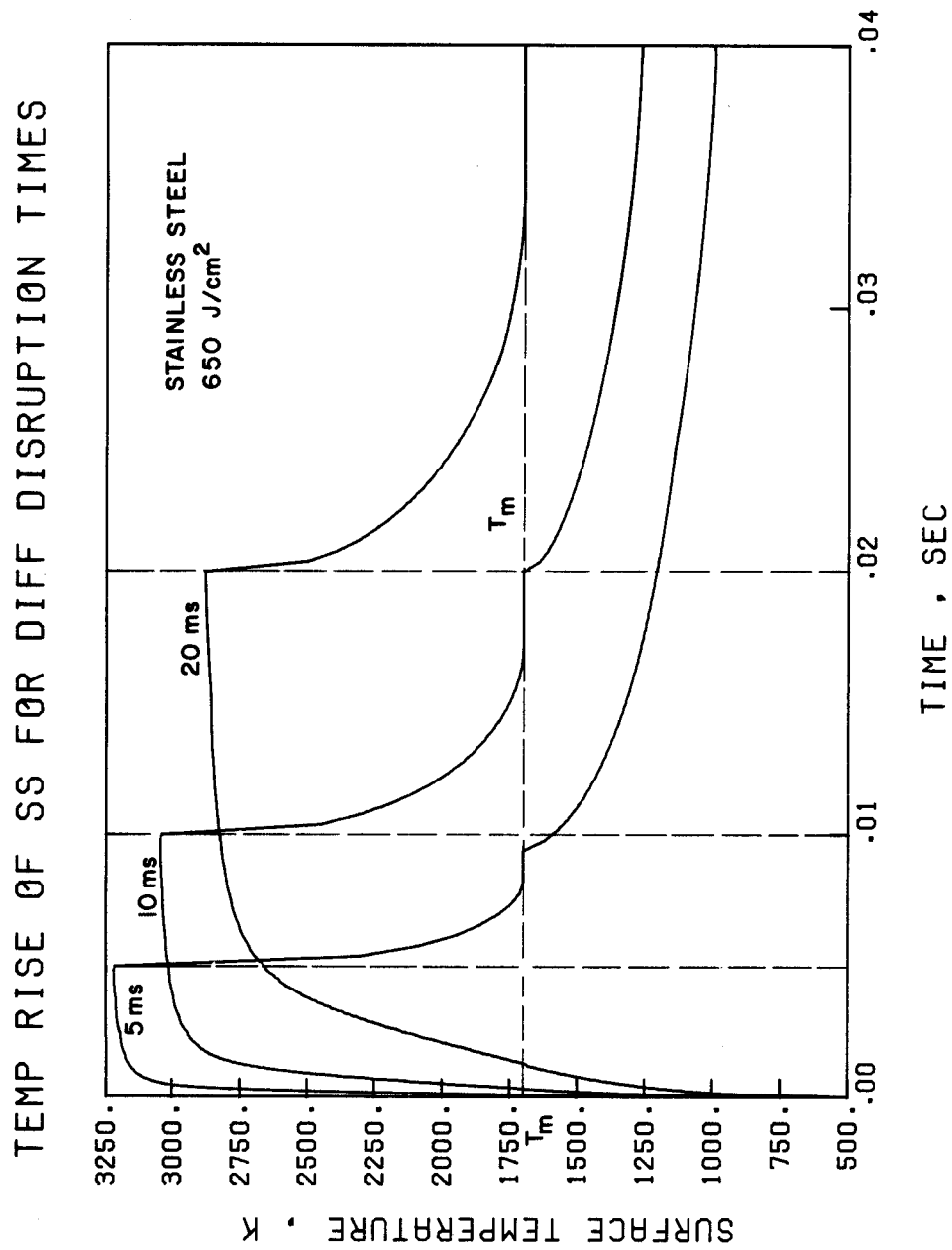


Fig. VII.B-8. Surface temperature rise of stainless steel for energy density of 650 J/cm² and different disruption times (no vapor shielding).

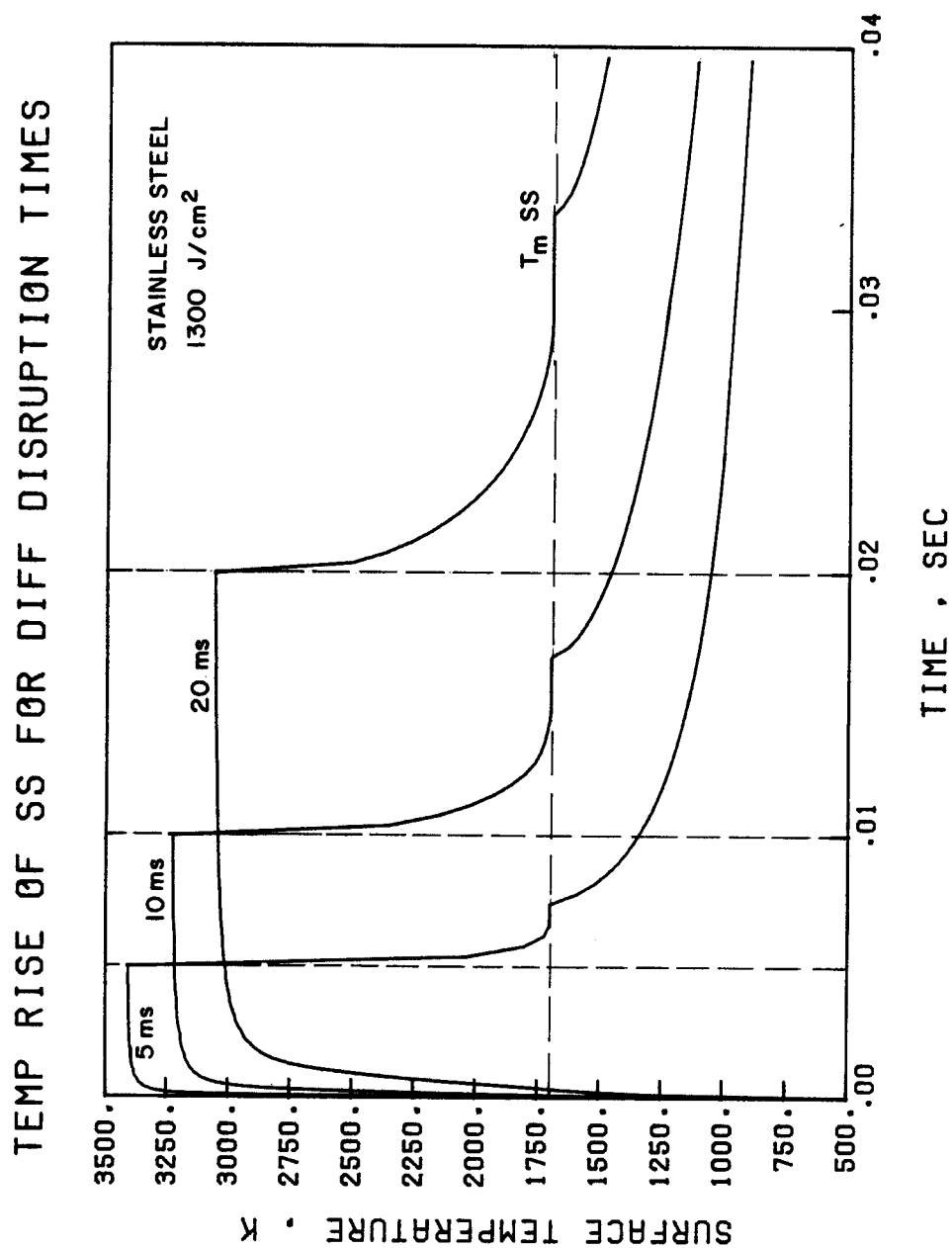


Fig. VII.B-9. Surface temperature rise of stainless steel for energy density of 1300 J/cm² and different disruption times (no vapor shielding).

surface temperature is higher and the rise in temperature is also higher. It can also be seen from Fig. VII.B-8 that the surface melt duration is a little shorter than the one shown in Fig. VII.B-7 for the cases of 5 and 10 ms disruption and longer for the 20 ms case. The reason for this behavior will be explained later. Figure VII.B-9 shows the surface temperature for input energy density of 1300 J/cm^2 . Again the surface temperature is higher and stays that way for longer duration and the slope of temperature rise is steeper than the other two cases of lower input energies. This will cause the evaporation to be higher as it will be shown later.

Comparing Figs. VII.B-7, VII.B-8, and VII.B-9 for the 20 ms disruption time it can be seen that the surface melt duration is the longest for input energy densities around 650 J/cm^2 . This can be explained as at high energies (1300 J/cm^2) a considerable amount of this energy will be used into vaporization, leaving a lower portion of the energy for melting the material and at lower energies (325 J/cm^2) although the temperature is above the melting temperature it is not high enough to cause more melting of the bulk material and the conduction cools the temperature faster. Longer surface melt duration usually means larger melt layer thickness. This fact can be seen from Fig. VII.B-10 where the maximum melting thickness is calculated for different disruption times as a function of input energy densities for stainless steel. From this figure the maximum melting thickness (for energy densities greater than 300 J/cm^2) is larger for longer disruption times (20 ms). This can be explained easily from

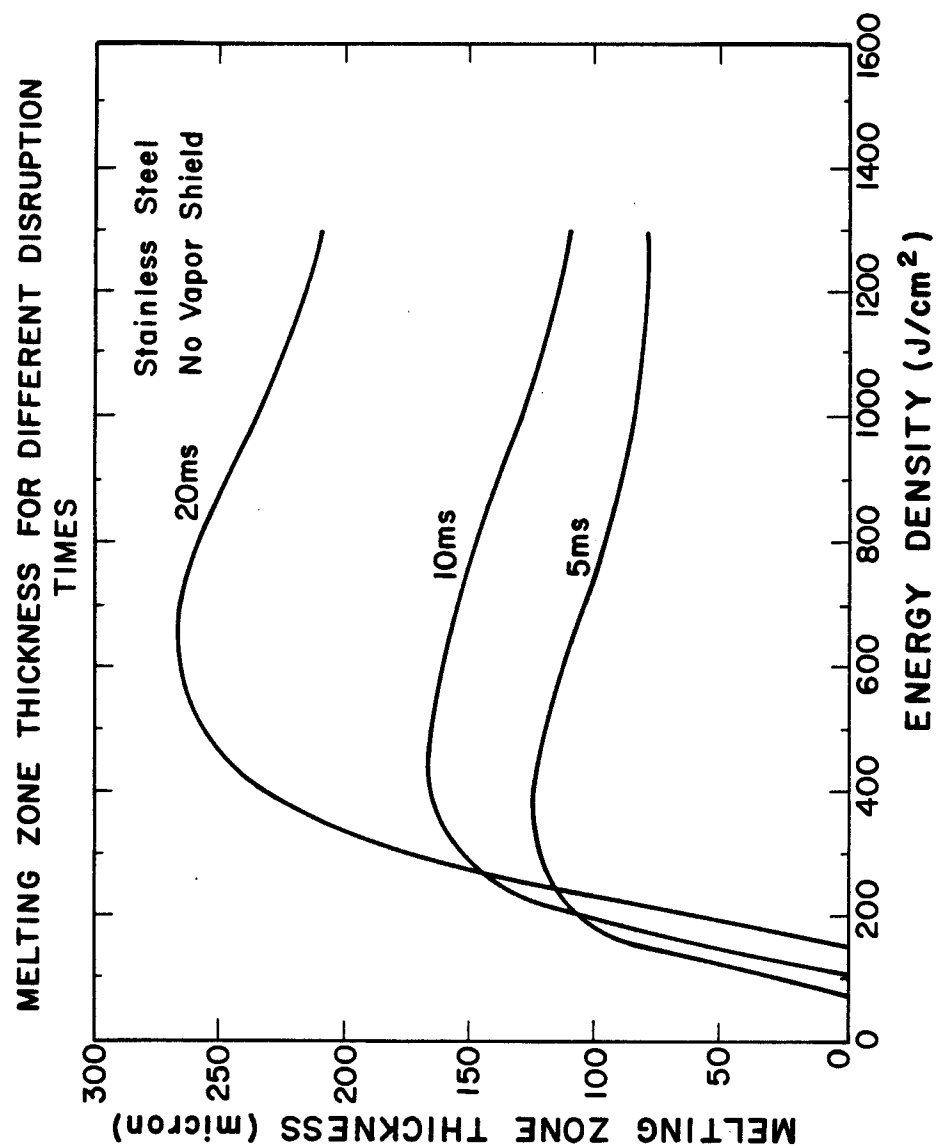


Fig. VII.B-10. Stainless steel melting zone thickness with no vapor shield as a function of energy density.

the fact that depositing the same energy in shorter times there will not be enough time for the heat to be conducted away, and consequently the surface temperature will be higher. Higher surface temperatures lead to higher evaporation rate, consuming larger fraction of the deposited energy and leaving less energy to be conducted into the material, hence less melting thickness. It can also be seen from Fig. VII.B-10 that melting requires a minimum or threshold energy density flux. This threshold depends both on the material and the rate of energy deposition. With increasing energy density, the melt layer thickness rises rapidly, reaches a maximum, and then declines somewhat.

B.5.1.b. Molybdenum

The surface temperature of molybdenum (Mo) as a function of time for the same set of energy densities, i.e. 325, 650, and 1300 J/cm² is shown in Figs. VII.B-11, VII.B-12, and VII.B-13. These results are obtained with the thermophysical properties given in Refs. (4,5) and for an initial temperature of $T_0 = 573^\circ\text{K}$. Figure VII.B-11 shows that the surface temperature for disruption times of 20 and 10 ms is below the melting temperature ($T_m = 2890^\circ\text{K}$). In case of the 5 ms disruption time the surface temperature exceeds the melting temperature for a short time of the order of 2 ms. In case of SS, input energy of 325 J/cm² will melt the steel for duration times longer than 10 ms for any of the considered disruption times (see Fig. VII.B-7). For energy densities deposited of the order of 650 J/cm² the Mo will melt for any of the three disruption times studied.

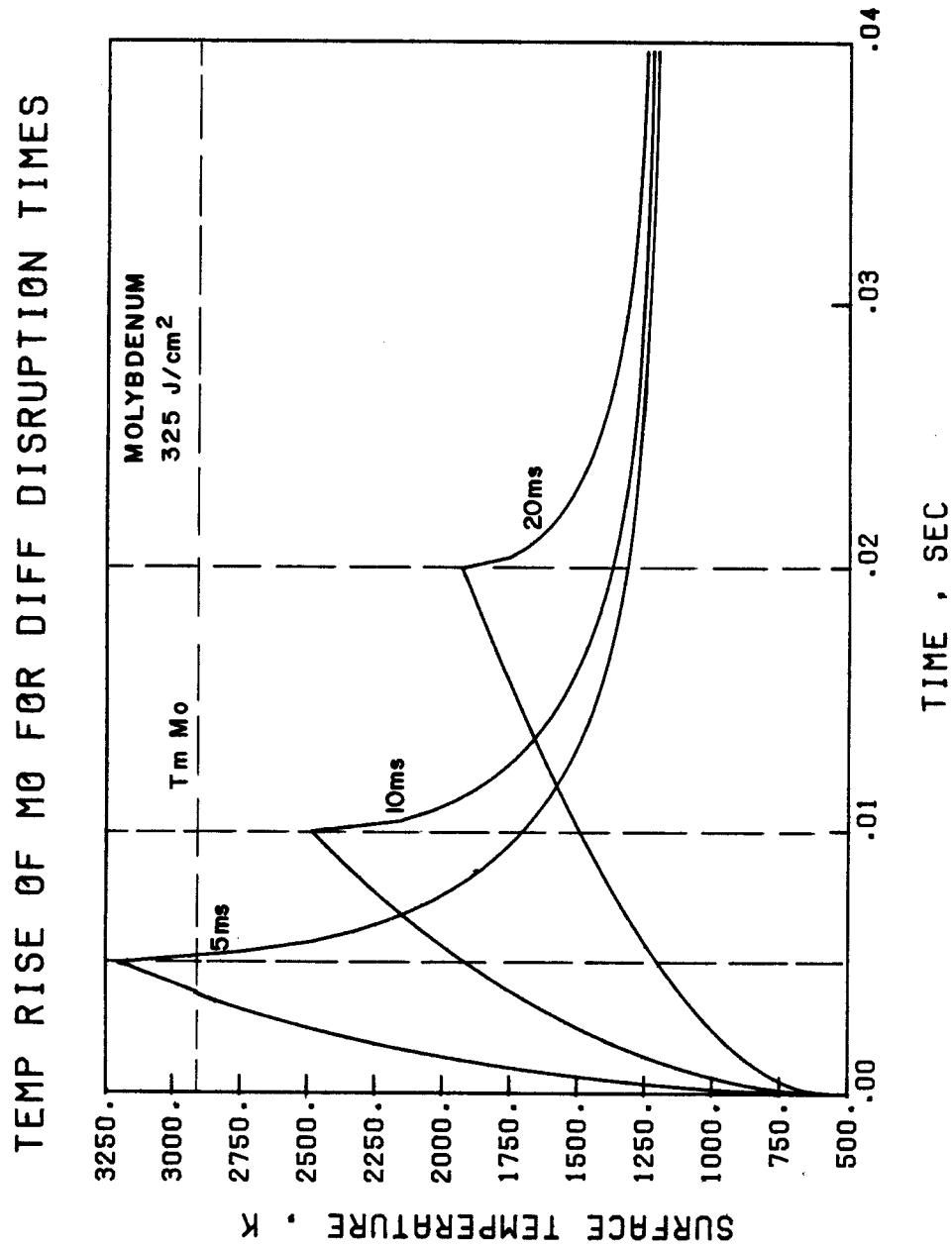


Fig. VII.B-11. Surface temperature rise of Mo for energy density of 325 J/cm² and different disruption times (no vapor shielding).

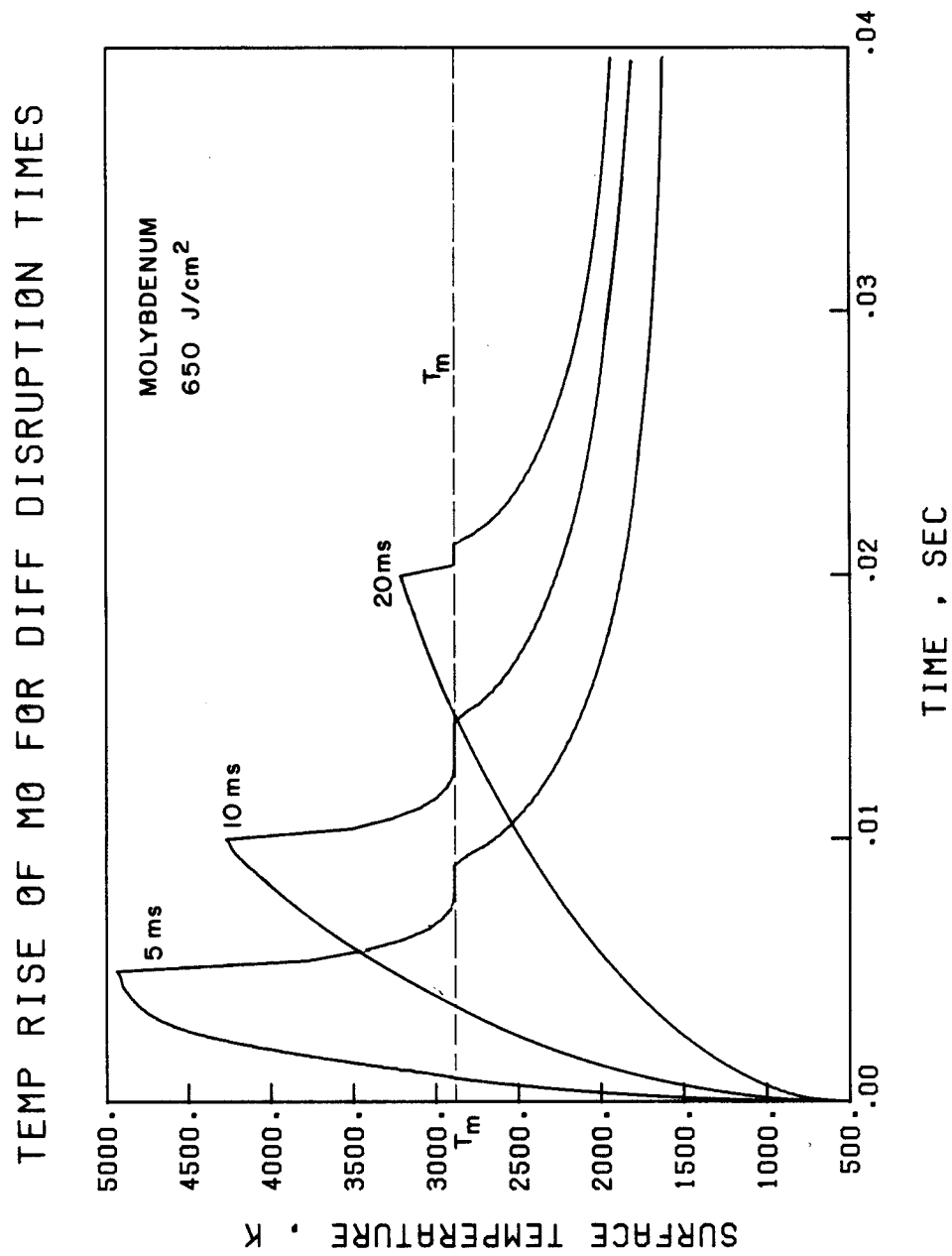


Fig. VII.B-12. Surface temperature rise of Mo for energy density of 650 J/cm² and different disruption times (no vapor shielding).

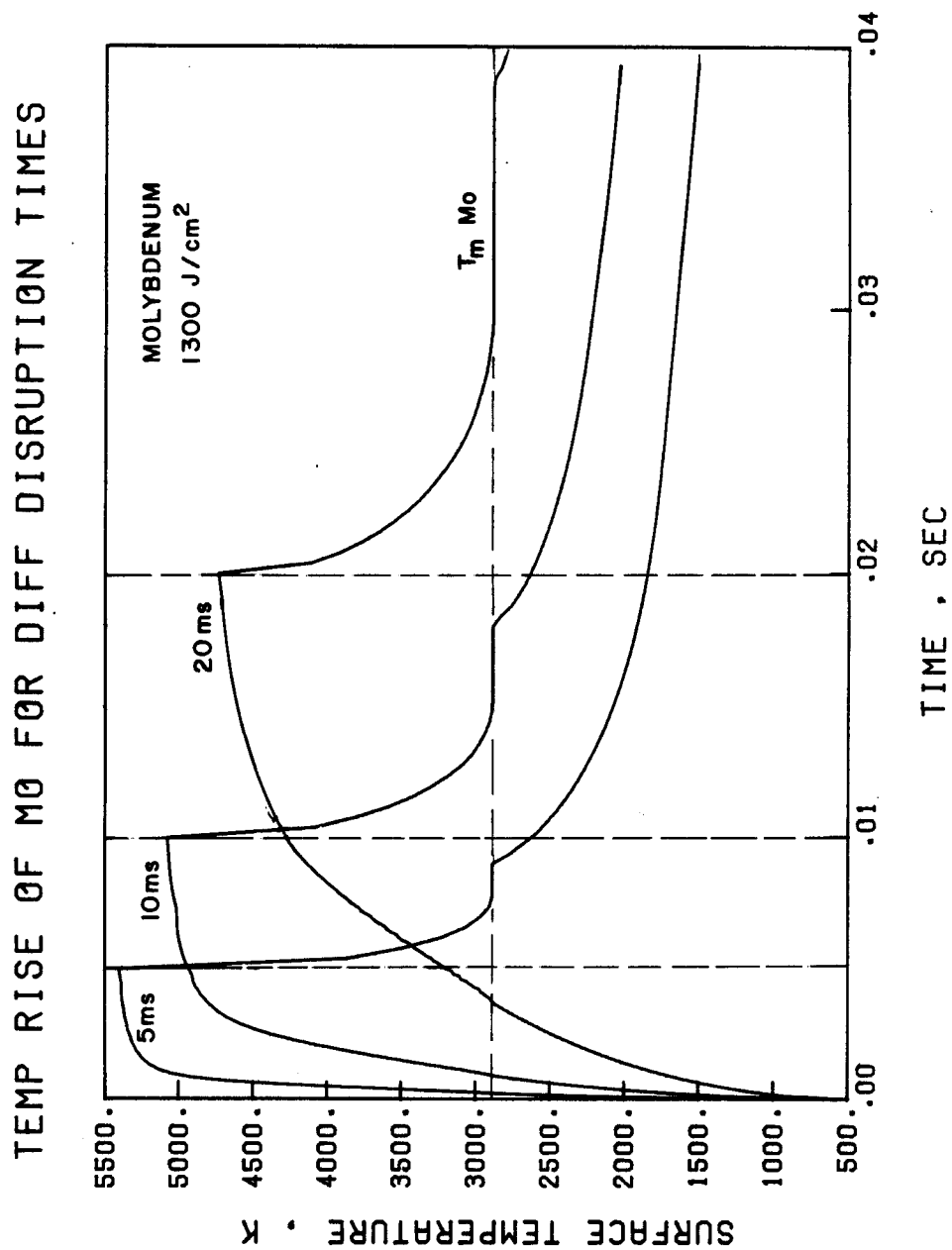


Fig. VII.B-13. Surface temperature rise of Mo for energy density of 1300 J/cm² and different disruption times (no vapor shielding).

Comparing Figs. VII.B-11 and VII.B-12, the change in the maximum temperatures from doubling the deposited energy is much larger than that change in the maximum temperature of SS (Figs. VII.B-7 and VII.B-8). Opposite to the steel case the surface melt duration is lowest for the 20 ms case in the 650 J/cm^2 . This means that the melting thickness of Mo at that energy is lower for 20 ms than the other two disruption times. For input energies of 1300 J/cm^2 , the slope of the temperature rise is steeper than that for the lower energy cases and the change in the maximum temperature between this case and the 650 J/cm^2 case is not as large as compared to the change in the temperature between the two lower energy cases. For this case (1300 J/cm^2) the surface melt duration is larger for the longer disruption time. The maximum melting thickness as a function of the deposited energy density is shown in Fig. VII.B-14. It can be seen, as in the case for steel (Fig. VII.B-10), that there is a threshold for each disruption time below which there is no melting. This threshold energy is much larger than that for the stainless steel case. At higher input energy densities than 1300 J/cm^2 a similar behavior of Fig. VII.B-14 to follow Fig. VII.B-10 is expected where the melting thickness will be decreasing as input energies increasing and most of the energy will be used in vaporizing more material, leaving less energy for melting and conduction.

B.5.1.c. Carbon

Graphite (C) has been considered as a suitable material for both limiters and first wall protection. In its latter capacity, it is

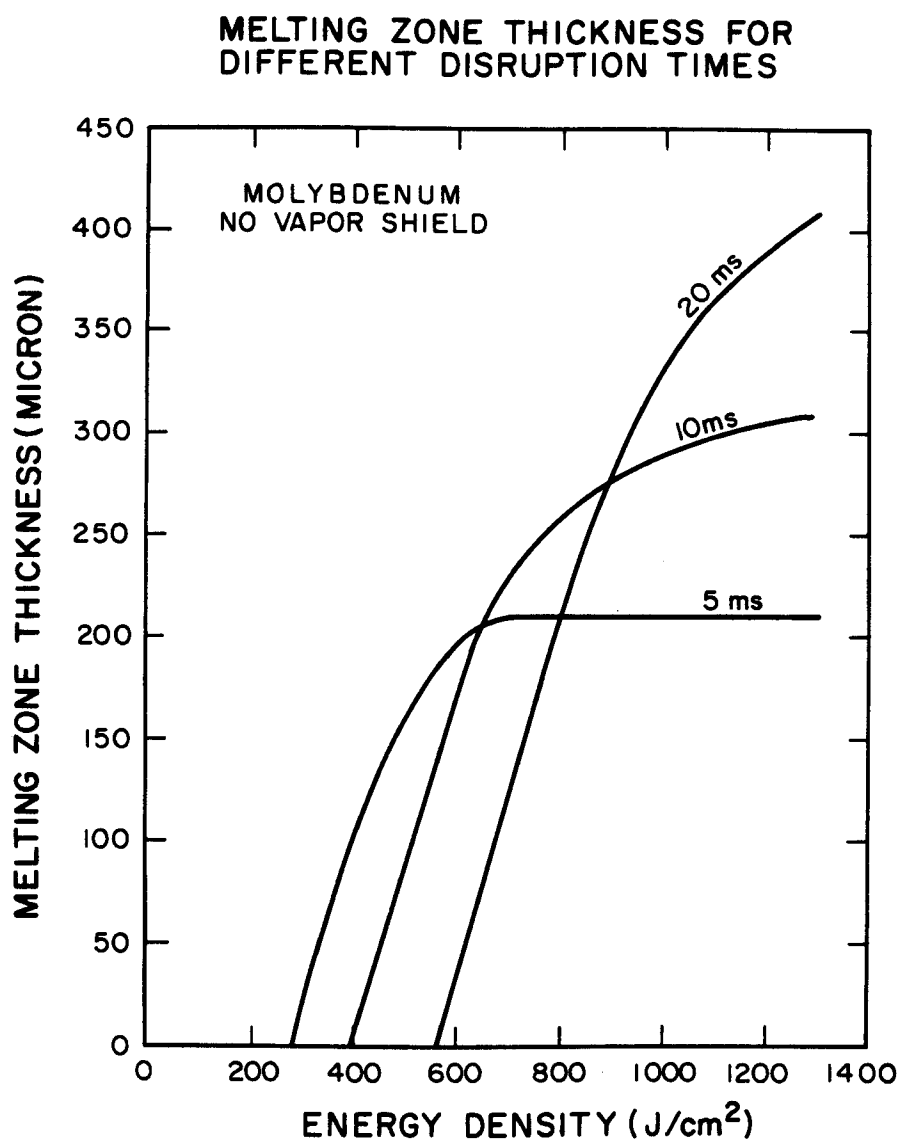


Fig. VII.B-14. Molybdenum melting zone thickness with no vapor shield as a function of energy density.

expected that the surface temperature is high before a plasma disruption. Hence, the calculations for graphite are carried out with $T_0 = 1500$ K; the thermophysical properties are those given in Ref.

(6). The carbon surface temperature for the three input energy densities is shown in Figs. VII.B-15, VII.B-16, and VII.B-17. Carbon does not melt and at higher temperatures it sublimates. The change in the maximum temperature for the three input energy densities for each corresponding disruption time is small compared to that for Mo. But the slope of temperature rise is much steeper as the input energy becomes higher so that the temperature approaches almost a constant value during earlier times after the disruption starts.

B.5.2. Comparison of Surface Temperatures

In this section we present a graphic comparison between the three different materials for the same cases discussed above. Figure VII.B-18 shows the surface temperature rise for the three materials at energy density of 325 J/cm^2 and 20 ms disruption time. Mo has the lowest surface temperature and its maximum surface temperature is much lower than its melting point. Stainless steel surface melts for a duration of about 30 ms for the same conditions. Carbon has the highest surface temperature mainly because its initial temperature is taken as $T_0 = 1500^\circ\text{K}$ compared to $T_0 = 573^\circ\text{K}$ for both Mo and SS. Figure VII.B-19 shows the same calculation but for a disruption time of 10 ms. In this case the surface melt duration for SS is about 20 ms. Whereas Mo still has the lowest surface temperature. For lower disruption time of 5 ms and the same input energy of 325 J/cm^2 , the

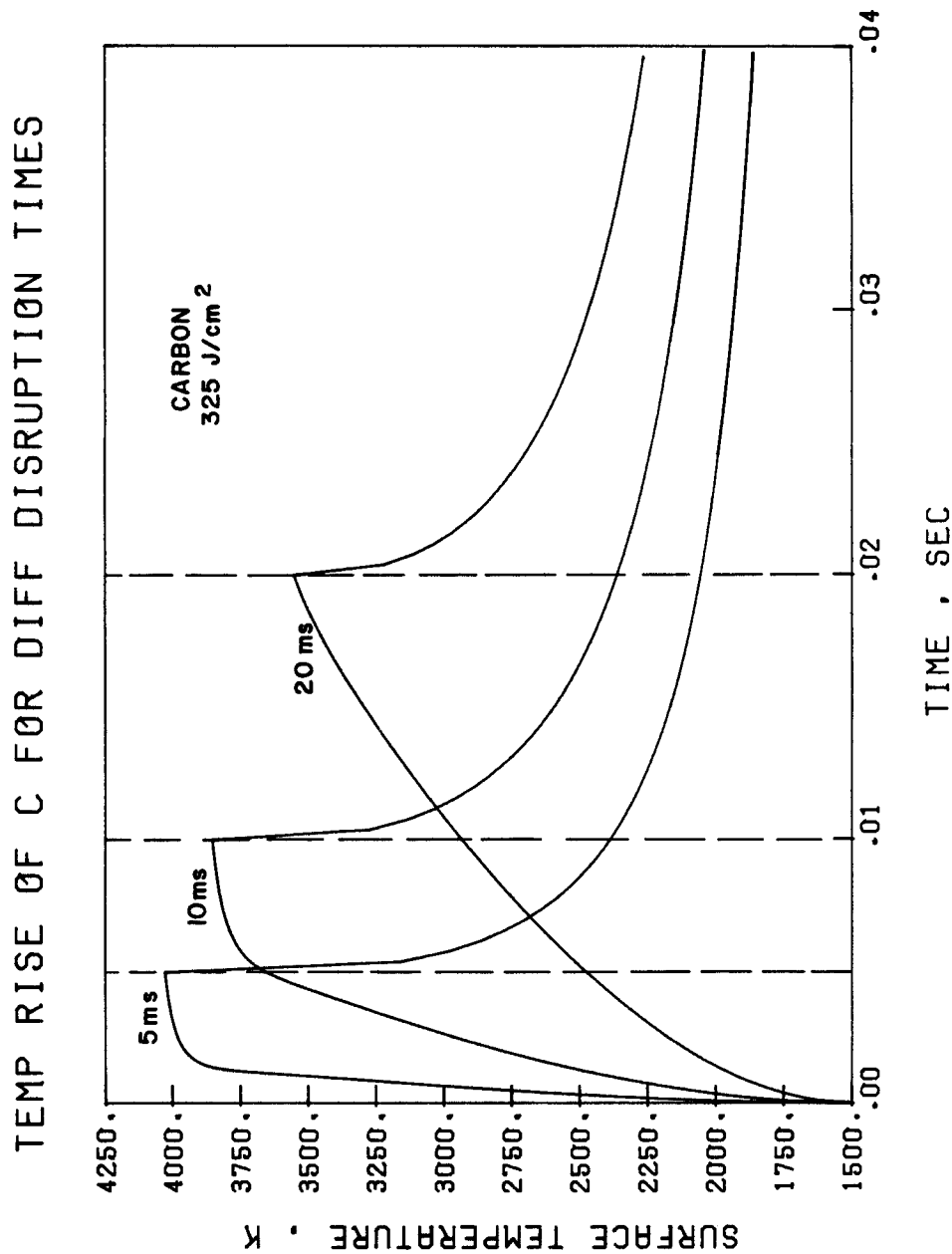


Fig. VII.B-15. Surface temperature rise of carbon for energy density of 325 J/cm² and different disruption times (no vapor shielding).

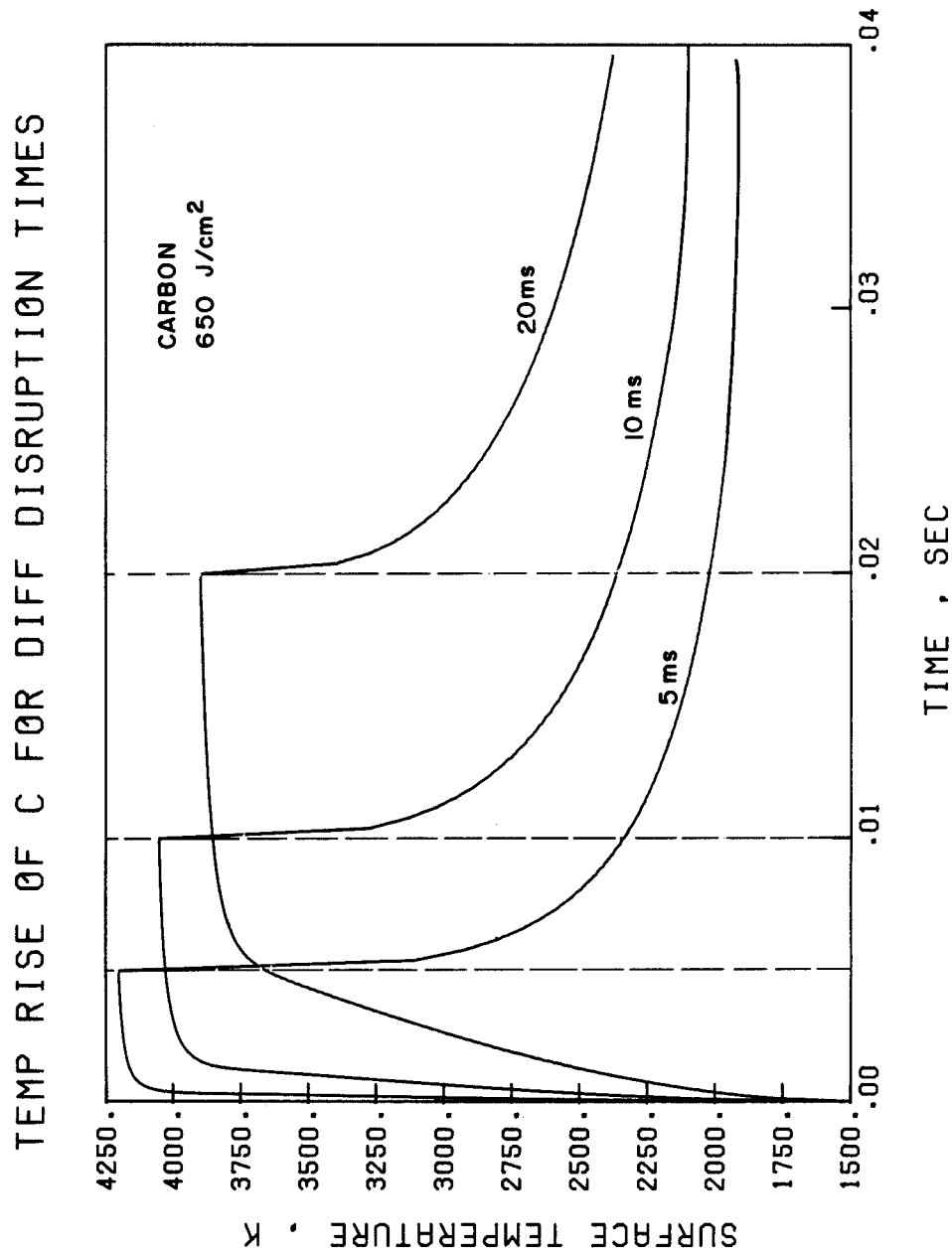


Fig. VII.B-16. Surface temperature rise of carbon for energy density of 650 J/cm² and different disruption times (no vapor shielding).

TEMP RISE OF C FOR DIFF DISRUPTION TIMES

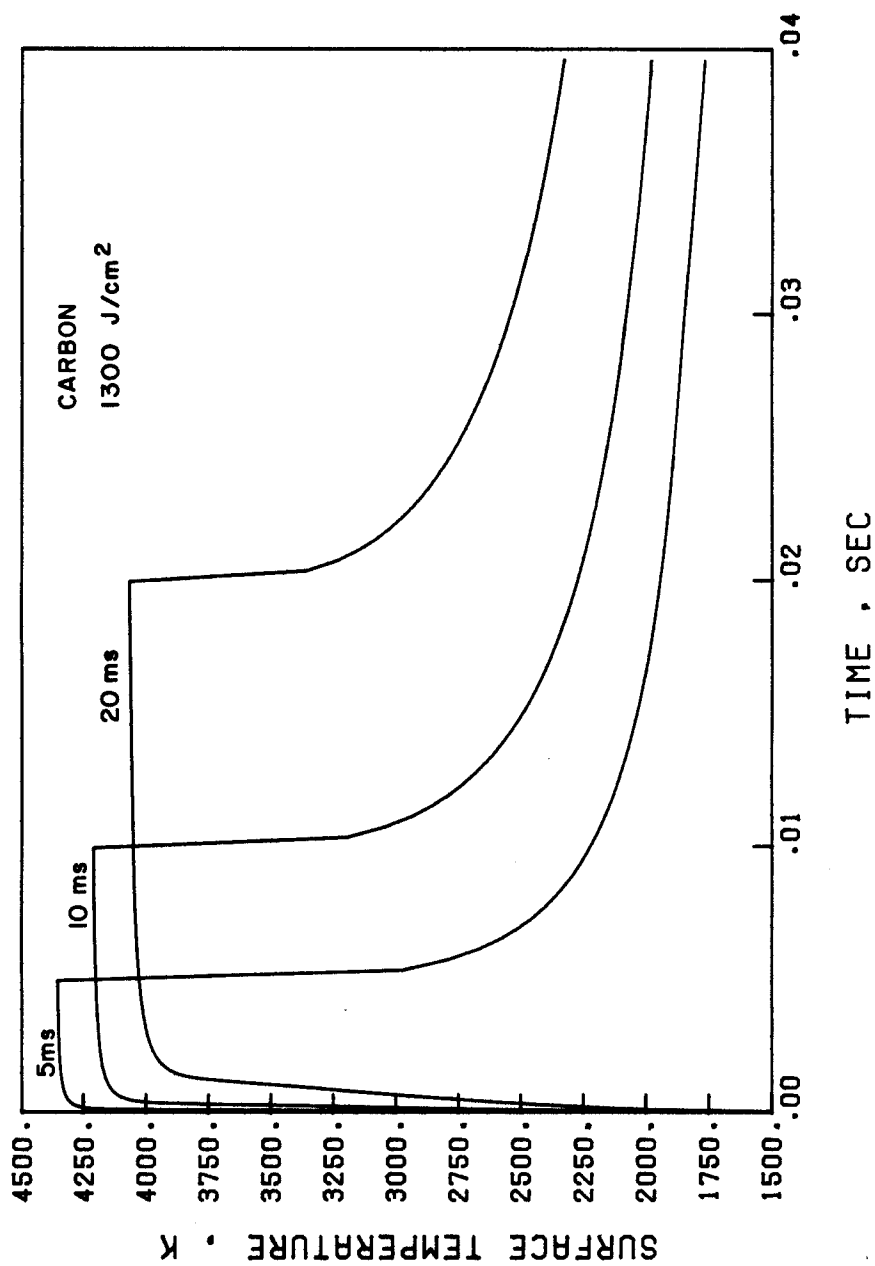


Fig. VII.B-17. Surface temperature rise of carbon for energy density of 1300 J/cm² and different disruption times (no vapor shielding).

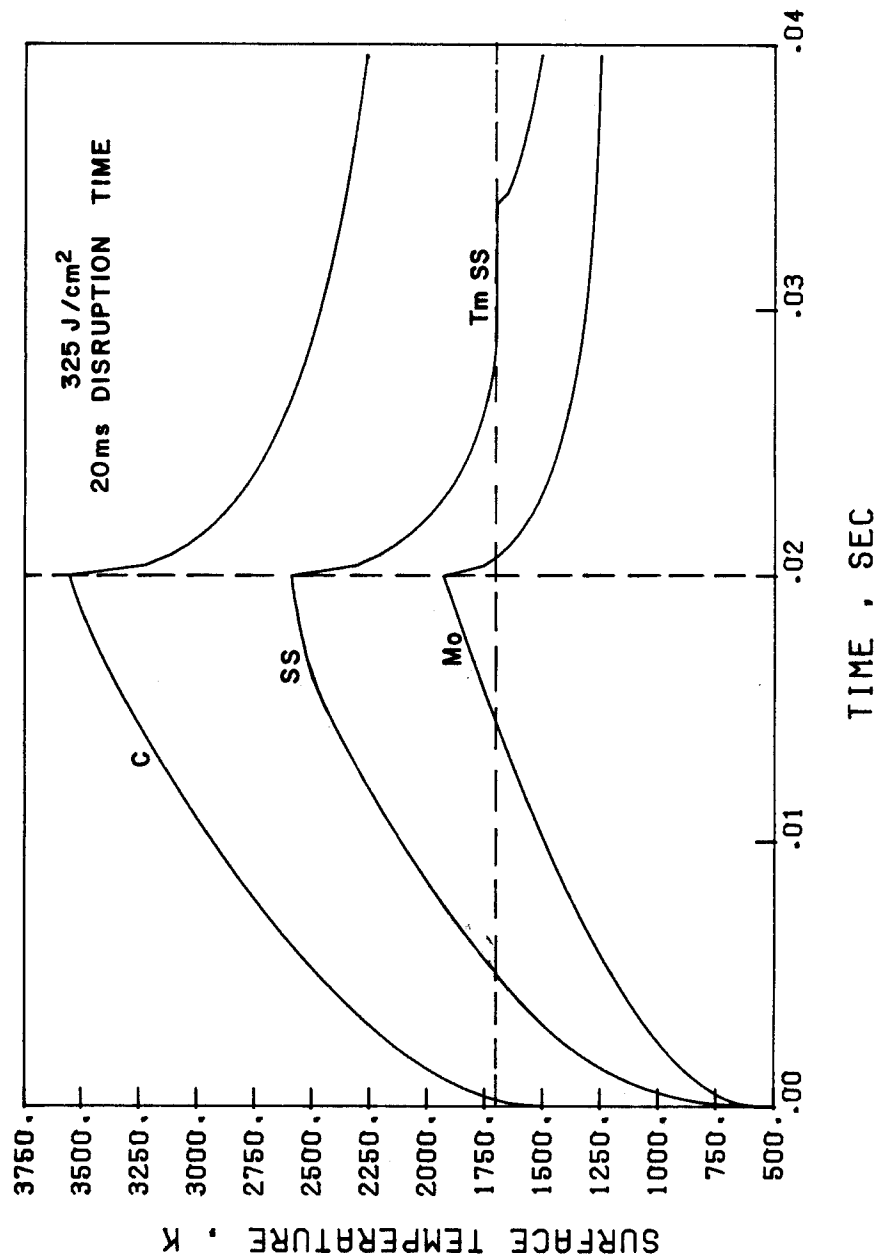


Fig. VII.B-18. Comparison of surface temperature rise for SS, Mo, and C for energy density of 325 J/cm² and 20 ms disruption time (no vapor shield).

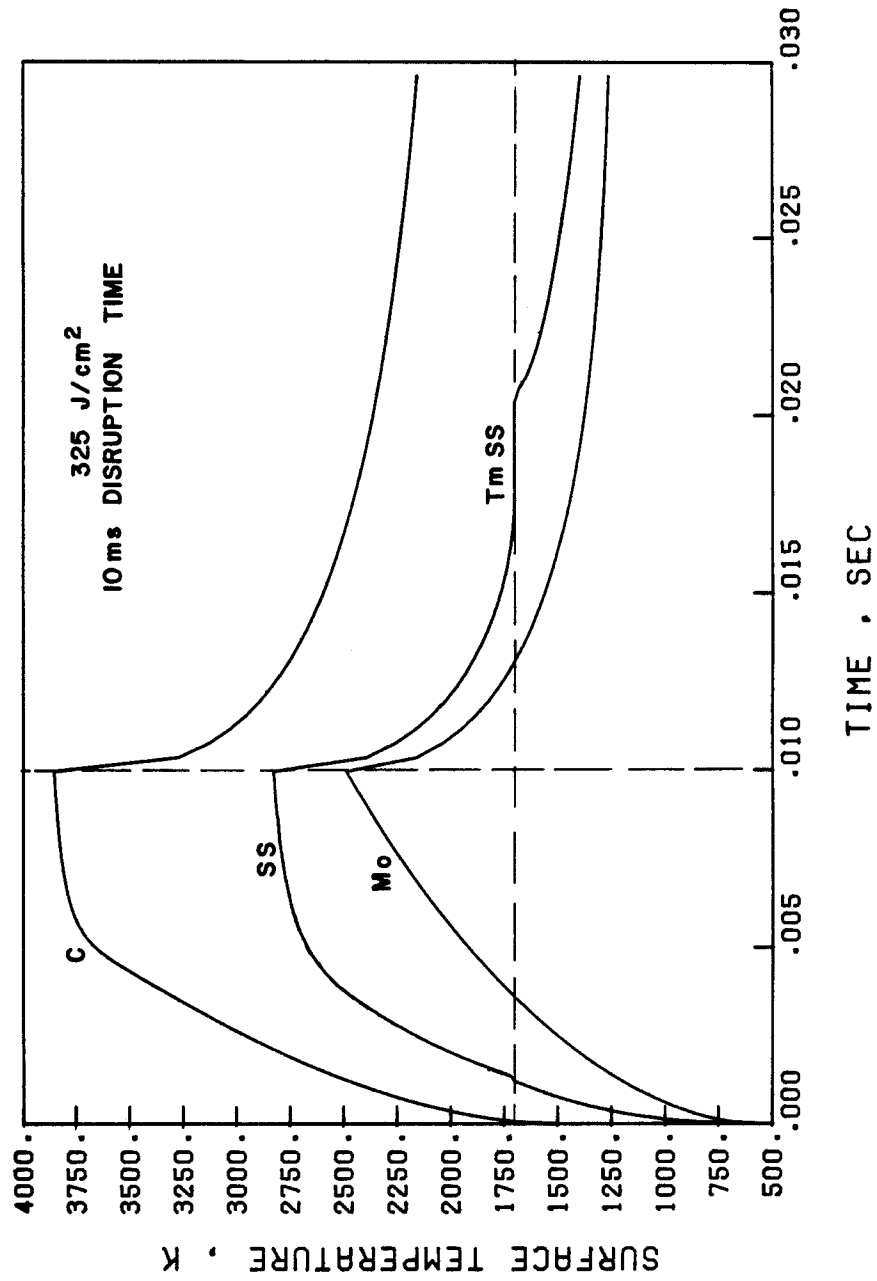


Fig. VII.B-19. Comparison of surface temperature rise for SS, Mo, and C for energy density of 325 J/cm² and 10 ms disruption time (no vapor shield).

surface temperature of Mo exceeds its melting point as shown in Fig. VII.B-20 and the maximum surface temperature is higher than that for SS in contrast to the other two cases of 10 and 20 ms disruption time. The surface melt duration is less than 2 ms for Mo and it is little over 10 ms for SS. Figures VII.B-21, VII.B-22, and VII.B-23 show the comparison between the three materials but with input energy densities of 650 J/cm^2 and for 20, 10 and 5 ms respectively. For the two cases of 10 and 5 ms disruption times the Mo has the highest surface temperature. The surface melting duration for Mo at 20 ms is much less than that for SS. But for lower disruption times the melt duration becomes closer to the SS case. Figures VII.B-24 through VII.B-26 show the same general behavior except that the Mo has the maximum surface temperature for all the three disruption times and the surface melting duration for Mo is longer than for SS for any of the disruption times considered.

B.5.3. Surface Velocity

The surface velocity, which is the velocity at which the front surface recedes away from the rest of the bulk due to evaporation, depends on the surface temperature as well as on material properties, such as vapor pressure. This velocity can be obtained as a result of the solution to the moving boundary problem presented in Chapter V. The integration of this velocity over the time gives the total amount of material evaporated.

The surface velocity for stainless steel for input energy densities 325, 650, and 1300 J/cm^2 is shown in Figs. VII.B-27, VII.B-28,

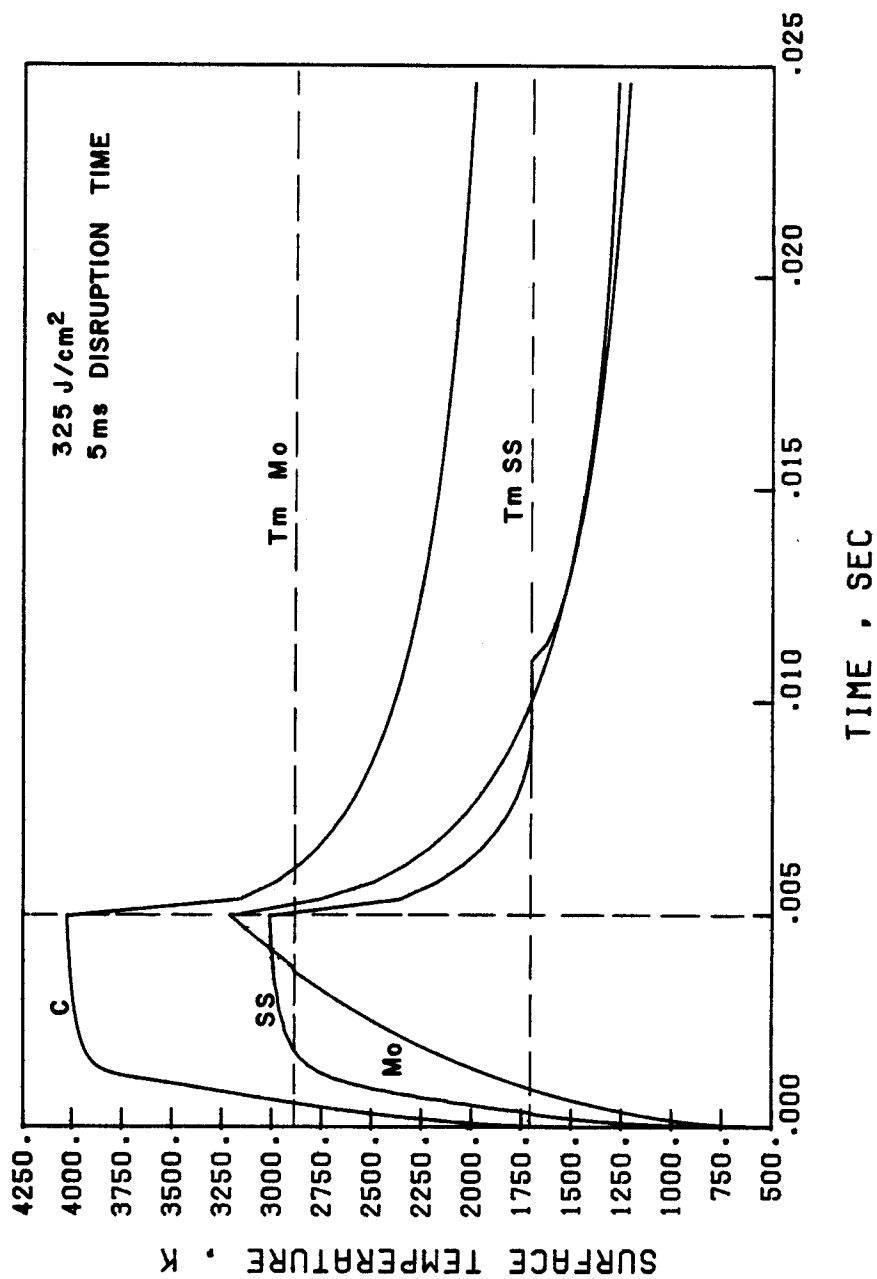


Fig. VII.B-20. Comparison of surface temperature rise for SS, Mo, and C for energy density of 325 J/cm² and 5 ms disruption time (no vapor shield).

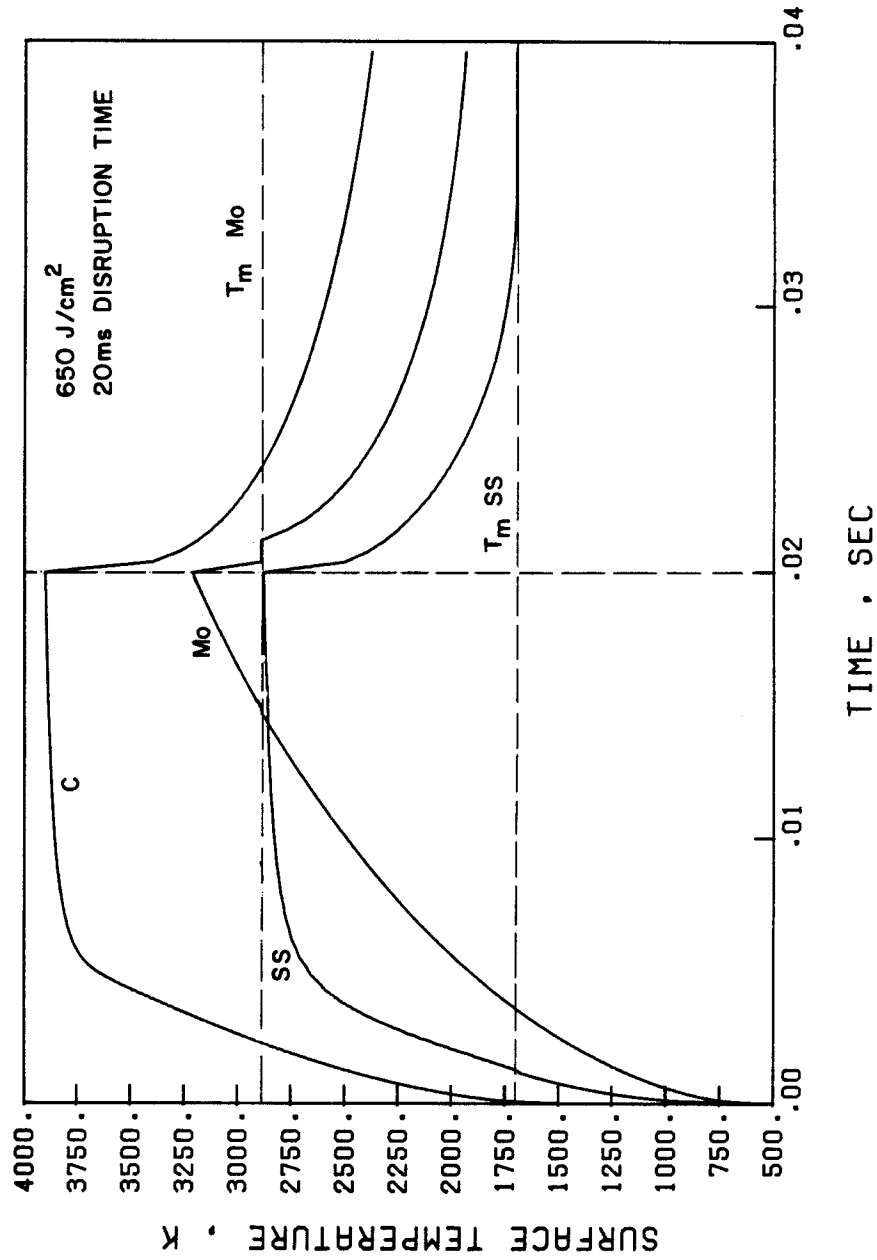


Fig. VII.B-21. Comparison of surface temperature rise for SS, Mo, and C for energy density of 650 J/cm² and 20 ms disruption time (no vapor shield).

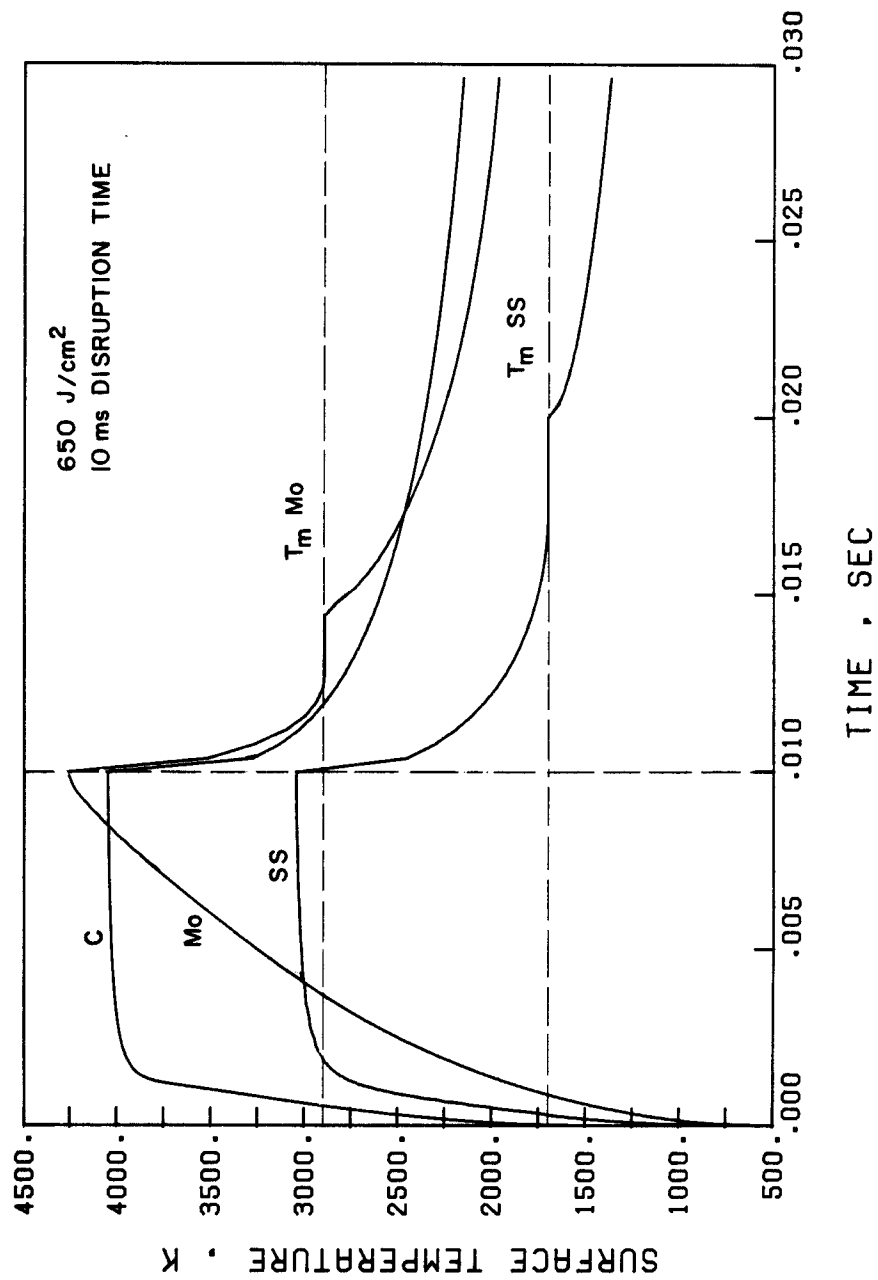


Fig. VII.B-22. Comparison of surface temperature rise for SS, Mo, and C for energy density of 650 J/cm² and 10 ms disruption time (no vapor shield).

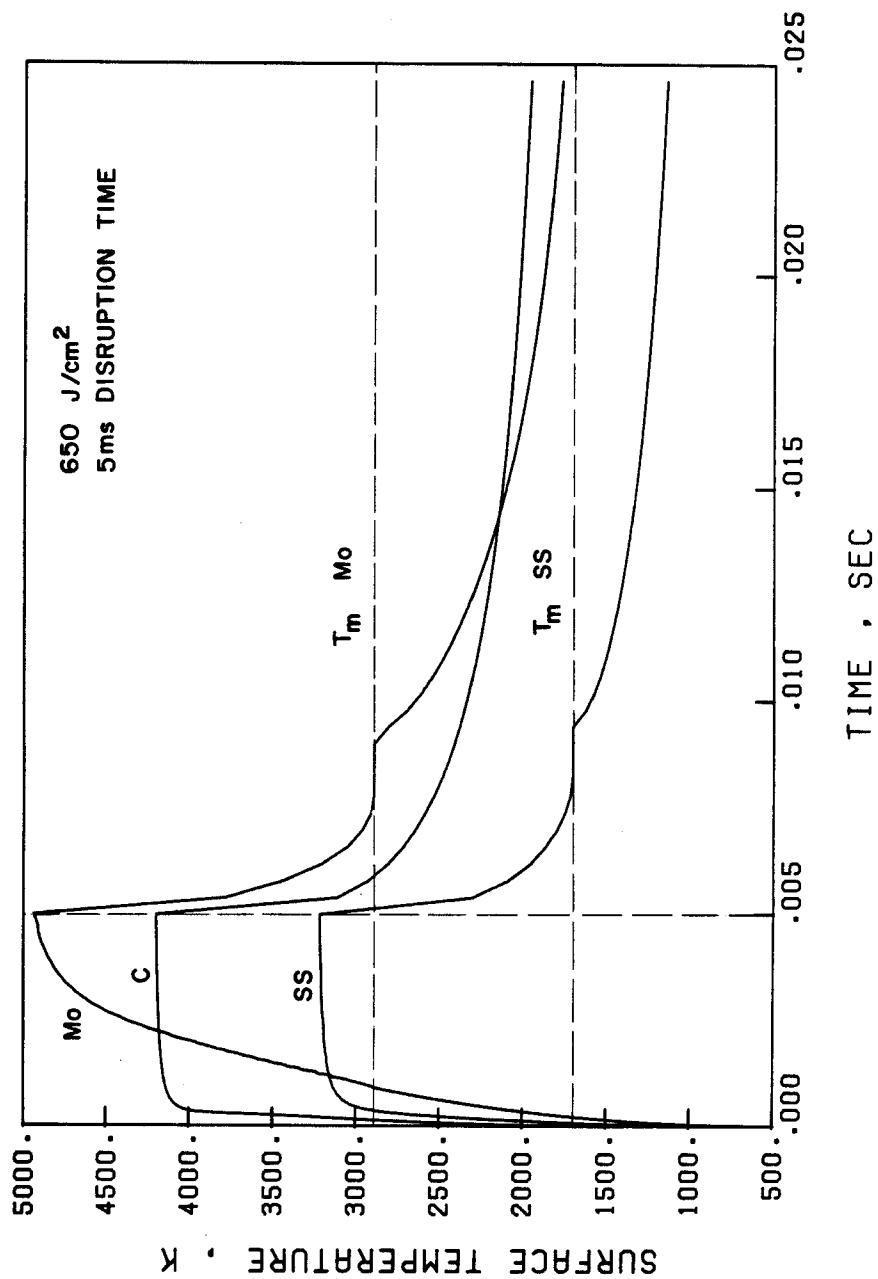


Fig. VII.B-23. Comparison of surface temperature rise for SS, Mo, and C for energy density of 650 J/cm² and 5 ms disruption time (no vapor shield).

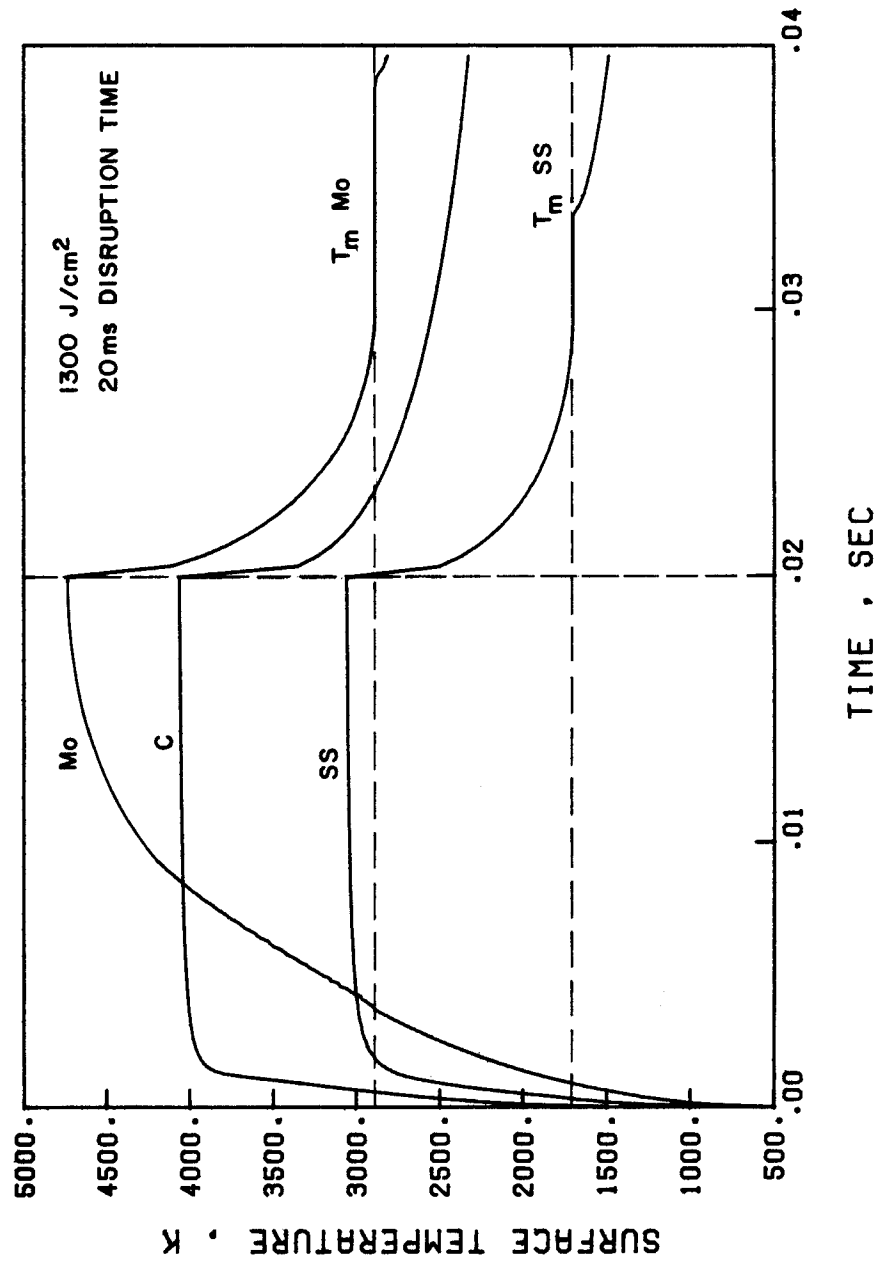


Fig. VII.B-24. Comparison of surface temperature rise for SS, Mo, and C for energy density of 1300 J/cm² and 20 ms disruption time (no vapor shield).

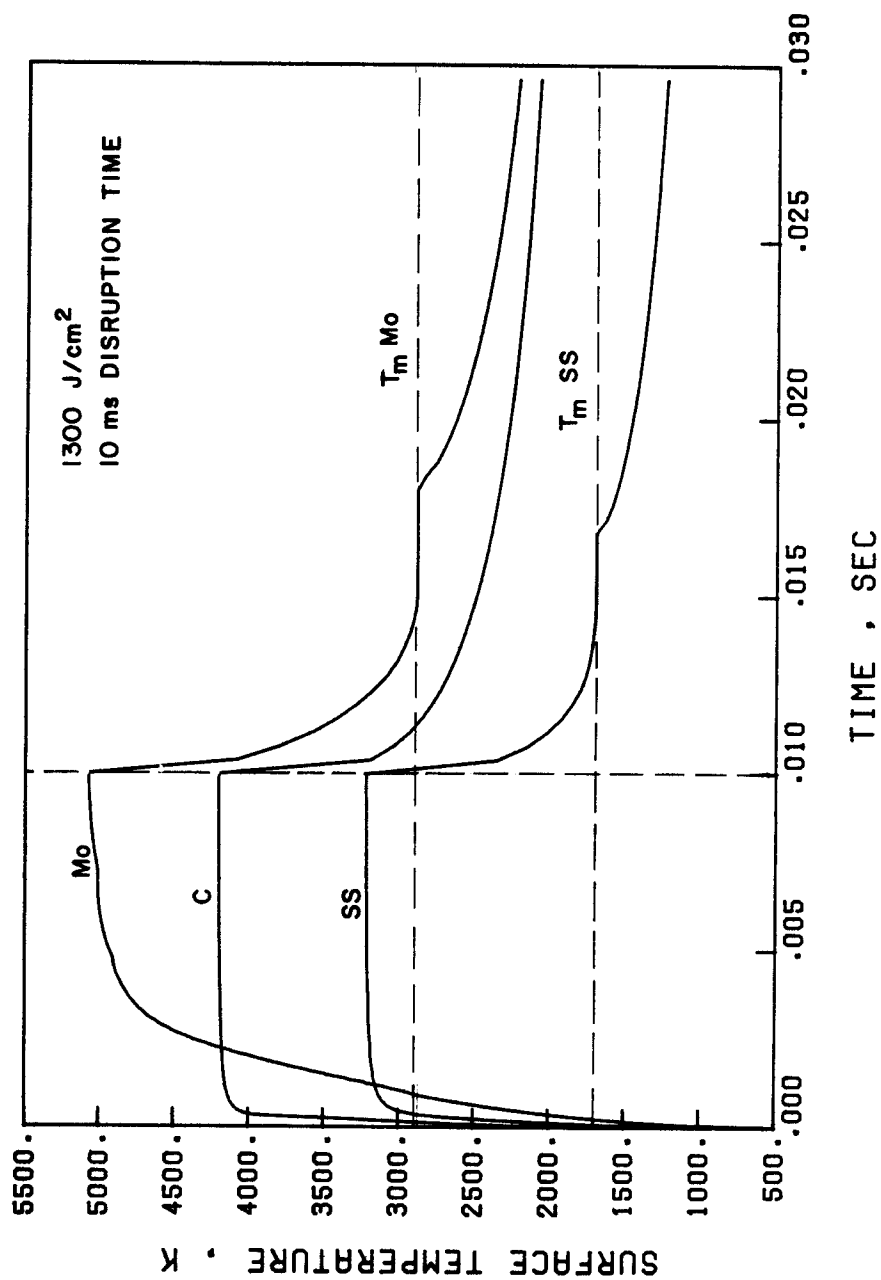


Fig. VII.B-25. Comparison of surface temperature rise for SS, Mo, and C for energy density of 1300 J/cm² and 10 ms disruption time (no vapor shield).

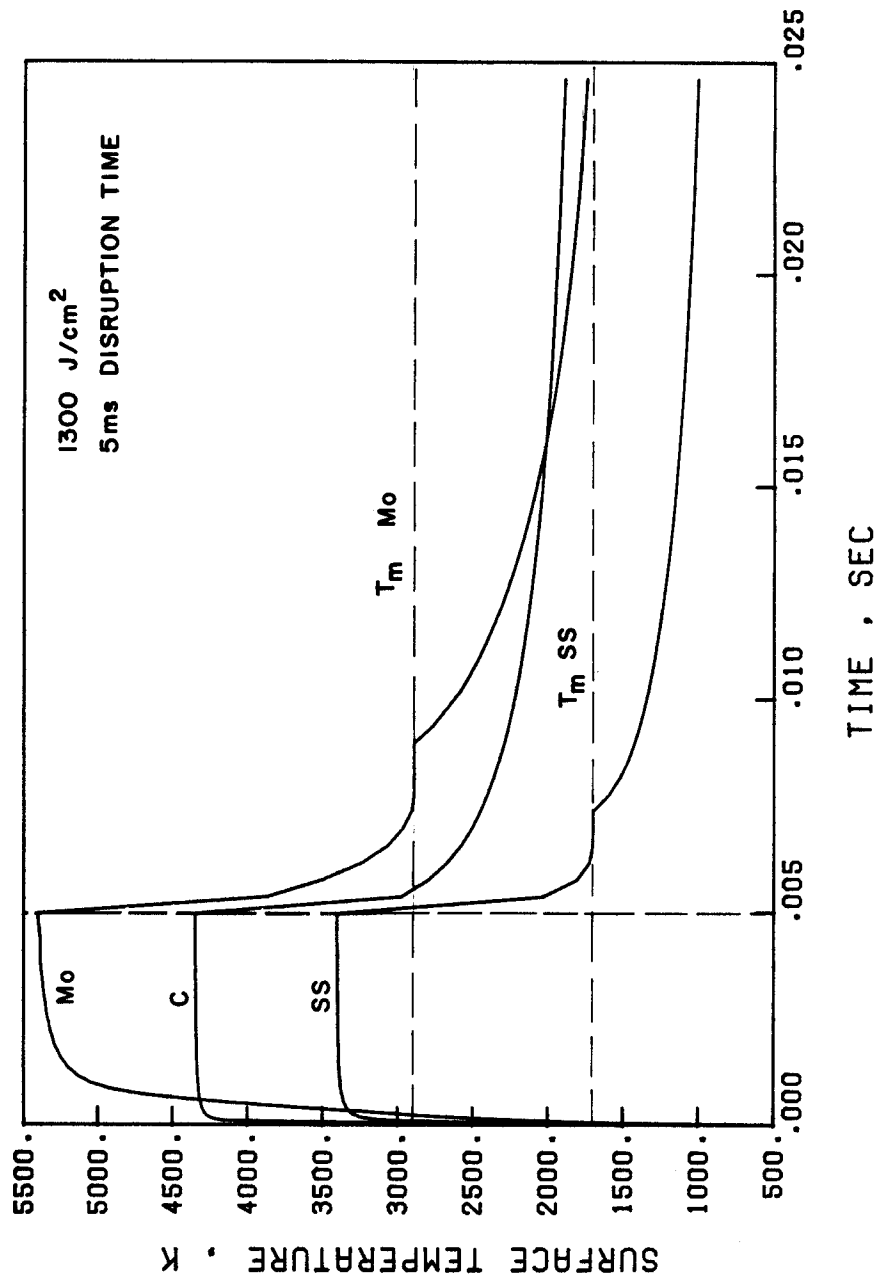


Fig. VII.B-26. Comparison of surface temperature rise for SS, Mo, and C for energy density of 1300 J/cm² and 5 ms disruption time (no vapor shield).

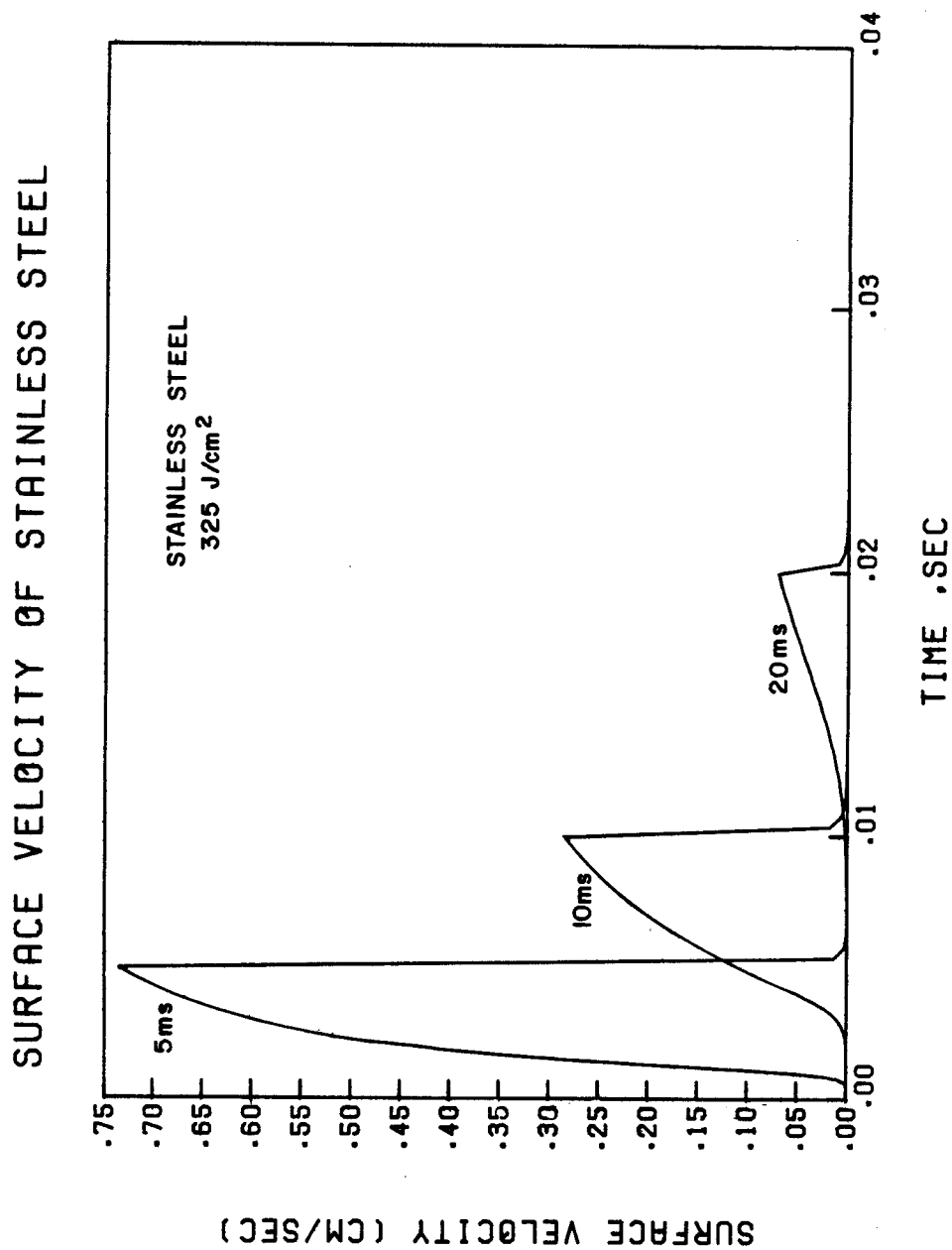


Fig. VII.B-27. Surface velocity of stainless steel for energy density of 325 J/cm² and different disruption times (no vapor shielding).

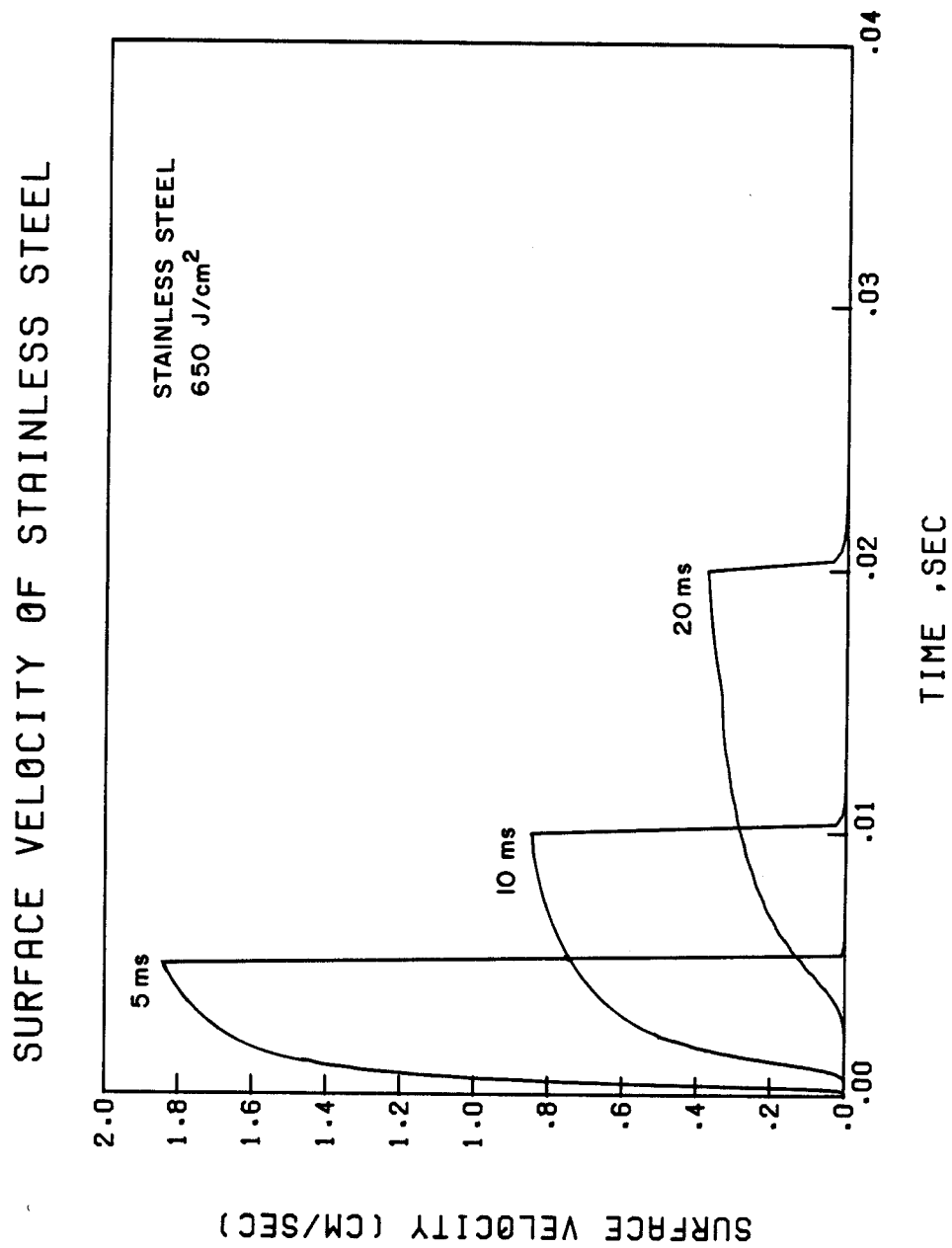


Fig. VII.B-28. Surface velocity of stainless steel for energy density of 650 J/cm² and different disruption times (no vapor shielding).

and VII.B-29 respectively. The general feature of these figures is that the lower the disruption time the higher the surface velocity and consequently, as will be shown later, the more material that is evaporated. Higher input energies not only largely increase the magnitude of the velocity but also the surface starts to recede earlier in time. This increases the vaporization enormously.

A comparison of the surface velocity for the three materials is shown in Fig. VII.B-30 for input energy density of 325 J/cm^2 in 20 ms. Stainless steel has higher surface velocity than carbon although carbon has higher surface temperature. This is mainly because carbon vapor pressure is lower than that for stainless steel. Molybdenum, for the same conditions, shows no receding velocity compared to stainless steel or carbon. This also means that there is no evaporation from Mo for 325 J/cm^2 deposited in 20 ms. In fact, Mo does not show any significant evaporation for this energy density at lower disruption times of 5 and 10 ms (Figs. VII.B-31, VII.B-32). At higher input energies of 650 J/cm^2 , Mo still does not show any significant surface velocity at 20 ms disruption time (Fig. VII.B-33). But for lower disruption times of 10 and 5 ms Mo shows small receding velocity compared to SS and C (Figs. VII.B-34, VII.B-35). This velocity becomes larger for lower disruption times. For input energy density of 1300 J/cm^2 and disruption time of 5 ms, Mo maximum surface velocity is larger than that for C but it is still lower than the SS velocity (Fig. VII.B-36).

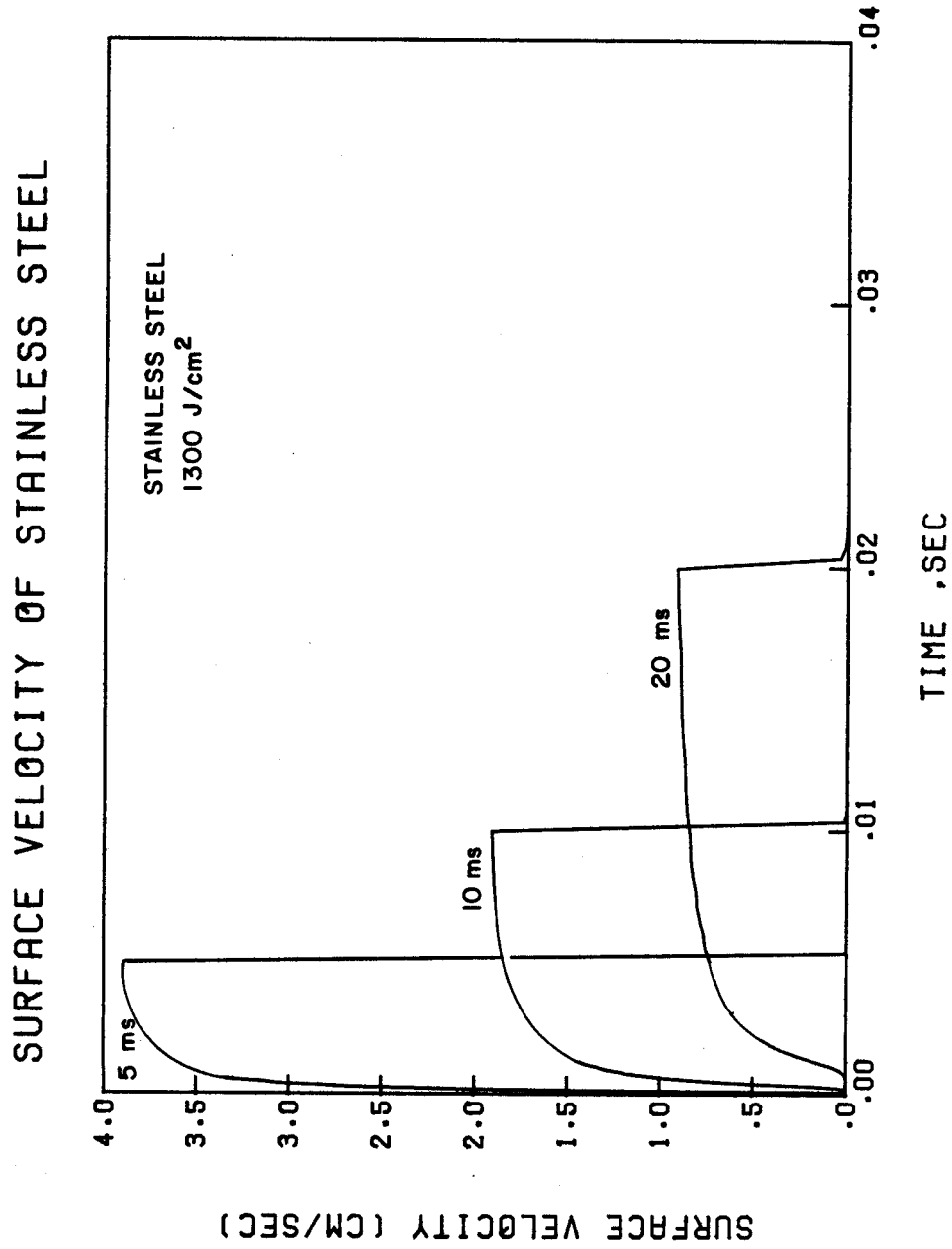


Fig. VII.B-29. Surface velocity of stainless steel for energy density of 1300 J/cm² and different disruption times (no vapor shielding).

SURFACE VELOCITY OF MO , C , SS

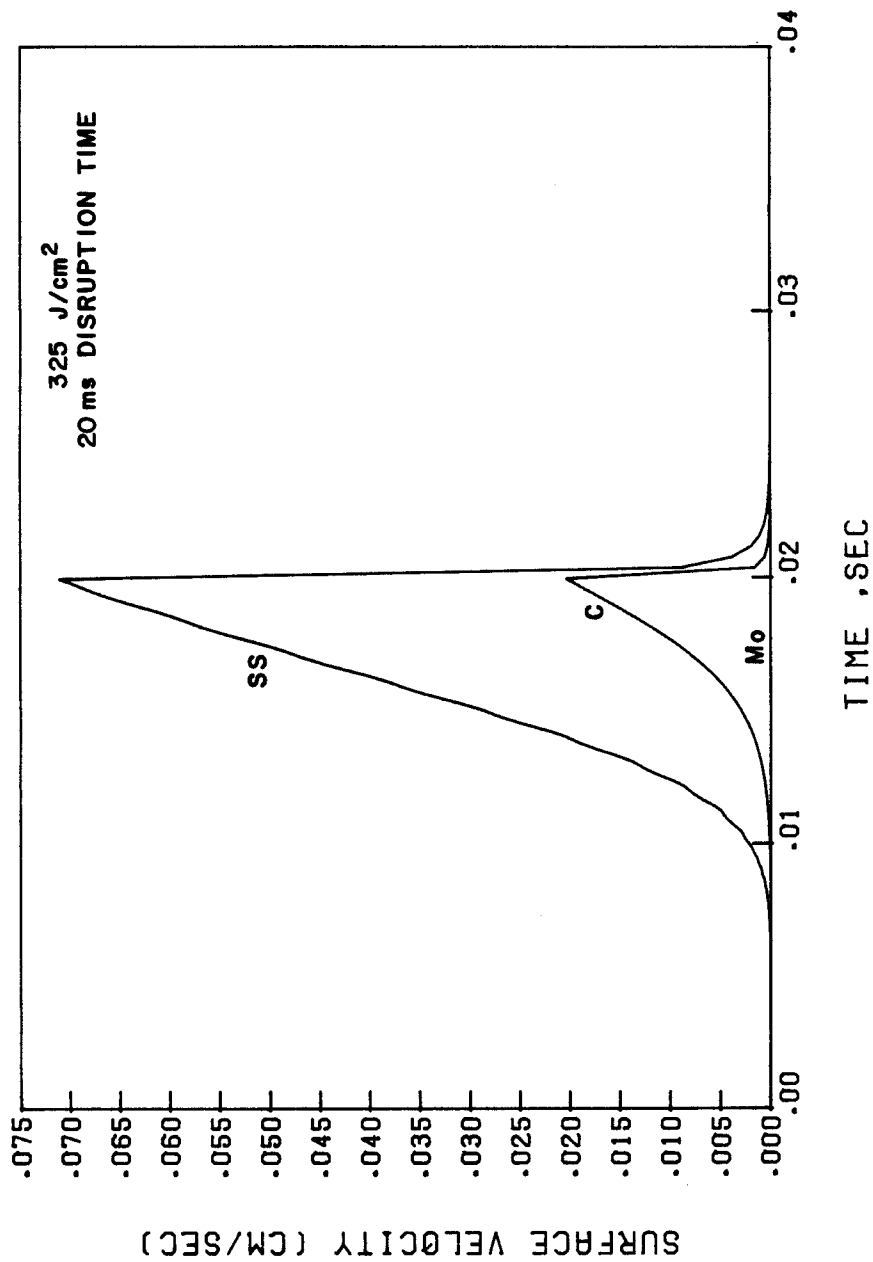


Fig. VII.B-30. Surface velocity of SS, Mo, and C for energy density of 325 J/cm² and 20 ms disruption time (no vapor shield).

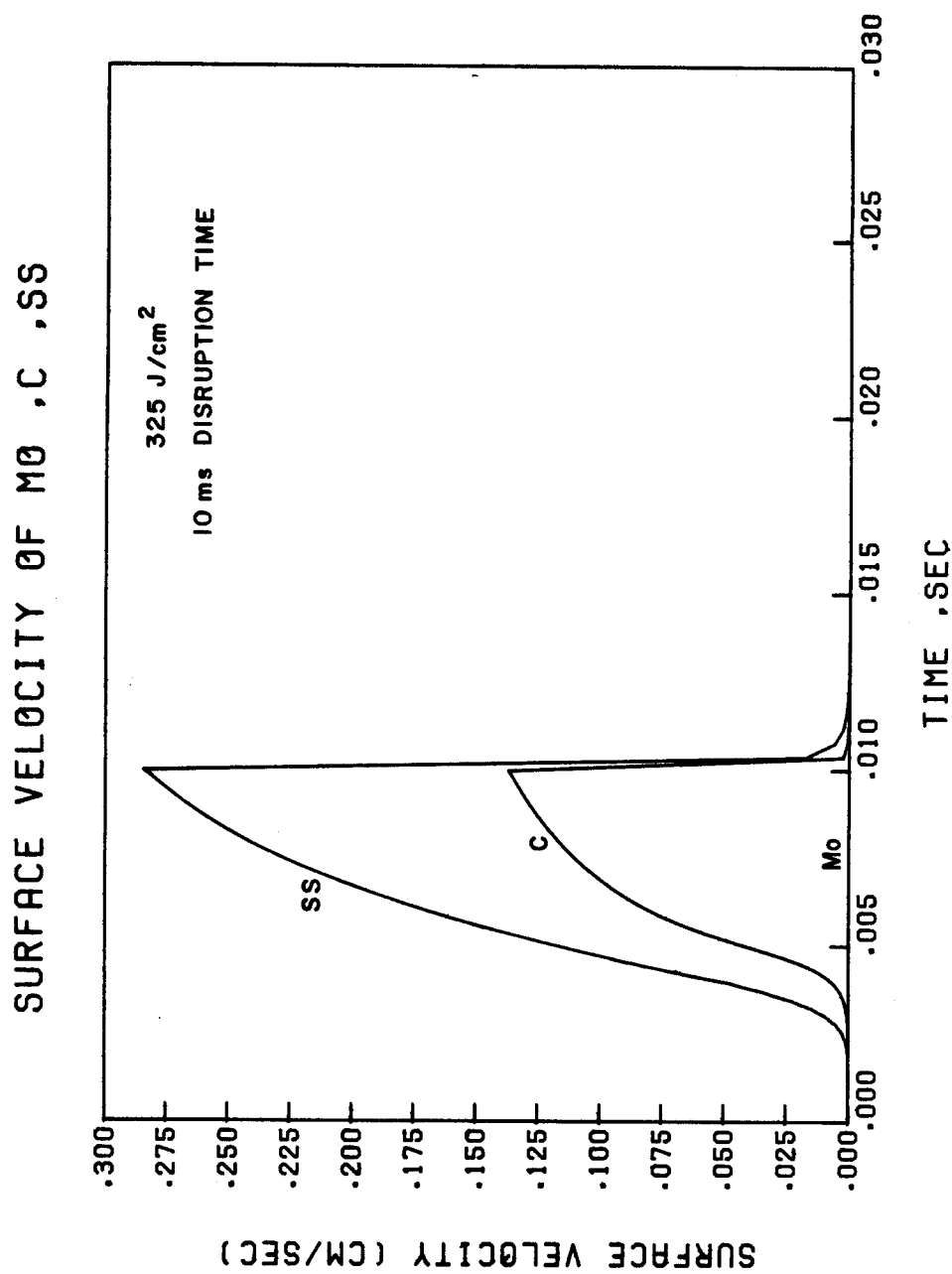


Fig. VII.B-31. Surface velocity of SS, Mo, and C for energy density of 325 J/cm² and 10 ms disruption time (no vapor shield).

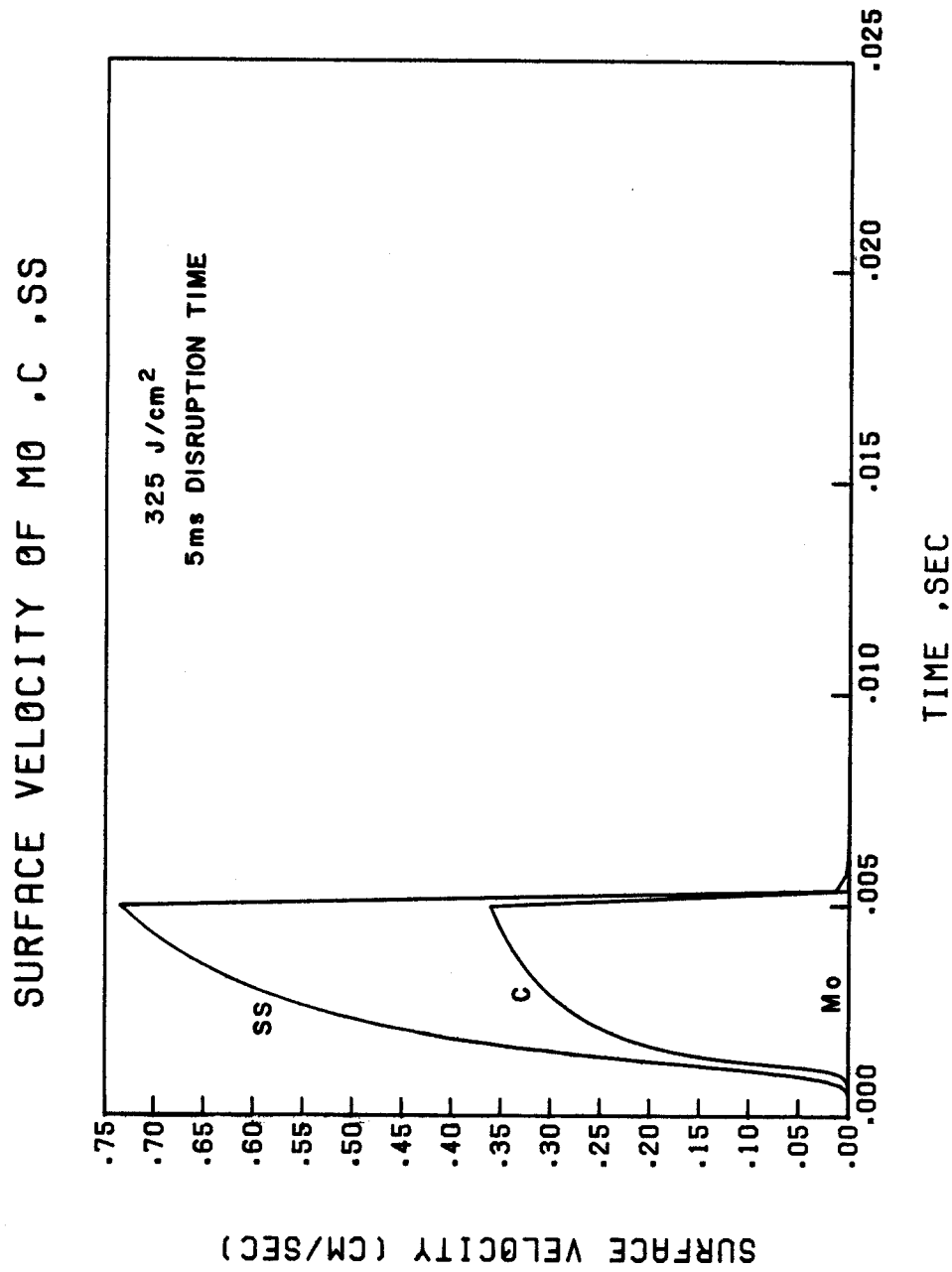


Fig. VII.B-32. Surface velocity of SS, Mo, and C for energy density of 325 J/cm² and 5 ms disruption time (no vapor shield).

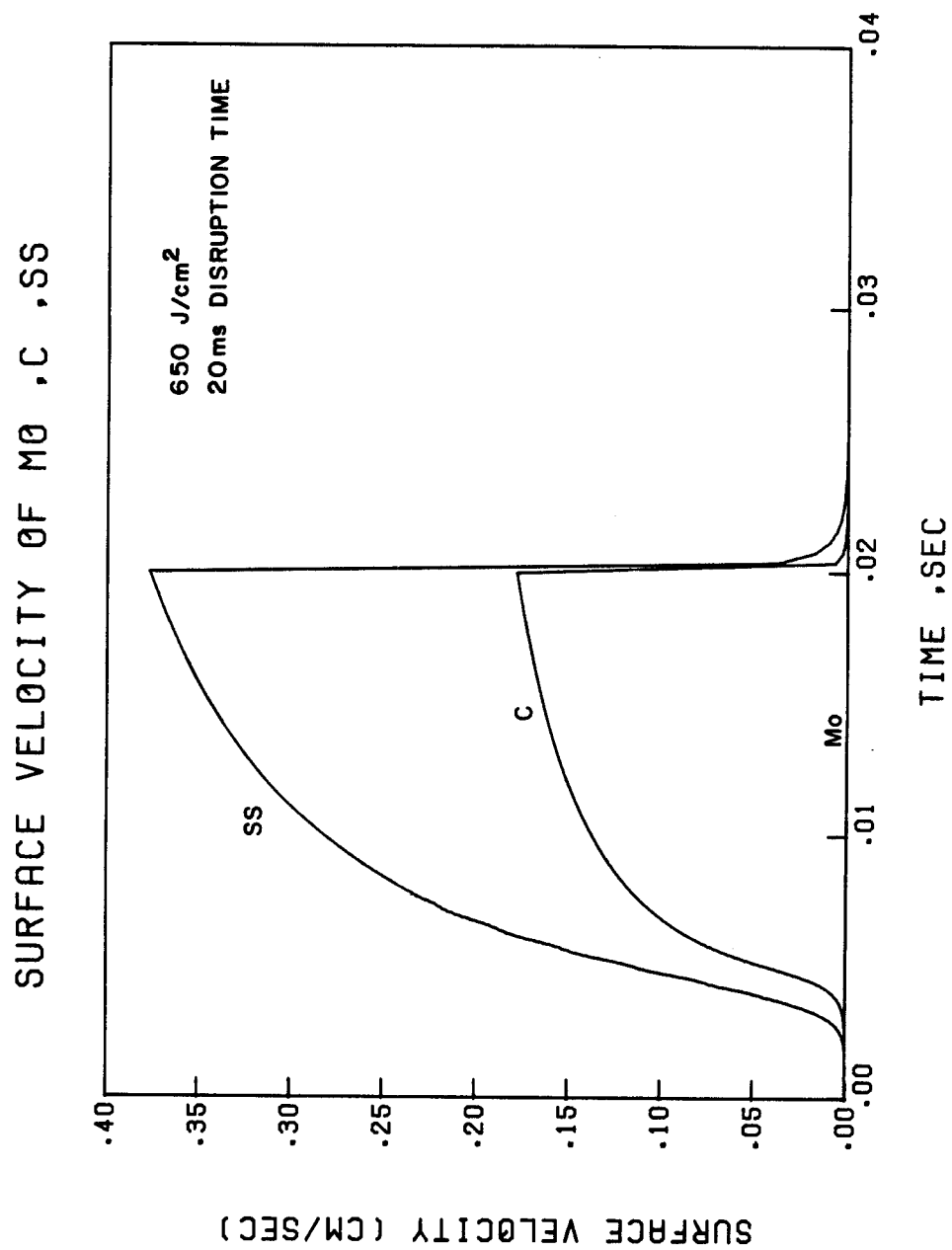


Fig. VII.B-33. Surface velocity of SS, Mo, and C for energy density of 650 J/cm² and 20 ms disruption time (no vapor shield).

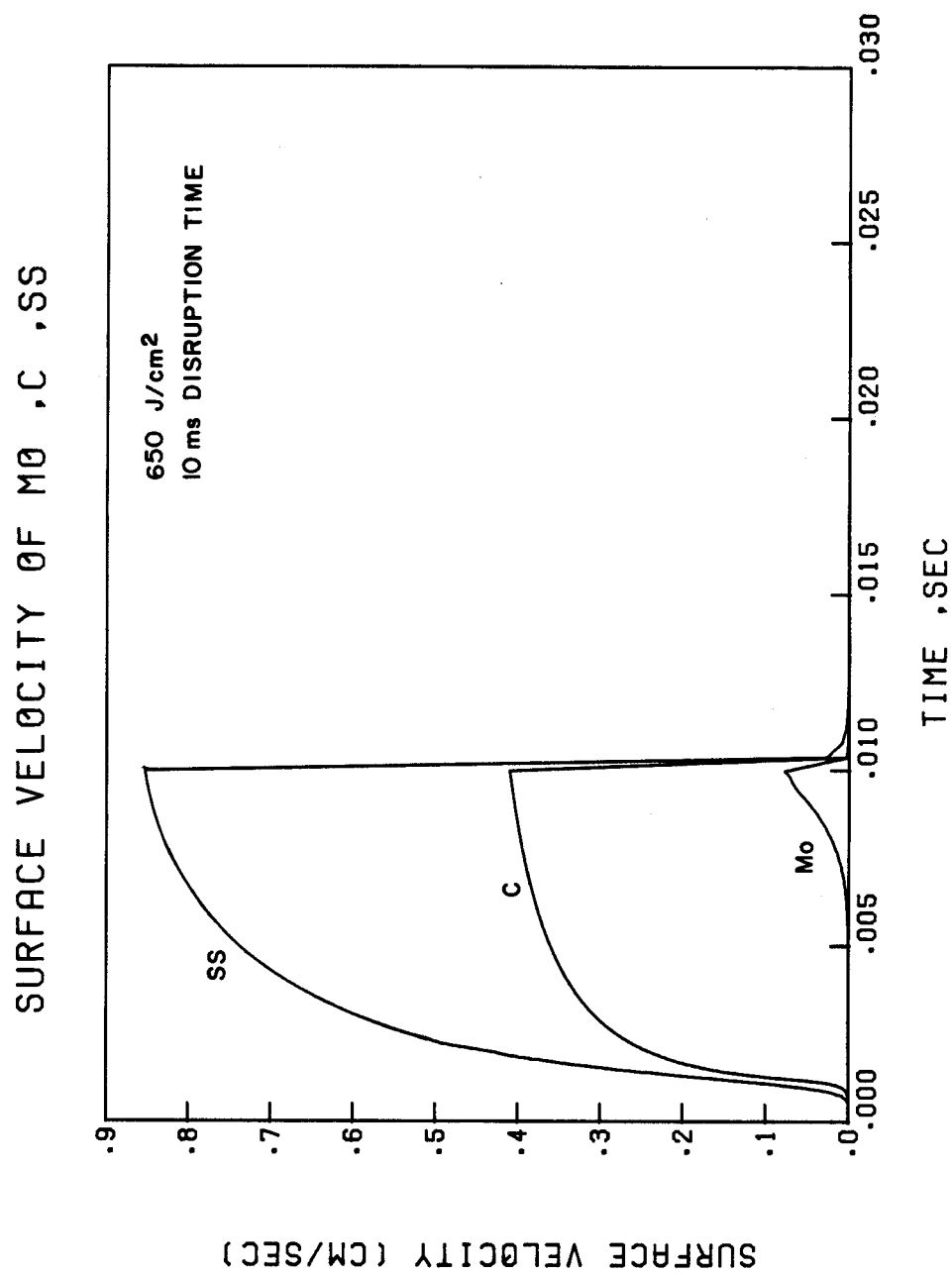


Fig. VII.B-34. Surface velocity of SS, Mo, and C for energy density of 650 J/cm² and 10 ms disruption time (no vapor shield).

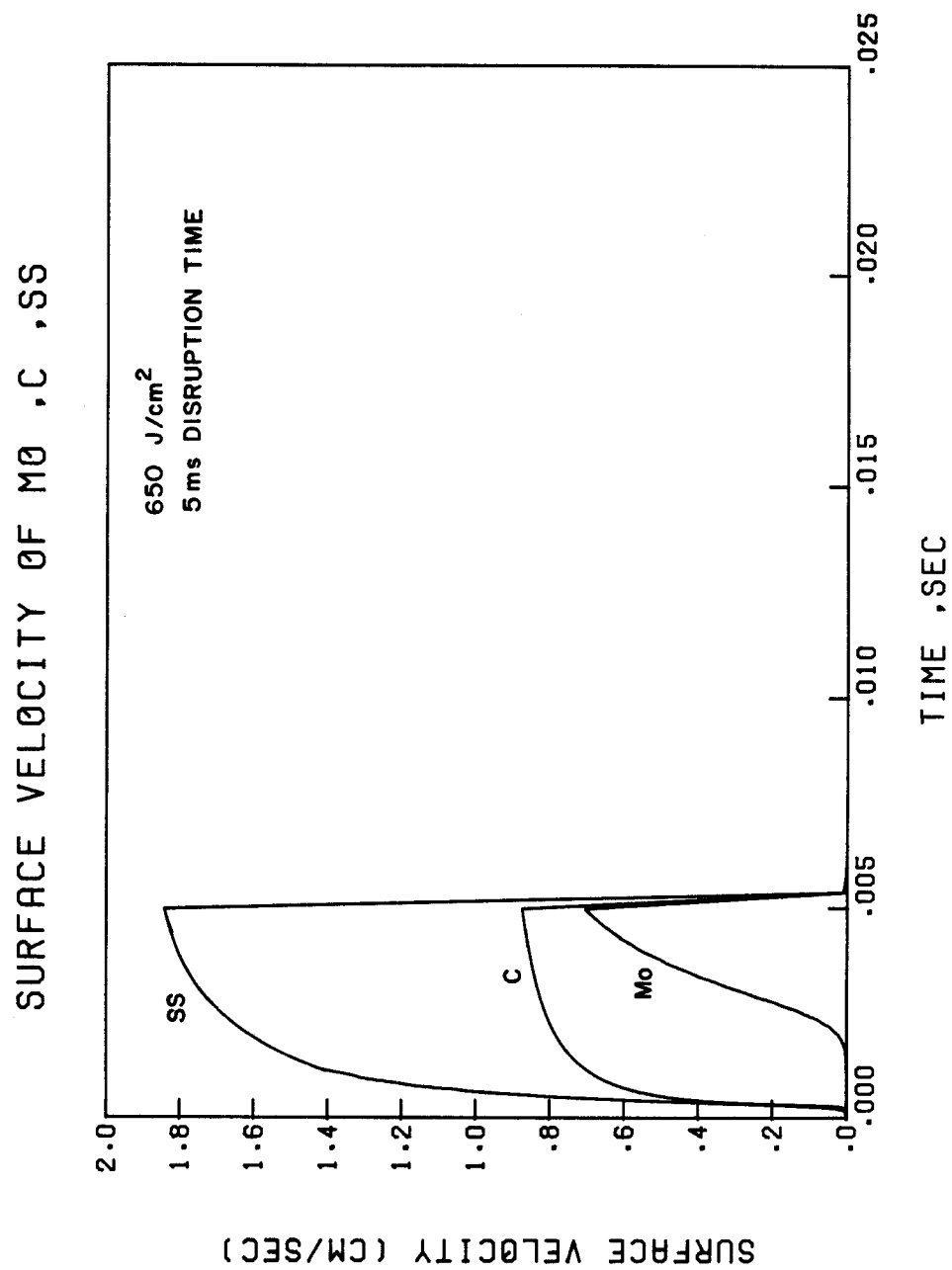


Fig. VII.B-35. Surface velocity of SS, Mo, and C for energy density of 650 J/cm² and 5 ms disruption time (no vapor shield).

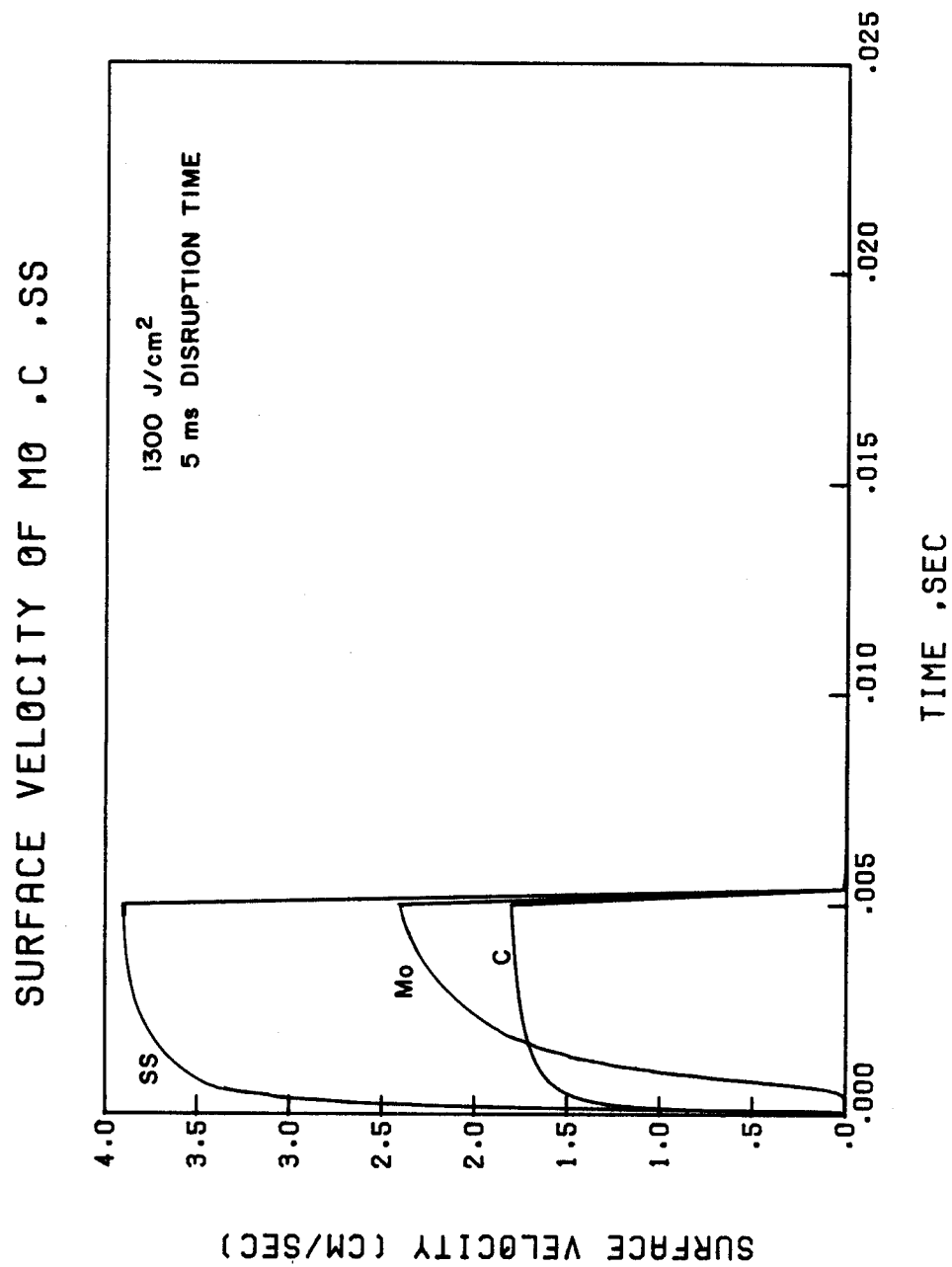


Fig. VII.B-36. Surface velocity of SS, Mo, and C for energy density of 1300 J/cm² and 5 ms disruption time (no vapor shield).

B.5.4. Vapor Shielding

The simple model developed in Chapter V to account for the stopping of the incoming plasma ions by the vapor layer developed in front of the wall is used to study the effect of this shielding on the melting and vaporized zone thickness. The vapor layer, in the process of stopping the plasma ions, will be partially ionized, excited, and heated. Subsequently, the energy stored in this vapor layer will be emitted in the form of x-rays, optical radiation, and thermal diffusion of the hot vapor atoms. These kind of radiations are more isotropic and will be distributed over larger areas as discussed in Chapter V.

B.5.4.a. Effect of Vapor Shielding on Surface Temperature

The surface temperature of stainless steel as a function of time for energy density of 325 J/cm^2 is shown in Fig. VII.B-37 with vapor shielding calculations. The surface temperature has two peaks. The first peak is an indication that there is enough material vaporized and effectively starts shielding the wall. The temperature rise after the first peak is when the vapor reradiates some of its energy back into the wall. The second peak, i.e. the normal peak, is at the end of the disruption time and consequently the end of the deposited energy. The first peak, which is related to the vapor shielding, is sharper and occurs earlier in time for lower disruption times. Comparing Fig. VII.B-37 with Fig. VII.B-7, i.e. the same conditions without vapor shielding, it can be seen that in case of vapor shielding the surface temperature is lower and the surface melt duration is

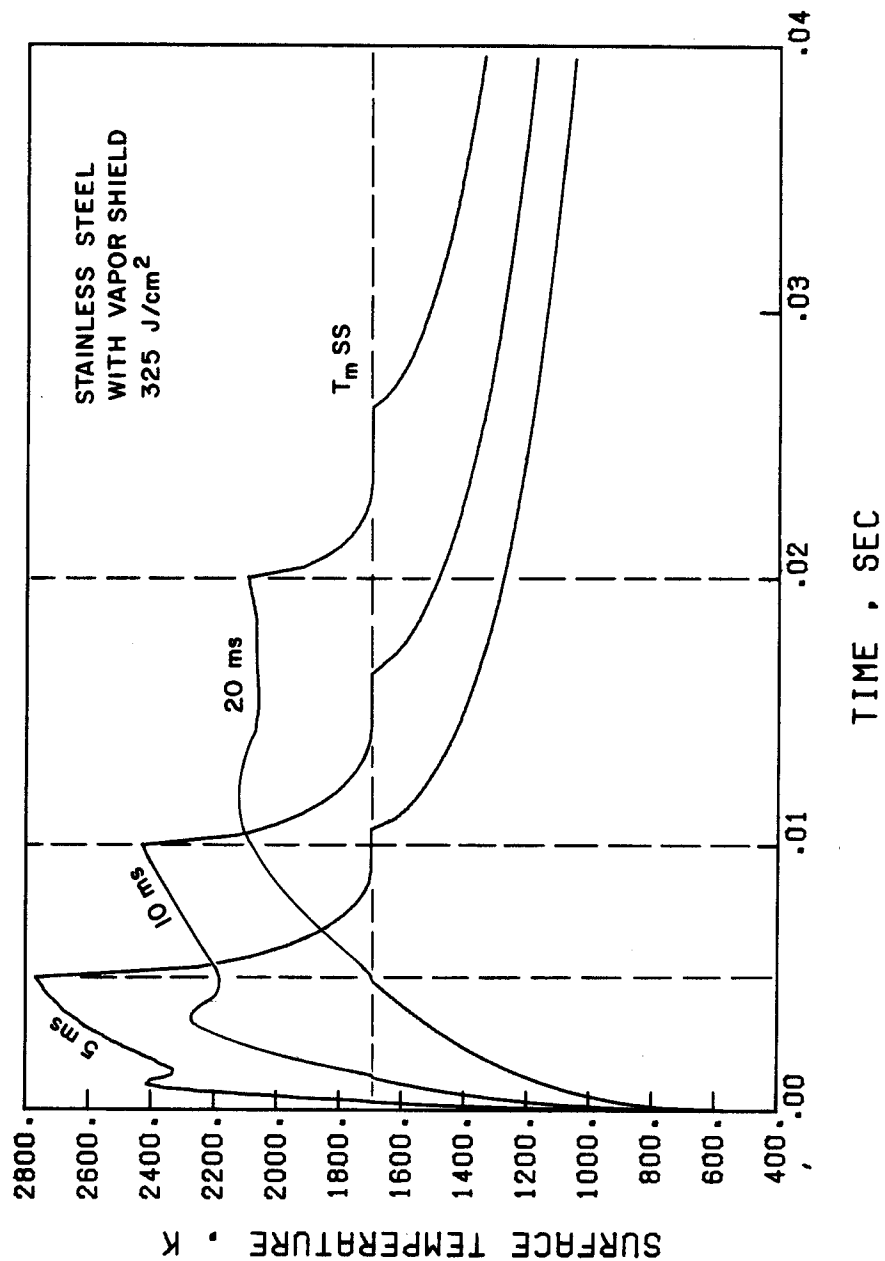


Fig. VII.B-37. Surface temperature rise of stainless steel for energy density of 325 J/cm² and different disruption times with vapor shield.

shorter for input energy of 325 J/cm^2 . This generally means that less material evaporated and smaller thickness melted as will be shown later. For large input energies of 1300 J/cm^2 as shown in Fig. VII.B-38, the surface temperature is lower and the rise in the temperature after the first peak is slower for the vapor shield than that shown in Fig. VII.B-9 without the shielding. The first peak occurs much earlier in time and is much narrower than the lower energy case. Opposite to the 325 J/cm^2 case, the surface melt duration is longer with the vapor shielding.

The effect of vapor shielding on C, Mo, and SS surface temperature is shown in Fig. VII.B-39 where 650 J/cm^2 is deposited in 20 ms disruption time. The vapor shielding effectively decreases the surface temperature for C and SS compared to without shielding calculations shown in Fig. VII.B-21. A small change in the surface temperature for Mo is noticed. The reason is that there is not enough vaporized material from Mo to effectively shield the incoming plasma ions during the disruption. On the other hand, for the same input energy density of 650 J/cm^2 but for lower disruption time of 10 ms, the effect of vapor shielding on the surface temperature of Mo can be seen from Fig. VII.B-40 by comparing without shielding case shown in Fig. VII.B-22. Although Mo has the highest surface temperature without the shielding of the vapor, its temperature largely decreased and the maximum temperature occurs early before the end of the disruption. The surface melt duration is shorter for Mo with

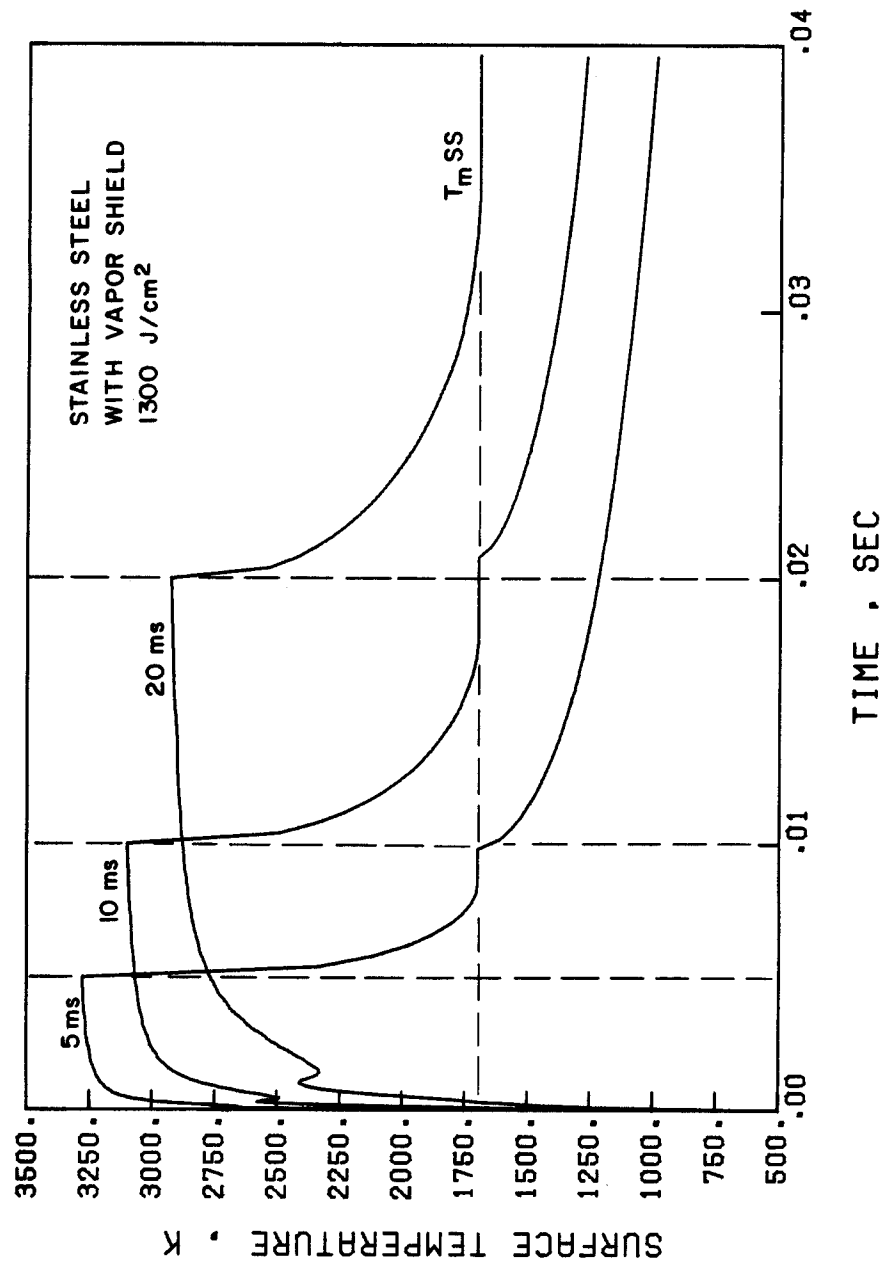


Fig. VII.B-38. Surface temperature rise of stainless steel for energy density of 1300 J/cm² and different disruption times with vapor shield.

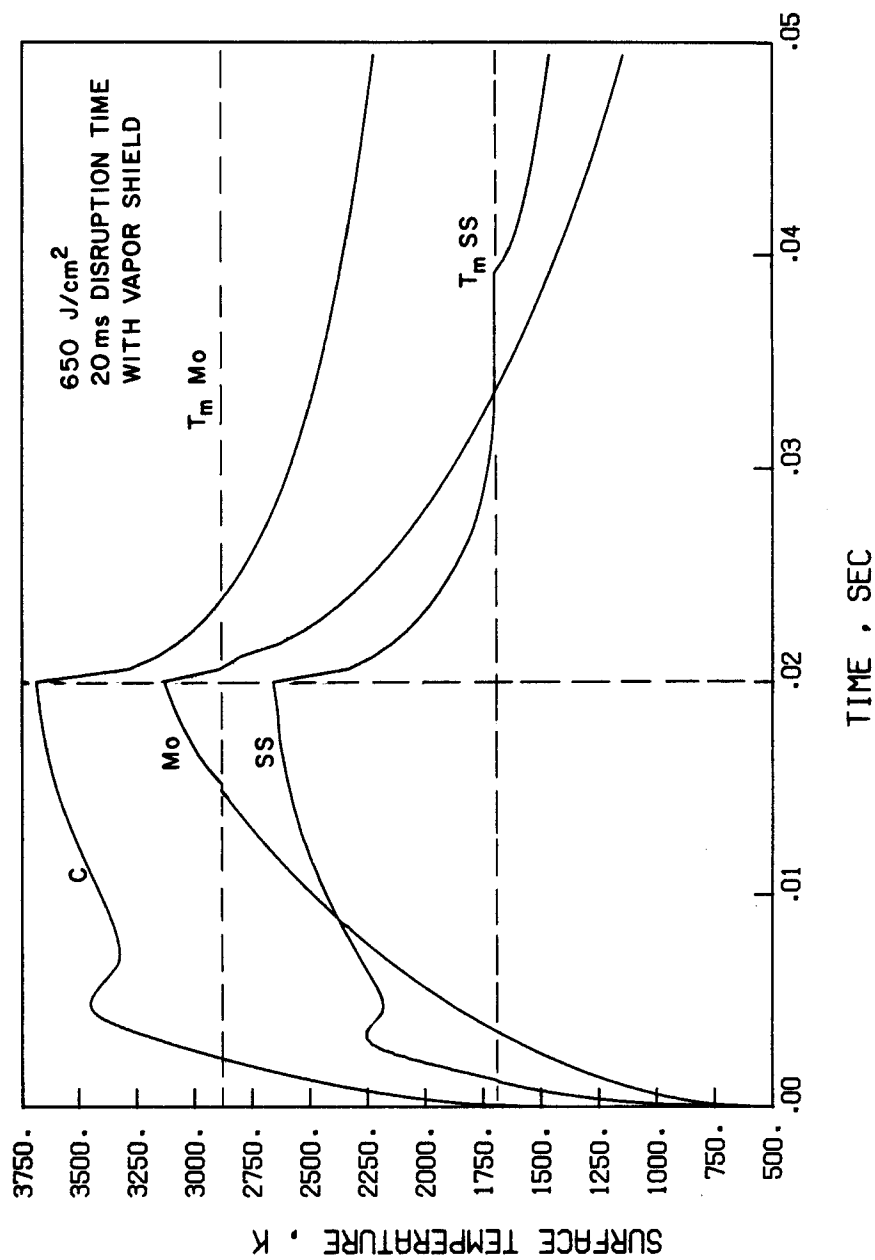


Fig. VII.B-39. Surface temperature rise of SS, Mo, and C for energy density of 650 J/cm² and 20 ms disruption time with vapor shield.

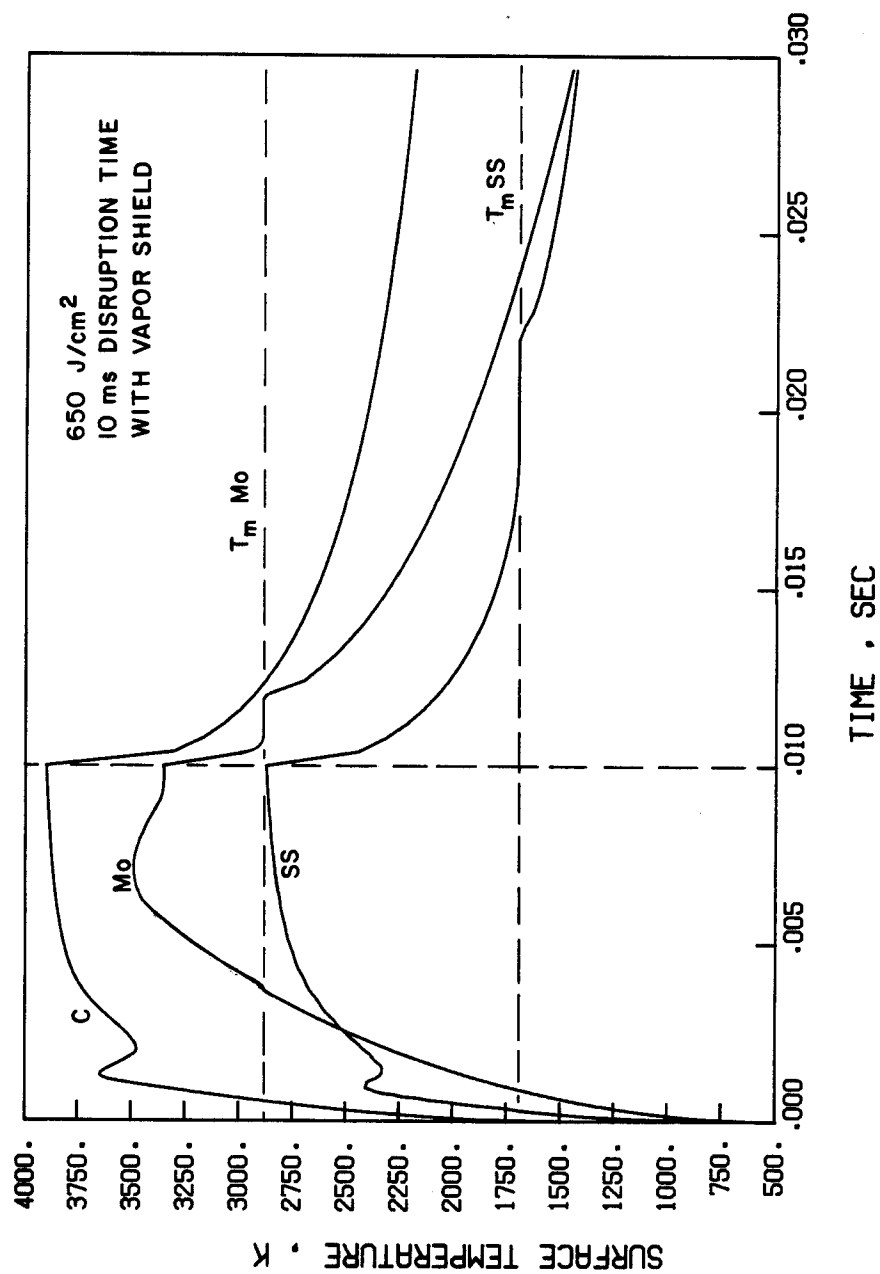


Fig. VII.B-40. Surface temperature rise of SS, Mo, and C for energy density of 650 J/cm² and 10 ms disruption time with vapor shield.

vapor shielding but it is longer for stainless steel compared to no vapor shield case.

B.5.4.b. Effect of Vapor Shielding on Melting Thickness

The maximum melting thickness for stainless steel with vapor shielding is shown in Fig. VII.B-41. There are no large differences in the general behavior compared with the case of no vapor shield shown in Fig. VII.B-10. At energy densities just above the threshold values, the vapor shielding tends to decrease the melting thickness and at high energy densities the vapor shielding increases the melting thickness (see Fig. VII.B-42). This can be explained by the fact that at lower energies, where there is just enough vapor to stop the incoming plasma ions, the heat flux from the vapor radiation is not sufficient to cause as much melting. But at higher total energies, the heat flux from the radiating vapor is not high enough to cause more evaporation; but instead, most of the energy will cause more material to melt.

The effect of vapor shielding on the maximum melting thickness of Mo is shown in Fig. VII.B-43. It can be seen that vapor shielding effectively decrease the melting thickness of Mo for energy ranges considered in this study. This is because Mo has high threshold energies to start melting and at high incident energy fluxes the energy reradiated from the vapor back into the wall will be high but not enough to cause larger material to melt as in the case of no vapor shielding.

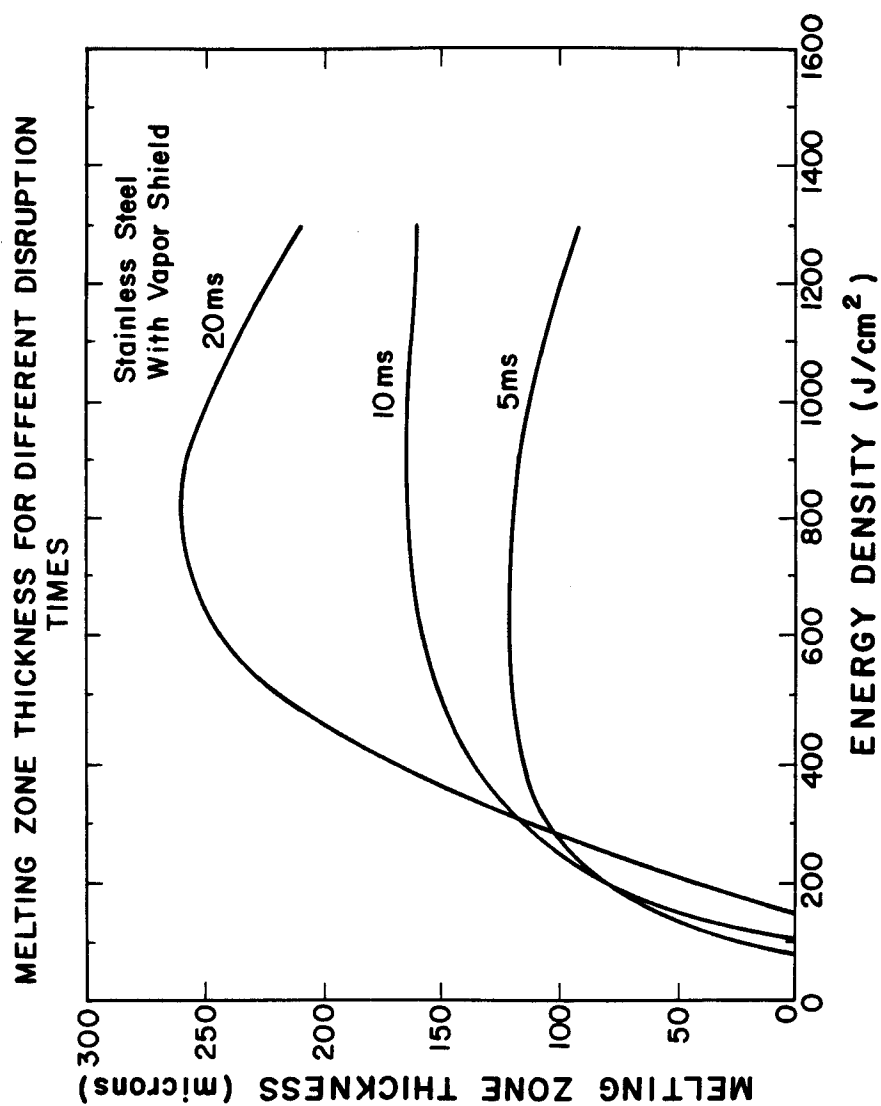


Fig. VII.B-41. Stainless steel melting zone thickness with vapor shield as a function of energy density.

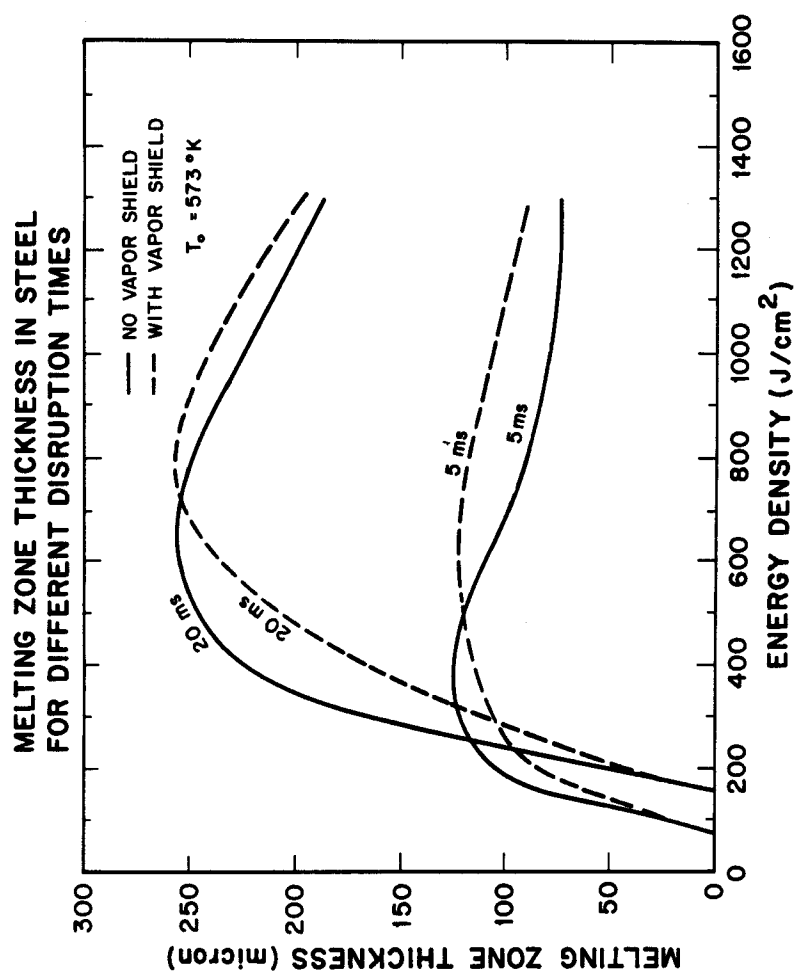


Fig. VII.B-42. Effect of vapor shielding on melt layer thickness of stainless steel.

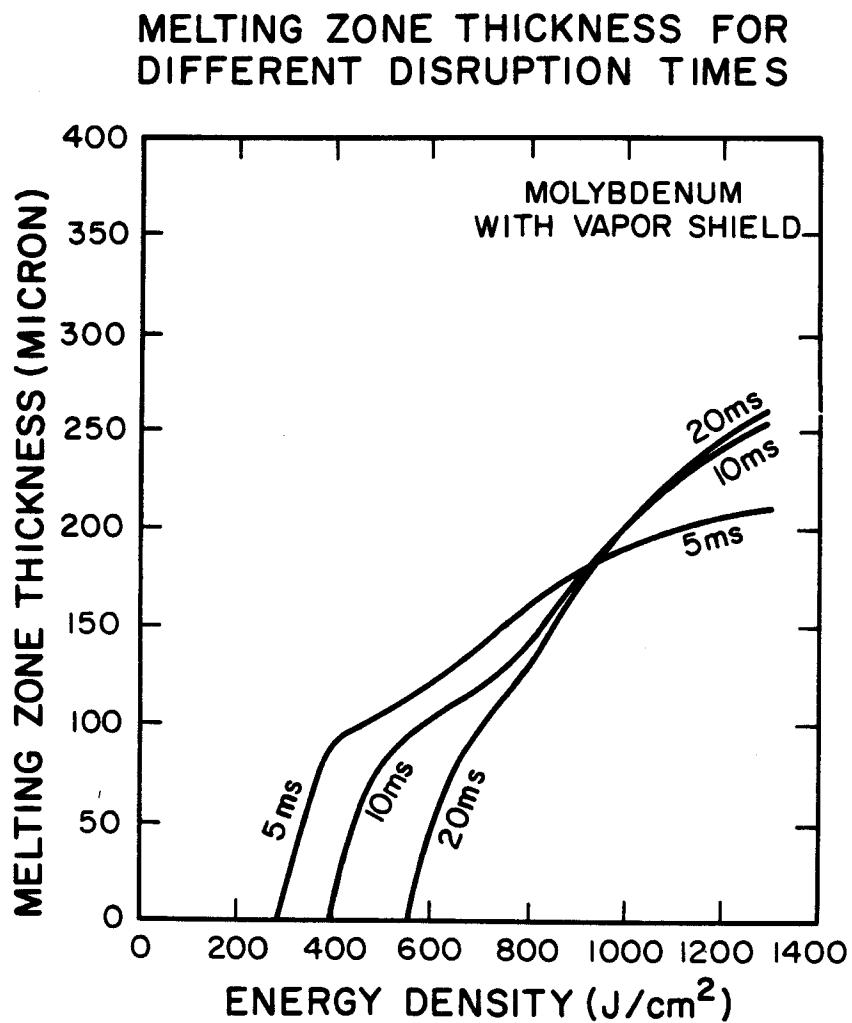


Fig. VII.B-43. Molybdenum melting zone thickness with vapor shield as a function energy density.

B.5.4.c. Effect of Vapor Shielding on the Material Vaporized

The total material evaporated is calculated by integrating the velocity of the receding surface over the time. A more detailed description of the models developed in this thesis to calculate the evaporation is given in Chapter V. Figure VII.B-44 shows the thickness of the evaporated layer of stainless steel for 1000 disruptions without and with vapor shielding. Whereas vapor shielding has only a minor effect on the melt layer thickness, it affects the evaporation by at least an order of magnitude. The insensitivity of the melt layer thickness to vapor shielding is due to the fact that melting of stainless steel precedes evaporation by a relatively large time interval. This is expected for all metals with a relatively low melting point. It also can be seen from Fig. VII.B-44 that the shorter the disruption time the more material evaporated. This is because at shorter disruption times, the surface temperature becomes higher since there is not enough time for the heat to be conducted away. Higher temperatures mean higher receding velocities which in turn cause more material to evaporate. Figure VII.B-45 shows the material evaporated from Mo for 1000 disruptions with and without the vapor shielding. Mo, as compared to stainless steel, requires a higher threshold energy density for melting to occur. Consequently, the evaporation is substantially less than for stainless steel. However, since Mo has a higher atomic number, small amounts of Mo impurities are detrimental to plasma stability. For this reason, Fig. VII.B-45 shows the evaporation thickness down to 10^{-6} cm per

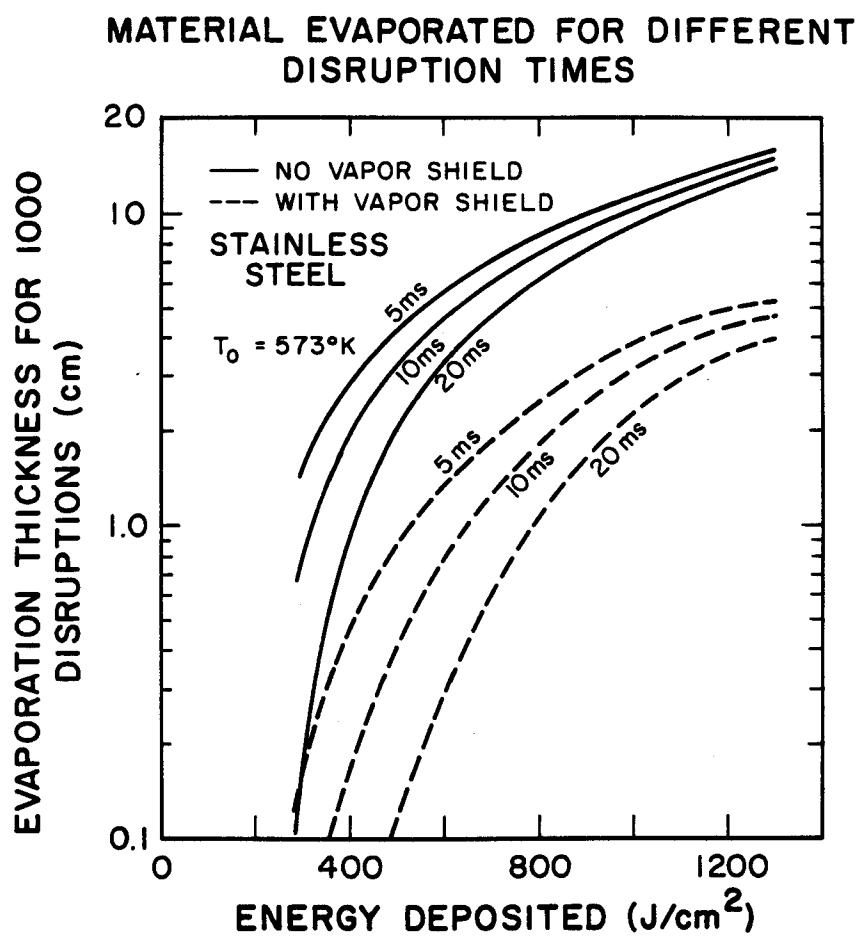


Fig. VII.B-44. Evaporation thickness of stainless steel for 1000 disruptions for different energy deposited.

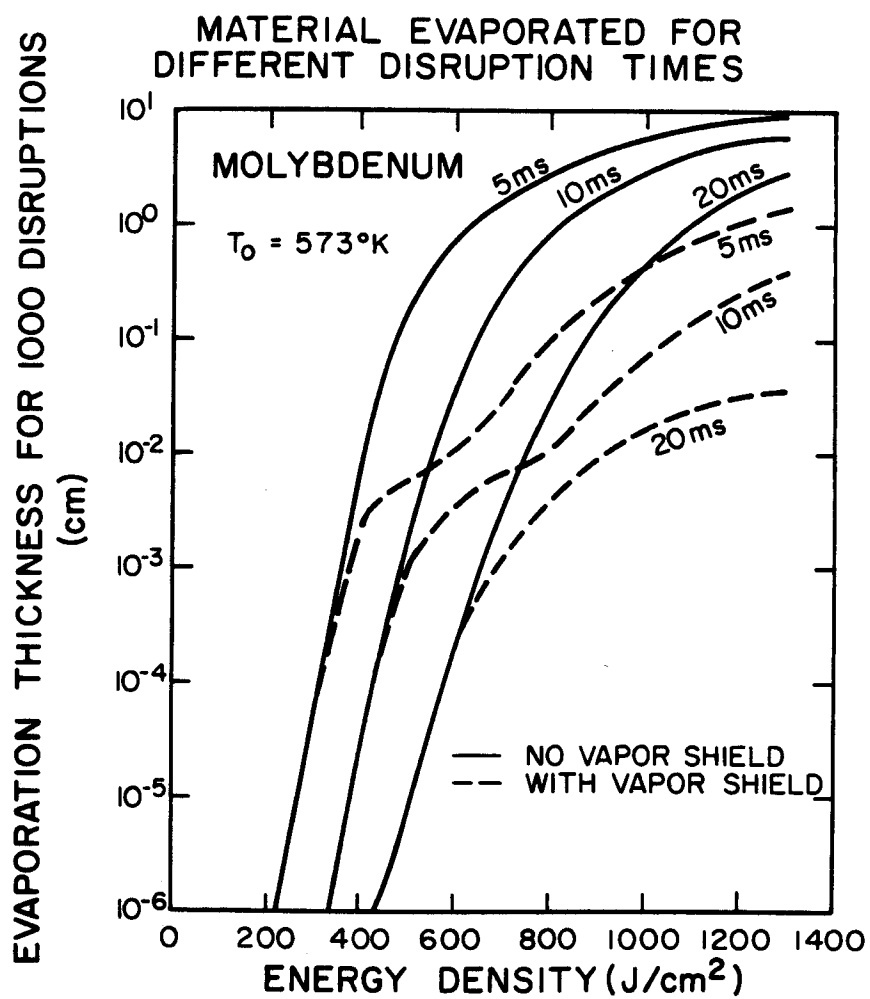


Fig. VII.B-45. Evaporation thickness of molybdenum for 1000 disruptions as a function of energy density.

1000 plasma disruptions, even though these low values are of little concern to the structural integrity of a component made of Mo. The material evaporated from carbon for 1000 disruptions with and without vapor shielding is shown in Fig. VII.B-46. Again the vapor shielding effectively decreases the amount of carbon vaporized. The amount of material evaporated from carbon is lower than the amount evaporated from stainless steel for the same corresponding energy densities and disruption times. The results for the evaporation thickness from carbon are obtained assuming that the vapor species is monatomic carbon. It is however known that in the saturated vapor of graphite at $T = 2733^\circ\text{K}$, the trimer population is higher by a factor of 9 than the monomer population.⁽⁷⁾ Therefore, if it were assumed that the dominant vapor species is C_3 rather than monatomic carbon, then the evaporation thicknesses in Fig. VII.B-46 would have to be increased by a factor of $\sqrt{3}$.⁽⁸⁾

B.5.5. Effect of Disruption Time

There is great uncertainty as to the time scale for plasma disruptions. For example, estimates range from 1 ms to possibly 100 ms, and in some cases, less than a millisecond. This impacts significantly as seen from the previous cases whether melting, vaporization, or both will dominate during a disruption.⁽⁹⁾ Figure VII.B-47 shows melted and evaporated material from stainless steel for input energy density of 325 J/cm^2 in disruption times range from 100 μs to 100 ms. At lower disruption times, most of the energy goes into vaporization. Then vaporization decreases as the disruption time becomes longer and

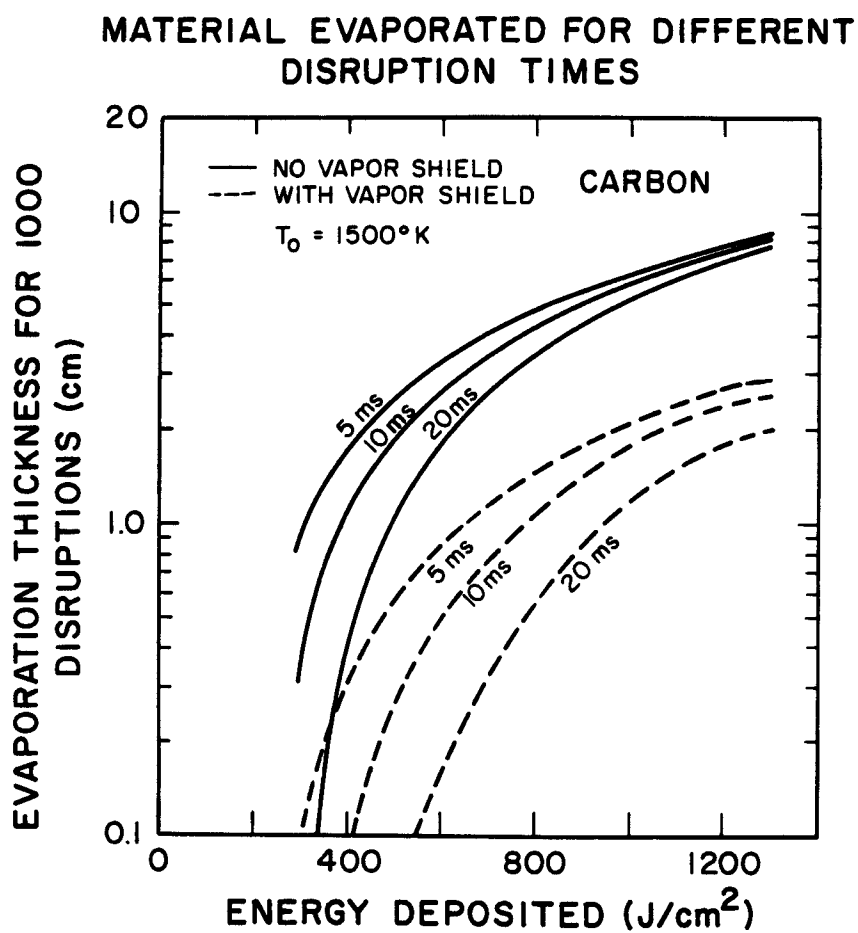


Fig. VII.B-46. Evaporation thickness of carbon for 1000 disruptions as a function of energy density.

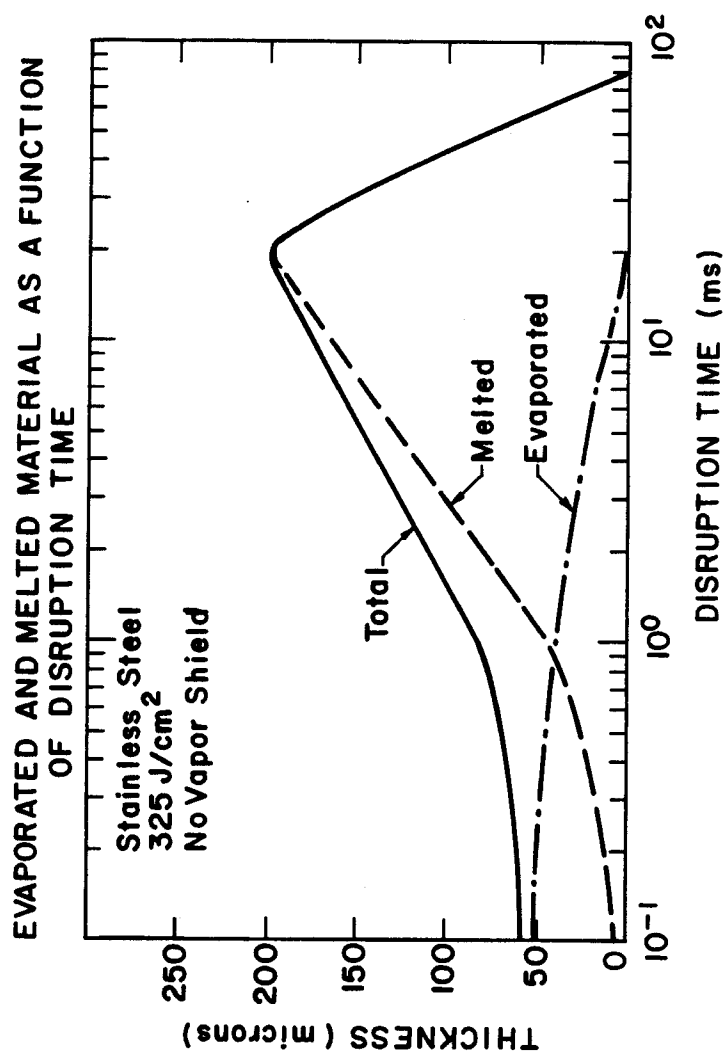


Fig. VII.B-47. Effect of disruption on the amount of melted and evaporated material from SS for 325 J/cm² with no vapor shield.

for disruption times longer than 20 ms no significant vaporization occurs. Consequently at lower disruption times no significant melting occurs simply because there is not enough time for the heat to be conducted away. As the disruption time becomes longer, the melted material rises rapidly, reaches a maximum around 20 ms, and then decreases and for disruption times greater than 80 ms there is no melting occurring. For higher input energy density of 650 J/cm^2 , the general behavior of the melted and evaporated material as a function of the disruption time does not change very much as shown in Fig. VII.B-48. In this case, doubling the input energy, the maximum material evaporated (which occurs at the lowest disruption time considered of 100 μs) is more than twice the maximum amount for the lower energy case. The maximum melted material occurs around 80 ms compared to 20 ms for 325 J/cm^2 input energy as shown in Fig. VII.B-47. Disruption times as long as 200-300 ms are needed to prevent melting in the case of 650 J/cm^2 .

If the melted material is sloughed off the surface as fast as it is formed, the total material removed from the surface will be much more than just the total sum of the melted and vaporized material given in Figs. VII.B-47 and VII.B-48. This is because for vaporization to occur, needs much more input energies than just to cause melting.

B.5.6. Effect of Pulse Shape

The effect of different pulse shapes on the surface temperature and on the amount of material melted and evaporated is studied by

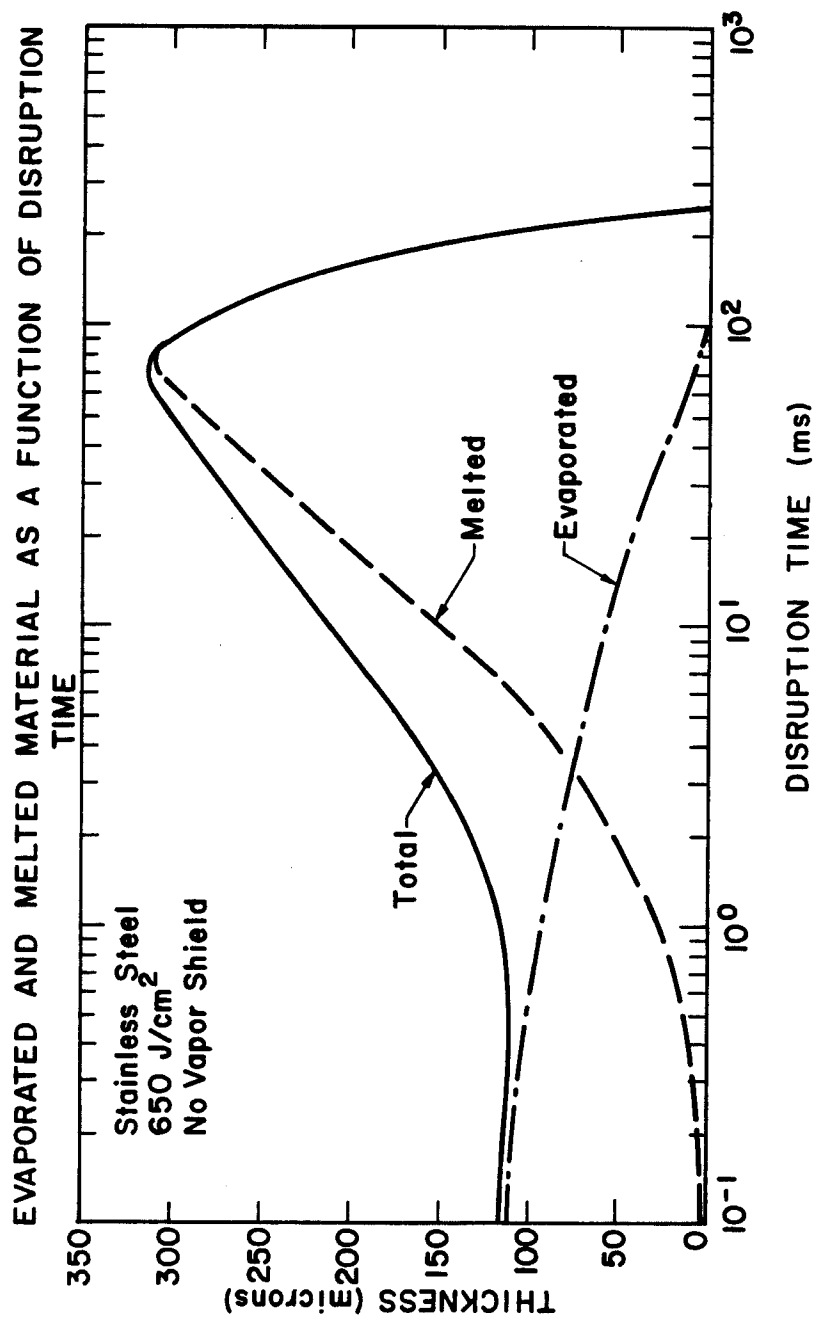


Fig. VII.B-48. Effect of disruption on the amount of melted and evaporated material from SS for 650 J/cm² with no vapor shield.

considering two different shapes, i.e. square and triangular pulses. Figure VII.B-49 shows the surface temperature as a function of time for energy density of 325 J/cm^2 deposited in 10 ms. It can be seen that stainless steel has a higher surface temperature with the triangular pulse than for the square pulse. This will cause more material to evaporate for the triangular pulse. This can be seen from Fig. VII.B-50 where the surface velocity for both pulses is plotted as a function of time. The integration of this velocity over the time is found to predict about 25% more evaporation for the triangular pulse. It can also be seen from Fig. VII.B-49 that stainless steel has shorter surface melt duration for the triangular pulse than for the square pulse. This means that less material melted with a triangular pulse. For the case given above, it is found that the triangular pulse would decrease the melted thickness by about 15% less than the square pulse.

B.6. Conclusions

The models developed in Chapter V to solve the heat conduction problem with phase changes and two moving boundaries have been applied to study melting and evaporation during plasma disruptions. Results are shown for stainless steel, Mo, and graphite as first wall materials. The following conclusions have been obtained:

1. The energy expended in both melting and evaporation cannot be neglected for an accurate solution of the heat conduction problem.

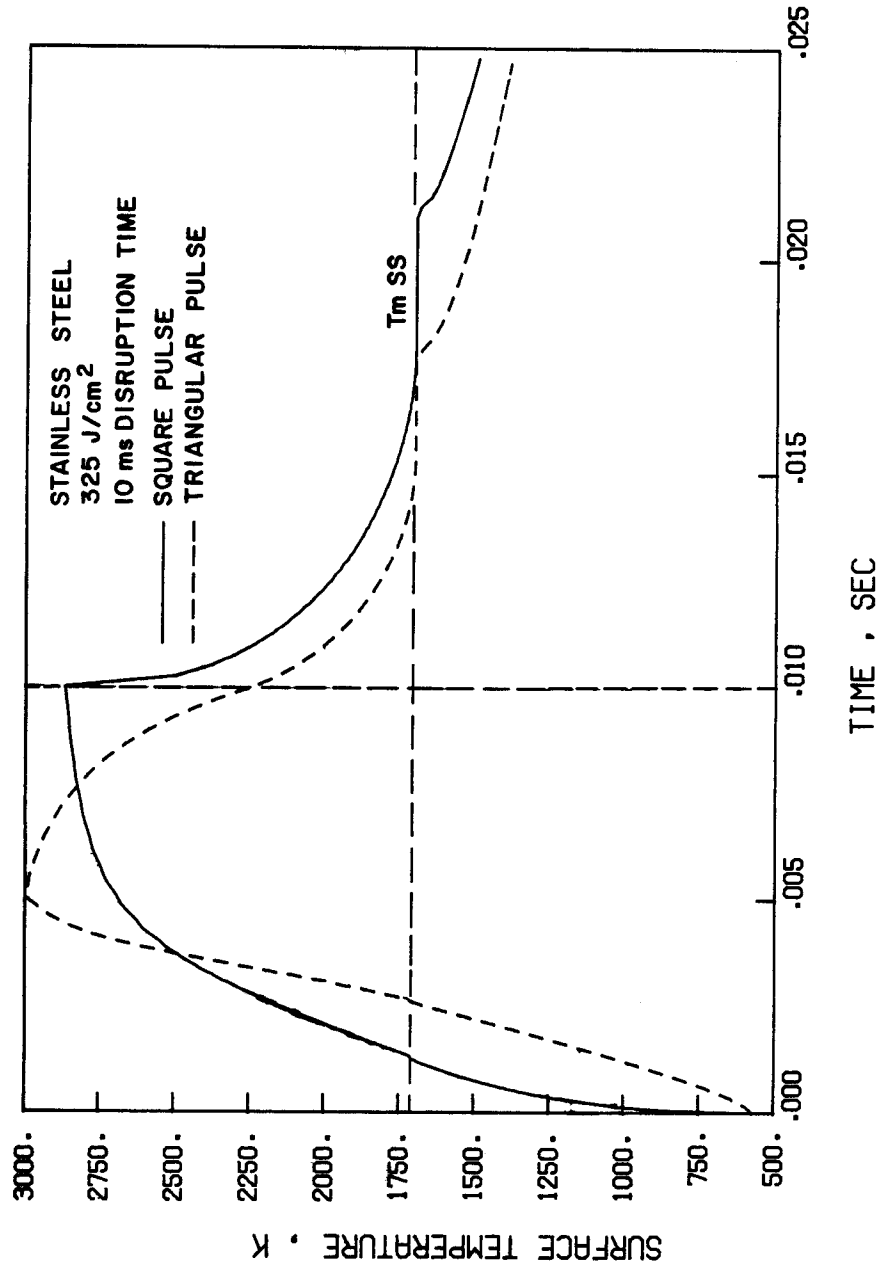


Fig. VII.B-49. Comparison of SS surface temperature rise for square and triangular pulse shape.

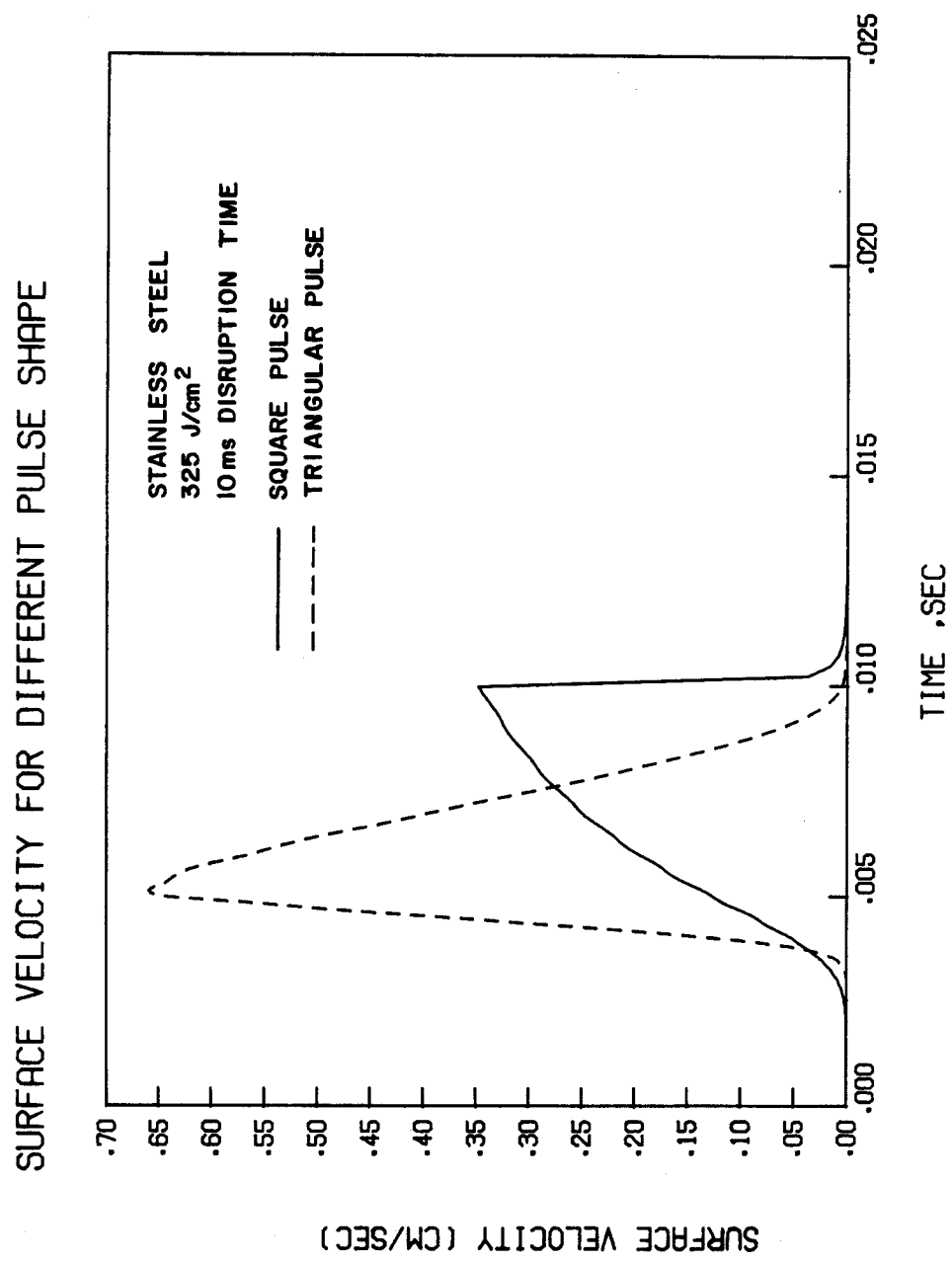


Fig. VII.B-50. Comparison of SS surface velocity for square and triangular input pulses.

2. The temperature dependence of all thermophysical properties for both solid and liquid phase must be included in the model.
3. The net evaporation flux reduces with time and approaches 80% of the vacuum evaporation flux after 20 collision times in the vapor phase.
4. At high input energies it is found that the recondensation flux causes more evaporation, than in the case where there is no condensation flux is assumed.
5. Significant melting or evaporation occurs only above a characteristic energy density. This threshold depends on both the material and the rate of energy deposition.
6. Vapor shielding, i.e. the stopping of plasma ions by the vapor, leads to a significant reduction of the material evaporated in a disruption.
7. At lower energies, near the threshold, vapor shielding tends to decrease both melting and evaporated material. But at higher energies than the threshold, vapor shielding decreases the evaporation and slightly increases the melting thickness.
8. The melt layer thickness is largely affected by vapor shielding only for materials with high melting points.
9. The lower the disruption times the larger the material evaporated and the thinner the melted material layer.
10. Evaporation from Mo is substantially less than for both stainless steel and carbon at the same input energy densities and disruption times.

11. When the total energy deposited is kept constant but the disruption time is varied, it is found that the total thickness of evaporated and melted material remains almost constant for small disruption times, but then increases with disruption time above 1 ms until it reaches a maximum value characteristic of the material. For this characteristic time value, the evaporation has become negligible, and all the deposited energy is dissipated in melting and conduction. For disruption times greater than this characteristic value, the melt layer thickness decreases sharply due to thermal conduction of the energy.
12. For equal energy deposition and disruption times, the surface melt duration is shorter for a triangular pulse than for a square pulse. On the other hand, the amount of evaporated material and the maximum surface temperature reached are significantly higher for the triangular pulse.
13. Fusion devices which cannot stand more than 1 cm erosion per 1000 disruptions are limited to less than 180 J/cm^2 in 20 ms or 100 J/cm^2 in 5 ms. For INTOR level energy fluxes (300-600 J/cm^2) the first wall may be eroded away in 30 to 100 disruptions.

References for Section VII.B

1. R.L. Miller et al., INTOR/PHY/80-14, June 1980.
2. G.L. Kulcinski, W.G. Wolfer, and A.M. Hassanein, "Evaporation of a Metallic First Wall During a Plasma Disruption," JAERI/University of Wisconsin-Madison, March 25, 1981.
3. S. Kim Choong, "Thermophysical Properties of Stainless Steels," ANL-75-55, Argonne National Laboratory, September 1975.
4. G. Betz and M.G. Froberg, "Enthalpy Measurements on Solid and Liquid Molybdenum by Levitation Calorimetry," High Temperatures-High Pressures 12, (1980) 169-178.
5. U. Seydel, H. Bauhof, W. Fucke, and H. Wadle, "Thermophysical Data for Various Transition Metals at High Temperatures Obtained by Submicrosecond-Pulse-Heating Methods," High Temperatures-High Pressures 11 (1979) 635-642.
6. N.S. Rasor and J.D. McClelland, "Thermal Properties of Graphite, Molybdenum and Tantalum to Their Destruction Temperatures," J. Phys. Chem. Solids 15, (1959) 17-26.
7. K.A. Gingerich, D.L. Cocke, and J.E. Kingcade, Inorg. Chimica Acta 17, (1976), L1.
8. A.M. Hassanein, G.L. Kulcinski, and W.G. Wolfer, "Vaporization and Melting of Materials in Fusion Devices," presented at 2nd Topical Mtg. on Fusion Reactor Materials, 9-12 August 1981, Seattle, WA; also UWFD-422. (To be published in J. Nucl. Mat.)
9. A.M. Hassanein, G.L. Kulcinski, and W.G. Wolfer, "Surface Melting and Vaporization Caused by Plasma Disruptions," to be submitted to Nuclear Fusion.

C. Application (C): The Solution of the Moving Boundaries Problem

Using the Green's Function

C.1. Introduction

In Chapter IV a method was developed to solve the heat conduction equation with different volumetric deposition functions, by the use of the Green's function. In this chapter, the solution of the heat conduction equation in moving boundary conditions developed in Chapter V is presented by the use of the Green's function method. A comparison between the Green's function solution and the finite difference solution developed in Chapter V is also presented. This comparison with finite difference methods is made with and without the variation of the thermal properties with temperature.

C.2. Method of Solution

The general heat-conduction equation with constant thermal properties is given by:

$$\rho c \frac{\partial T}{\partial t} - k \nabla^2 T = \dot{q}(x, t) \quad (1)$$

where ρ , c , k are independent of temperature. For a semi-infinite medium, the Green's function is given by:

$$G(x, t, x', t') = \frac{1}{2\sqrt{\pi\alpha(t-t')}} \left\{ e^{-\frac{(x-x')^2}{4\alpha(t-t')}} + e^{-\frac{(x+x')^2}{4\alpha(t-t')}} \right\} \quad (2)$$

where α is the thermal diffusivity. The general solution for the temperature rise due to any deposition function is given by

$$T(x,t) = \int_{t'} \int_{x'} \frac{1}{\rho c} \dot{q}(x',t') G(x,t,x',t') dx' dt' \quad . \quad (3)$$

The modified heat conduction equation in a moving coordinate system

$$z(t) = x - s(t) \quad , \quad (4)$$

(for which the surface always remains at $z = 0$) developed in Chapter V but with constant thermal properties can be written as:

$$\rho c \frac{\partial T}{\partial t} - \rho c v(t) \frac{\partial T}{\partial z} - k \nabla^2 T = \dot{q}(z,t) \quad . \quad (5)$$

The surface boundary condition is given by

$$F(t) = -k \left. \frac{\partial T}{\partial z} \right|_{z=0} + \rho L_v v(t) + \sigma (T_v^4 - T_o^4) \quad (6)$$

where: $v(t)$ is again the velocity of the receding surface,

$F(t)$ is the incident heat flux.

Equation (5) can be written as

$$\rho c \frac{\partial T(z,t)}{\partial t} - k \nabla^2 T(z,t) = \dot{q}(z,t) + \rho c v(t) \frac{\partial T(z,t)}{\partial z} \quad . \quad (7)$$

The right-hand side of Eq. (7) consists of the volumetric energy deposition function and a convective term $\rho c v(t) \frac{\partial T}{\partial z}$ which could be

treated as a part of the deposition function. Then Eq. (7) can be written as

$$\rho c \frac{\partial T(z,t)}{\partial t} - k \nabla^2 T(z,t) = \dot{q}'(z,t) \quad (8)$$

where

$$\dot{q}'(z,t) = \dot{q}(z,t) + \rho c v(t) \frac{\partial T(z,t)}{\partial z} \quad (9)$$

The solution for the temperature rise due to the deposition function given by Eq. (9) and boundary condition in Eq. (6) is given by

$$\begin{aligned} T(z,t) = & \int_{t'} \int_{x'} \frac{1}{\rho c} \dot{q}'(z',t') G(z,t,z',t') dz' dt' \\ & - \alpha \int_{t'} dt' G(z,t,0,t') \frac{\partial T(0,t')}{\partial z} \quad (10) \end{aligned}$$

From Eq. (6) the gradient of the temperature can be represented by

$$k \frac{\partial T(0,t)}{\partial z} = \rho L_v v(t) + \sigma(T_v^4 - T_o^4) - F(t) \quad (11)$$

Substituting Eqs. (11) and (9) into Eq. (10) yields

$$\begin{aligned}
T(z,t) = & \frac{1}{\rho c} \int_{t'} \int_{x'} (\dot{q}(z',t') + \rho c v(t') \nabla T(z',t')) G(z,t,z',t') dz' dt' \\
& + \frac{1}{\rho c} \int_{t'} G(z,t,0,t') (F(t') - \rho L_v v(t') - \sigma(T_v^4 - T_o^4)) dt'
\end{aligned} \tag{12}$$

where: $\nabla T(z,t) = \frac{\partial T(z,t)}{\partial z}$

$$T_v = T(0,t) \quad .$$

The difficulty in calculating the temperature rise from Eq. (12) is that both $v(t)$ and $\nabla T(z,t)$ are functions of the current temperatures which are unknown. This is also true for the radiative heat transfer term in the second integral of Eq. (12). Although calculating the surface velocity, $v(t)$, requires only the knowledge of the surface temperature, the term $\nabla T(z,t)$ requires the current temperature distribution throughout the entire space.

A good approximation for the solution of Eq. (12) is to use the numerical techniques developed in Chapter IV. Assuming that we divide space and time into many divisions, the solution for the temperature increase is given by:

$$T(x_n, t_n) = \sum_{t'_i=0}^{t_{n-1}} w_i \Delta t_i \int_0^\infty \frac{1}{\rho c} [\dot{q}(x', t'_i) + \rho c v(t'_i) \nabla T(x', t'_i)] \quad (13)$$

$$\cdot G(x_n, t_n, x', t'_i) dx' + w_n \Delta t_n \lim_{t'_i \rightarrow t_n} \int_0^\infty \frac{1}{\rho c} [\dot{q}(x', t'_i) + \rho c v(t'_i) \nabla T(x', t'_i)]$$

$$\cdot G(x_n, t_n, x', t'_i) dx' + \frac{1}{\rho c} \sum_{t'_i=0}^{t_{n-1}} \Delta t_i [F(t'_i) - \rho L_v v(t'_i) - \sigma(T^4(0, t'_i) - T_o^4)]$$

$$\cdot G(x_n, t_n, 0, t'_i) + \frac{1}{\rho c} \Delta t_n [F(t_n) - \rho L_v v(t_n) - \sigma(T^4(0, t_n) - T_o^4)]$$

$$\cdot \frac{1}{2\sqrt{\pi\alpha\Delta t_n}} e^{-x_n^2/4\alpha\Delta t_n}$$

where again

$$\Delta t_n \ll \Delta t_i, \quad i \neq n \quad (14)$$

and

$$t_{n-1} = t_n - \Delta t_n. \quad (15)$$

It was shown in Chapter IV that

$$\lim_{\epsilon \rightarrow 0} \frac{1}{2\sqrt{\pi\alpha\epsilon}} e^{-\frac{(x-x')^2}{4\alpha\epsilon}} \rightarrow \delta(x - x'). \quad (16)$$

Substituting Eq. (16) in Eq. (13) and by using the methods described in Chapter IV, the temperature rise in Eq. (13) reduces to:

$$\begin{aligned}
 T(x_n, t_n) = & \dots + w_n \Delta t_n \frac{1}{\rho c} [\dot{q}(x_n, t_n) + \rho c v(t_n) \nabla T(x_n, t_n)] \\
 & + \frac{1}{\rho c} \sum_{t'_i=0}^{t_{n-1}} \Delta t_i [F(t'_i) - \rho L_v v(t'_i) - \sigma(T^4(0, t'_i) - T_o^4)] \\
 & + \frac{1}{\rho c} [F(t_n) - \rho L_v v(t_n) - \sigma(T^4(0, t_n) - T_o^4)] \\
 & \cdot \frac{1}{2\sqrt{\pi\alpha}} e^{-\frac{x_n^2}{4\alpha\Delta t_n}} \frac{1}{\sqrt{\Delta t_n}}
 \end{aligned} \tag{17}$$

where $\int_0^\infty dx' \dot{q}(x', t_n) \delta(x_n - x') = \dot{q}(x_n, t_n)$

and $\int_0^\infty dx' \nabla T(x', t_n) \delta(x_n - x') = \nabla T(x_n, t_n)$.

Again the R.H.S. of Eq. (17) contains terms which are functions of the current unknown temperature. This can be approximated by using the temperatures from the previous time step which are known. By choosing the increments between time steps small enough, the solution of Eq. (17) yields an accurate approximation to the integral Eq. (12). These choices always involve a compromise between accuracy and computer time.

The solution of Eq. (17) is contained in the computer code A*THERMAL. This equation can be used to determine the thermal

response of fusion first walls both in inertial and in magnetic confinement reactors due to any kind of incident radiation, such as laser, x-rays, heat flux and ions (light or heavy) for inertial confinement and plasma ions in magnetic confinement reactors.

C.3. Test Case

To test the accuracy of the solution for the moving boundary developed in this chapter, a comparison with the finite difference methods is made. An example of the plasma disruptions cases discussed in Section VII.B is considered where 400 J/cm^2 is deposited in a carbon first wall in 20 ms. The comparison is made between the finite difference with and without the variations of the thermal properties with temperature. In the Green's function methods it is assumed that the thermal properties are constant and equal to that of the finite difference with constant properties. Perturbation methods to account for the variation of thermal properties with temperature in the Green's function methods are developed in Chapter IV and Ref. (1). A solution for the two moving boundaries problem where the material could change phase beside the surface moving boundary using the Green's function is also contained in the computer code A*THERMAL.

C.4. Results and Discussion

The surface temperature as a function of the deposition time for the three methods, i.e. finite difference with variable properties, finite difference with constant properties, and the Green's function is shown in Fig. VII.C-1. The agreement between the Green's function

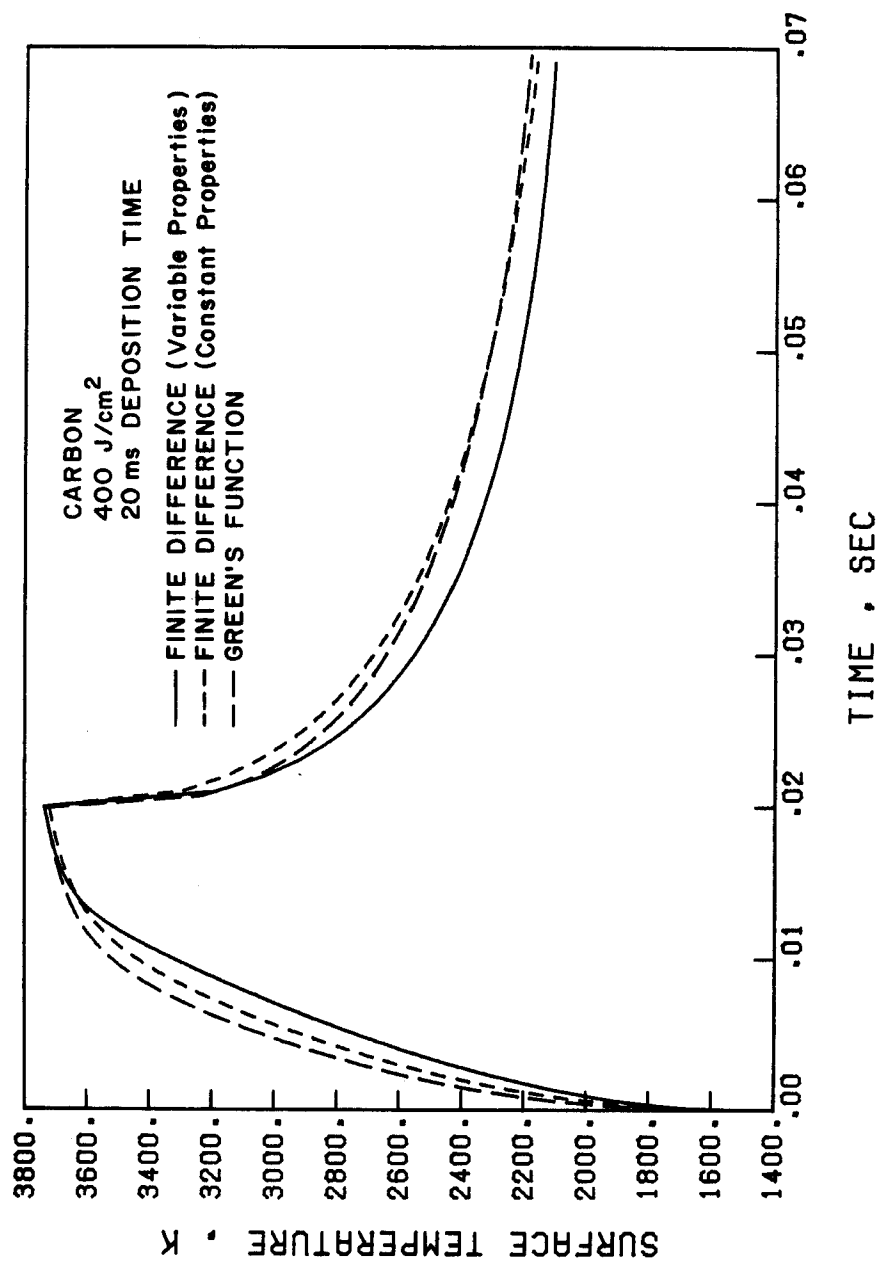


Fig. VII.C-1. Comparison of surface temperature rise for carbon for 400 J/cm 2 deposited in 20 ms by different methods.

and the finite difference with constant properties is very good as seen from Fig. VII.C-2. The little difference between the two methods which is less than 3% could be explained by the size of time step chosen for each method. The size of time step for Green's function problem is much larger than that for finite difference. This is chosen to keep the computer cost for the two problems relatively the same. The Green's function method required more calculations than the finite difference but with a much larger time step. The effect of the variation of thermal properties on the surface temperature can also be seen from Fig. VII.C-1. The constant thermal properties chosen for the Green's function and the finite difference was an average over a high temperature range. Because the lower the temperature, the higher the conductivity for carbon, the finite difference with variable properties has lower temperature than the other two methods either at earlier time in the pulse or at longer times after the end of the disruption.

The velocity of the receding surface, $v(t)$, as a function of time for the three methods of calculation is shown in Fig. VII.C-3. The lower surface velocity at earlier times for the finite difference with variable properties is because of the lower surface temperature due to higher thermal conductivity. The difference between the finite difference with constant properties and the Green's function is illustrated in Fig. VII.C-4. The agreement between the two methods is considered very good. The slightly higher velocity predicted by the Green's function is because of the slightly higher

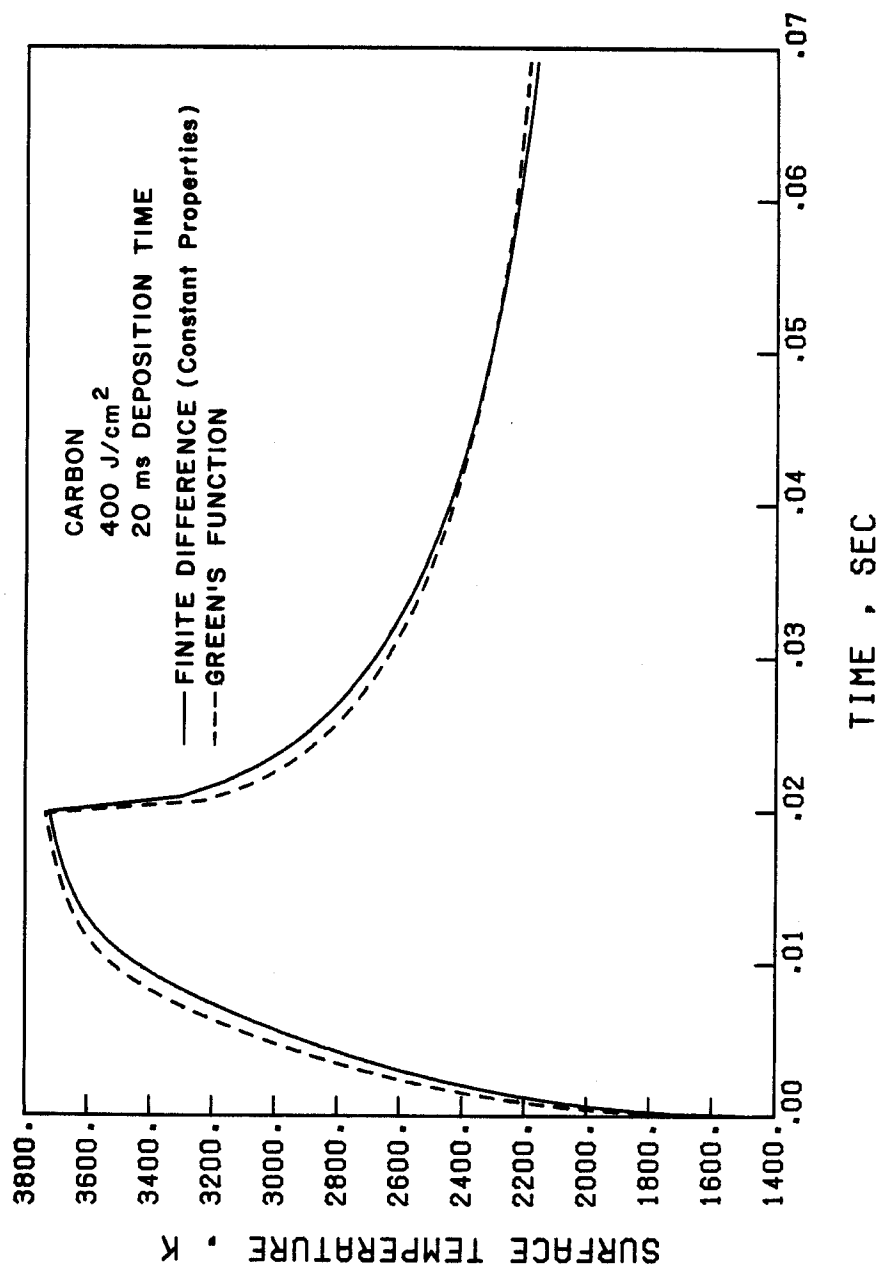


Fig. VII.C-2. Surface temperature rise for carbon by finite difference and Green's function methods.

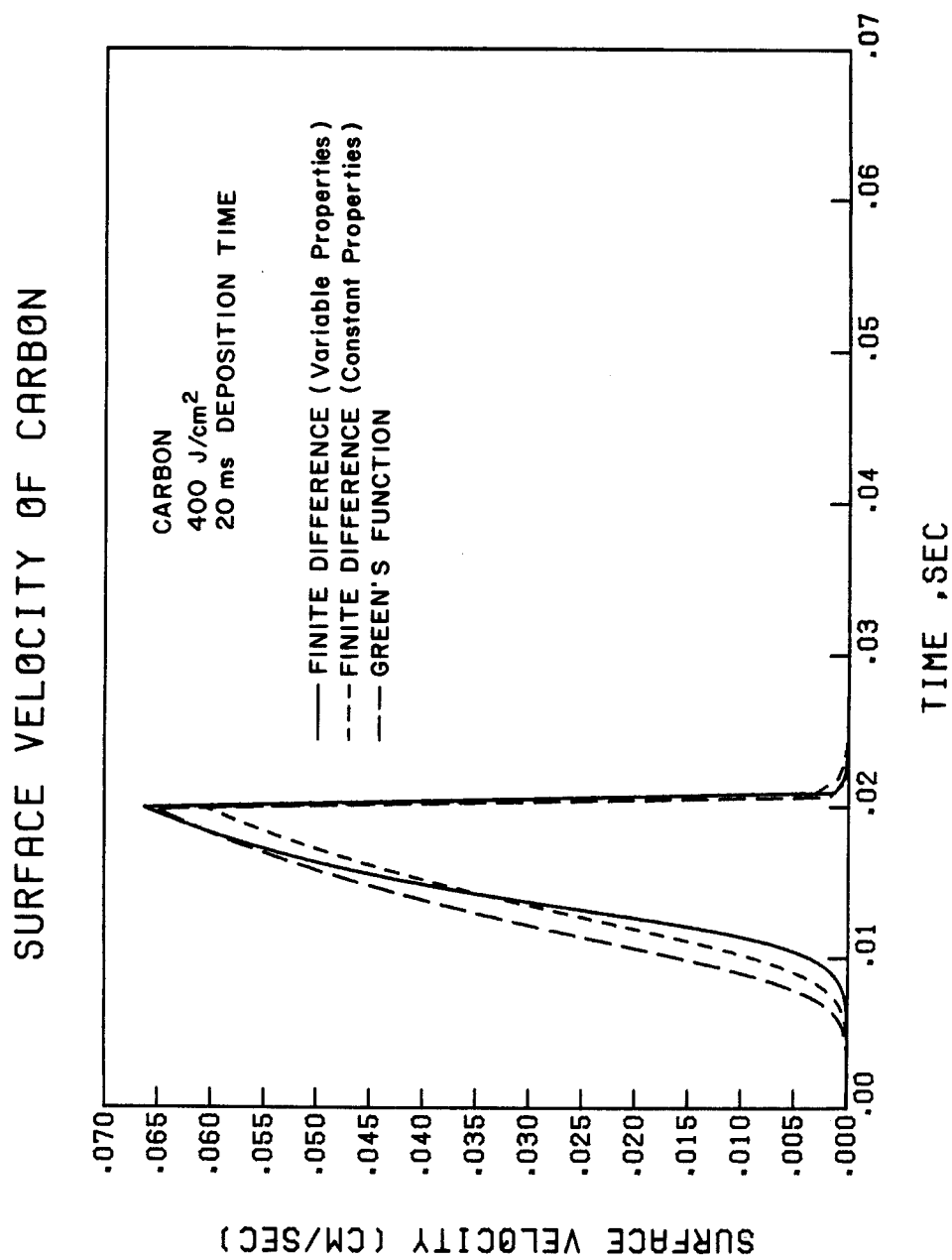


Fig. VII.C-3. Carbon surface velocity for 400 J/cm² deposited in 20 ms by different methods.

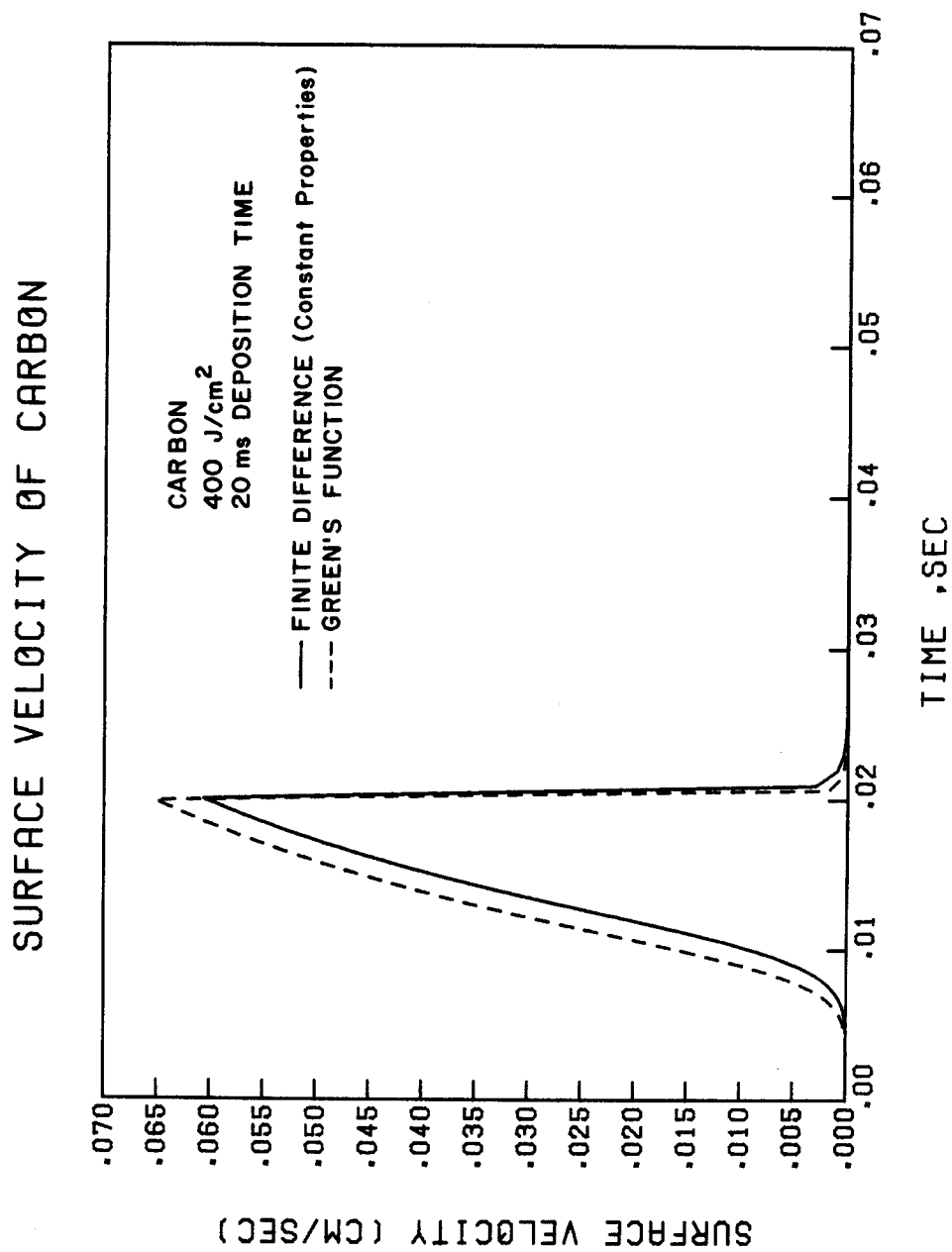


Fig. VII.C-4. Surface velocity of carbon for 400 J/cm² deposited in 20 ms with finite difference and Green's function methods.

surface temperature. Because of the highly nonlinear dependence of the surface velocity on the surface temperature, the difference between the surface velocity calculation by the Green's function and by the finite difference methods is larger than the difference in calculating the surface temperature.

The amount of the total material vaporized can be estimated by integrating the velocity of the receding surface over the pulse duration time. Figure VII.C-5 shows the amount of carbon vaporized as calculated by the three different methods. The good agreement between both the finite difference methods, i.e. with and without the variation of thermal properties, is not because of the insignificance of the variation of the thermal properties with temperature, but rather because of the chosen value for the constant properties. This can be seen from Fig. VII.C-4 where although the velocity of the surface for the variable properties is lower at earlier time of the pulse, it becomes higher than the velocity for the constant properties near the end of the pulse. This has the effect of producing almost equal material vaporized from carbon for these two methods. On the other hand, Fig. VII.C-6 shows about 10% higher total material vaporized by the Green's function methods than the finite difference with constant properties. Although the surface temperature calculated using the Green's function is only slightly higher than that calculated by the finite difference and even lower after the end of the disruption time, the strong dependence of the evaporated material on the surface temperature and the integration of the surface veloci-

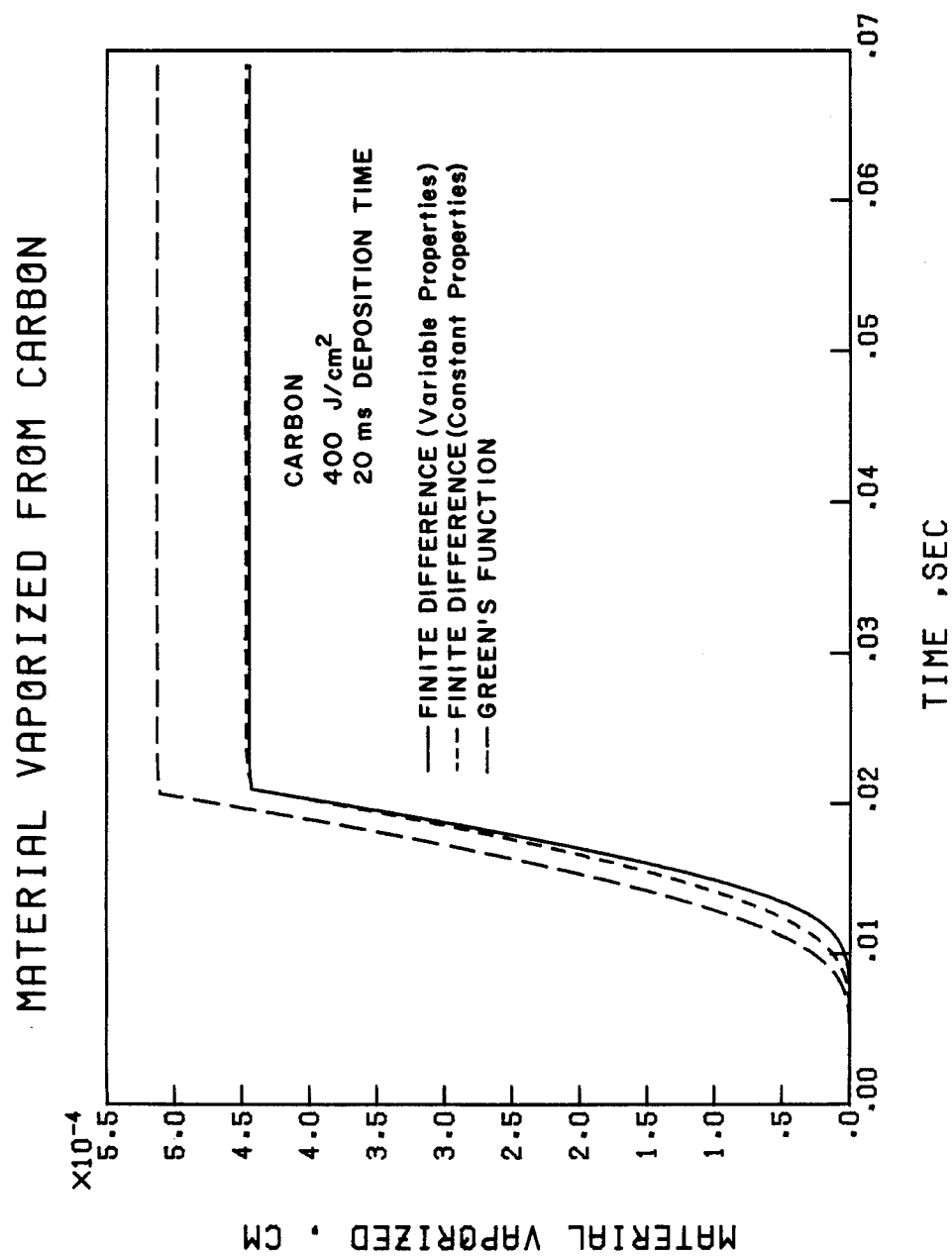


Fig. VII.C-5. Evaporated material from carbon by different methods.

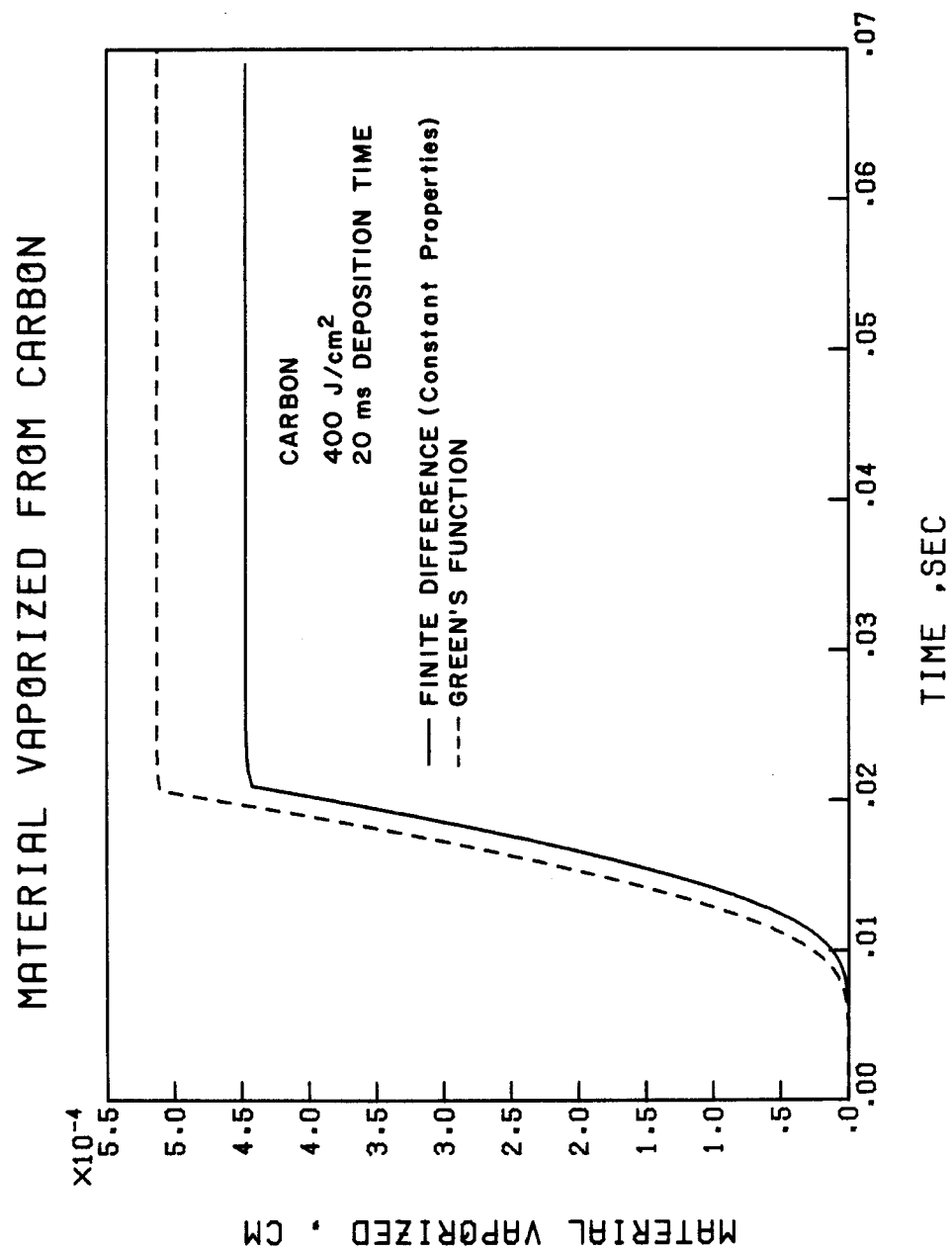


Fig. VII.C-6. Carbon material evaporated as calculated by finite difference and Green's function methods.

ty over all the pulse duration causes larger differences. After the end of the pulse the temperature drops very fast to where there is no significant vaporization occurs. So the slightly lower surface temperature calculated by the Green's function after the end of the pulse will not affect the total material evaporated.

The temperature distribution inside the bulk of the first wall material is also calculated using the three methods. Figures VII.C-7 through VII.C-10 show the temperature distribution of carbon at distance $x = 14$ and 70 microns from the surface. Because of the lower temperature inside the material the difference (at $x = 14$ and 70 microns) between the finite difference with variable properties is larger than the difference between the other two methods. The larger the distance into the material the lower the temperature the higher the effect of the thermal properties. The agreement between Green's function and the finite difference with constant properties at larger distances into carbon is still very good as can be seen from Figs. VII.C-8 and VII.C-10.

C.5. Conclusions

A method has been developed to solve the heat conduction problem with moving boundaries and other boundary conditions by the use of the Green's function. The agreement of this solution with the method of the finite difference developed in previous chapters to solve the same problem is seen to be very good. The variation of the thermal properties with temperature can be very important in calculating accurate temperatures, especially in the case of very high energy

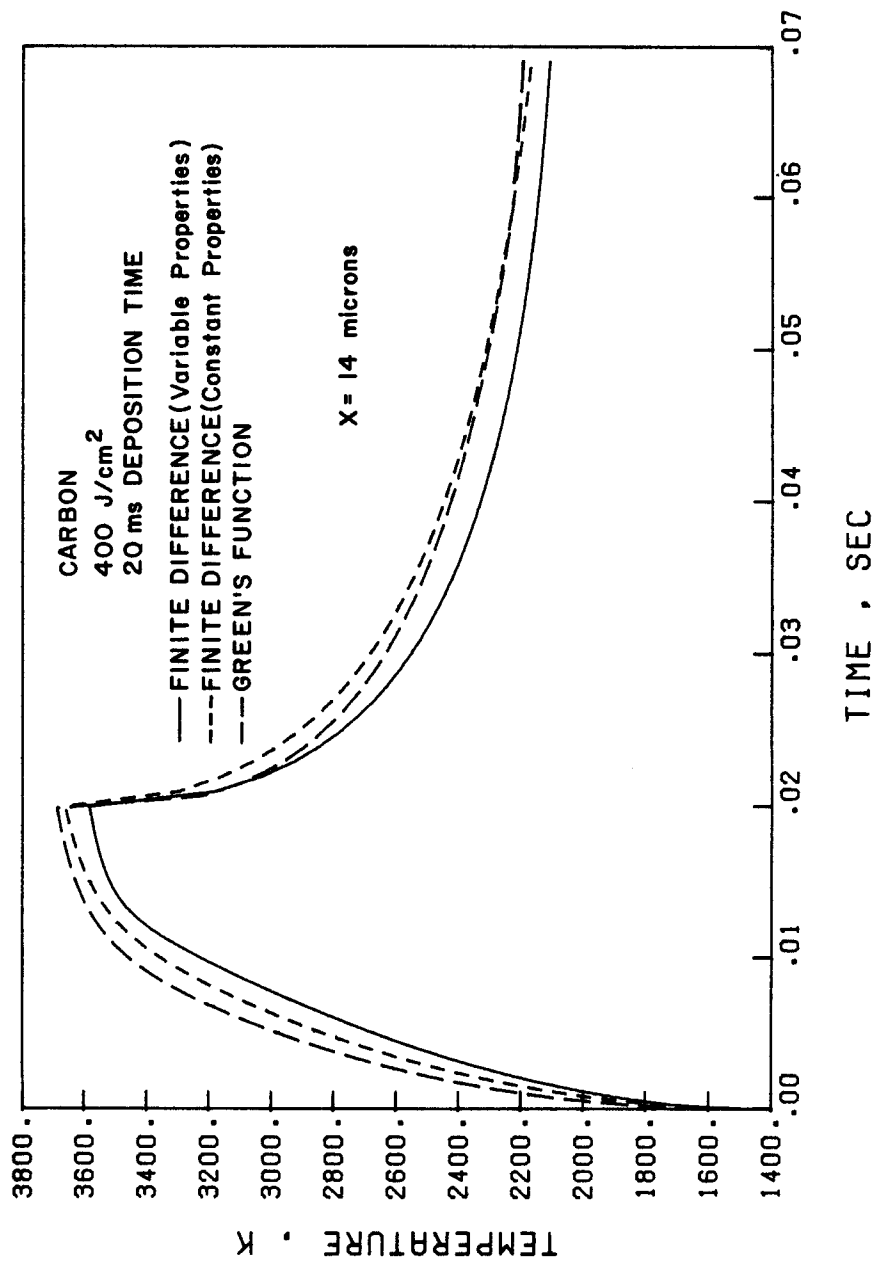


Fig. VII.C-7. Comparison of temperature rise for carbon for 400 J/cm² deposited in 20 ms by different methods at x = 14 microns.

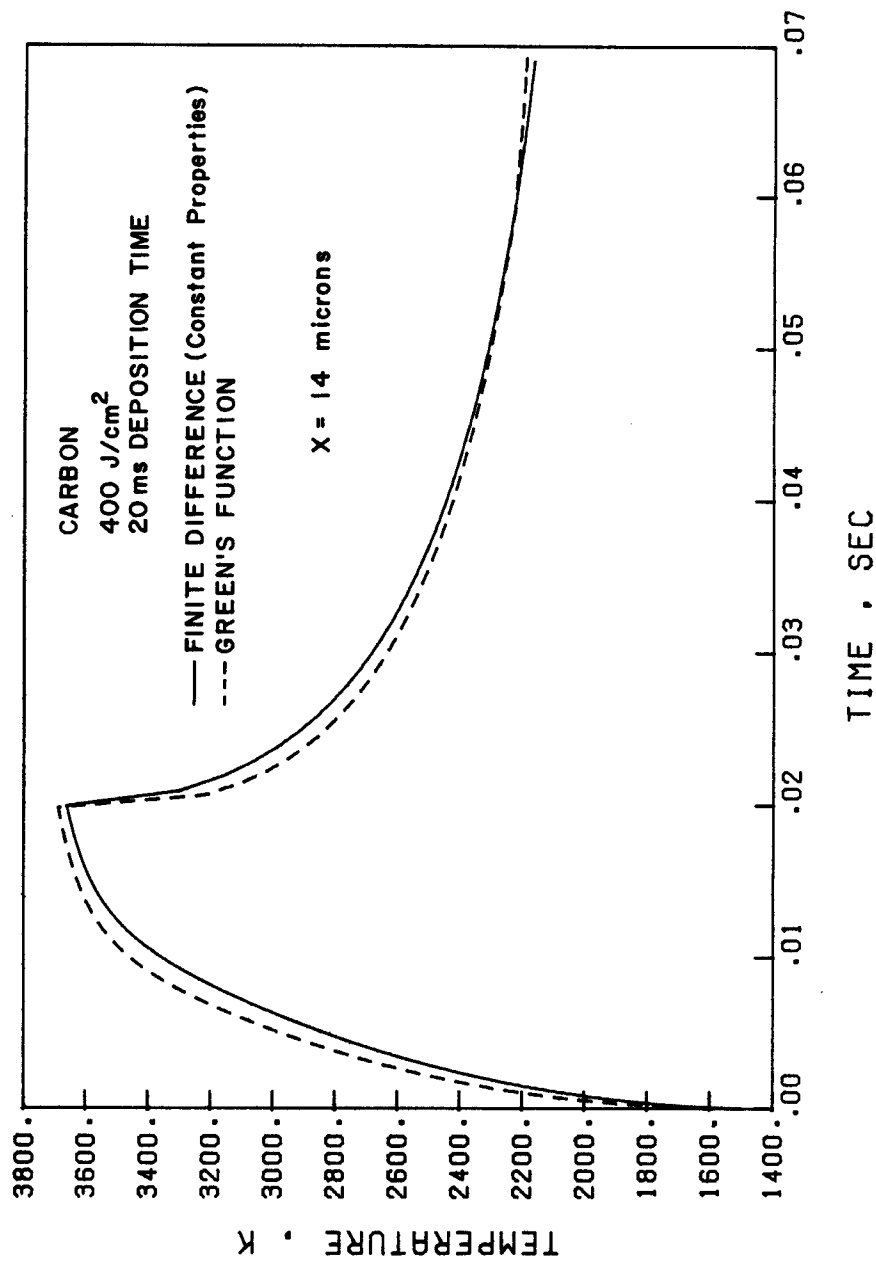


Fig. VII.C-8. Temperature rise of carbon at $x = 14$ microns by finite difference and Green's function methods.

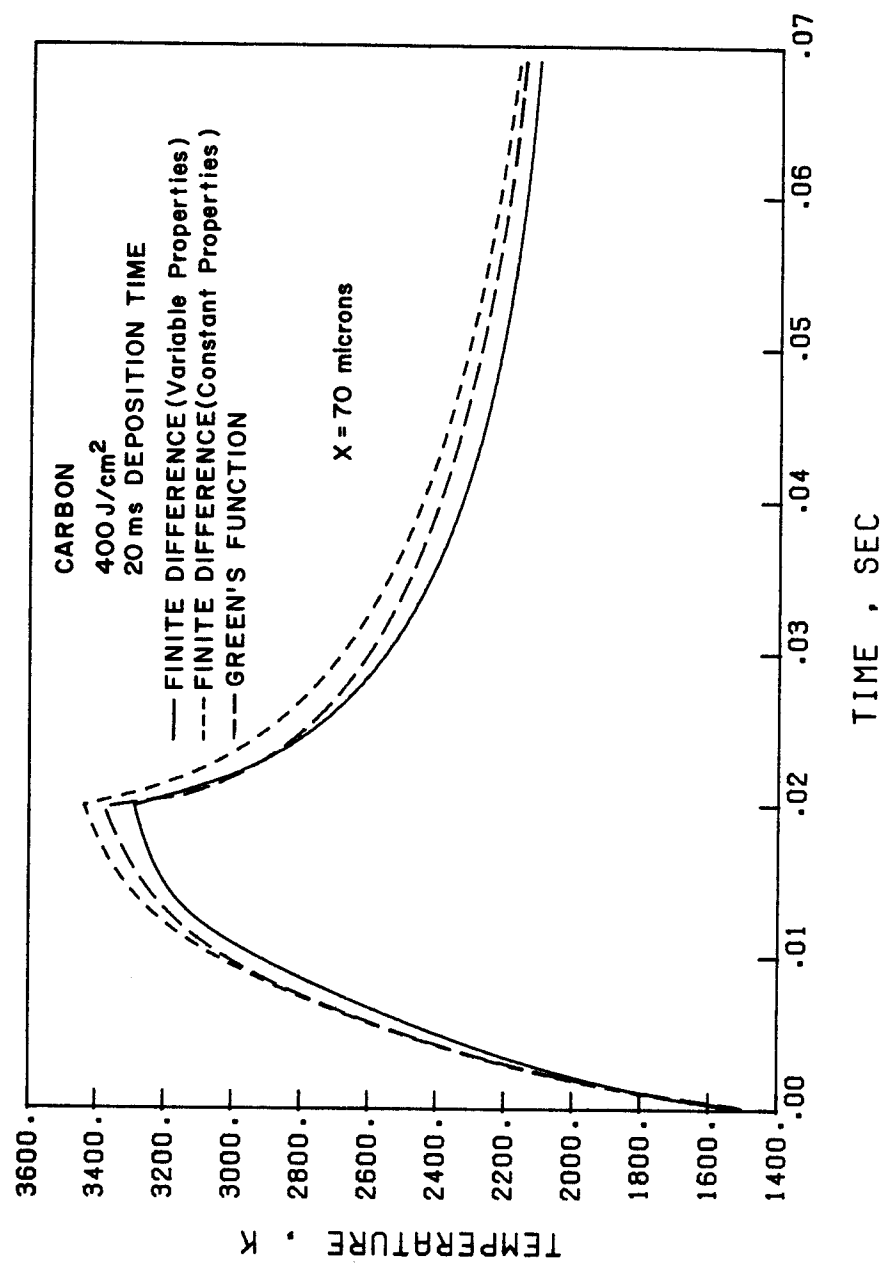


Fig. VII.C-9. Comparison of temperature rise for carbon for 400 J/cm² deposited in 20 ms by different methods at x = 70 microns.

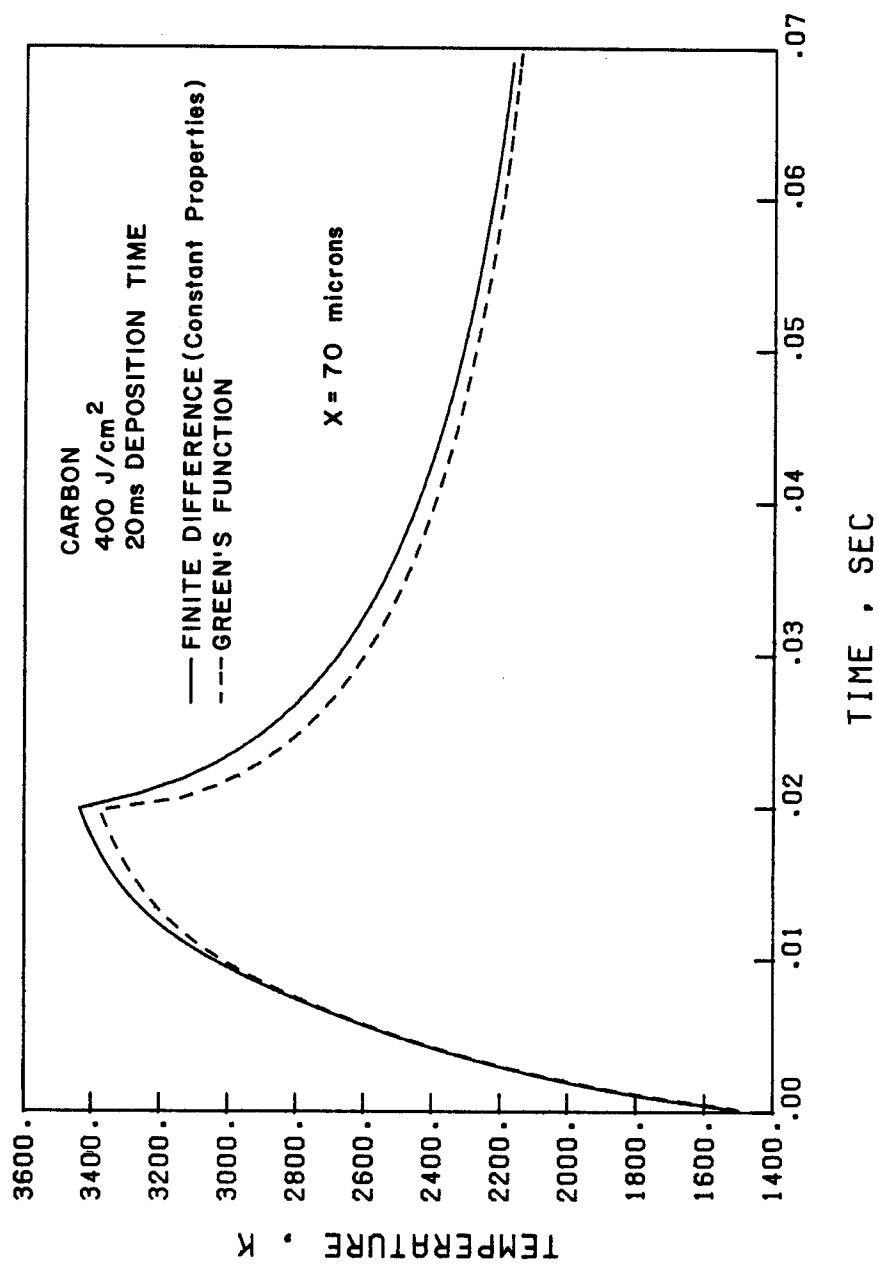


Fig. VII.C-10. Temperature rise of carbon at $x = 70$ microns by finite difference and Green's function methods.

depositions or if the material undergoes a change of phase. This is because of the larger differences between the solid and liquid phase properties. Because of the highly nonlinear dependence of the receding surface velocity on the surface temperature, a small change in calculating the surface temperature could result in large differences in the surface velocity and consequently larger differences in calculating the total material removed from the surface by evaporation.

References for Section VII.C

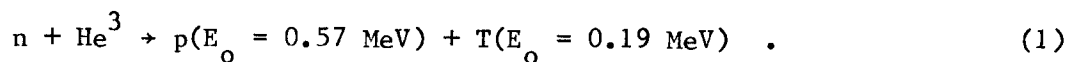
1. A.M. Hassanein and G.L. Kulcinski, "Numerical Methods for Calculating the Temperature Increase in ICF First Walls," University of Wisconsin Fusion Engineering Program Report, UWFD-397, November 1980.

D. Application (D): Simulation of Fusion First Wall Environment in Fission Reactors

D.1. Introduction

It has recently been proposed by Hsu and Miller⁽¹⁾ that one can use a thermal fission reactor to produce bulk neutron and surface effects which are similar to those experienced by the first walls in a DT fusion reactor. The main idea is to use the (n, α) reaction in Ni^{59} to produce a high internal helium content in the metal while using the $\text{He}^3(n, p)\text{T}$ reaction in the gas surrounding the specimen to produce an external heat and particle flux. The He^3 gas would be contained in an annulus around the material to be tested as depicted in Fig. VII.D-1. The pressure of the gas could be varied to change the particle flux and energy which, in turn, would change the heat flux, the erosion rate, and the displacement rate in the test material.

The basic problem is to calculate the partitioning of the reaction energy; i.e., how much of the recoil energy is deposited on the wall? It is also of interest to know the energy spectrum of the protons and tritium ions which strike the wall as a result of the following reaction:



The objectives of this chapter are:

- (1) To calculate the energy spectrum of the charged particles at the

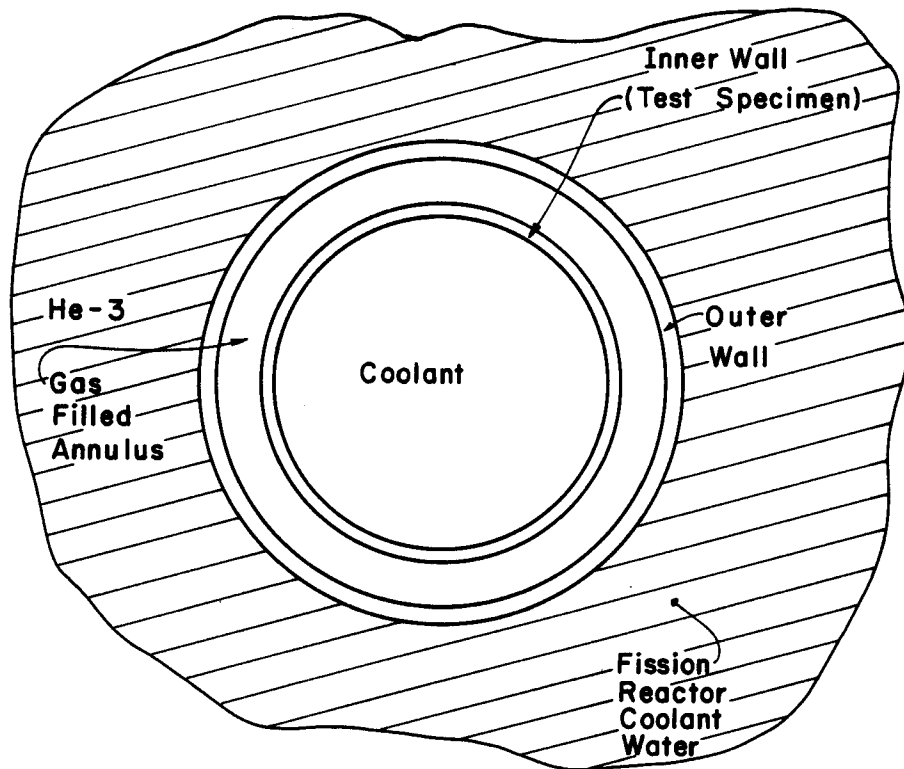


Fig. VII.D-1. Simplified schematic drawing of fusion blanket test module proposed by EG&G to be placed in the thermal fission test reactor.

inner first wall of a 1 cm thick gap filled with various pressures of He^3 gas;

- (2) To calculate the total heat flux at the same inner wall for typical operating conditions in the Experimental Test Reactor (ETR);
- (3) To calculate the total erosion rate at the inner wall;
- (4) To calculate the damage rate (dpa/sec) in the stainless steel inner wall;
- (5) To calculate the concentration of implanted protons and tritium in the stainless steel inner wall; and
- (6) To repeat the above calculations for the outer wall.

D.2. Calculational Model

D.2.1. General Features

In this study, the problem will be modeled as an infinite slab with 1 cm thick gas gap although other thicknesses could be used. An exponential variation in the $\text{He}^3(n,p)\text{T}$ reaction rate distribution will be assumed (see Fig. VII.D-2).

Consider a layer of thickness dx where protons and tritium are produced at rate given by:

$$R = \Sigma \phi_0 e^{-\Sigma(d-x)} \text{ cm}^{-3} \text{ sec}^{-1} \quad (2)$$

where Σ is the total absorption cross section (cm^{-1}),

ϕ_0 is the neutron flux incident at the outer wall ($\# \text{ cm}^{-2} \text{ sec}^{-1}$),

d is the thickness of the gas gap.

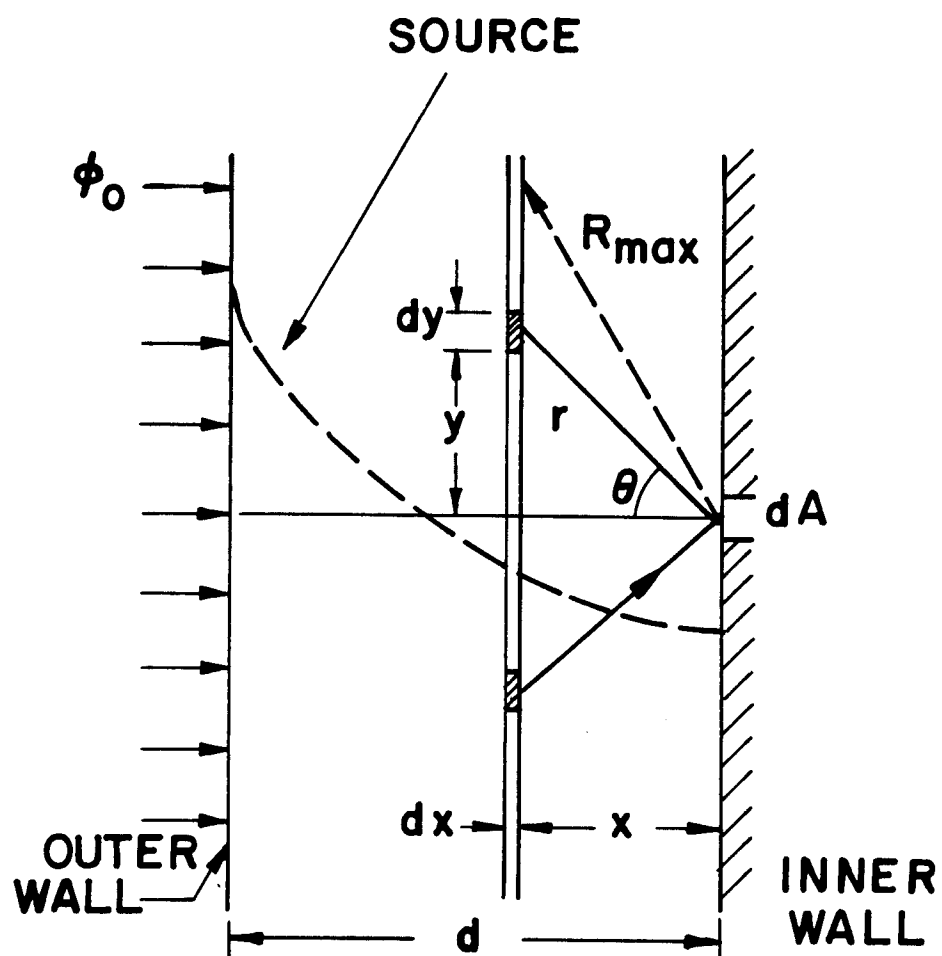


Fig. VII.D-2. Schematic representation used in modeling the problem.

The protons and tritium ions are assumed to be produced isotropically at every location y as shown in Fig. VII.D-2.

The fraction of the particles produced in the annular ring (defined by x , y , dx , dy) which start toward dA is:

$$f = \frac{dA \cos \theta}{4\pi r^2} . \quad (3)$$

The particle flux from this ring going towards dA is then given by:

$$dF_p = \Sigma \phi_o e^{-\Sigma(d-x)} \cdot 2\pi y \, dy \frac{dA}{4\pi r^2} \frac{x}{\sqrt{x^2 + y^2}} \, dx . \quad (4)$$

To get the total number of particles produced at x from the volume element between x and $x + dx$, we integrate over the annular ring:

$$F_p/dA = \frac{1}{2} \Sigma \phi_o e^{-\Sigma(d-x)} x \, dx \int_0^{\sqrt{R_{\max}^2 - x^2}} \frac{y}{(x^2 + y^2)^{3/2}} \, dy . \quad (5)$$

where: R_{\max} is the maximum range of the particles at the corresponding He^3 gas pressure,

$$x^2 + y^2 = r^2$$

and $y \, dy = r \, dr$ (at constant x) .

The flux of particles per unit area is then:

$$\begin{aligned}
 F_p/dA &= \frac{1}{2} \Sigma \phi_0 e^{-\Sigma(d-x)} x dx \int_{r=x}^{r=R_{\max}} \frac{dr}{r^2} \\
 &= \frac{1}{2} \Sigma \phi_0 e^{-\Sigma(d-x)} \left(1 - \frac{x}{R_{\max}}\right) dx .
 \end{aligned}
 \tag{6}$$

For the rest of this paper, the particle and heat fluxes will be normalized to the units of $\Sigma \phi_0$ (where ϕ_0 is the flux of incident neutrons at the outside wall, assuming no shielding from this wall), i.e.

$$F_{p_a} = \frac{1}{2} e^{-\Sigma(d-x)} \left(1 - \frac{x}{R_{\max}}\right) dx \tag{7}$$

and the units are $\left(\frac{\text{particles}}{\text{cm} \cdot \text{sec}}\right) / \left(\frac{\text{reaction}}{\text{cm}^3 \cdot \text{sec}}\right)$.

To obtain the total number of particles that reach the area element dA from all gas regions, we integrate over all the volume,

$$F_{\text{tot}} = \int_0^L F_{p_a} dx \quad (F_{p_a} = \text{flux from region between } x, x + dx) \tag{8}$$

where L is the lesser between R_{\max} and d , i.e.,

$$F_{\text{tot}} = \int_0^L \frac{1}{2} e^{-\Sigma(d-x)} \left(1 - \frac{x}{R_{\max}}\right) dx . \tag{9}$$

In fact, this last integral can be solved analytically, and the result is given by:

$$F_{\text{tot}} = \frac{1}{2\Sigma} [e^{\Sigma(L-d)} (1 + \frac{1}{\Sigma R_{\text{max}}} - \frac{L}{R_{\text{max}}}) - e^{-\Sigma d} (1 + \frac{1}{\Sigma R_{\text{max}}})] \quad (10)$$

where again L is the lesser between d and R_{max} . Again, it should be noticed that F_{tot} is normalized to the units of $\Sigma \phi_0$.

The total flux given by the last integral in Eq. 10 is strongly dependent on the He^3 gas pressure in the gap. This pressure dependence enters through the absorption cross section, Σ , and the range of the particles in the gas, i.e. R_{max} .

D.2.2. Heat Flux

The heat flux to the inner wall from the volume element between x and $x + dx$, H_x , is given by:

$$H_x = \frac{1}{2} e^{-\Sigma(d-x)} x dx \int_{r=x}^{R_{\text{max}}} E(r) \cdot \frac{dr}{r^2} \left[\frac{\text{watt}}{\text{cm}^2} / (\text{reaction}/\text{cm}^3 \text{ sec}) \right] \quad (11)$$

and the total heat flux, H_T , is given by:

$$H_T = \frac{1}{2} \int_{x=0}^L x e^{-\Sigma(d-x)} \int_{r=x}^{R_{\text{max}}} E(r) \frac{dr}{r^2} dx \quad (12)$$

where $E(r)$ is the energy that reaches the wall from particles born with energy E_0 at the volume element dx and at a distance r from the first wall.

To simplify the last integral, since straggling is negligible for light ions, we can calculate an average distance \bar{r} (defined as the average distance travelled by those particles born within the slab volume element x and $x + dx$). The energy of the particles that

traverse this distance, is $E(\bar{r})$ and the total heat flux is then given by

$$\begin{aligned}
 H_T &= \frac{1}{2} \int_0^L e^{-\Sigma(d-x)} x E(\bar{r}) \int_{r=x}^{R_{\max}} \frac{dr}{r^2} dx \\
 &= \frac{1}{2} \int_0^L e^{-\Sigma(d-x)} \left(1 - \frac{x}{R_{\max}}\right) E(\bar{r} = f(x)) dx .
 \end{aligned}
 \tag{13}$$

To get \bar{r} , we have to calculate the average distance travelled over the solid angle $d\Omega$, i.e.,

$$\bar{r} = \frac{\int_0^{\theta_{\max}} r d\Omega}{\int_0^{\theta_{\max}} d\Omega}
 \tag{14}$$

where $d\Omega = 2\pi \sin \theta d\theta$. Substituting for $r = \frac{x}{\cos \theta}$ (as shown in Fig. VII.D-3) we find,

$$\begin{aligned}
 \bar{r} &= \frac{\int_0^{\theta_{\max}} \frac{x}{\cos \theta} 2\pi \sin \theta d\theta}{\int_0^{\theta_{\max}} 2\pi \sin \theta d\theta} = \frac{x \int_0^{\theta_{\max}} \tan \theta d\theta}{\int_0^{\theta_{\max}} \sin \theta d\theta} \\
 &= x \frac{\ln \sec \theta_{\max}}{1 - \cos \theta_{\max}} .
 \end{aligned}
 \tag{15}$$

Substituting $\cos \theta_{\max} = \frac{x}{R_{\max}}$ yields

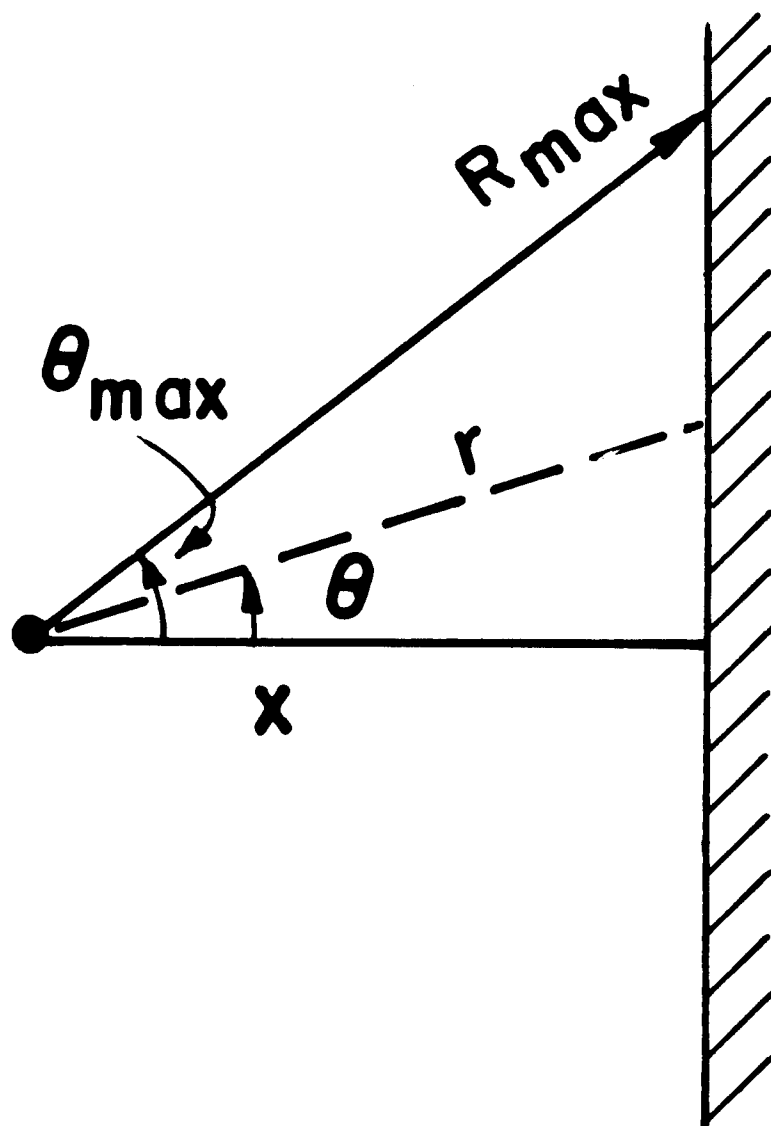


Fig. VII.D-3. Dependence of distance r on angle θ .

$$\bar{r} = x \frac{\ln (R_{\max}/x)}{(1 - \frac{x}{R_{\max}})} . \quad (16)$$

This value of \bar{r} can then be substituted into Eq. 13. On the other hand, if the energy $E(\bar{r})$ can be represented by a suitable polynomial or any other function, the entire problem can be done analytically, even without the approximation of \bar{r} .

In this study the integrals are solved numerically. The gas zone is broken up into 100 regions (i.e., each with 0.01 cm thickness). The energy of the ions reaching the inner surface was calculated in the following manner. First, the Brice⁽²⁾ formulation was used to calculate the electronic energy loss rate of the proton and tritium ions in the He³ gas. Second, the method discussed in Chapter III for light ions ($Z < 2$) is used to calculate the energy at any given distance from the point of birth. This method is valid for low atomic weight particles because the electronic loss mechanism is far greater than the nuclear energy loss mechanism down to a few keV. Because the electronic energy loss (small angle scattering) is much greater than the nuclear energy loss (large angle scattering), the total particle flux given by Eq. 8 is a good approximation. A more exact solution of the problem would require a lengthy and more expensive transport calculation.

D.2.3. Sputtering Rate

D.2.3.a. Introduction

The bombardment of the first wall in a fusion reactor by the incoming ion fluxes from the microexplosion can produce surface erosion from sputtering. This sputtering process is the result of near surface atoms which acquire sufficient momentum normal to the surface to escape the binding potential. Theories to explain the magnitude and spectra of sputtered ions have been developed. A summary of these theories and validity of their application is given by many authors, e.g., McCracken.⁽³⁾

Experimental studies indicate that the sputtering yield, i.e. the number of atoms sputtered per incident ion, shows an energy dependence which is proportional to energy at low ion energy, reaches a maximum value, and then at higher energy is inversely proportional to energy. This dependence on ion energy is in agreement with the theory of Sigmund,⁽⁴⁾ which relates the sputtering yield to the energy transferred into nuclear processes at the surface. Experimental studies also show a dependence of sputtering yield on the impact angle of the incoming ion. Bohachevsky⁽⁵⁾ developed empirical expression for this dependence. In this research the analysis for the sputtering erosion is limited to normal incident ions.

Among the many models to calculate the energy dependence of the sputtering yield is the work of Smith.⁽⁶⁾ He developed a formula which shows the proportionality to E at low energies and $1/E$ at higher energies. The sputtering yield is simply given by

$$S = \frac{C}{U_0} f_1(z, M) f_2(E, z) \quad (17)$$

where: C is an empirical constant,

U_0 is the surface binding energy,

f_1 is the mass dependence function,

f_2 is the energy dependence function.

The mass dependence function of the sputtering yield is a simple relation for the atomic number and mass dependence of the nuclear cross section which is given by:

$$f_1(z, M) = z_1 z_2 \frac{M_1}{M_2}$$

where: z_1, M_1 is the charge and mass of incident ion,

z_2, M_2 is the charge and mass of struck ion.

The energy dependence factor is given by:

$$f_2(E, z) = \frac{z_1 z_2 E}{(E + 50 z_1 z_2)^2}$$

where E is the ion energy in electron volts and the factor 50 was empirically determined from the data at the energy peak. Substituting the last two equations into the sputtering yield equation gives:

$$S = \frac{20}{U_0} z_1^2 z_2^2 \frac{M_1}{M_2} \frac{E}{(E + 50 z_1 z_2)^2} \cdot$$

D.2.3.b. Simulation Calculation

Fitting the above form of the equation to the experimental data of Sigmund⁽⁴⁾ gives

$$S(E) = 19.4 \frac{z_1^2}{z_2^2} \frac{M_1}{M_2} \frac{E}{(E + 166.8 z_1 z_2)^2}, \quad (18)$$

where $S(E)$ = sputtered atoms/ion.

For protons and tritium ions on Cu the above equation transforms to:

$$S(E) = 0.257 \frac{E(\text{keV})}{(E + 4.837)^2} \quad \text{protons} \quad (19)$$

$$S(E) = 0.771 \frac{E(\text{keV})}{(E + 4.837)^2} \quad \text{tritium} \quad (20)$$

Then the total sputtering rate, \dot{S}_T , can be given by:

$$\dot{S}_T = \frac{1}{2} \int_0^L x e^{-\Sigma(d-x)} \int_{r=x}^{R_{\max}} S(E(r)) \cdot \frac{dr}{r^2} dx. \quad (21)$$

If we use an average value of $E(\bar{r})$, and take it out of the second integral, in Eq. 21, the total erosion rate in units of [(cm/sec)/(reaction/cm³/sec)] will be given by,

$$\dot{S}_T = \frac{1}{2} S_1 \int_0^L e^{-\Sigma(d-x)} \left(1 - \frac{x}{R_{\max}}\right) \frac{E(\bar{r})}{(E(\bar{r}) + 4.837)^2} dx \quad (22)$$

where: $S_1 = 0.257$ for protons

$S_1 = 0.771$ for tritium.

It should also be noticed that the total erosion rates are normalized to units of $\Sigma \phi_0$.

D.2.4. Displacement Response

The radiation damage in the first wall of the fusion blanket test module will be due to both neutrons and ion bombardment. The damage production by the ions will be limited to the first few microns near the exposed surface and the spatial extent of the damage will be determined by the amount of energy lost in nuclear collisions at any location.

The amount of displacement damage by ions can be determined at any location in the material at which the energy of the ion is known by⁽⁷⁾

$$D(x) = F_p(x) \int_{E_d}^{\Delta E_1} \sigma(E_1, E) v(E) dE \quad (23)$$

where: F_p = local ion flux at position x ,

E_d = effective displacement energy,

ΔE_1 = maximum primary knock-on atom (PKA) energy =

$$\frac{4 M_1 M_2}{(M_1 + M_2)^2} E_1,$$

σ = cross section for transfer of energy E to PKA from ion of energy E_1 ,

$v(E)$ = number of displaced atoms from PKA of energy E .

Again, since straggling is very small for light ions, the local ion flux at any position x can be approximated by a single energy. This is even true in the region where the most of the damage occurs.

The local displacement rate can be estimated by assuming suitable cross sections in Eq. 23 and integrating. However, the spatial distribution of damage requires knowledge of the ion energy at a given location. The methods discussed in Chapter III for calculating the transport of the ions through materials with proper partitioning of nuclear and electronic energy losses are used in this simulation study. The deposition of bombarding species is also determined by these methods.

The displacement production from an arbitrary spectrum of charged particles can also be determined upon specification of the spatial and temporal distributions of the fluxes and an appropriate dpa cross section.

Two alternative procedures for calculating an appropriate displacement cross section. The first is a binary Rutherford interaction model which accounts for the effective charge of the ion. The second is the Lindhard (LSS)⁽⁸⁾ model based on a Thomas-Fermi potential.

In the Rutherford interaction model, the differential cross section is given by

$$d\sigma(E) = \frac{BY^2}{E} \frac{dT}{T^2}$$

where: $B = \frac{4\pi a_0^2 M_1 z_1^2 z_2^2 E_r^2}{M_2}$

a_0 = Bohr radius = 0.53 Å

E_r = 13.6 eV

T = PKA energy

γ = effective charge given by Bichsel⁽⁹⁾ as:

$$\exp(-1.316y + 0.112y^2 - 0.0650y^3)$$

$y = 100\beta/z_1^{2/3}$

$\beta = v/c$

v = ion velocity

c = velocity of light.

A displacement cross section can be determined from the differential cross section if the number of displacements produced by a PKA of energy T can be obtained. This is usually accomplished by the selection of an energy partition model and a secondary displacement model.

The energy partition model accounts for the relative distribution of the PKA energy loss between the electrons and nuclei. The latter process is the only one used in determining displacements. A convenient form which approximates the function discussed in LSS theory is given by Robinson⁽¹⁰⁾ as

$$T_{\text{damage}} = \frac{T}{g(\epsilon)} \quad (24)$$

where

$$g(\epsilon) = 1 + k\epsilon + 0.40244k\epsilon^{3/4} + 3.4008k\epsilon^{1/6} \quad (25)$$

k = LSS stopping parameter which for PKA's is

$$k = 0.1337 z_1^{2/3} / A^{1/2}$$

A = atomic mass

ϵ = Lindhard reduced energy = T/E_L

$$E_L = 0.08693 z_1^{7/3}$$

The secondary displacement model accounts for the displacements produced in a cascade of a PKA with a specified damage energy. This number of displacement is given by⁽¹¹⁾

$$\begin{aligned} N_d &= 0 & T < E_d \\ N_d &= 1 & E_d \leq T < 2 E_d \\ N_d &= \frac{0.8}{2E_d} T_{\text{dam}} & 2E_d \leq T \end{aligned} \quad (26)$$

where E_d is the displacement energy. Combining Eqs. (24), (25), and (26) yields the displacement cross section as

$$\sigma_d(E) = \frac{BY^2}{E} \left\{ \int_{E_d}^{2E_d} \frac{dT}{T^2} + \int_{2E_d}^{T_{\text{max}}} \frac{0.8}{2E_d} T \frac{dT}{g(T)} \right\} \quad (27)$$

where $T_{\text{max}} = \Lambda E_i$.

Another method for calculating the displacement damage in terms of dpa cross section is to use the nuclear stopping power derived in LSS theory. The major difference between this approach and the modified Rutherford method discussed above is the treatment of electron

screening. In the LSS model, the screening is treated explicitly by assuming an interaction potential based on Thomas-Fermi model. On the other hand the modified Rutherford model accounts implicitly for screening by allowing the charge of the moving ion be a function of the energy.

The differential cross section based on the LSS model was given in Chapter III (Eq. 3), in terms of the Lindhard tabulated screening function. Winterbon et al.,⁽¹²⁾ also give the analytic approximation

$$d\sigma(E) = \frac{\pi a^2}{2} \lambda t^{-4/3} [1 + (2\lambda t^{2/3})^{2/3}]^{-3/2} dt \quad (28)$$

where: $\lambda = 1.309$

$$t = \epsilon^2 T / T_{\max} = \epsilon^2 \sin^2 \theta / 2$$

$$a = 0.468 (z_1^{2/3} + z_2^{2/3})^{-1/2} \text{ \AA}$$

$$\epsilon = E / E_L$$

$$E_L = \frac{1 + A}{A} \frac{z_1 z_2 e^2}{a}$$

$$A = M_2 / M_1$$

$$T = \text{PKA energy}$$

$$E = \text{ion energy.}$$

A more complete description of the nuclear energy loss calculation using these cross sections is given by Hunter.⁽¹³⁾

D.3. Computational Procedure

A computer code, A*IDAHO,⁽¹⁴⁾ (a part of A*THERMAL code) has been developed to calculate the steady-state values of particle and heat flux to the wall. The erosion rate, spatial distribution of

implanted particles, and damage rate of both the inner and outer walls can be calculated from this code for any value of He^3 gas pressure. Output from this code can be obtained in either tabulated form or in a graphical form, but in this paper we will only present the graphical results.

D.4. Results and Observations

Results of two different He^3 gas pressures, 1 and 32.7 atmospheres, in the annulus between the specimen and the outside of the module are presented here. (The latter number corresponds to 480 psi originally proposed for the experiment.⁽¹⁾) Calculations for other values of pressure are given in Ref. (15). The variation in the particle flux, heat flux and erosion rate with pressure will be shown both for the inner and outer wall. The results are given in several different ways:

- A) The differential particle flux as a function of energy to the first inner wall per unit of $\Sigma \phi_0$ for both protons and tritium ions.
- B) The differential heat flux to the first inner wall per unit of $\Sigma \phi_0$ as a function of energy for both protons and tritium ions.
- C) The spatial concentration, per unit of $\Sigma \phi_0$, of both protons and tritium particles implanted into the stainless steel inner wall.
- D) The damage rate, (displacement per atom per second (dpa/sec)), per unit of $\Sigma \phi_0$ from both protons and tritium ions as a function of distance into the stainless steel inner wall.

E) The same calculations above but for the outer wall of the blanket test module.

The graphical representation of the results (Figs. VII.D-4 through VII.D-11) begins by showing the particle and heat flux for both protons and tritium. This is followed by the concentrations of the particles and the displacement rate in the stainless steel wall for both protons and tritium. Then the calculations are repeated for the outer wall of the blanket test module at the same He^3 gas pressure in the annulus. Finally, the above calculations are given for 1 and 32.7 atm of He^3 gas.

The variations of the total particle flux, total heat flux and the erosion rate with He^3 gas pressure are shown in Figs. VII.D-12 through VII.D-14 for both protons and tritium. In these calculations we have used $\phi_0 = 2.5 \times 10^{14}$ neutrons/cm² · sec, a typical value for ETR. The results could be easily adjusted to other values characteristic of different reactor environments.

D.5. Observations

D.5.1. Particle and Heat Flux

1. Because of the higher energy of the protons (i.e., longer range in the helium gas) the flux of the protons to the walls will be greater than for the tritium ions.
2. The total particle flux on the inside wall is maximum at ~ 4 atm of He^3 gas and it is significantly reduced at 32.7 atm.

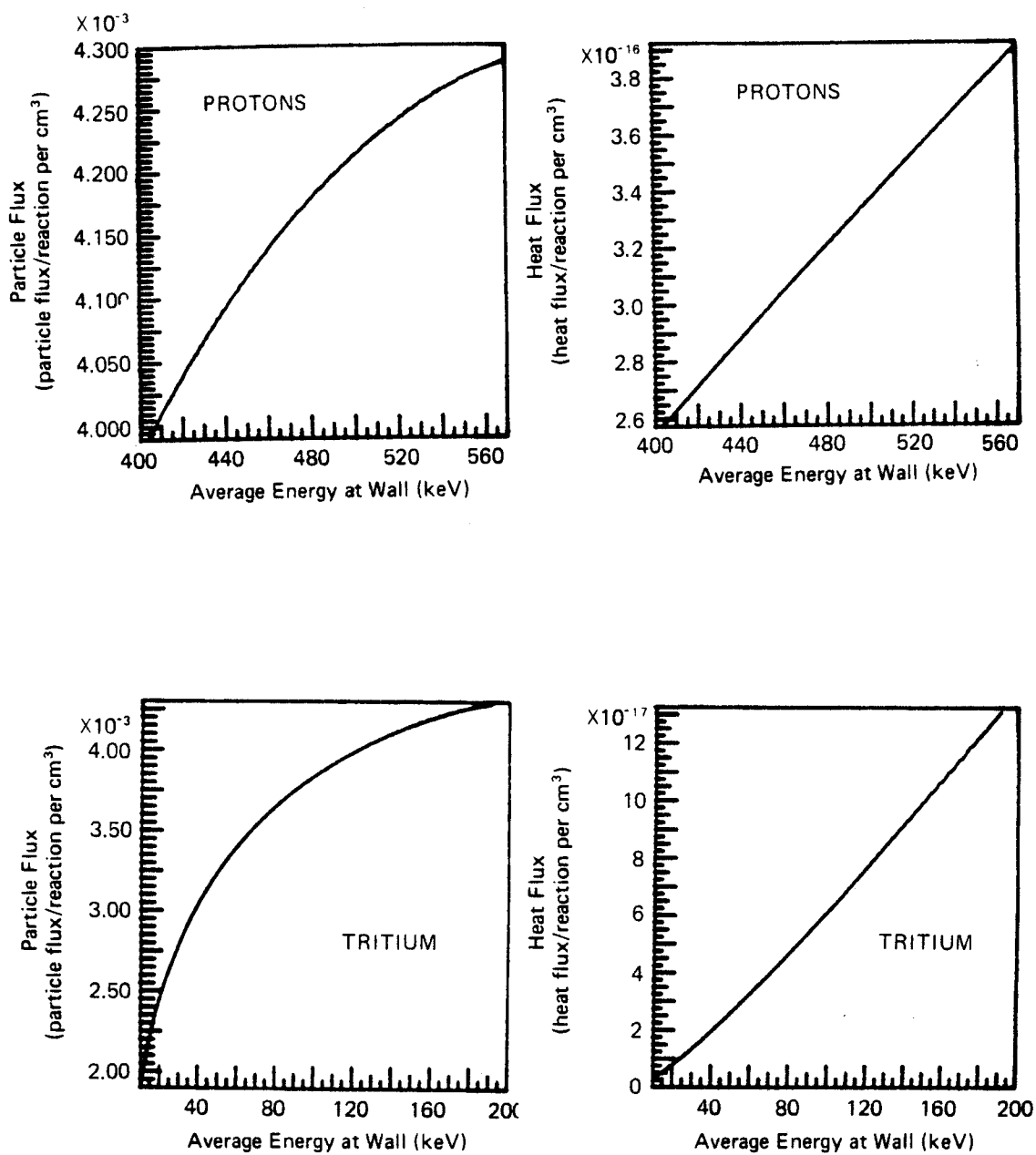


Fig. VII.D-4. Particle and heat flux to the inside wall at 1.0 atm of He^3 gas for protons and tritium.

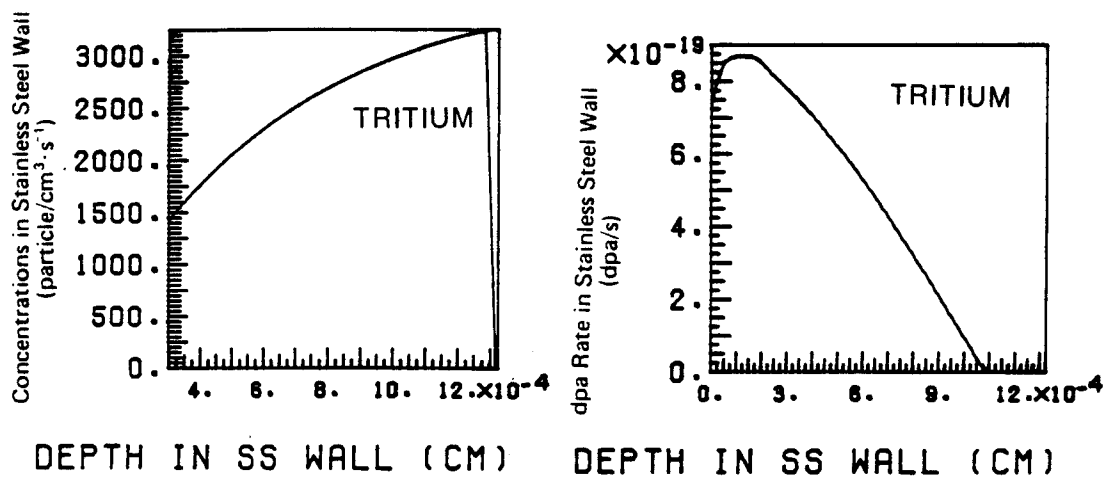
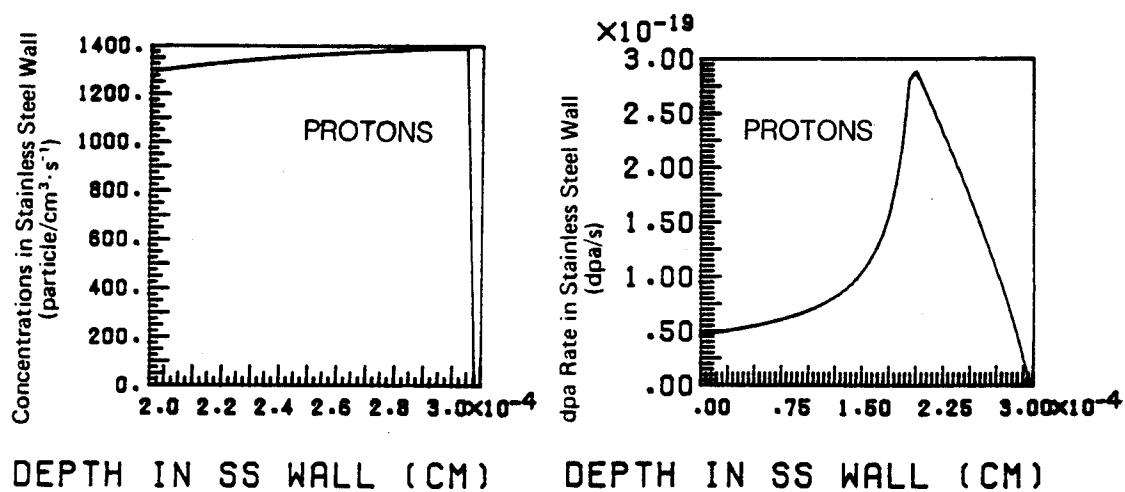


Fig. VII.D-5. Implantation and damage rate to the inside wall at 1.0 atm of He³ gas for protons and tritium.

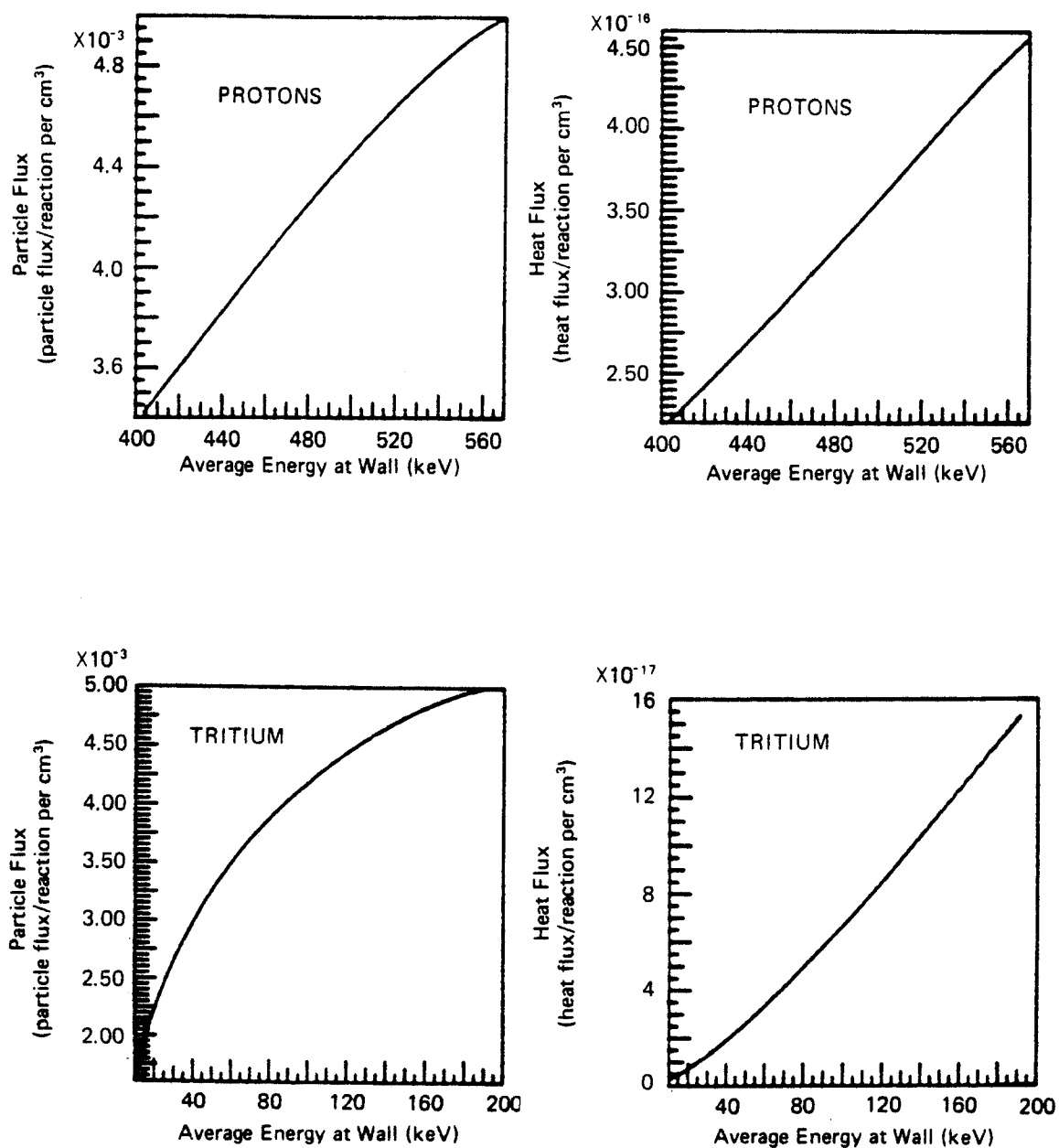
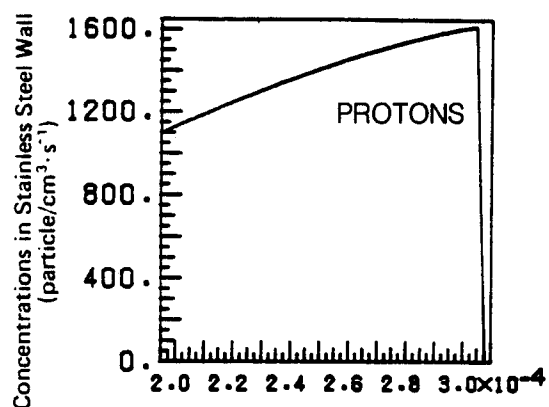
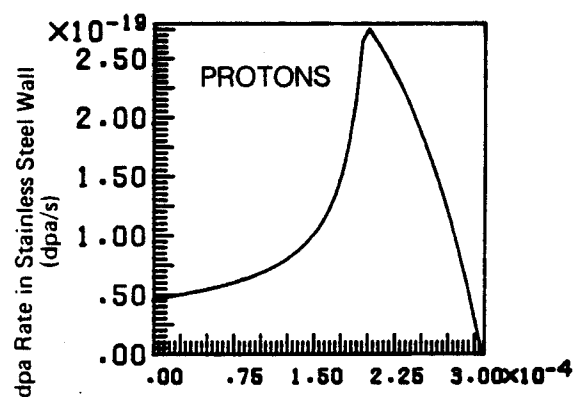


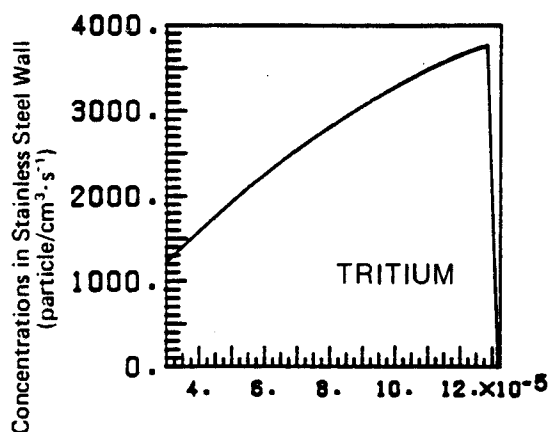
Fig. VII.D-6. Particle and heat flux to the outside wall at 1.0 atm of He^3 gas for protons and tritium.



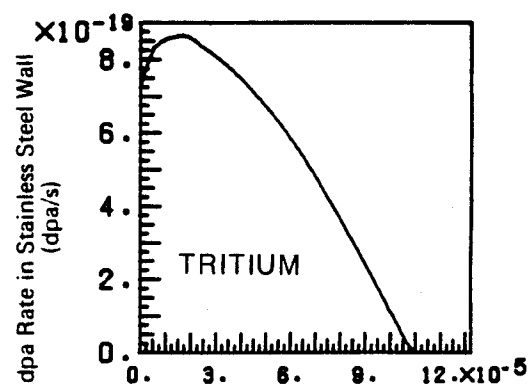
DEPTH IN SS WALL (CM)



DEPTH IN SS WALL (CM)



DEPTH IN SS WALL (CM)



DEPTH IN SS WALL (CM)

Fig. VII.D-7. Implantation and damage rate to the outside wall at 1.0 atm of He³ gas for protons and tritium.

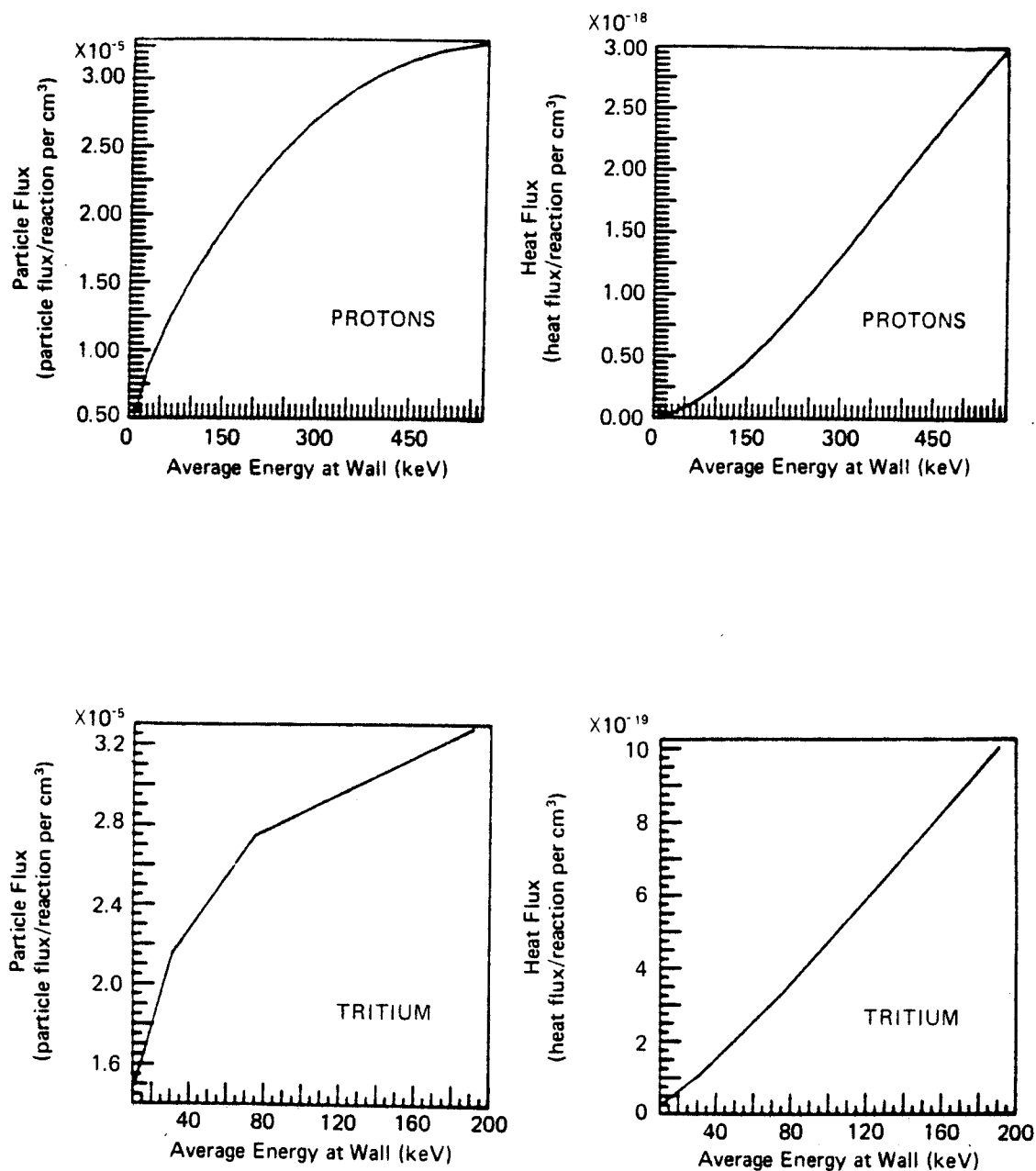


Fig. VII.D-8. Particle and heat flux to the inside wall at 32.7 atm of He^3 gas for protons and tritium.

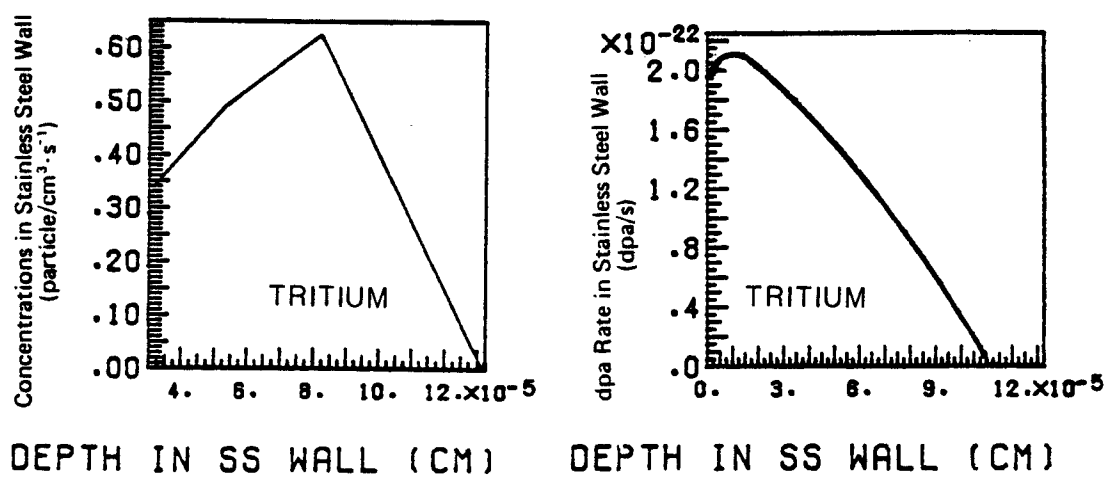
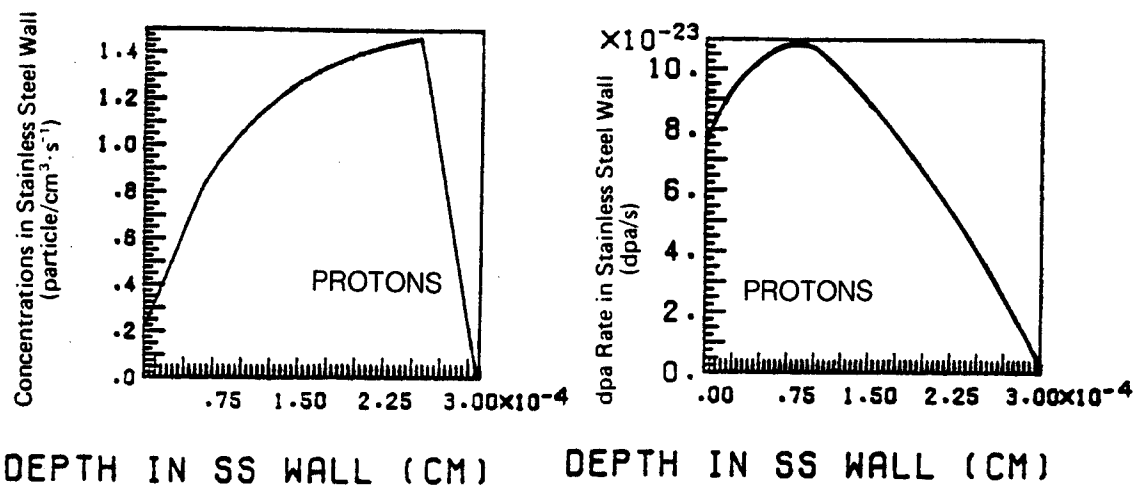


Fig. VII.D-9. Implantation and damage rate to the inside wall at 32.7 atm of He³ gas for protons and tritium.

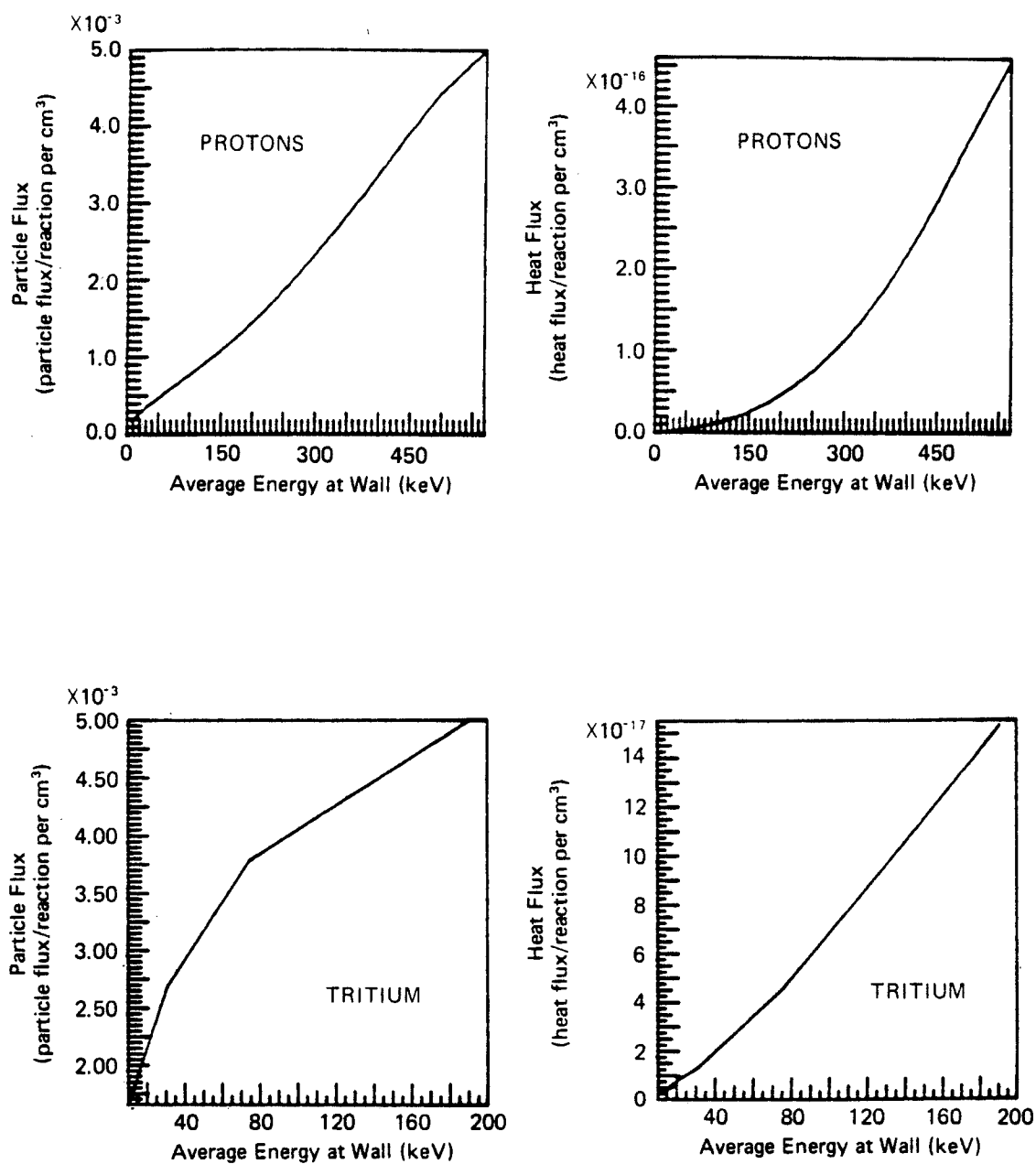


Fig. VII.D-10. Particle and heat flux to the outside wall at 32.7 atm of He^3 gas for protons and tritium.

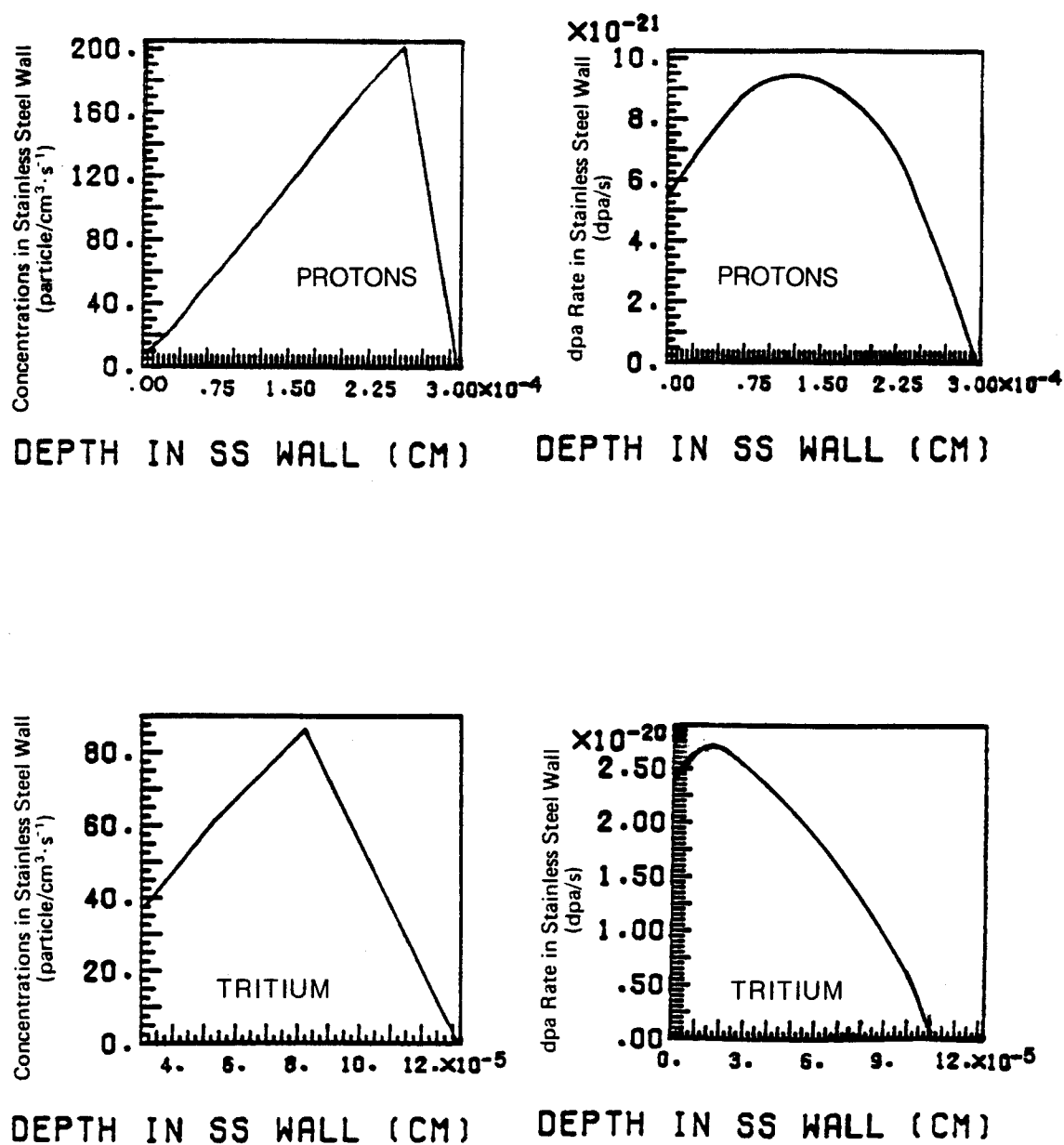


Fig. VII.D-11. Implantation and damage rate to the outside wall at 32.7 atm of He³ gas for protons and tritium.

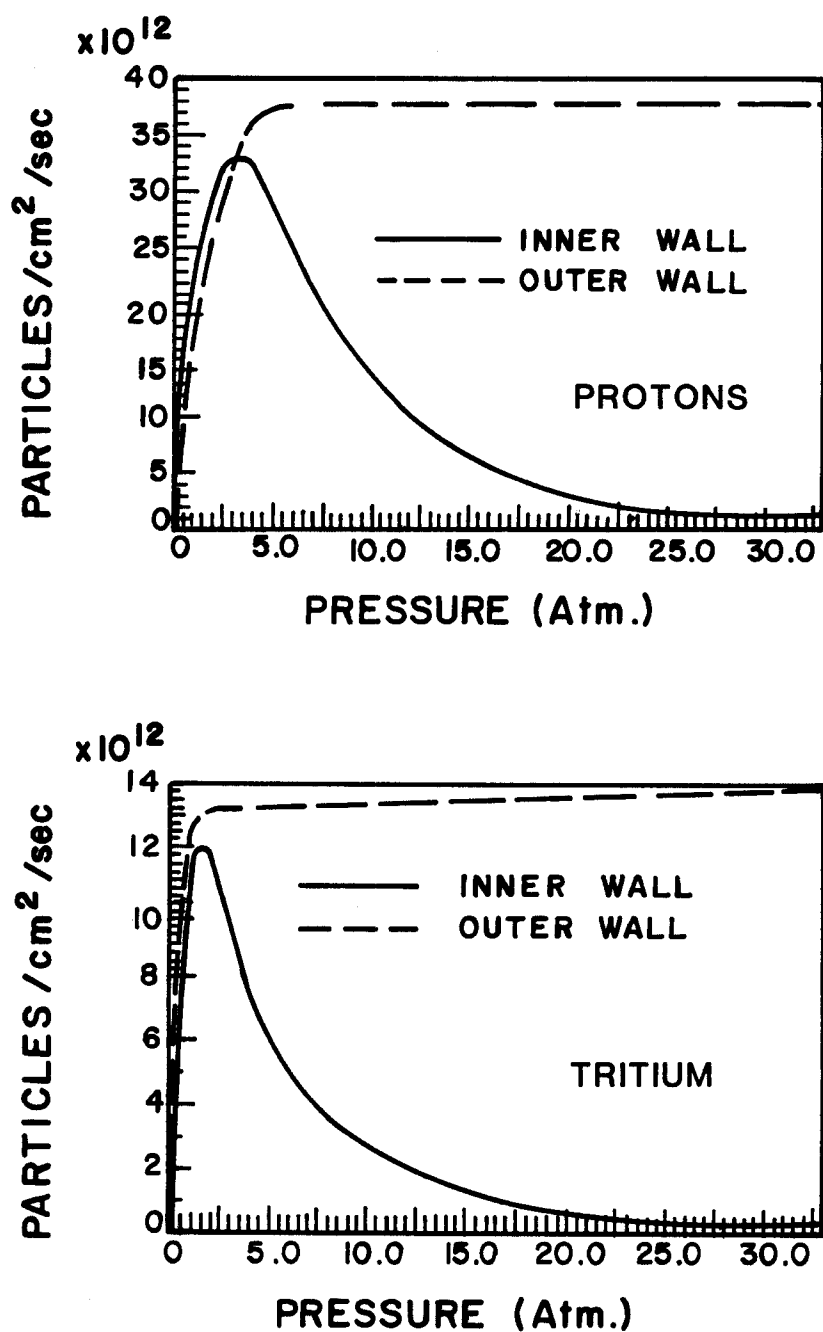


Fig. VII.D-12. Total particle flux as a function of He³ gas pressure at the inside and outside wall for protons and tritium.

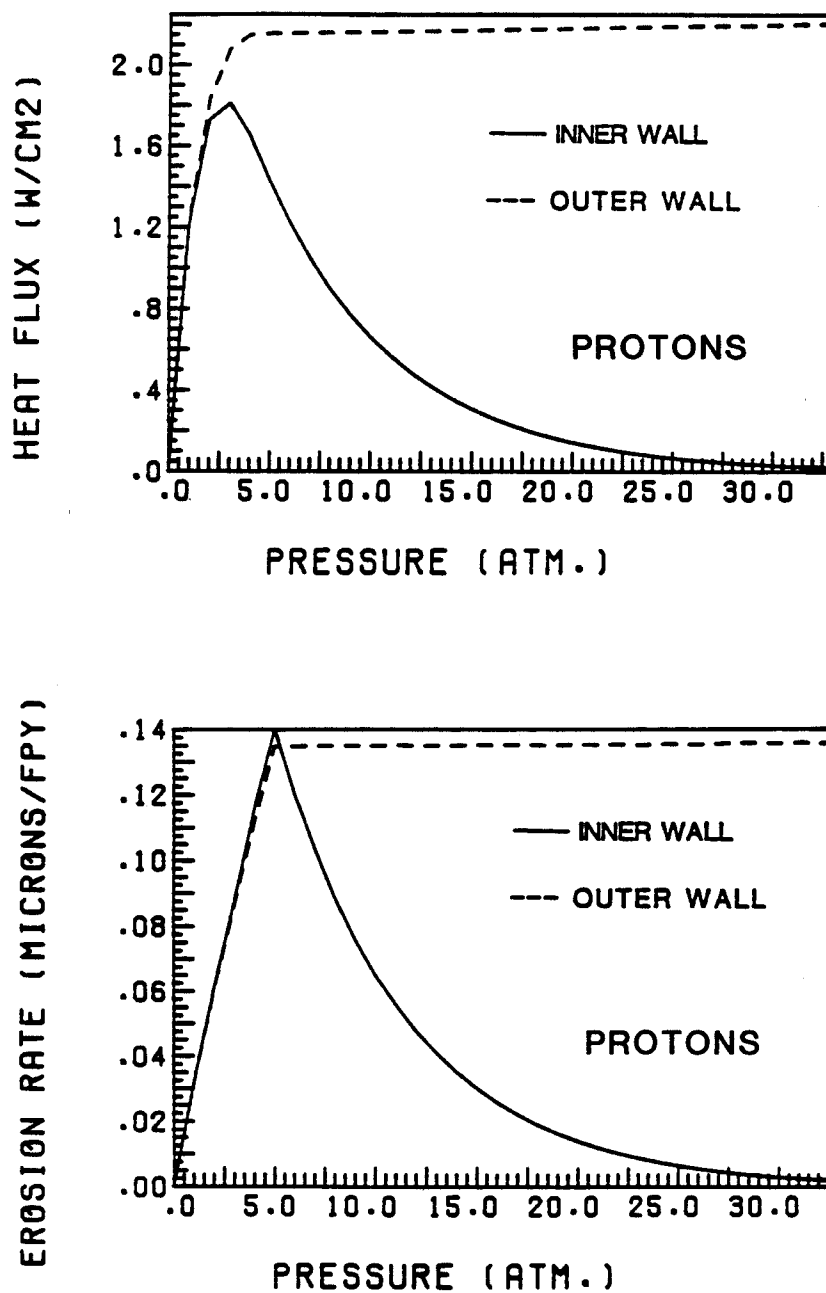


Fig. VII.D-13. Heat flux and erosion rate as a function of He^3 gas pressure for protons.

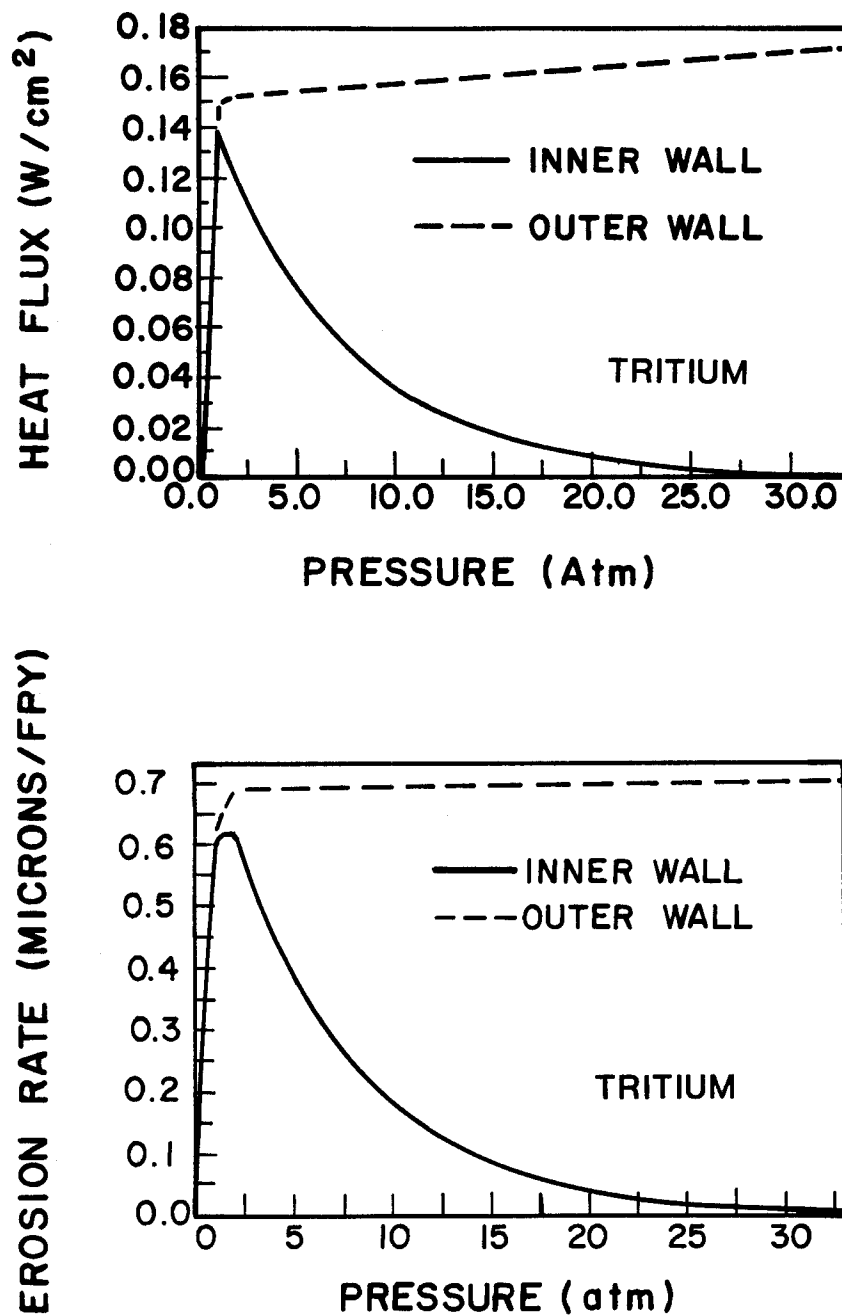


Fig. VII.D-14. Heat flux and erosion rate as a function of He^3 gas pressure for tritium.

3. The maximum particle flux of the high energy protons (e.g. 500 keV) is roughly twice those of lower energy (~ 100 keV) on the inside wall.
4. The heat flux of the protons is much higher than that for tritium since the average energy and particle flux is higher for protons.
5. The particle and heat flux to the outer wall are both rather insensitive to the He^3 gas pressure above 3 atm.
6. Both the particle and heat flux to the outer wall are higher than those at the inner wall for both protons and tritium. This is because the particle production rate due to the neutronic reaction, $\text{He}^3(\text{n},\text{p})\text{T}$, is higher near the outer wall.

D.5.2. Erosion Rate

1. Unlike the particle and heat flux, which are dominated by the protons, the erosion rate is dominated by the tritium ions. This is because of the higher sputtering coefficient of tritium at lower energies.
2. The erosion rate for the outer wall is also relatively insensitive to the gas pressure above 3 atm. In fact, it increases slightly with pressure in contrast to the case for the inner wall. This is because the reaction rate increases slightly faster than the slowing down of the particles in the gas at higher pressures.
3. For protons on the inside wall (which can be seen better from tabulated data), the particle flux is a maximum around 4 atm and the heat flux is a maximum around 3 atm, while the erosion rate

is a maximum at around 5 atm. This can be explained as follows. The maximum value of the heat flux depends on the product of both the particle flux and the energy spectrum of the particles at the inner wall. The energy of the particles at the inner wall is higher at lower pressures because of reduced energy loss in the gas and the particle flux is peaked around 4 atm (it is sharply decreased at lower and higher pressures). The combination of these two effects explains why the heat flux peaks around 3 atm, a value slightly lower than the corresponding value for the peak particle flux (i.e. 4 atm). In case of the erosion rate, the maximum value is increased towards higher pressures because the energy at the inner wall is lower and consequently, the erosion rate is higher. And, again, because the particle flux decreases sharply at higher pressures, i.e., the maximum of the erosion rate is increased slightly towards higher pressures, i.e., around 5 atm.

4. In any case, for a typical ETR flux ($\phi_0 = 2.5 \times 10^{14}$ neutrons/cm²·sec) the total erosion rate is about 1 micron per FPY (Full Power Year) which is still very small compared to values expected in fusion reactor first walls, namely about 100 to 1000 microns/FPY.

D.5.3. Implantation

1. The concentration of protons and tritium atoms in the outside wall is about twice that of the inner wall at low pressure (5

atm) and is much higher at higher pressures (32.7 atm) (see Refs. 15 and 16 for more details).

2. The maximum concentration of protons in the walls is greater than the concentration of the tritium even though the range of the tritium ions is about 3 times lower than that for protons.
3. The high concentration of protons and tritium inside both the inner and outer walls might cause blistering.

D.5.4. Damage Rate

1. Tritium ions produce the highest displacement rates for both the inner and outer walls.
2. The maximum dpa rate for tritium occurs almost at the surface for both walls.
3. For protons, the highest dpa rate occurs between 0.7 microns to 2.0 microns from the surface depending on the energy flux corresponding to a particular He^3 gas pressure.
4. A typical value for dpa rate ($\phi_0 \approx 2.5 \times 10^{14}$ neutrons/cm²·sec) is about 4×10^{-5} dpa/sec which is about 400 times higher than that due to neutron irradiation in fusion reactors.

D.6. Conclusions

We have examined the potential for performing fusion first wall testing in a fission reactor as proposed by Hsu et al.⁽¹⁾ Preliminary results from the test case show that a number of important fusion technology issues could be tested experimentally in a high power thermal fission reactor. In terms of particle and heat flux, we found that a layer of He^3 gas can provide a considerable amount of

surface heating. The surface and bulk heating in the first wall can be correlated with He^3 pressure and reactor power to give temperature profiles similar to those expected in fusion reactors. The total erosion rate, of about 1 micron/FPY for a typical ETR flux, is still very small compared to values expected in fusion first walls. On the other hand, critical issues of high hydrogen implantation and possible causes of blistering can be examined easily with such a facility because of the high particle flux. The concept clearly warrants further study.

References for Section VII.D

1. P.Y.S. Hsu et al., Fusion Technology Development - First Wall/Blanket Systems and Component Testing in Existing Nuclear Facilities, EGG-FT-5281, December 1980, Idaho National Engineering Laboratory.
2. D.K. Brice, Physical Review A 6, No. 5, 1791, (Nov. 1972).
3. G.M. McCracken, "Behavior of Surfaces under Ion Bombardment," Rep. Prog. Phys. 38, (1975).
4. P. Sigmund, "Theory of Sputtering I. Sputtering Yield of Amorphous and Polycrystalline Targets," Phys. Rev. 184(2), (August 1969).
5. I.O. Bohachevsky and J.F. Hafer, "Dependence of Sputtering Erosion on Fuel-Pellet Characteristics," LA-6991-MS, Los Alamos National Laboratory, (November 1977).
6. D.L. Smith, "Physical Sputtering Model for Fusion Reactor First-Wall Materials," Trans. Am. Nucl. Soc. 27, (1977) 265.
7. D.R. Olander, Fundamental Aspects of Nuclear Reactor Fuel Elements, TID-26711-P1, USERDA, 1976.
8. J. Lindhard et al., "Range Concepts and Heavy Ion Ranges, " Mat. Fys. Medd. Dan. Vid. Selsk. 33(14), (1963) 3.
9. H. Bichsel, "Passage of Charged Particles Through Matter," American Institute of Physics Handbood, 3rd Ed., (1972) 8-142.
10. J.W. Corbett and L.C. Ianniello, eds., "Radiation-Induced Voids in Metals," National Technical Information Service, CONF-710601, (April 1972), 397.
11. D.G. Doran et al., "Report of the Working Group on Displacement Models and procedures for Damage Calculations," HEDL-TME 73-76, Hanford Engineering Development Laboratory, December 1973.
12. K.B. Winterbon, P. Sigmund and J.B. Sanders, "Spatial Distribution of Energy Deposited by Atomic Particles in Elastic Collisions," Kgl. Danske Videnskab. Selskab. Mat-Jup. Medd. 37(14), (1970).
13. T.O. Hunter and G.L. Kulcinski, "Description of the Response of Materials to Pulsed Thermonuclear Radiation (Part 2)," UWFD-217, University of Wisconsin, Madison, (Oct. 1977).
14. A.M. Hassanein and G.L. Kulcinski, to be published.

15. A.M. Hassanein, G.L. Kulcinski, and G.R. Longhurst, "Heat Flux, Erosion Rate, Implantation, and Damage Rate to the Walls of the EG&G Fusion Blanket Test Module," UWFD-389, University of Wisconsin, Madison (Oct. 1980).
16. A.M. Hassanein, G.L. Kulcinski, and G.R. Longhurst, "Simulation of Fusion First Wall Environments in Fission Reactors," accepted for publication in Nucl. Tech./Fusion, Sept. 1981.

CHAPTER VIII

SUMMARY AND CONCLUSIONS

This thesis provides the basis for a general, comprehensive set of models which can be used to determine the dynamic transient thermal response and erosion of materials subject to many different radiation species in both inertial and magnetic fusion reactors. Previously developed models for ion energy deposition are substantially modified and improved to assure conservation of energy between the incident ion energy content and the total energy deposited into the material. Large differences in both the temporal and spatial dependence of the energy deposition profile between the procedure developed in this thesis and previous models which did not satisfy energy conservations were observed.

More precise models are developed to calculate the temperature increase. These models take into account possible phase changes, the variations of thermal properties with temperature for both solid and liquid phases, and other boundary conditions, such as thermal radiation losses. The solution of the heat conduction equation is developed with two moving boundaries; one for the melt-solid interface, and one for the evaporating surface.

Models to calculate the amount of material evaporated during large energy depositions from different kinds of radiation species are also developed. These models are based on time dependent kinetics and transport theory to account for recondensation flux.

A model is developed to study the "self-shielding" or the stopping of the incoming ions by the vapor species of the vaporized first wall. The effect of this shielding on the net amount of material vaporized is most notable in the reduction of the erosion rate.

The temperature rise due to radiation energy deposition into a first wall material is also calculated using the methods of Green's function. A new method has been developed to avoid the singularities associated with the Green's function. Several models for calculating the temperature increase are discussed using this new technique. An approximate solution for the nonlinear heat conduction equation using perturbation theory in which the specific heat and the thermal conductivity vary linearly with temperature is developed.

A method has been developed to solve the heat conduction problem with moving boundaries and other boundary conditions also by the use of the Green's function. This method is compared to the finite difference solution of the same problem developed in this thesis to calculate the temperature rise, the velocity of the receding surface and the material evaporated from sudden deposition of energy.

All the models developed for the transient responses of materials are incorporated into the A*THERMAL computer code. This code can be used to study energy depositions, thermal effects and erosion rates for various materials subject to various radiation spectra in ICF reactors or to a wide range of heat fluxes resulting from plasma disruption in magnetic fusion reactors. Response to a complete set of radiation spectra incident instantaneously on an ICF first wall

can be obtained. This set may consist of x-rays, heat flux (e.g., from cavity gas reradiation), and several light and heavy ions. In addition parametric studies are performed for characteristic photon and ion spectra. Parametric studies to investigate the response of different materials to plasma disruptions in magnetic fusion reactors are performed for a wide variations of input heat fluxes and disruption times. Data are presented for the response of stainless steel, carbon, and molybdenum.

Various applications of the models developed in this thesis are used to study the performance of materials to fusion reactor environments. These applications first include the thermal response and evaporation of first wall, in a gas filled cavity for protection, from unattenuated target x-rays and from reradiation emitted by the cavity gas. The conclusions from each application are given below.

A. Conclusions from Application of Models to ICF Reactor

1. The parametric study of first wall evaporation from x-rays shows that the lower x-ray attenuation coefficient of carbon gives it an advantage over stainless steel as a permanent first wall material. It is also shows that softer x-rays have a greater tendency to induce evaporation than hard x-rays. Therefore, for targets which produce large amounts of x-rays, a low Z material first wall will offer better protection than high Z material wall.

2. Evaporation from gas reradiation shows that the low vapor pressure of carbon causes it to have a lower evaporative erosion rate than stainless steel.
3. The evaporative erosion of carbon could increase as the time over which energy is reradiated by the gas increases if heat conduction is too sluggish. This phenomena is not observed for SS because of its relatively higher thermal conductivity.
4. As the ambient buffer gas density in the cavity increases, the evaporative erosion decreases. The reduction is more pronounced for high Z gases than low Z gases.

B. Conclusions from Application of Models to Study Plasma

Disruptions in Magnetic Fusion Reactors

1. Significant melting or evaporation occurs only above a characteristic energy flux. This threshold depends on both the material and the rate of energy deposition.
2. At high input energies it is found that the recondensation flux causes more evaporation than in the case where no condensation flux is assumed.
3. Vapor shielding, i.e. the stopping of plasma ions by the vapor, leads to a significant reduction of the material evaporated in a disruption.
4. At lower energies, near the threshold, vapor shielding tends to decrease both the melt layer thickness and evaporated material. However, at energy fluxes higher than the threshold, vapor

shielding decreases the evaporation and slightly increases the melting thickness.

5. The melt layer thickness is largely affected by vapor shielding only for materials with high melting points.
6. The lower the disruption times, the larger the material evaporated and the thinner the melted material layer.
7. Evaporation from Mo is substantially less than for both stainless steel and carbon at the same input energy densities, disruption times, and initial temperature.
8. When the total energy deposited is kept constant but the disruption time is varied, it is found that the total thickness of evaporated and melted material remains almost constant for small disruption times. However, it increases with disruption time above 1 ms until it reaches a maximum value characteristic of the material. For this characteristic time value, the evaporation has become negligible, and all the deposited energy is dissipated in melting and conduction. For disruption times greater than this characteristic value, the melt layer thickness decreases sharply due to thermal conduction of the energy.
9. For equal energy deposition and disruption times, the surface melt duration is shorter for a triangular pulse than for a square pulse. On the other hand, the amount of evaporated material and the maximum surface temperature reached are significantly higher for the triangular pulse.

10. Fusion devices which cannot stand more than 1 cm erosion per 1000 disruptions are limited to less than 180 J/cm^2 in 20 ms or 100 J/cm^2 in 5 ms. For INTOR level energy fluxes ($300\text{--}600 \text{ J/cm}^2$) the first wall may be eroded away in 30 to 100 disruptions if the melt layer is unstable.

C. Conclusions from the Models Developed Using the Green's Function Solution

1. The agreement of the moving boundary solution developed by the Green's function and by finite difference methods developed in this thesis is very good and the difference in the results is less than 3%.
2. The variations of the thermal properties with temperature can be very important in calculating accurate temperatures, especially in the case of very high energy depositions or if the material undergoes a change of phase.
3. Because of the highly nonlinear dependence of the receding surface velocity on the surface temperature, a small variation in calculating the surface temperature could result in large differences in the surface velocity and consequently larger differences in calculating the total material removed from the surface by evaporation.

D. Conclusions from Simulation of Fusion First Wall Environment in Fission Reactors

1. A number of important fusion technology issues could be tested experimentally in a high power thermal fission reactor.

2. A layer of He^3 gas can provide a considerable amount of surface heating due to the $\text{He}^3(n,p)\text{T}$ reaction. The surface and bulk heating in the first wall can be correlated with He^3 pressure and reactor power to give temperature profiles similar to those expected in fusion reactors.
3. The total erosion rate, of about 1 micron/FPY for a typical ETR flux, is still very small compared to values expected to fusion first walls.
4. Much higher values for damage rate (dpa) can be obtained with this facility than those due to neutron irradiation in fusion reactors.
5. Critical issues of high hydrogen implantation and possible causes of blistering can be examined easily with such a facility because of the high particle flux.

E. Other Applications and Future Work

The methods of analysis developed in this thesis can provide the basis for numerous investigations of the effect of deposition and thermal response on subsequent material behavior. Stress calculations, plastic deformations, and lifetime analysis are some of these issues that could be studied more precisely as a result of this analysis. Laser annealing of materials such as semi-conductors is another example applied directly as a result of this work.

The need for more precise data such as target spectra in ICF reactors is very important. Currently, the most pertinent data is classified and researchers are forced to perform parametric studies

which diffuse the issues and make any definite conclusions difficult to assess. Also, the characteristics of beam transmission in a background gas should be investigated more.

In magnetic fusion reactors the physics of disruptions should be analyzed more precisely. This includes mode of plasma energy transmitted to the wall, fraction of surface area over which disruption takes place, and disruption time. More studies should be done in the area of melt layer stability under the existing forces in the fusion reactors. Of these forces are the effect of magnetic field, gravity, and ablation pressure. Another area of research which needs more investigation is the vapor shielding. More careful analysis of the effect of magnetic fields on the ionized particles is also needed.